NASA Technical Memorandum 86390

Active and Passive Microwave Measurements in Hurricane Allen

Victor E. Delnore, Gilbert S. Bahn,
William L. Grantham, Richard F. Harrington,
and W. Linwood Jones

NOVEMBER 1985

NASA

NASA Technical Memorandum 86390

Active and Passive Microwave Measurements in Hurricane Allen

Victor E. Delnore and Gilbert S. Bahn
PRC Kentron, Inc.
Hampton, Virginia

William L. Grantham and Richard F. Harrington
Langley Research Center
Hampton, Virginia

W. Linwood Jones
Harris Corporation
Melbourne, Florida

National Aeronautics
and Space Administration

**Scientific and Technical
Information Branch**

1985

CONTENTS

ACKNOWLEDGMENTS

The airborne microwave remote sensing of Hurricane Allen was a considerable undertaking. This field experiment and the subsequent analysis reported here were possible only through the efforts of several persons with whom the authors have had the pleasure of working. R. W. Burpee, D. P. Jorgensen, F. D. Marks, and H. E. Willoughby, of the NOAA National Hurricane Research Laboratory, contributed calculations pertaining to the behavior of the storm. H. W. Davis, F. J. Merceret, and T. Schricker, of the NOAA Research Facilities Center, assisted in the interpretation of data from the aircraft digital systems. C. L. Britt and P. R. Schaffner, of Research Triangle Institute (RTI), and K. K. Kiley, formerly of RTI, provided the post-mission recovery and initial processing of the microwave data tapes. R. H. Couch, A. E. Cross, J. C. Fedors, D. P. Oliver, and H. F. Thornton, of the NASA Langley Research Center (LaRC), A. L. Jones, formerly of LaRC, and C. A. Lipp, of PRC Kentron, Inc., developed, built, installed, and prepared for flight many of the subsystems of the two microwave instruments. Also, Mr. Couch and Mr. Oliver assisted in the operation of those instruments during the penetrations of Hurricane Allen.

C. T. Swift, of the University of Massachusetts, and P. G. Black, of the National Hurricane Laboratory, were responsible for much of the interagency coordination which resulted in the Hurricane Allen field experiment and subsequent analysis. Of particular note is Dr. Black's contribution of the NOAA rain radar calculations and navigational data.

SYMBOLS AND ABBREVIATIONS

A,B	footprint dimensions perpendicular to and along flight path, respectively
A_t	effective area of antenna footprint on surface
c	speed of light
f	frequency
G	antenna gain (dimensionless)
h	aircraft altitude
L	miscellaneous waveguide losses (dimensionless)
N	number of independent samples
P_r, P_t	received and transmitted power, respectively
R	slant range
$T_{A,1}, T_{A,2}$ $T_{A,3}, T_{A,4}$	antenna brightness temperatures at the four radiometer frequencies (4.498, 4.994, 5.586, and 6.594 GHz)
U_{ins}	flight level INS wind speed
U_r	flight level radiometric wind speed
V_g	ground speed of aircraft
V_c	output voltage of integrator during calibration
V_s	output voltage of integrator during surface observation
Z	reflectivity factor (dimensionless)
α_c	programmable attenuation during calibration (dimensionless)
α_ℓ	receiver calibration loop attenuation (dimensionless)
α_s	programmable attenuation during surface observation (dimensionless)
β_d	Doppler bandwidth of received power
β_{eq}	effective pencil-beam antenna width
θ	incidence angle
λ	wavelength
σ^o	normalized radar cross section

τ opacity due to rain and clouds (dimensionless); also, integration time, sec

χ horizontal angle between wind direction and scatterometer antenna beam

Subscripts:

H regime H

L regime L

Abbreviations:

A/D analog to digital

GMT Greenwich Mean Time

IF intermediate frequency

IFOV instantaneous field of view

INS inertial navigation system

NHRL National Hurricane Research Laboratory

NOAA National Oceanic and Atmospheric Administration

SASS-1 Seasat geophysical algorithm relating σ^o to wind vector

TDA tunnel-diode amplifier

TWT traveling wave tube

1. SUMMARY

This report summarizes the NASA Langley Research Center analysis of the airborne microwave remote sensing measurements in Hurricane Allen obtained on August 5 and 8, 1980. The primary objective of this report is to evaluate the performance of the microwave instruments in a severe storm. Explanation of the meteorological aspects of the storm itself, based on this and similar data sets, is under way at the NOAA National Hurricane Research Laboratory and is not included here.

The NASA instruments were the C-band stepped frequency microwave radiometer and the Ku-band airborne microwave scatterometer. They were carried aboard a NOAA C-130 aircraft making storm penetrations at an altitude of 3000 m and are sensitive to rain rate, surface wind speed, and surface wind vector. The wind speed is calculated from the increase in antenna brightness temperature above the estimated calm-sea value. The rain rate (actually liquid water content of the air column) is obtained from the difference between antenna temperature increases measured at two frequencies, after correcting for other dispersive effects. The wind vector is determined from the sea-surface normalized radar cross section measured at several azimuths.

Comparison wind data were provided through the use of the inertial navigation systems (INS) aboard both the C-130 aircraft at 3000 m and a second NOAA aircraft (a P-3) operating at altitudes between 500 and 1500 m. Comparison rain rate data were obtained with a rain radar aboard the P-3. It was the original intent that the microwave-derived surface winds would be compared with surface winds calculated with a planetary boundary layer model using as input winds measured with the INS aboard the P-3 at 500 m (the assumed nominal top of the boundary layer); however, extreme turbulence forced that aircraft to fly at 1500 m most of the time. Therefore, the surface winds obtained with the two microwave instruments could be compared only with each other and with the flight-level winds. Nevertheless, several important conclusions have been drawn from these comparisons.

The analysis shows that the radiometer accurately predicts flight-level wind speeds and rain rate (liquid water content) and that the scatterometer produces well-behaved and consistent wind vectors for the rain-free periods. Analysis of scatterometer data obtained in the presence of rain (which attenuates the scatterometer signal) has not been completed and is not reported here.

2. INTRODUCTION

Development of microwave instruments for remote sensing of environmental variables has been under way for several decades, involving many government agencies, universities, industry, and private laboratories, both in the United States and abroad. Microwave scatterometers, which are active devices, have been employed to detect and measure sea ice, sea-surface wind vectors and large-scale waves, and other features of the Earth's surface (Jones et al. 1982). Microwave radiometers, which are passive devices, have been applied to the measurement of sea ice, soil moisture, atmospheric water vapor, and ocean surface temperature, salinity, and wind speed. The NASA Langley Research Center has developed both types of sensors for a wide range of remote sensing experiments.

Aircraft reconnaissance of hurricanes has been conducted by the National Oceanic and Atmospheric Administration and by the Department of Defense since World War II; a brief history of these programs is given by Frey (1980). Until the early 1970's, the aircraft served primarily as a carrier of meteorologists and of in situ sensors such as barometers, accelerometers, navigation instruments (including radar), and air samplers into the storm. However, during the past decade, the aircraft has also functioned as a platform for remote sensing devices. The early development of these efforts may be traced by consulting Ross et al. (1974), Black and Schricker (1978), Kaupp and Holtzman (1979), and Kidder, Gray, and Vonder Haar (1980).

In 1980, NOAA and NASA conducted a cooperative program to improve the reliability of rain rate and surface wind vector estimates by applying microwave remote sensing technology. This program resulted in the Hurricane Allen field measurements and the subsequent analysis reported herein.

3. MISSION DESCRIPTION

The 1980 hurricane season was highlighted by Hurricane Allen, which stands as the most intense North Altantic storm ever penetrated by aircraft. Lawrence and Pelissier (1981) discuss the storm and its impact. The meteorological aspects of the storm itself are discussed by Willoughby, Clos, and Shoreibah (1982). On August 5 and 8, 1980, the NASA Langley Research Center's Ku-band airborne microwave scatterometer and C-band stepped frequency microwave radiometer were flown into Hurricane Allen aboard a NOAA C-130 aircraft (fig. 1) as part of a three-aircraft experiment conducted by the NOAA National Hurricane Research Laboratory (NHRL). Ocean surface normalized radar cross section and brightness temperature were measured with the scatterometer and radiometer, respectively. These data have been analyzed and compared with measurements from the aircraft data systems to evaluate the ability of the microwave instruments to estimate surface wind speeds and directions and rain rates within the storm. Actually, it is atmospheric liquid water content between the sea surface and the aircraft that is measured by the radiometer. For convenience, this is represented here as an equivalent rain rate for an air column height of 3000 m. The specific purposes of this mission were (1) to obtain data for the improvement of the geophysical algorithms for both microwave instruments and (2) to demonstrate the feasibility of combined active and passive microwave remote sensing techniques at high altitudes to obtain information that could, at least until the time of Hurricane Allen, be obtained only at considerable risk from aircraft at low altitudes.

A preliminary report, based on a limited amount of the data, appeared in Science (Jones et al. 1981). At the time of publication of that article, plans to archive the entire data set had not yet been developed. The primary objectives of this report are to evaluate the performance of the microwave instruments and to archive data for all passes through Hurricane Allen.

The microwave sensors were flown on the C-130 at an altitude of approximately 3000 m. A low-altitude P-3 (at 500 to 1500 m) flew beneath the C-130 and generally along the same flight lines. This low-altitude aircraft was intended to measure winds near the top of the hurricane planetary boundary layer. Another NOAA P-3 flew at 5000 m. All three aircraft carried nose, tail, and/or lower fuselage radars, from which composites of rain rate were later constructed.

The vertical stacking of the three aircraft is shown schematically in figure 2. The actual flight altitude histories for the eyewall penetrations by the two lower altitude aircraft are given in figure 3. The C-130 maintained a certain barometric

altitude; therefore, its actual (geometric) altitude varied as shown. The flight paths with respect to the storm's moving center are presented in figures 4 and 5.

The time-dependent track of the storm center was determined by NHRL through the use of cubic spline equations fitted to the positions of atmospheric pressure minima. These pressure minima were located by triangulation from successive aircraft positions along each airplane's passes through the storm. For each aircraft and for each day, separate equations were generated for latitude and for longitude. For purposes of this report, the inertial navigation system (INS) of the P-3 at 500 and 1500 m and that of the C-130 at 3000 m were considered equally reliable, so that the storm center location at any instant was taken as the average given by the two sets of equations. From this procedure, the general position of the storm center during August 4-10, 1980, was determined and is presented in figure 6 with the locations of aircraft penetrations given.

The number of eyewall penetrations made by the two lower altitude aircraft on each flight day is given below:

Date	No. of eyewall penetrations by -	
	P-3 (500 and 1500 m)	C-130 (3000 m)
August 5	16	16
August 8	16	14

Because of the differences in ground speed, the P-3 moved ahead of the C-130 on both days. To allow data from the two aircraft to be compared, pass names were assigned to identify 26 pairs of penetrations. Table 1 gives start and stop times of all paired passes. The paired passes are numbered chronologically from 1 to 26, and the letter N, S, E, or W is appended to indicate the general bearing of each pass track from the storm center.

4. MICROWAVE SENSORS

NASA Langley Research Center microwave instruments used during the Hurricane Allen flights were the stepped frequency microwave radiometer and the airborne microwave scatterometer. (These instruments and their footprint geometry are described in detail in appendix A.) Wind speed is calculated from the radiometer data through knowledge of the increase in sea-surface brightness temperature (measured with the radiometer) above the calm-sea value estimated by regression on part of the August 8 data. Rain rate (actually liquid water content of the air column) is obtained from the difference between antenna brightness temperature increases (over calm-sea values) measured at two frequencies, after other dispersive effects are accounted for. Wind vector is calculated from the sea-surface normalized radar cross section (σ^o) measured with the scatterometer for several azimuths, by using the SASS-1 geophysical algorithm to relate σ^o to wind vector.

The relationship between brightness temperature and wind speed is shown in figure 7(a) and between brightness temperature and rain rate in figure 7(b) for the

first pass through the hurricane. A uniform increase in antenna brightness temperature for all four radiometer frequencies would indicate higher wind speed and no rain, while a dispersion in antenna brightness temperature over the various frequencies would indicate the presence of rain. Most of the features on the brightness temperature plot (center panels, figs. 7(a) and 7(b)) show a combination of rain and wind and are keyed to the labeled features on the rain radar composite shown in the upper panels of figures 7(a) and 7(b).

4.1 Stepped Frequency Microwave Radiometer

Passive microwave remote sensing measurements of sea-surface wind speed and rain rate were derived from antenna brightness temperatures measured with the stepped frequency microwave radiometer. The radiometer is a balanced Dicke-switched, noise feedback radiometer and was operated during the Hurricane Allen flights at 4.498, 4.994, 5.586, and 6.594 GHz with a 50-MHz bandwidth and 1.0-second integration time, using a circularly polarized, corrugated horn antenna (Harrington 1980).

The radiometric antenna brightness temperature of the sea surface, as measured with the radiometer, is the sum of the cosmic background radiation and the radiation from the atmosphere (both reflected from the sea surface) and the radiation emitted from the sea surface itself. All three are attenuated by the intervening atmosphere.

The amount of electromagnetic radiation emitted by the sea surface is affected by the surface roughness, breaking waves, and foam, all attributed (to first order) to the force of the wind. Because rain is only weakly attenuating at the C-band microwave frequencies used, the surface emission variation due to wind speed change at the ocean surface is detectable from flight altitudes above a rain layer.

Furthermore, microwave emission by rain is dispersive, varying as an inverse power of electromagnetic wavelength. Therefore, simultaneous measurement of wind speed and rain rate is possible whenever the instrument is operated at more than one frequency (as was done 85 percent of the time). This dispersion due to rain is shown in figure 7(b), with the heaviest rain near the radius of maximum winds (points A and D on the rain radar composite).

4.2 Airborne Microwave Scatterometer

Active microwave remote sensing measurements of surface wind speed and direction were obtained during the Hurricane Allen flights with the airborne microwave scatterometer. The 14.6-GHz scatterometer measures the normalized radar cross section (σ^{o}) of the ocean surface at various incidence and azimuth angles. The strength of the radar backscatter is a function of the wind-driven capillary wave amplitude, which is proportional to the wind stress at the sea surface. The radar backscatter is anisotropic in azimuth; therefore, wind direction can also be derived from scatterometer measurements. The dual-linear polarized parabolic antenna for the scatterometer is mounted on a two-axis servo-controlled pedestal to provide independent elevation and azimuth pointing. The pointing of the antenna and all other functions of the scatterometer were under the control of a programmable microprocessor. During the Hurricane Allen flights, σ^{o} was measured with the antenna in one of three basic modes as described in table 2: fixed azimuth and elevation (mode 8), fixed azimuth and varying elevation (mode 3), and varying azimuth and fixed elevation (mode 2). The remaining numbers (1 and 4-7) identify calibration modes.

Wind vector (both speed and direction) is best determined from radar cross sections obtained with the scatterometer in mode 2, in order to accumulate σ^{o} measurements over a range of azimuths. The SASS-1 geophysical algorithm, described by Jones et al. (1982) and Schroeder et al. (1982), may produce alias wind vectors, differing primarily in wind direction. One of these directions is usually within a few degrees of the true surface wind. In a cyclonic storm such as Hurricane Allen, the wind's general direction can be estimated if the bearing of the measurement point from the storm center is known. (The bearing plus 90° equals the approximate wind direction, ignoring friction.) This fact, along with the INS measurement of wind direction, is used in selecting from among the aliases yielded by the wind vector algorithm.

Further discussions of wind vector determination from backscatter measurements are available in Jones and Schroeder (1978) and Thompson, Weissman, and Gonzalez (1983). Moore et al. (1982) have evaluated the effect of precipitation on a Ku-band scatterometer, and Dome (1975) discusses the choice of frequency for a wind-measuring scatterometer. L-band measurements of sea-surface backscatter in hurricane force winds are reported in Weissman, King, and Thompson (1979).

5. AIRCRAFT SENSORS

5.1 Inertial Navigation Systems

Flight-level wind speed and wind direction data are provided by the INS as part of the flight navigation system of each aircraft. Also provided are the altitude, roll, pitch, yaw, and ground speed; all are needed in the computation of σ^{o}. Merceret and Davis (1981) fully describe the P-3 INS, and Haydu and Darby (1983) describe the C-130 system.

5.2 Aircraft Radars

The two P-3's were equipped with rain-rate-measuring nose radars (120° horizontal scan), lower fuselage radars (360° horizontal scan), and tail radars (360° vertical scan). Because of power requirements, only two radars could be operated simultaneously aboard each airplane. The C-130 at 3000 m was equipped with one 120° horizontally scanning nose radar. Data from the aircraft radars were used by NHRL to construct pass-by-pass profiles and 4-hour averages of rain rates derived from radar reflectivity in the air volume. Of the various rain radar composites, those made from the low-altitude P-3 data were the most appropriate for comparison with the radiometer rain rate, as will be shown in section 6.

6. MISSION RESULTS

This section presents definitions, the organization of the data, and the results of comparison between the microwave measurements and corresponding aircraft measurements. Digital tapes containing the data are available from the National Technical Information Service, 5285 Port Royal Road, Springfield, VA 22161. Requestors should ask for Data Tape Supplement to NASA TM-86390. The format of the digital tapes is described in appendix B.

6.1 Introduction and Definitions

6.1.1 Eyewall Penetrations (Passes) and Transits

All data except the averaged composites from the rain radars are identified by pass or transit name. A pass is defined as one excursion of the two lower altitude aircraft between a point on the periphery of the storm and a point near the storm center, with travel generally along a radial in either direction. A pass name was assigned to every eyewall penetration made jointly by the C-130 at 3000 m and the P-3 at 500 to 1500 m. Because of differences in ground speed, the two aircraft did not penetrate the eyewall at the same time, but for each pass were flying along nearly the same radial and in the same direction. Pass names are chronologically numbered 1 to 12 for August 5, and 13 to 26 for August 8, 1980, and have a letter (N, S, E, or W) assigned to indicate the general bearing of the aircraft from the storm center. A list of pass pairs is given in table 1.

A transit is defined as any excursion around the periphery of the storm or an excursion through the storm center for which no obvious pass pairing can be assigned. For each of the two lower altitude aircraft on each day, the transits are numbered chronologically and are distinguished from the pass numbers by a T, for example, T1, T2. Data from the transits are displayed in appendix C.

6.1.2 Partitioning of Data

INS and radiometer measurements were originally obtained and recorded about 1 sec apart. These were then time-averaged into bins of 0.004 hr (14.4 sec), which corresponds to aircraft movement of slightly less than 1 n.mi. at the ground speeds experienced during Hurricane Allen. The scatterometer data were also averaged into 14.4-sec bins except that a bin was closed early and a new bin started if the antenna incidence angle or azimuth angle changed by more than 5° or 30°, respectively. Scan settings for elevation and azimuth 5° and 30° apart, respectively, were chosen in flight. Any instantaneous differences between the actual angles and the chosen angles were the result of aircraft motion. Inspection of the data reveals that these differences were nominally 2° or less, for either elevation or azimuth. Means for each parameter (INS wind speed, INS direction, latitude, longitude, radiometric brightness temperature for each radiometer frequency, scatterometer normalized radar cross section (σ^{o}), and antenna angles) were calculated for each bin.

6.1.3 Time Lines

Figures 8 and 9 are plots, on a coarse time scale, of instrument status, pass name, transit name, and certain other information. These figures indicate the operation of sensors in various configurations during the various passes and transits.

6.2 Aircraft INS and Radar Measurements

The INS and rain radar measurements are described in this section. INS wind speeds obtained with the C-130 at 3000 m were compared with those from the P-3 that flew at either 500 m or 1500 m. This was to establish the C-130 INS winds as a standard with which those calculated from the microwave remote sensing instruments (the scatterometer and the radiometer, both aboard the C-130) could be compared. By using

the C-130 INS winds as the standard, rather than those from the P-3, the two-aircraft collocation problem was eliminated.

Wind speed data from the second P-3 (flying at 5000 m) were not used in this study. Therefore, no further mention will be made of data from that aircraft, and "P-3" will hereafter mean the low-altitude (500 to 1500 m) aircraft only.

6.2.1 INS Wind Speed and Direction

The flight-level wind speeds measured on August 5 with the INS's aboard the P-3 (at 1500 m) and the C-130 (at 3000 m) are compared in figure 10. The wind speeds for the various passes are superimposed in figure 10(a) for the P-3 and in figure 10(b) for the C-130. To eliminate azimuthal asymmetry, the wind speeds have been corrected for the forward motion of the storm, and the resulting tangential wind speeds are plotted against distance from the storm center. The peak in wind speed at 20 n.mi. is clear at both altitudes. Figures 10(c) and 10(d) are scatter plots to compare the INS wind speeds at both altitudes. This comparison considers two regions: within the eyewall (fig. 10(c)) and outside the eyewall (fig. 10(d)).

Figure 11 presents analogous results for August 8. The peak in wind speed is observed at 9 n.mi. from the storm center. These distances to maximum wind speed agree with those given by Willoughby, Clos, and Shoreibah (1982). In the outer regions of the storm, the P-3 data for some quadrants show a stronger upturn than the C-130 data. As will be shown in the next section, this upturn was also seen with the microwave instruments for the same quadrants.

INS wind speeds for the two passes at 500 m made on August 5 by the P-3 are compared in figure 12 with those made comparably by the C-130 at 3000 m (same flight track, about half an hour later).

The reason the data are divided into two storm zones for the scatter plots is that strong wind gradients inside and near the eyewall cause large differences in measured aircraft winds when small errors are made in relative aircraft location. The winds shown in the scatter plots of figures 10, 11, and 12 were not adjusted for the forward motion of the storm, because to do so would decrease the range of wind speeds available for comparison. All the data contained in the scatter diagrams of figures 10, 11, and 12 were obtained within 50 n.mi. of the storm center. This limit was imposed because, beyond that distance, vertical similarity in the INS winds was found to diminish.

Flight-level wind directions measured with the INS aboard each aircraft are presented with the wind speeds on a pass-by-pass basis later in this report (section 6.4).

A study was conducted to determine the importance of collocating the wind measurements accurately from each aircraft. Small navigational errors (1 to 3 n.mi.), typical in INS navigation, can cause large differences in wind values near the eyewall because of the strong radial gradients. Knowledge of the along-track coherence of the winds is necessary in the comparison of the microwave-derived winds with those of the INS. This is because the footprint of the scatterometer is not directly below the C-130 and because tilt of the eyewall causes the radius of maximum winds to increase with altitude. The latter causes horizontal collocation errors near the eyewall (between the radius of maximum surface winds and that for flight-level winds) to

have significant effects. Therefore, INS-microwave comparisons in the vicinity of the eyewall were avoided.

To determine the effect of collocation error on the comparison of wind speeds from any two instruments, the radial coherence of wind speeds from a single instrument was studied first. The C-130 flight-level INS wind record for pass 1N was used to form two identical distance-ordered series. These identical wind records were then plotted against each other with one record successively shifted in 1 n.mi. increments. The resulting scatter diagrams are shown in figure 13(a) for measurements inside the eyewall and in figure 13(b) for measurements outside the eyewall. The effect of collocation error on the interpretation of wind speed data is much greater inside the eyewall than outside. A similar result is seen in figure 14, in which scatter diagrams for pass 2S are shown. (Diagrams for zero shift are not shown, since all points would necessarily lie on the line of perfect agreement.)

Because of the great sensitivity to collocation error inside the eyewall, suggested by figures 13 and 14, pass-by-pass comparison between the microwave-derived winds and the INS winds is restricted to the region outside the eyewall. Those comparisons are presented in section 6.4.

6.2.2 Rain Rate From Aircraft Radars

Atmospheric liquid water reflectivity data from the NOAA aircraft radars were used for evaluating the ability of the radiometer to measure rain rate. Since the radiometer was aboard the C-130 (at 3000 m) and was sensitive to the amount of liquid water in the air volume below, the reflectivity data from the lower fuselage radar on the low altitude P-3 were chosen as the most suitable for comparison. The radar measurements therefore did not include the rain between the flight levels of the P-3 and the C-130, which the radiometer did see. (Recall from fig. 2 that there was no equivalent rain radar on the C-130.)

To minimize the effects of noise, time composites of the single-sweep data were constructed for each P-3 pass through the storm (Marks 1981). These in turn were combined into several P-3 multipass composites in order to further decrease the measurement uncertainty. The C-130 flight tracks were then laid over the P-3 radar multipass composites to obtain profiles of reflectivity, ordered according to C-130 along-track distance. The reflectivity values were converted to radar rain rate in mm/hr from

$$\text{Radar rain rate} = (Z/300)^{-1.35} \qquad (1)$$

where Z is a unitless reflectivity factor (Jorgensen and Willis 1982). A rigorous treatment of Z may be found in Rogers (1976).

Rain rate profiles were obtained for C-130 passes 1 to 6 and 13 to 25. Each is paired with its respective radiometer rain rate profile in section 6.4. Radar rain rate profiles for August 5 and 8, averaged over 360° in azimuth, are presented in figure 15. Profiles averaged over the indicated azimuth ranges for August 5 and August 8 are given in figures 16 and 17. Rain rate differs significantly from quadrant to quadrant.

Note that for most hurricane research flights, underwing instruments are used for obtaining the distribution of rain droplet sizes. This distribution enters into the radar rain calculation. The results for Hurricane Allen were degraded by an unknown amount because the underwing instruments failed.

6.3 Microwave Sensor Measurements

6.3.1 Radiometer Calculations

Rain rate.- Rain rate is calculated from the difference in brightness temperature at two radiometer frequencies, by the method of Gloersen and Barath (1977). For the altitude and frequencies at which the radiometer was operated, the Gloersen and Barath equation for rain rate in mm/hr becomes

$$\text{Radiometer rain rate} = [(106.84\tau + 27.087)^{1.2} - 52.398]^{0.833} \qquad (2)$$

where τ, the unitless opacity due to both rain and clouds, is related to the difference in the brightness temperatures at two frequencies through

$$\tau = 0.01091[T_{A,i} - T_{A,j} - \Delta T(0.996)] - 0.0075 \qquad (3)$$

where $T_{A,i}$ and $T_{A,j}$ are the brightness temperatures at any two radiometer frequencies, ΔT is the observed temperature difference in no-wind, no-rain brightness temperatures at the two frequencies, 0.996 is a correction for the atmospheric attenuation due to O_2, and 0.0075 is the opacity due to clouds. The no-wind, no-rain antenna temperatures for the various frequencies were obtained during an August 4 flight from Miami to San Juan. The aircraft flew over a strip of 150 n.mi. between Long and Mayaguana Islands in the Bahamas, known to be at a nearly time-invariant sea-surface temperature of 28.0° to 28.2°C (Peter G. Black, NHRL, personal communication). Radiometer rain rates are computed using equations (2) and (3), and are presented as pass-ordered data in section 6.4.

Alternative methods for estimating rain rate are possible, using $T_{A,i}/T_{A,j}$ rather than $T_{A,i} - T_{A,j}$. One such method has been formulated by Swift (Jones et al. 1981).

Wind speed.- The relationship between wind speed and brightness temperature, even in the absence of the dispersive effects of clouds and rain, is nonlinear. Apparently there are two nearly linear regimes (Harrington 1980), although the transition between these two may comprise a third one. In the lower wind speed regime (regime L), brightness temperature increases only slightly with increasing wind speed. In the higher wind speed regime (regime H), brightness temperature increases substantially with increasing wind speed. Lower bounds on regime H were assigned by inspection of figure 18(a), which is a plot of brightness temperature ($T_{A,1}$) against C-130 flight-level INS wind speed (U_{ins}). The data include only those points lying between 10 and 50 n.mi. from the storm center and for which the computed rain rate was less than 6 mm/hr. This rain rate limit is a trade-off between a lower value, which would have decreased dispersion, and a higher value, which would have

permitted higher wind speeds (because the highest wind speeds were accompanied by substantial rain). Simply by inspection, any data point for which the wind speed was less than 22.5 m/sec, or the brightness temperature was less than 120.7 K, was assigned to regime L. All other data points (Wind speed > 22.5 m/sec and T_A > 120.7 K) were assigned to regime H.

For all brightness temperature measurements meeting the above criteria for regime H, stepwise regression calculations were performed for all data from August 8 between 10 and 40 n.mi. from the storm center. The C-130 INS wind speeds were regressed against $T_{A,1}$ and $(T_{A,4} - T_{A,1})$, where frequency 1 is 4.498 GHz and frequency 4 is 6.594 GHz. The resulting equation for predicting flight-level wind speed from radiometric measurements is, in meters per second,

$$U_{r,H} = 1.065T_{A,1} - 0.616(T_{A,4} - T_{A,1}) - 99.66 \pm 3.4 \tag{4}$$

Since the difference ΔT in no-wind, no-rain values of $T_{A,1}$ and $T_{A,4}$ is 2.24 K, equation (4) becomes, after some rearranging,

$$U_{r,H} = 1.065[T_{A,1} - 0.5784(T_{A,4} - T_{A,1}) - 93.58] \pm 3.4 \tag{5}$$

$$= 1.065[T_{A,1} - 0.5784(T_{A,4} - T_{A,1} - 2.24) - 94.87] \pm 3.4 \tag{6}$$

The adjustment of brightness temperature due to rain is thus given by

$$T'_{A,1} = T_{A,1} - 0.5784(T_{A,4} - T_{A,1} - 2.24) \tag{7}$$

so that equation (6) becomes

$$U_{r,H} = 1.065(T'_{A,1} - 94.87) \pm 3.4 \tag{8}$$

The prime indicates adjustment for the effects of rain.

This separation into two equations, (7) and (8), is necessary because the scatter in the data of regime L precludes definition of a rain adjustment. The rain adjustment must be the same for either regime, so equation (7) can be applied to regime L. Figure 18(b) presents the results of the stepwise regression, showing the computed $U_{r,H}$ plotted versus U_{ins}. The results are satisfactory because of the cohesive structure of the storm on August 8, which assures a more correlated proportionality between U_{ins} and the surface wind speed that resulted in the measured brightness temperature values. The data scatter can be attributed (in part) to the microscale structure of the winds.

Figure 18(c) shows adjusted values of brightness temperature, $T'_{A,1}$ plotted against U_{ins} for regime L. Included are all data points obtained from 0 to 3 and 10 to 87 n.mi. from the storm center. Points lying between 3 and 10 n.mi. were excluded because of the tilt of the hurricane eyewall. The equation assigned for regime L is

$$U_{r,L} = 6.35(T'_{A,1} - 116.36) \tag{9}$$

Figure 18(d) shows the results of this equation plotted against the corresponding INS wind speed.

The two linear equations, (8) and (9), produce identical values of 27.5 m/sec for wind speed at adjusted brightness temperatures of 120.7 K, the demarcation point between the two equations. Figure 19(a) merges the results of the two equations, each applied to the data points in its respective regime. (Those data points in regime H that lie beyond 40 n.mi. from the storm center are not included.) Figure 19(b) similarly merges the two sets of adjusted brightness temperature data. Figures 19(c) and 19(d) show, for August 5 and 8, respectively, scatter plots for all passes, relating U_r to U_{ins}. The data for August 5 are restricted to between 20 and 40 n.mi. from the storm center, and those for August 8 to between 10 and 40 n.mi. The restriction for August 5 results in only one equation being represented in figure 19(c), that for $T_{A,1} > 120.7$ K (regime H).

6.3.2 Scatterometer Calculations

Azimuth scans.- Since σ^o is such a strong function of both azimuth (with respect to the wind direction) and incidence angle, the scatterometer data had to be partitioned according to those parameters. The primary operating mode for the scatterometer was the azimuth scan (mode 2 in table 2). These data were partitioned first by incidence angle (19°, 39°, and 52°), then by azimuth (bins of not more than 30° change). No bin was allowed to contain data obtained more than 14.4 sec apart (this limit was explained in section 6.1.2). Mean values of σ^o, incidence angle, and azimuth from enough successive bins to give an azimuth spread sufficient for proper operation of the SASS-1 geophysical algorithm were then used to compute wind vectors. The output of the algorithm includes the aliases described in section 4.2. Some of the mode 2 scatterometer measurements made during Hurricane Allen had to be eliminated because of obvious instrument problems (due to a faulty polarization change-over switch) or severe beam attenuation (due to precipitation). In the present study, a radiometer rain rate estimate of 2 mm/hr or less was the basis for estimating when the scatterometer data were nominally rain free.

The result of this editing is that all scatterometer data for August 5 (excessive rain) and all horizontal-polarization data on August 8 (instrument problem) were eliminated. Sufficient data were obtained on August 8 to form 34 values of derived wind vector. These are listed in table 3, together with simultaneously obtained results from the INS and the radiometer.

The partitioned σ^o data for the first pass on August 8 are shown in figure 20. Each data bin is represented by a square, and the bins for each solution are displayed together on a single polar plot. On these plots, true north is always to the top, and the tick mark on the outer circle indicates the flight-level wind direction

measured with the C-130 INS. The arrow indicates the wind direction of the algorithm-returned alias closest in direction to the INS and simultaneously chosen because of quadrant (see section 4.2). The circle itself represents a σ^o value 10 dB higher than the center (i.e., Radius = 10 dB). The absolute σ^o scale may vary from plot to plot, so the value at the center is given at the upper right. Each square represents one bin, plotted at its mean azimuth and its mean σ^o. The closed contour is the graph of σ^o versus azimuth from the SASS-1 table, for the scatterometer wind speed given in table 3. The individual squares in figure 20 each represent about 6 sec of data (six 0.5-sec integrations at 50-percent duty cycle for each polarization), taken at one azimuth. The 6-sec interval is far less than the equivalent anemometer averaging time recommended by Pierson (1983) for a spot observation of any wind-related quantity (such as σ^o). This explains the data scatter in the individual measurements of σ^o (the squares) about the SASS-1 prediction of σ^o (the closed contour). However, each vector solution (represented by one polar plot), comprised of measurements at 8 to 20 azimuths, required up to 2 minutes of data. This duration at least approaches the several minutes recommended by Pierson. However, to obtain measurements at 8 to 20 azimuths, a strip of ocean surface 3 to 8 n.mi. long must be sampled (see appendix A). Over that distance in a hurricane, much variability can be expected, especially along a radial. Even for synoptic-scale winds, Pierson calculates an expected standard deviation of 1 to 2 m/sec in scatterometer-measured winds for a 10-km sampling cell. Partitioned σ^o data for the other passes which yielded nominally rain-free data are given in figures 21 to 27.

Figure 28 presents the 34 scatterometer solutions in comparison with radiometer rain rate and INS wind speeds. These plots show that the difference in INS wind speeds at the two August 8 flight levels is not a strong function of rain rate (fig. 28(a)), that the difference between wind speeds from the C-130 INS and from the scatterometer is not a discernible function of distance from the storm center (fig. 28(c)), and that the C-130 INS and scatterometer measurements compare well for both wind direction (fig. 28(b)) and wind speed (fig. 28(d)).

Values of measured σ^o are plotted against C-130 INS flight-level wind speed in figure 29, for $\theta = 19°$. Each of the six panels of the figure is for a given range of χ, within the 30° window, where χ is the horizontal angle between the wind direction and the scatterometer antenna beam. The solid line is σ^o from the SASS-1 geophysical algorithm. Figures 30 and 31 display similar information for $\theta = 39°$ and 52°, respectively.

Elevation scans.- Mode 3 (elevation scan) data are sometimes used for absolute bias determination of the scatterometer and to gather data to further refine the geophysical algorithm. Numerous elevation scans were obtained during Hurricane Allen, and σ^o from an example scan is given in figure 32. For Hurricane Allen, absolute bias in the scatterometer instrument was determined through laboratory measurement of waveguide losses and a calibration in which precision spheres were used as targets.

6.4 Geophysical Comparisons

Wind vector and rain rate results from the microwave instruments are presented with the INS and rain radar measurements on a pass-by-pass basis in figures 33 to 58. Each figure contains (at the upper left) information needed to locate the flight tracks with respect to the storm center. The upper right panel shows the profiles of radiometer brightness temperature at as many frequencies as were available. Beneath

the brightness temperature data is the profile of radiometric wind speed, and in the bottom right panel is the profile of radiometer rain rate. INS wind speeds from both aircraft are shown in the wind speed panel, and profiles from the rain radar composites, whenever they exist, are given in the rain rate graph at the bottom right. Beneath the flight track diagrams on the left is a scatter diagram comparing the radiometric wind speed with the C-130 INS flight-level wind speed (20 to 40 n.mi. from the storm center on August 5; 10 to 40 n.mi. on August 8). Below that, at the lower left, is the INS flight-level wind direction information from each aircraft.

In a multi-aircraft experiment, the surface winds beneath a higher altitude aircraft, if not measured directly, are normally inferred from the lower altitude INS flight-level winds. This is acceptable provided that the aircraft remain within or not far above the planetary boundary layer. These conditions were not met in the case of the flights through Hurricane Allen. However, the INS winds at the two flight levels were found to be comparable (figs. 10, 11, and 12), at least from the radius of maximum winds to 40 n.mi. from the storm center. Therefore, the decision was made to compare the microwave-derived surface wind speed estimates with the INS winds from 3000 m, in order to eliminate the aircraft collocation problem. To use the 1500-m winds would have degraded the comparison because of nonregistration of aircraft tracks and passage times and gusting.

The 34 scatterometer solutions from mode 2 calculations are shown in figures 33 to 58 for passes where they apply. Each of the solutions appears as a square. Scatterometer-derived wind speeds are shown in the wind speed profile and in the scatter diagram. Wind directions from these same calculations are displayed in the lower left, with INS wind direction profiles from both aircraft. In some instances, especially near the storm center, the INS wind direction varied too erratically to be displayed.

7. DISCUSSION OF RESULTS

The conclusions, detailed below, are (1) that the measured INS winds at all available flight levels up to 3000 m are very similar, (2) that the radiometer has produced the first available radiometric measurements of wind speeds up to 70 m/sec, while (3) simultaneously measuring rain rates up to 60 mm/hr, and (4) the scatterometer is skillful at determining sea-surface wind vector at wind speeds up to 28 m/sec and has provided the beginning of a data set that may be used to improve current scatterometer geophysical algorithms for higher wind speeds.

7.1 Use of 3000-m INS Winds as Estimator for Sea-Level Winds

The INS wind speed measurements do not reveal any large variation due to altitude, at least between the radius of maximum winds (20 n.mi. on August 5; 9 n.mi. on August 8) and 40 n.mi. from the storm center. This is apparent not only from the comparison of pass-ordered P-3 and C-130 wind profiles (figs. 33 to 58), but also from the collected profiles and resulting scatter plots for each flight day (figs. 10 to 12). Vertical similarity inside the eyewall does not prevail, probably because of the pronounced slant of the eyewall (30° relative to the horizontal on August 5 and 45° on August 8, according to Jorgensen (1984)). For radial distances greater than 50 n.mi. the similarity is decreased, probably because beyond that distance the vertical motions in the hurricane are insufficient to overcome the atmosphere's usual vertical shear structure.

The similarity, however, between the 1500-m and the 3000-m INS winds is obvious between the radius of maximum winds and 40 n.mi. from the storm center. Also, the limited INS data set obtained at 500 m (fig. 12) leads to the same conclusion. Thus, any planetary boundary layer model that acts upon the winds from any of the three flight levels could be used with winds from either 1500-m or 3000-m flight-level measurements.

7.2 Radiometer Wind Speed

The radiometer wind speeds are compared with those from the 3000-m INS for 12 passes on August 5 (fig. 19(c)), 14 on August 8 (fig. 19(d)), and for each pass (figs. 33 to 58). The range of speeds is 35 to 70 m/sec on August 5 and 20 to 65 m/sec on August 8. Some quadrant dependence is noted on August 5 (the radiometer measurement is too low on the north passes and too high on the south passes). The radiometer may be responding differently in the north and south quadrants, or the boundary layer coupling from sea level to flight level may depend on quadrant. That this is not observed on August 8 may be due to the storm being much more tightly organized on that day.

Aside from this quadrant dependence on August 5, the radiometer wind speeds correspond very closely to those from the 3000-m INS. It was shown in section 6.3.1 how the radiometer brightness temperatures were regressed on INS wind speed over a selected portion of the data from August 8. Then the resulting algorithm was applied to all the data for both days. The good agreement between radiometer and INS over such a large range of wind speeds depends on the use of data at two microwave frequencies rather than at one, which also enables the measurement of rain rate. This is important, since heavy precipitation so frequently accompanies high winds.

This success of the radiometer in measuring wind speeds up to 70 m/sec in Hurricane Allen marks the highest known wind speeds measured by any microwave radiometer to date.

7.3 Radiometer Rain Rate

The simultaneous measurement of brightness temperature at more than one frequency yields an estimate of the amount of liquid water in the atmospheric column beneath the aircraft carrying the radiometer. The best available comparison data set is that from the 360° lower fuselage radar on the P-3 aircraft (see section 6.2.2 and fig. 2).

The P-3 rain radar profiles for passes 1 to 6 and 13 to 25 are shown superimposed on those from the radiometer in figures 33 to 58. The results agree qualitatively; that is, the two measurements generally agree in detecting areas of no, low, and high rainfall. Lack of better quantitative agreement is due partly to the uncertainties inherent in both measurement systems, but partly to the limitations imposed by comparing the nearly instantaneous radiometer measurement with the time-composite constructions of the rain radar data. One possible source of error is the liquid water content of the air between the two airplanes. Each composite was built from data obtained over approximately six aircraft passes.

It is obvious from figures 33 to 58 that the radiometer is useful for detecting such meteorologically important areas as the rain-free storm center, the eyewall, and the inner and outer rain bands.

7.4 Scatterometer Wind Vector

Scatterometer-derived values of surface wind speed and wind direction are compared with flight-level INS values obtained at 3000 m. (It was concluded earlier that the INS measurements from 3000 m are as satisfactory as those from lower altitudes for use as a surface comparison data set.)

Figure 28(d) reveals that the scatterometer compares very well with the INS for wind speeds up to about 27 m/sec, but that its wind speed predictions are too low for greater wind speeds. The following explanations for this were investigated: (1) incorrect SASS-1 algorithm, from which the σ^o values were converted to wind vector, (2) instrument bias resulting in incorrect σ^o, or (3) invalid assumptions regarding the degree of coupling between the surface winds and those at altitude. Included in the first is the possibility of decreased sensitivity of σ^o at very high wind speeds, which is not modeled in the SASS-1 geophysical algorithm. It must be remembered, however, that the SASS-1 algorithm is based on Seasat and aircraft data obtained before Hurricane Allen and is limited to about 30 m/sec (Jones et al. 1982). Seasat did not provide high-wind-speed data to improve the SASS-1 algorithm, because a typical resolution cell was not small enough to separate the occasional high-wind rain-free areas from surrounding regions of low winds and/or heavy precipitation. The scatterometer was able to do this during Hurricane Allen. The resulting comparison with the flight-level INS does leave unresolved the question of σ^o sensitivity at high wind speeds.

The second possiblity, scatterometer instrument bias, was the subject of an exhaustive study at the NASA Langley Research Center, wherein an absolute bias of -1.1 dB was found through a precision target-sphere calibration. Correction for this bias was applied to all Hurricane Allen data, and thus instrument bias was eliminated as a source of wind speed error.

The third possiblity for disagreement between the scatterometer-derived surface wind speeds and those from the INS at altitude is boundary layer dependence. Since the frictional boundary layer of Hurricane Allen has not been specified to the extent that surface wind speeds can be defined, the INS measurements remain the best estimator.

The wind direction comparison between the scatterometer and the 3000-m INS (fig. 28(b)) suggests a 12° difference. This is to be expected from the surface friction of a cyclonic boundary layer (Perry and Walker, 1977, p. 66), and does not depend on quadrant.

Within the limitations imposed by insufficient knowledge of the surface winds, the scatterometer results from Hurricane Allen may be useful for verifying or modifying the geophysical algorithm. A greater number of unique azimuths were available for each wind vector solution (figs. 20 to 27) for the scatterometer in Hurricane Allen than were available from the Seasat scatterometer experience; thus the wind speed and direction accuracy can be defined better.

The scatterometer is consistent in estimating wind direction. Note in particular scatterometer solutions 13 to 18, all obtained during pass 20E (fig. 23). All three incidence angles (19°, 39°, and 52°) are used, yet the wind direction for each case is 173° ± 6°. The same degree of consistency is seen for passes 21E and 24S (figs. 24 and 26), both of which used more than one incidence angle.

8. CONCLUSIONS

This report has summarized the NASA Langley Research Center analysis of the airborne microwave remote sensing measurements obtained in Hurricane Allen. Radiometer wind speed was calculated from the increase in antenna brightness temperature over an estimated no-wind value, and radiometer rain rate was calculated from a corrected difference between antenna temperature increases at two frequencies. These data show that the stepped frequency microwave radiometer can simultaneously measure wind speed up to 70 m/sec and rain rate in excess of 60 mm/hr. Scatterometer wind vector was obtained from the sea-surface radar cross section measured at various azimuths.

The evaluation of each of the microwave instruments requires qualification for one or more conditions of the experiment. In the case of the radiometer rain rate verification, the failure of underwing droplet samplers degraded the calculation of in situ precipitation from the aircraft rain radars. Assessment of the scatterometer measurement of sea-surface radar cross section in high wind speed was influenced by the fact that the greatest surface wind speeds in a hurricane are generally in or near heavy rain, which attenuated the scatterometer signal. Correction for this attenuation using the radiometer-determined rain rates was not attempted in this analysis. However, the nonavailability of in situ surface wind measurements is the most serious limitation on the evaluation of wind speed results from either microwave instrument.

In this analysis, some light has been shed on the use of active and passive microwave sensors for measuring (from a safe altitude) the near-surface phenomena of interest to hurricane scientists.

NASA Langley Research Center
Hampton, VA 23665-5225
June 5, 1985

9. REFERENCES

Black, Peter G.; and Schricker, Terry 1978: Direct and Remote Sensing of Ocean Temperature From an Aircraft. Fourth Symposium on Meterological Observations and Instrumentation of the American Meteorological Soc., pp. 158-165.

Dome, George 1975: Effect of Precipitation on Choice of Frequency for SEASAT Scatterometer. NASA CR-132749.

Frey, Gary F. 1980: The Hurricane Hunters. J. American Aviat. Hist. Soc., vol. 25, no. 1, Spring, pp. 45-56.

Gloersen, Per; and Barath, Frank T. 1977: A Scanning Multichannel Microwave Radiometer for Nimbus-G and SeaSat-A. IEEE J. Oceanic Eng., vol. OE-2, no. 2, Apr., pp. 172-178.

Harrington, Richard F. 1980: The Development of a Stepped Frequency Microwave Radiometer and Its Application to Remote Sensing of the Earth. NASA TM-81847.

Haydu, Kenneth J.; and Darby, Evan R. 1983: Description and Operating Procedures for the NOAA-C130 AWRS System. NOAA TM-ERL RFC-11, U.S. Dep. Commerce, Mar. (Available from NTIS as PB83 197 053.)

Jones, W. Linwood; Black, Peter G.; Delnore, Victor E.; and Swift, Calvin T. 1981: Airborne Microwave Remote-Sensing Measurements of Hurricane Allen. Science, vol. 214, no. 4518, Oct. 16, pp. 274-280.

Jones, W. Linwood; and Schroeder, L. C. 1978: Radar Backscatter From the Ocean: Dependence on Surface Friction Velocity. Boundary-Layer Meteorol., vol. 13, nos. 1, 2, 3, 4, Jan., pp. 133-149.

Jones, W. Linwood; Schroeder, Lyle C.; Boggs, Dale H.; Bracalente, Emedio M.; Brown, Robert A.; Dome, George J.; Pierson, Willard J.; and Wentz, Frank J. 1982: The Seasat-A Satellite Scatterometer: The Geophysical Evaluation of Remotely Sensed Wind Vectors Over the Ocean. J. Geophys. Res., vol. 87, no. C5, Apr. 30, pp. 3297-3317.

Jorgensen, David P. 1984: Mesoscale and Convective-Scale Characteristics of Mature Hurricanes. Part I: General Observations by Research Aircraft. J. Atmos. Sci., vol. 41, no. 8, Apr. 15, pp. 1268-1285.

Jorgensen, David P.; and Willis, Paul T. 1982: A Z-R Relationship for Hurricanes. J. Appl. Meteorol., vol. 21, no. 3, Mar., pp. 356-366.

Kaupp, Verne H.; and Holtzman, Julian C. 1979: Skylab Scatterometer Measurements of Hurricane Ava: Anomalous Data Correction. IEEE Trans. Geosci. Electron., vol. GE-17, no. 1, Jan., pp. 6-13.

Kidder, Stanley Q.; Gray, William M.; and Vonder Haar, Thomas H. 1980: Tropical Cyclone Outer Surface Winds Derived From Satellite Microwave Sounder Data. Mon. Weather Rev., vol. 108, no. 2, Feb., pp. 144-152.

Lawrence, Miles B.; and Pelissier, Joseph M. 1981: Atlantic Hurricane Season of 1980. Mon. Weather Rev., vol. 109, no. 7, July, pp. 1567-1582.

Marks, Frank D., Jr. 1981: Evolution of the Structure of Precipitating Convection in Hurricane Allen. 20th Conference - Radar Meteorology, American Meteorol. Soc., pp. 720-725.

Merceret, Francis J.; and Davis, Harlan W. 1981: The Determination of Navigational and Meteorological Variables Measured by NOAA/RFC WP3D Aircraft. NOAA TM-ERL RFC-7, U.S. Dep. Commerce, Apr. (Available from NTIS as PB81 225 468.)

Moore, R. K.; Birrer, I. J.; Bracalente, E. M.; Dome, G. J.; and Wentz, F. J. 1982: Evaluation of Atmospheric Attenuation From SMMR Brightness Temperature for the SEASAT Satellite Scatterometer. J. Geophys. Res., vol. 87, no. C5, Apr. 30, pp. 3337-3354.

Perry, A. H.; and Walker, J. M. 1977: The Ocean-Atmosphere System. Longman Inc.

Pierson, Willard J., Jr. 1983: The Measurement of the Synoptic Scale Wind Over the Ocean. J. Geophys. Res., vol. 88, no. C3, Feb. 28, pp. 1683-1708.

Rogers, R. R. 1976: Statistical Rainstorm Models: Their Theoretical and Physical Foundations. IEEE Trans. Antennas & Propag., vol. AP-24, no. 4, July, pp. 547-566.

Ross, D.; Au, B.; Brown, W.; and McFadden, J. 1974: A Remote Sensing Study of Pacific Hurricane Ava. Proceedings of the Ninth International Symposium on Remote Sensing of Environment, Volume I, Willow Run Labs., Environmental Res. Inst. of Michigan, pp. 163-180.

Schroeder, Lyle C.; Boggs, Dale H.; Dome, George; Halberstam, Isadore M.; Jones, W. Linwood; Pierson, Willard J.; and Wentz, Frank J. 1982: The Relationship Between Wind Vector and Normalized Radar Cross Section Used To Derive SEASAT-A Satellite Scatterometer Winds. J. Geophys. Res., vol. 87, no. C5, Apr. 30, pp. 3318-3336.

Thompson, T. W.; Weissman, D. E.; and Gonzalez, F. I. 1983: L Band Radar Backscatter Dependence Upon Surface Wind Stress: A Summary of New SEASAT-1 and Aircraft Observations. J. Geophys. Res., vol. 88, no. C3, Feb. 28, pp. 1727-1735.

Weissman, David E.; King, David B.; and Thompson, Thomas W. 1979: Relationship Between Hurricane Surface Winds and L-Band Radar Backscatter From the Sea Surface. J. Appl. Meteorol., vol. 18, no. 8, Aug., pp. 1023-1034.

Willoughby, H. E.; Clos, J. A.; and Shoreibah, M. G. 1982: Concentric Eye Walls, Secondary Wind Maxima, and the Evolution of the Hurricane Vortex. J. Atmos. Sci., vol. 39, no. 2, Feb., pp. 395-411.

TABLE 1.- AIRCRAFT PASSES

[Times are Greenwich Mean Times given in hours, minutes, and seconds]

Pass	C-130		P-3			Storm center		
	Start, hr min sec	Stop, hr min sec	Start, hr min sec	Stop, hr min sec	Alt., m	Lat. N, deg min	Long. W, deg min	Time, hr min
August 5								
1N	11 33 50	11 44 24	11 30 14	11 42 43	1500	15°56'	70°20'	11 37
2S	11 44 38	12 04 34	11 42 58	11 57 36	1500	15°56'	70°25'	11 52
3W	12 38 10	12 46 48	12 24 58	12 36 00	1500	15°59'	70°38'	12 35
4E	12 47 02	13 07 55	12 36 14	12 52 48	1500	16°01'	70°43'	12 51
5S	13 30 58	13 46 05	13 03 22	13 15 22	500	16°04'	70°54'	13 24
6N	13 46 19	14 01 55	13 15 36	13 39 36	500	16°05'	70°57'	13 38
7N	15 03 22	15 14 53	14 42 58	14 59 31	1500	16°15'	71°22'	14 58
8S	15 15 07	15 29 46	16 09 50	16 31 12	500-1500	16°22'	71°39'	15 53
9S	15 30 00	15 46 48	16 35 02	16 54 00	1500	16°24'	71°45'	16 12
10N	15 47 02	15 57 50	16 54 14	17 06 43	1500	16°26'	71°50'	16 26
11N	15 58 05	16 09 22	17 20 10	17 29 17	1500	16°28'	71°56'	16 43
12S	16 09 36	16 15 36	17 29 31	17 50 24	1500	16°30'	72°01'	16 59
August 8								
13E	18 50 10	19 34 00	18 30 29	18 58 48	1500	24°09'	92°00'	19 02
14W	19 20 38	19 38 24	18 59 02	19 13 55	1500	24°11'	92°05'	19 18
15W	19 38 38	19 54 14	19 14 10	19 28 34	1500	24°12'	92°09'	19 34
16S	19 57 07	20 14 10	19 28 48	19 43 55	1500	24°13'	92°13'	19 51
17S	20 14 24	20 31 41	19 44 10	20 00 00	1500	24°14'	92°17'	20 07
18N	20 31 55	20 48 43	20 00 14	20 17 31	1500	24°15'	92°21'	20 24
19N	20 48 58	21 05 17	20 17 46	20 34 05	1500	24°16'	92°25'	20 41
20E	21 05 31	21 30 43	20 34 19	20 56 10	1500	24°17'	92°29'	21 02
21E	21 30 58	21 55 41	20 56 24	21 17 46	1500	24°19'	92°34'	21 26
22W	21 55 55	22 16 19	21 18 00	21 19 41	1500	24°20'	92°38'	21 47
23W	22 16 34	22 36 29	21 50 10	22 02 53	1500	24°21'	92°42'	22 13
24S	22 36 43	23 00 14	22 03 07	22 19 12	1500	24°22'	92°45'	22 31
25S	23 00 29	23 21 07	22 19 26	22 34 34	1500	24°23'	92°47'	22 50
26N	23 21 22	23 30 00	22 34 48	22 56 24	1500	24°24'	92°48'	23 02

TABLE 2.- MODE DEFINITIONS FOR SCATTEROMETER DURING HURRICANE ALLEN

Mode	Antenna azimuth (with respect to aircraft nose)	Antenna elevation (with respect to nadir)
Mode 2 (Azimuth scan)	15° to 345° in 30° increments	Any fixed elevation; usually 19°, 39°, or 52°
Mode 3 (Elevation scan)	Any fixed azimuth	0° to 60° in 5°, 6°, or 10° increments
Mode 8 (Fixed position)	Any fixed azimuth	Any fixed elevation

TABLE 3.- SCATTEROMETER SOLUTIONS

Sol. no.	Pass	Start GMT, hr min sec	Stop GMT, hr min sec	Dist. from storm center, n.mi.	Radiometer rain rate, mm/hr	Radiometer wind speed, m/sec	INS wind speed, m/sec	Scatterometer wind speed, m/sec	INS wind direct., deg	Scatterometer wind direct., deg	No. of aliases	No. of 30° sectors	No. of 0.5-sec integrations	Nominal incidence angle, deg	Prob. of selected alias, %
1	13E	19 06 15	19 07 12	47.4	0.6	28.0	24.9	24.1	200	190	2	9	79	39	72
2	13E	19 07 27	19 08 38	42.6	.6	27.7	25.2	24.1	200	185	2	8	87	39	46
3	13E	19 08 39	19 09 50	38.6	.6	29.6	24.9	23.0	198	195	2	10	98	39	91
4	13E	19 09 51	19 11 02	34.2	0	29.0	26.2	26.0	202	189	2	6	70	39	16
5	13E	19 11 03	19 12 14	30.4	1.0	29.4	27.4	26.6	205	196	2	7	93	39	98
6	14W	19 31 13	19 31 55	34.6	0	33.3	27.4	28.0	031	024	3	6	47	39	84
7	16S	20 12 01	20 13 12	58.4	1.6	20.1	17.6	19.5	291	283	2	10	81	39	54
8	17S	20 17 03	20 18 14	50.1	1.2	15.4	17.4	19.4	286	264	2	11	95	39	79
9	17S	20 18 59	20 20 10	43.6	1.1	13.9	18.7	19.9	285	282	2	6	67	39	53
10	17S	20 20 11	20 20 53	40.3	1.0	18.2	17.9	21.0	288	280	2	6	55	39	33
11	17S	20 21 07	20 22 19	35.8	.9	16.1	19.9	20.9	294	279	2	11	84	39	30
12	17S	20 22 20	20 23 31	31.2	.9	20.6	22.6	21.9	293	264	2	11	91	39	31
13	20E	21 14 39	20 14 46	32.0	0	28.9	29.2	24.6	194	176	2	6	84	52	53
14	20E	21 15 51	21 17 02	35.9	.2	28.3	28.8	22.6	189	166	2	6	101	52	65
15	20E	21 17 03	21 18 14	40.5	1.0	28.9	27.7	23.5	188	166	2	8	103	52	32
16	20E	21 18 44	21 19 55	46.5	.5	29.7	28.0	27.1	182	172	2	10	93	39	12
17	20E	21 19 56	21 21 07	50.5	.2	31.3	27.3	26.5	182	180	2	10	83	39	22
18	20E	21 21 08	21 22 19	55.6	.1	33.1	27.9	25.5	182	166	2	11	91	19	83
19	21E	21 40 05	21 41 17	50.8	.1	30.5	27.5	27.6	180	154	2	9	92	39	5
20	21E	21 42 29	21 43 41	42.1	.6	29.5	27.3	22.4	188	160	2	10	88	39	95
21	21E	21 43 42	21 44 53	38.8	.2	29.1	26.3	23.5	188	169	2	10	88	39	98
22	21E	21 45 08	21 46 19	33.8	0	29.3	28.0	21.4	193	171	3	6	86	52	8
23	22W	21 55 41	21 56 24	2.6	1.3	25.2	13.4	14.9	026	036	2	7	60	19	95
24	22W	22 06 15	22 07 26	41.4	.8	33.5	25.1	28.6	026	016	2	11	94	39	27
25	22W	22 07 27	22 08 38	45.5	.6	33.9	25.3	28.0	027	008	2	10	82	39	95
26	22W	22 13 27	22 14 38	68.2	.1	32.9	31.5	25.3	032	001	3	8	97	52	33
27	24S	22 49 41	22 50 53	41.7	.2	26.6	23.7	23.9	269	264	2	9	100	39	45
28	24S	22 50 54	22 51 50	45.9	0	28.6	23.8	23.6	271	267	2	9	79	39	45
29	24S	22 52 34	22 53 46	51.6	.1	27.9	24.2	23.5	275	266	2	9	99	19	67
30	24S	22 53 47	22 54 43	55.6	.2	27.8	24.8	23.2	272	265	2	7	69	19	46
31	25S	23 02 24	23 03 36	65.6	0	29.5	23.6	25.5	284	273	2	11	85	39	58
32	25S	23 03 37	23 04 19	62.0	0	29.7	24.4	25.2	282	276	2	6	61	39	66
33	26N	23 30 44	23 31 55	35.7	.9	28.9	34.7	28.2	114	100	2	8	75	39	71
34	26N	23 31 56	23 33 07	39.6	.9	31.8	33.6	27.6	115	082	2	8	98	39	13

Figure 1.- NOAA C-130 aircraft en route to Hurricane Allen, August 4, 1980.

L-85-143

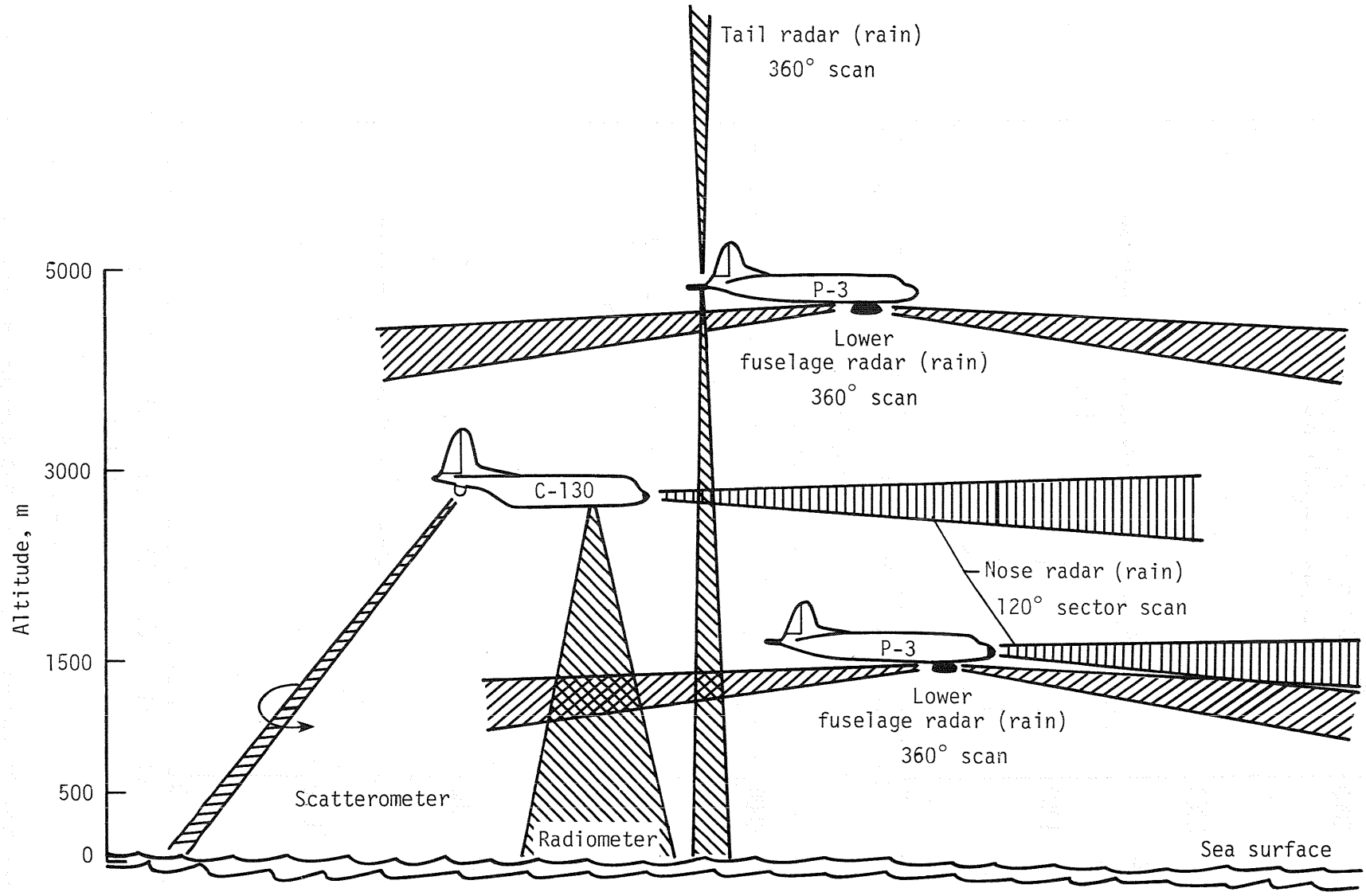

Figure 2.- Vertical stacking of NOAA aircraft in Hurricane Allen on August 5 and 8, 1980, showing NOAA rain radars and NASA microwave instruments.

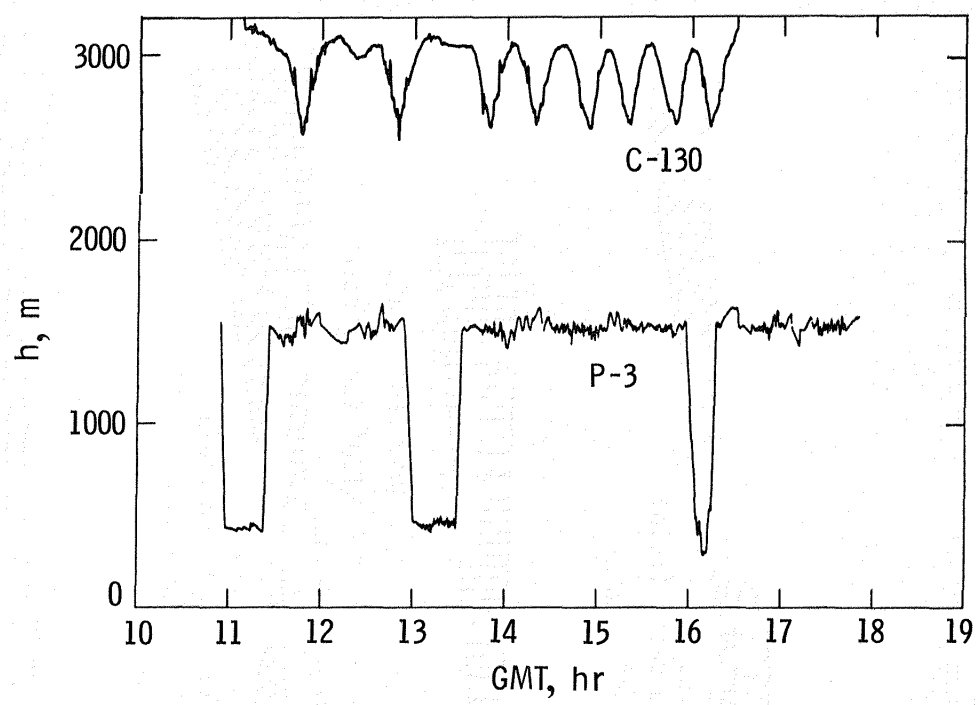

(a) August 5.

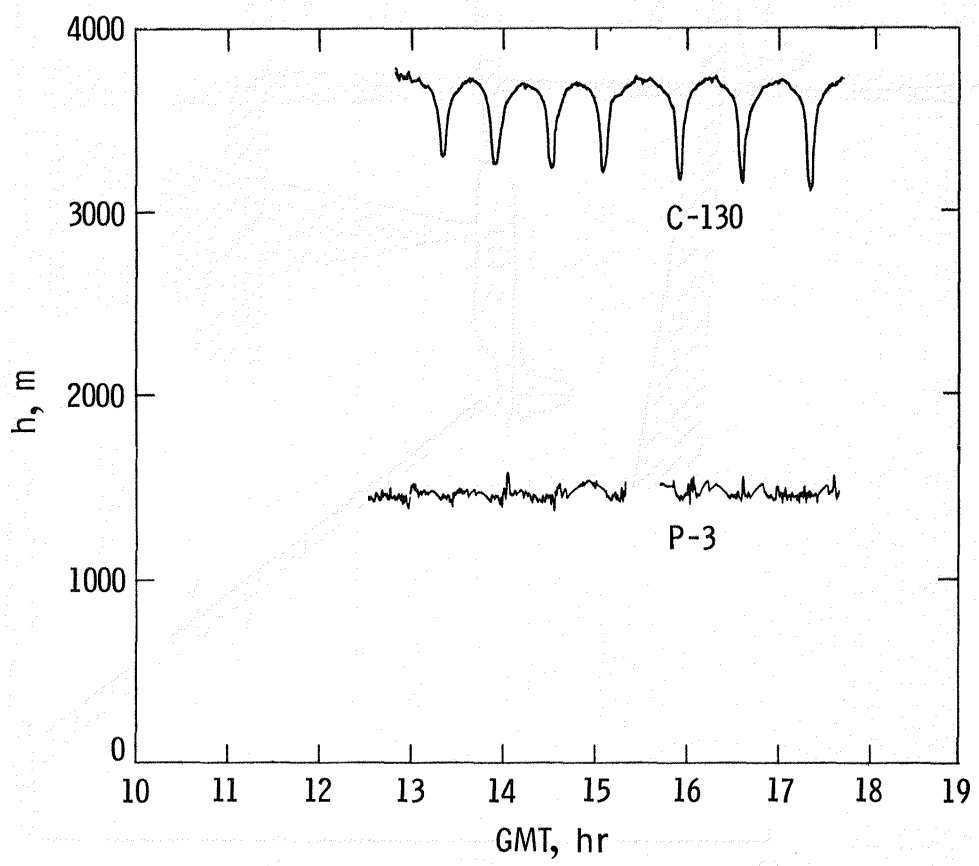

(b) August 8.

Figure 3.- Time histories of C-130 and P-3 altitude during storm penetrations.

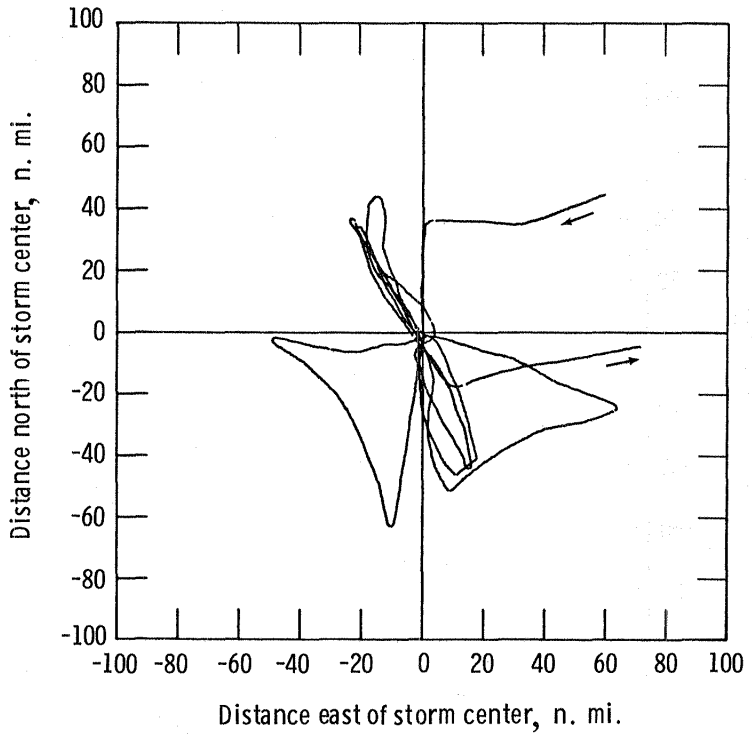

(a) C-130.

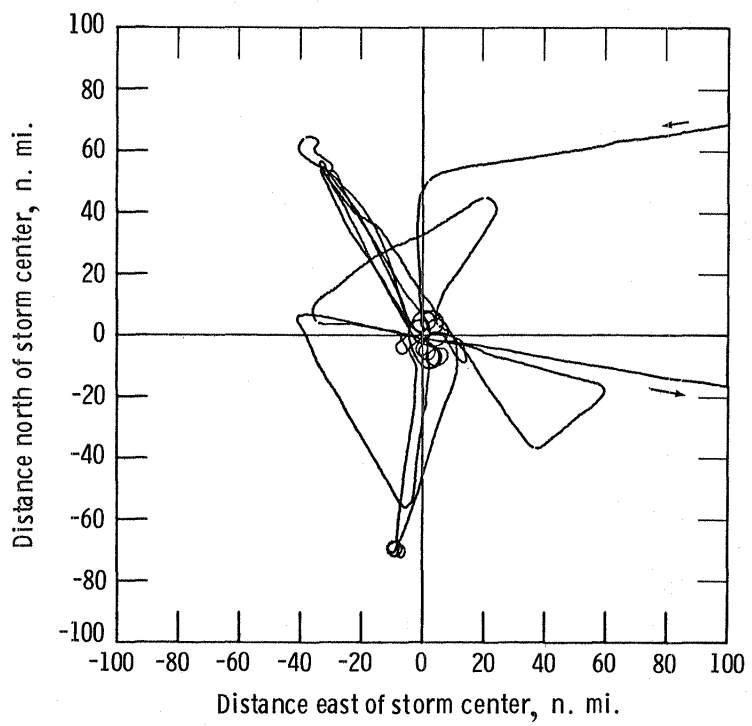

(b) P-3.

Figure 4.- Aircraft flight paths with respect to the storm's moving center on August 5.

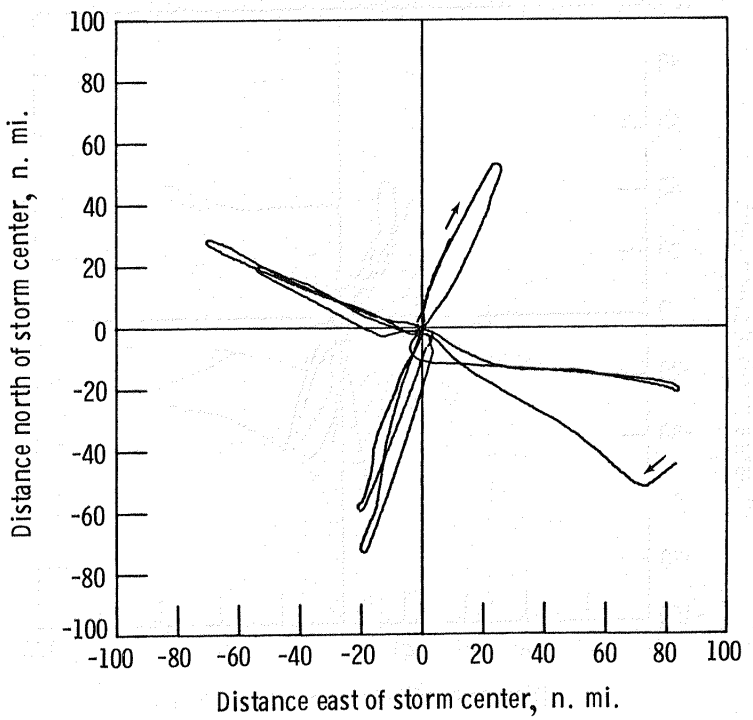

(a) C-130.

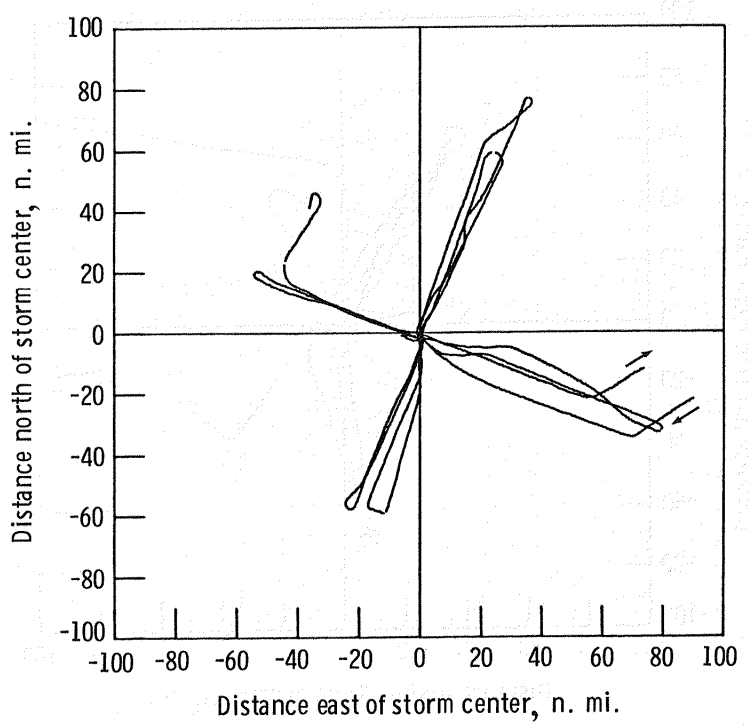

(b) P-3.

Figure 5.- Aircraft flight paths with respect to the storm's moving center on August 8.

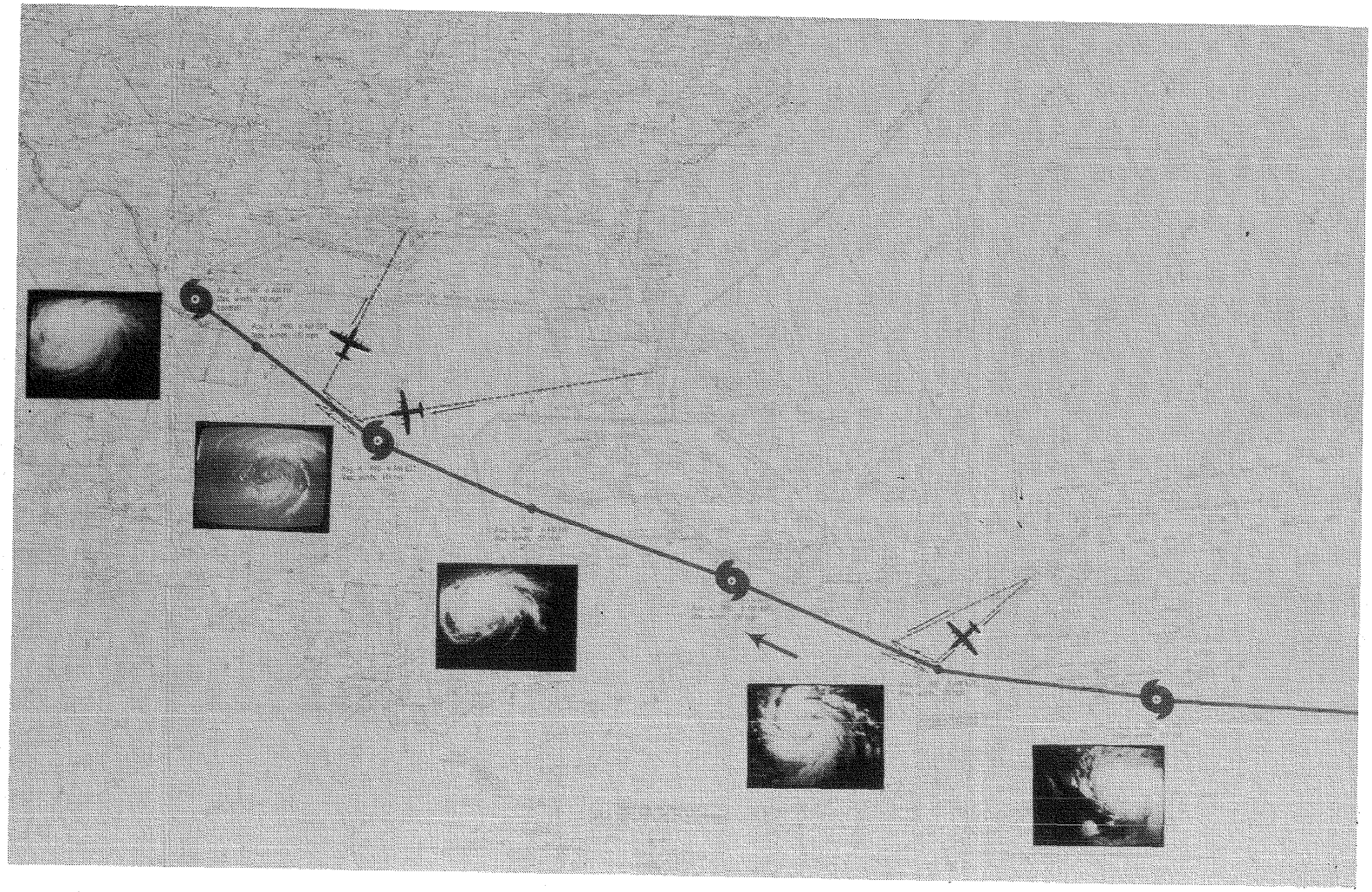

Figure 6.- Hurricane Allen track on August 4-10, 1980, showing locations of aircraft interceptions.

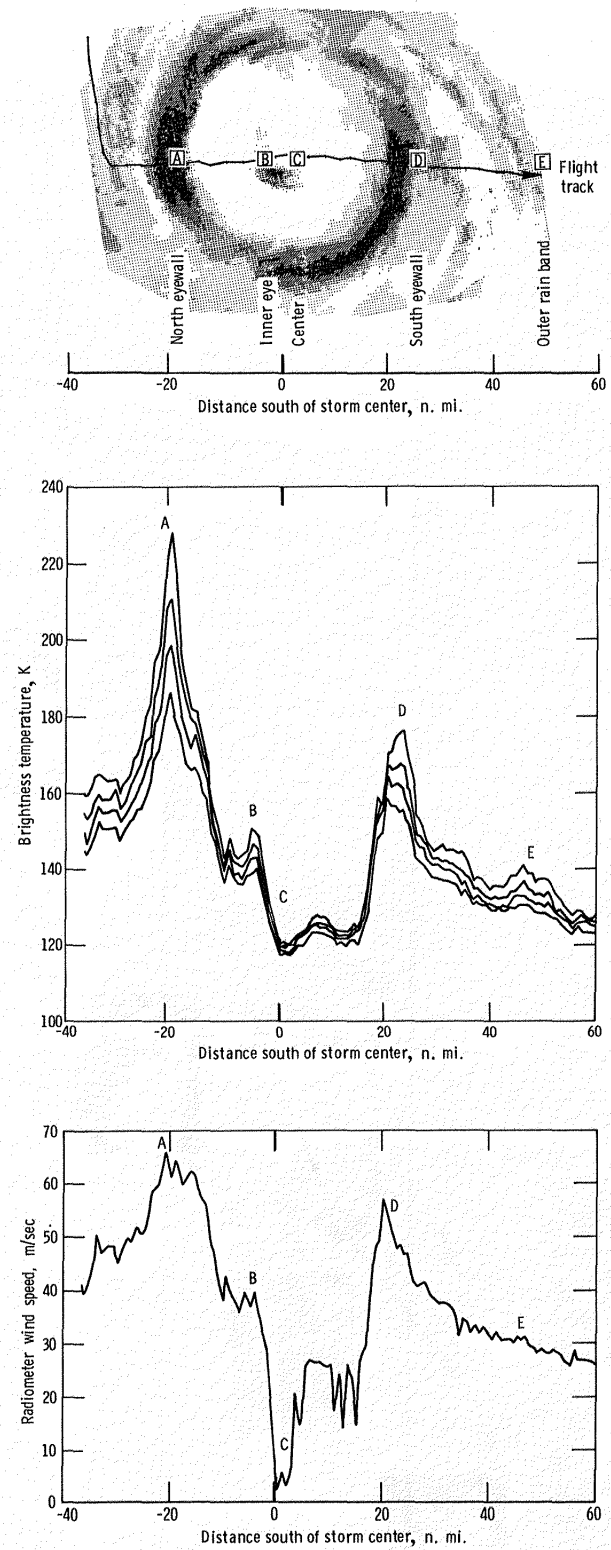

(a) Wind speed.

Figure 7.- Relationship between measured brightness temperature and calculated wind speed and rain rate for various features of Hurricane Allen.

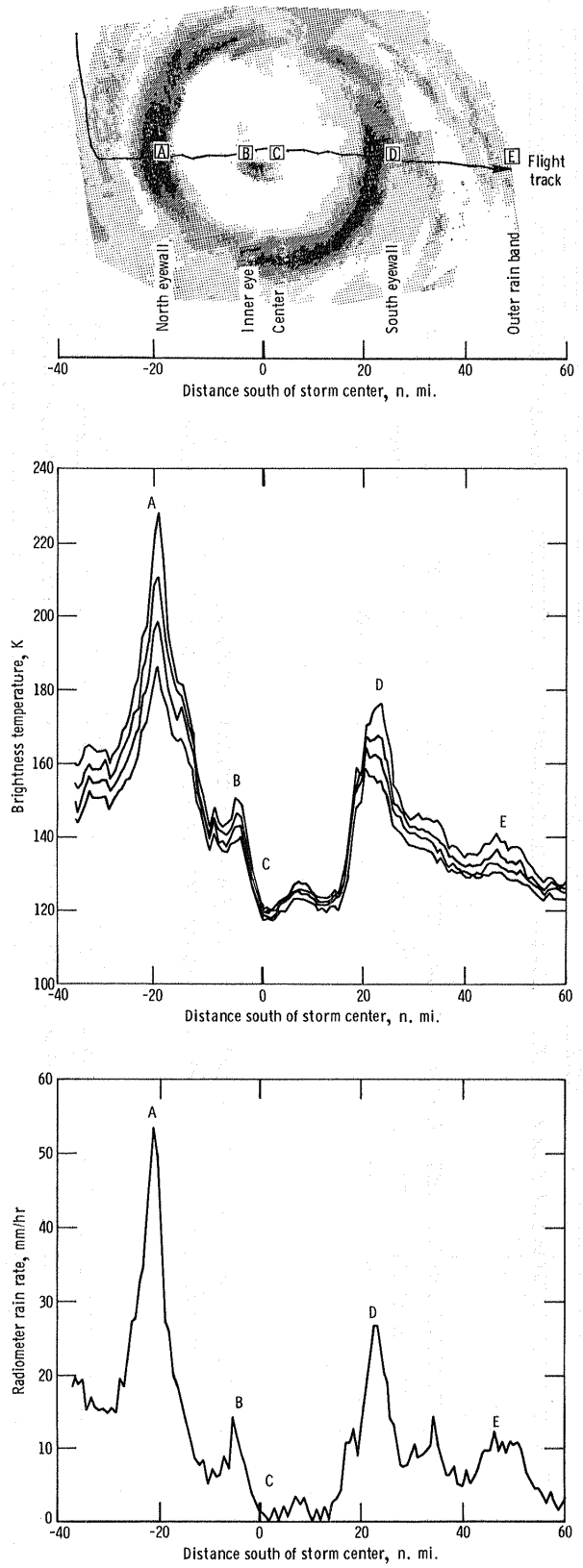

(b) Rain rate.

Figure 7.- Concluded.

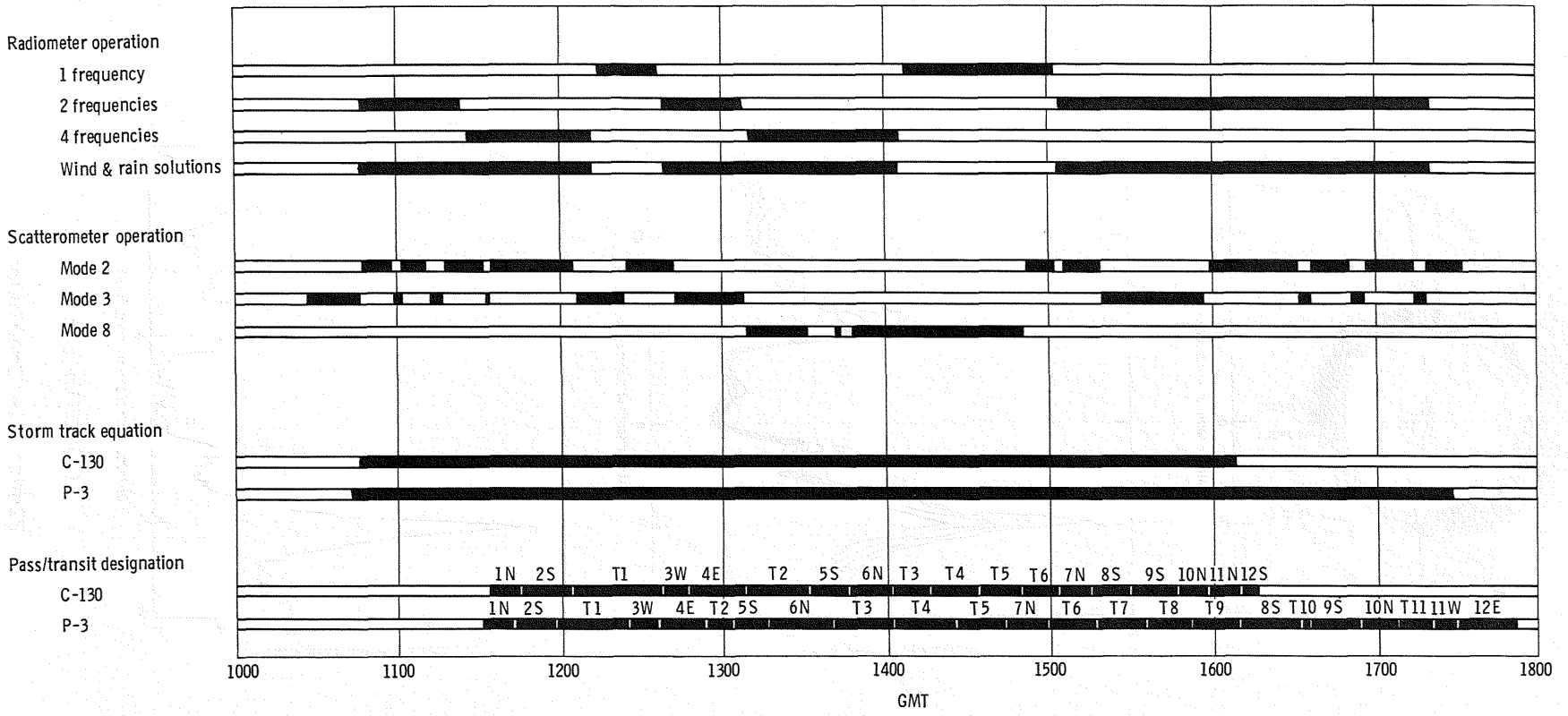

Figure 8.- Bar graph showing instrument status and pass number designations for August 5.

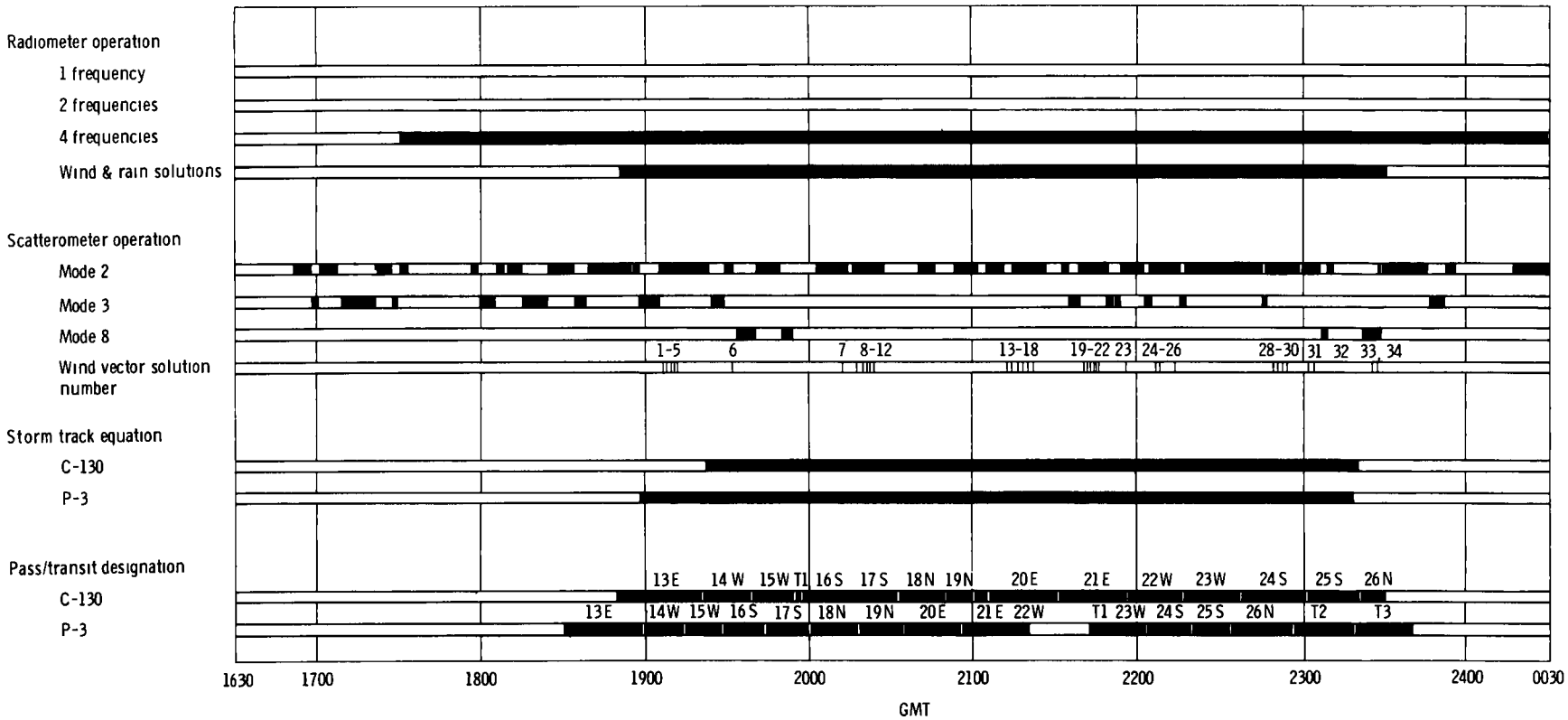

Figure 9.- Bar graph showing instrument status and pass number designations for August 8.

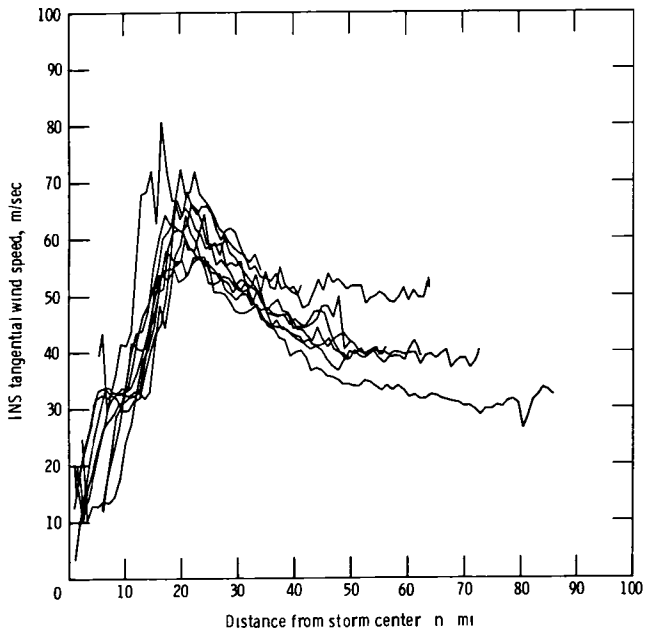

(a) P-3.

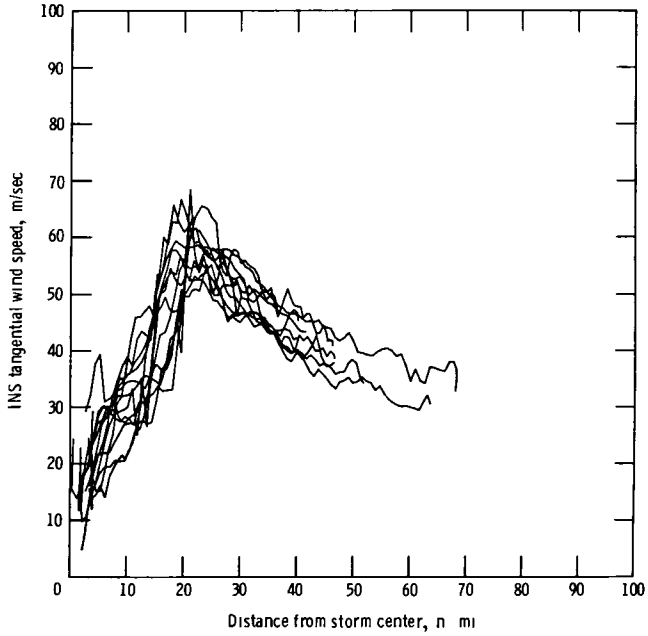

(b) C-130.

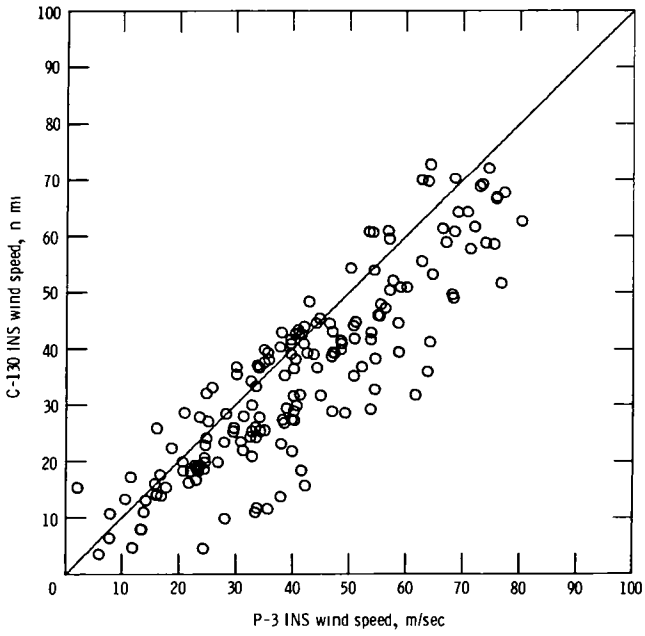

(c) P-3 vs. C-130 inside the eyewall.

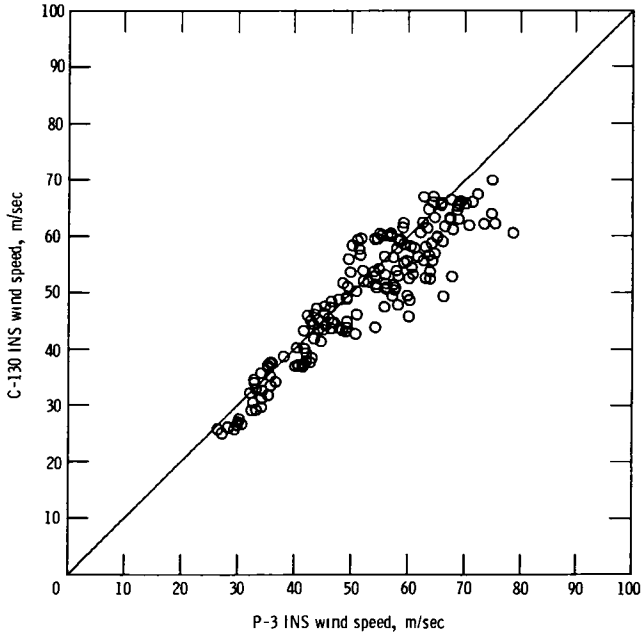

(d) P-3 vs. C-130 outside the eyewall.

Figure 10.- INS wind speeds corrected for forward motion of storm for August 5. P-3 at h = 1500 m.

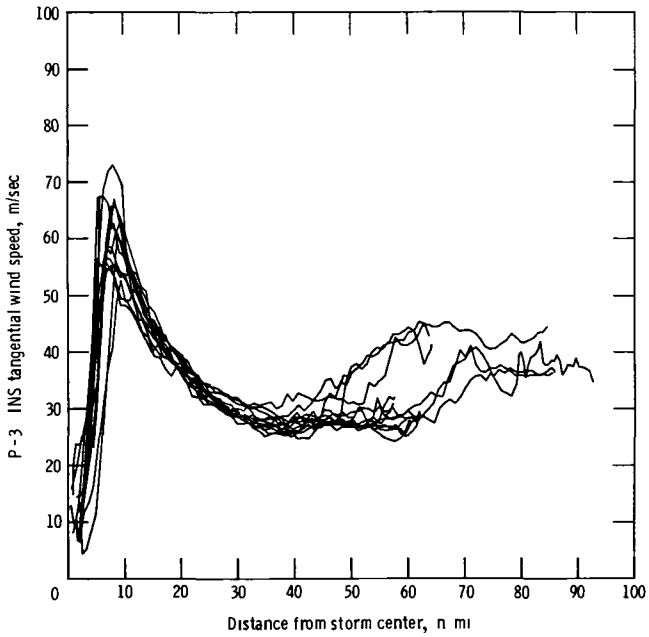

(a) P-3.

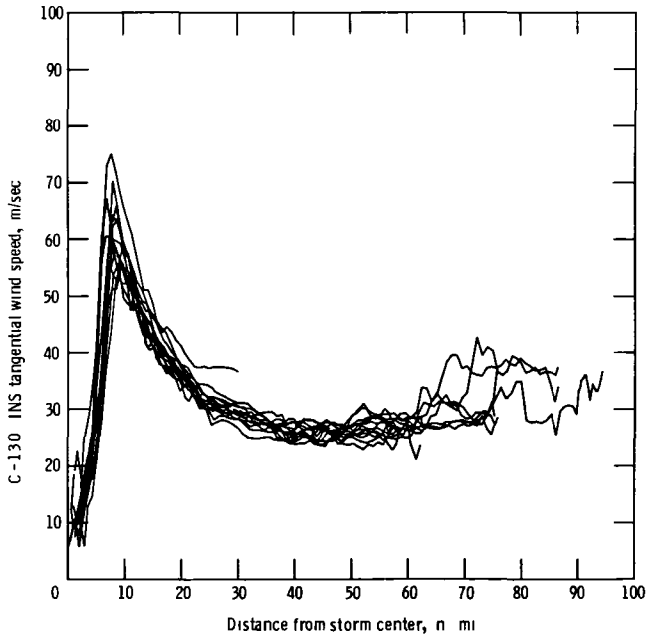

(b) C-130.

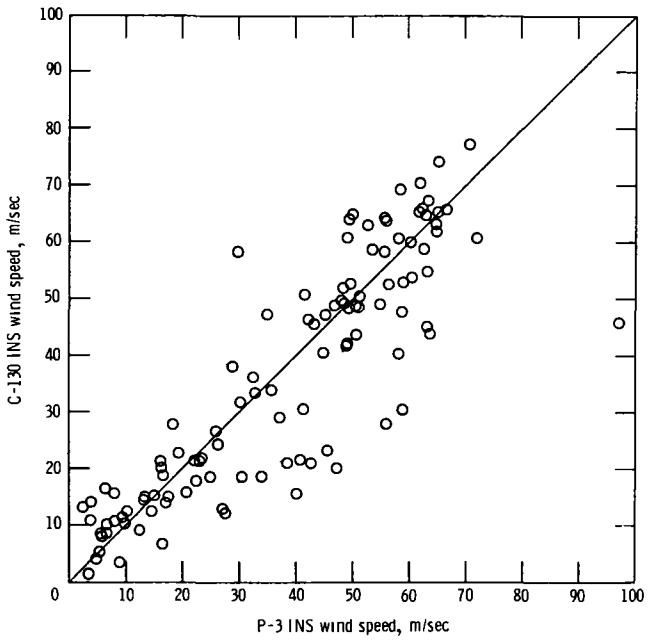

(c) P-3 vs. C-130 inside the eyewall.

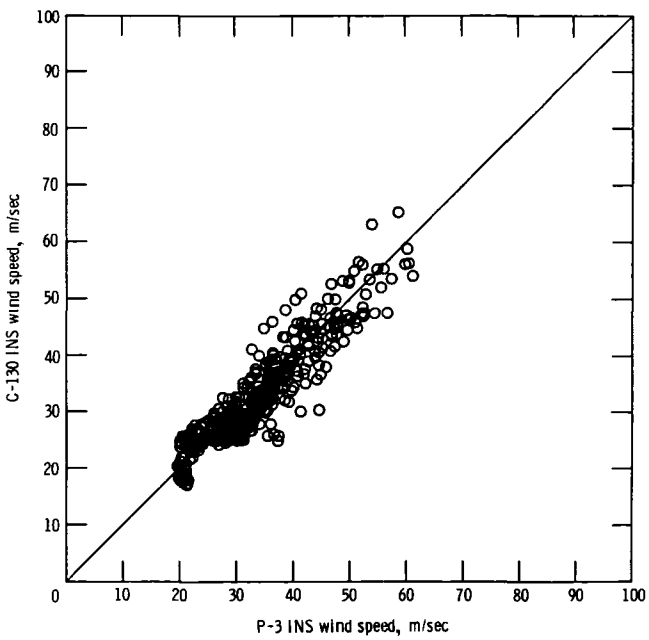

(d) P-3 vs. C-130 outside the eyewall.

Figure 11.- INS wind speeds corrected for forward motion of storm for August 8. P-3 at h = 1500 m.

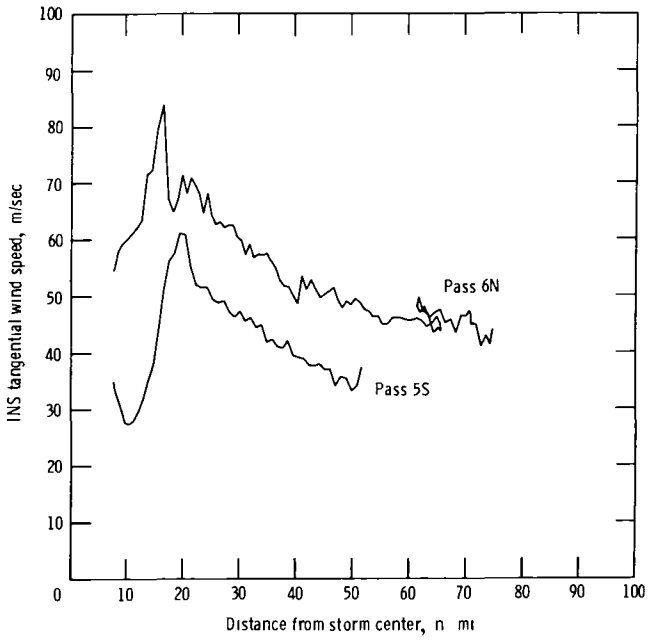

(a) P-3.

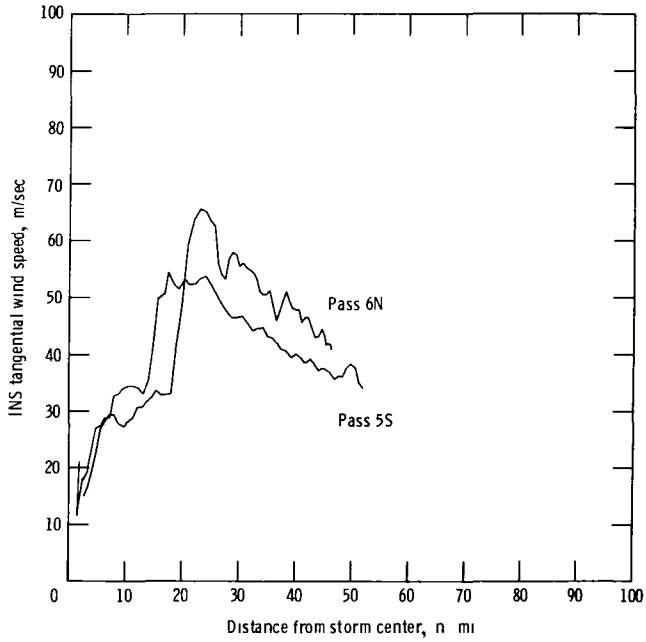

(b) C-130.

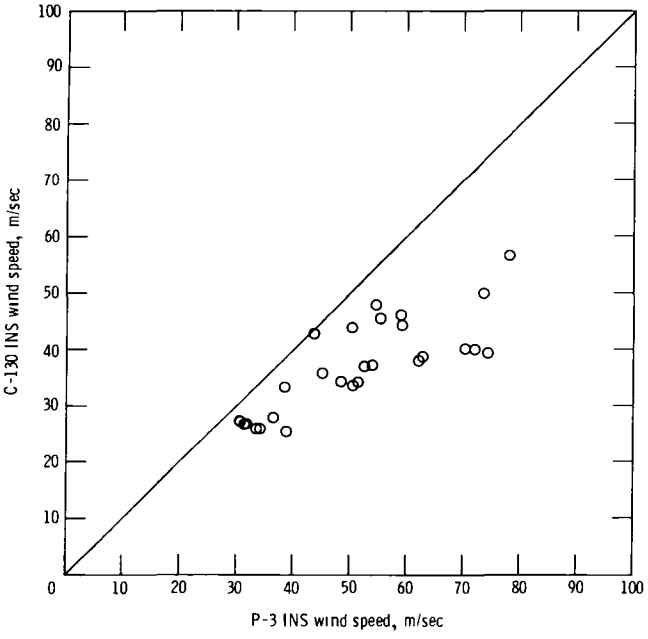

(c) P-3 vs. C-130 inside the eyewall.

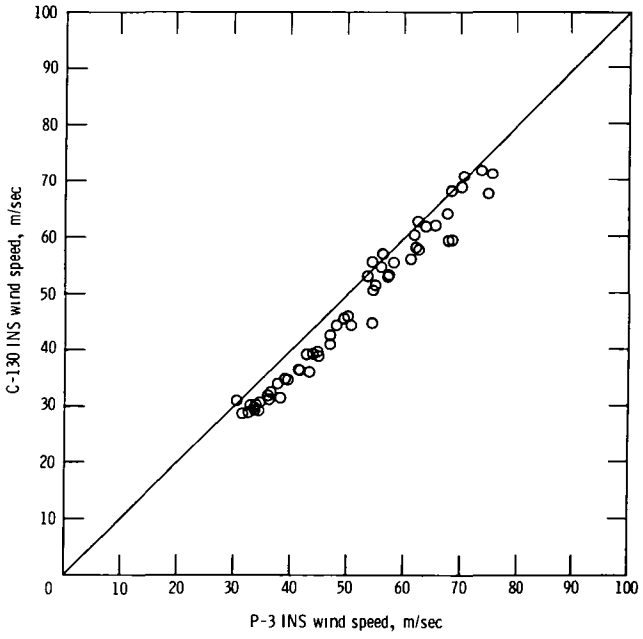

(d) P-3 vs. C-130 outside the eyewall.

Figure 12.- INS wind speeds corrected for forward motion of storm for August 5. P-3 at h = 500 m.

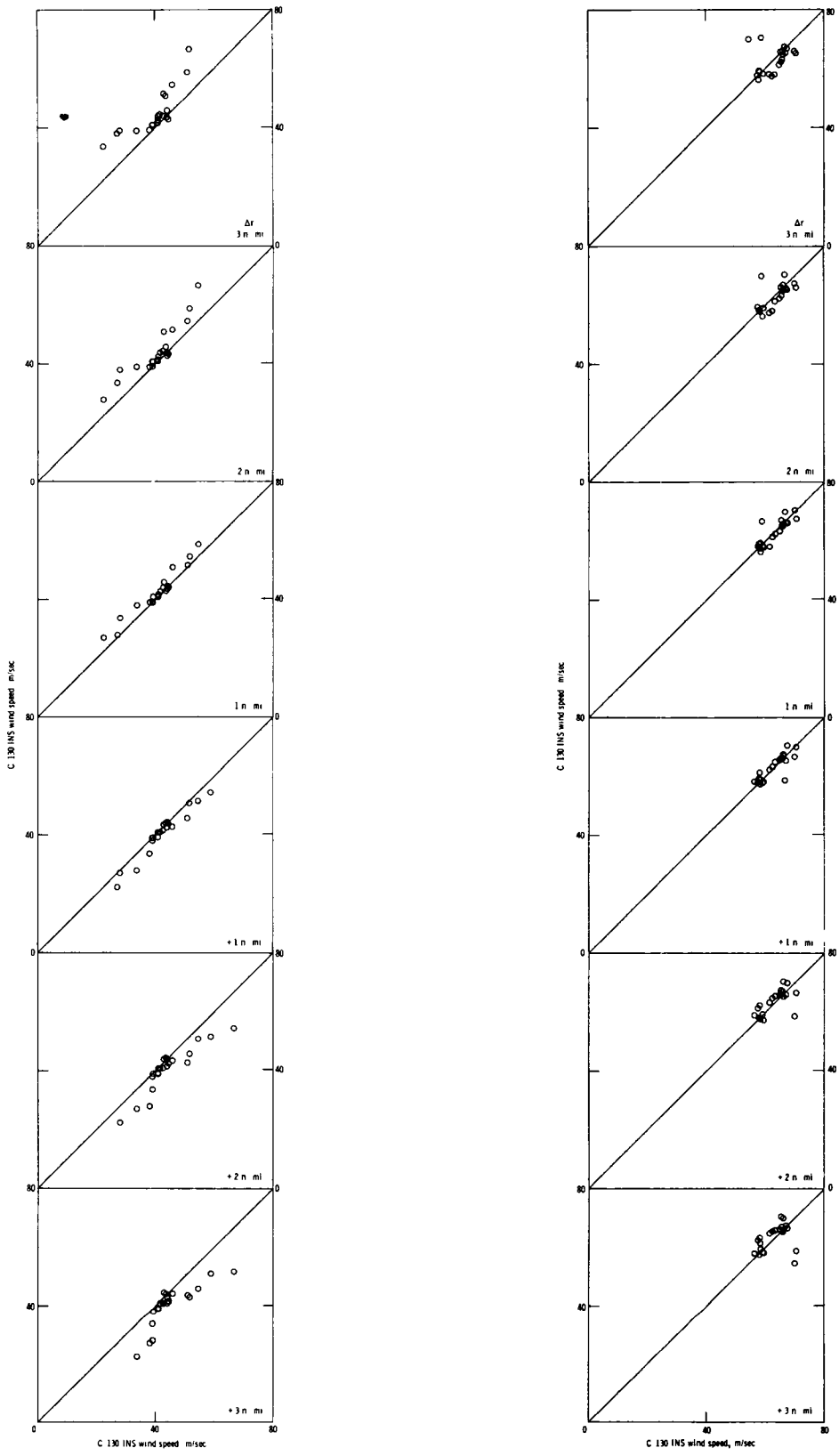

(a) Inside the eyewall.

(b) Outside the eyewall.

Figure 13.- C-130 INS wind speed plotted against itself for along-track shifts of -3 to +3 n.mi. Pass 1N.

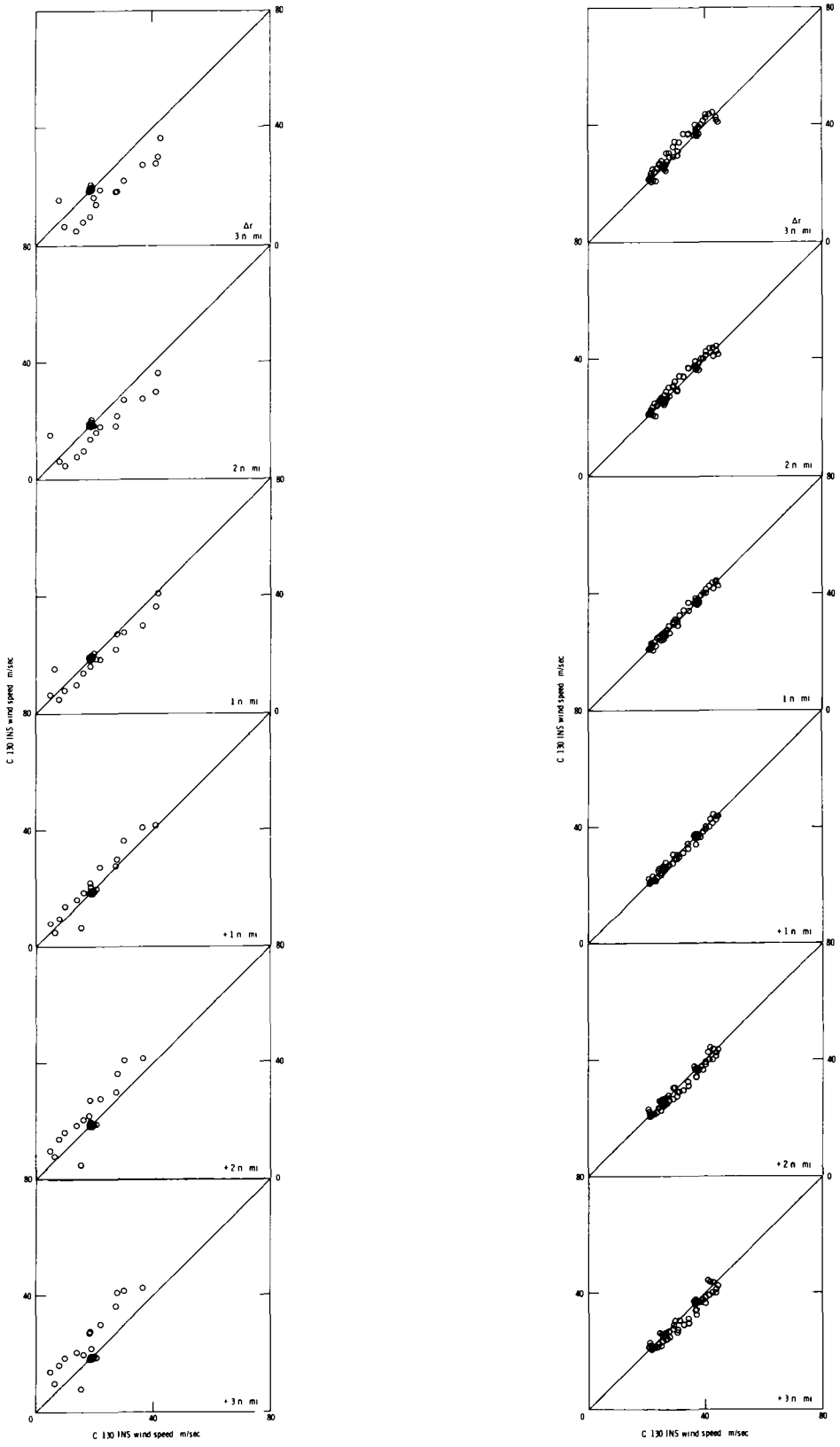

(a) Inside the eyewall.

(b) Outside the eyewall.

Figure 14.- C-130 INS wind speed plotted against itself for along-track shifts of -3 to +3 n.mi. Pass 2S.

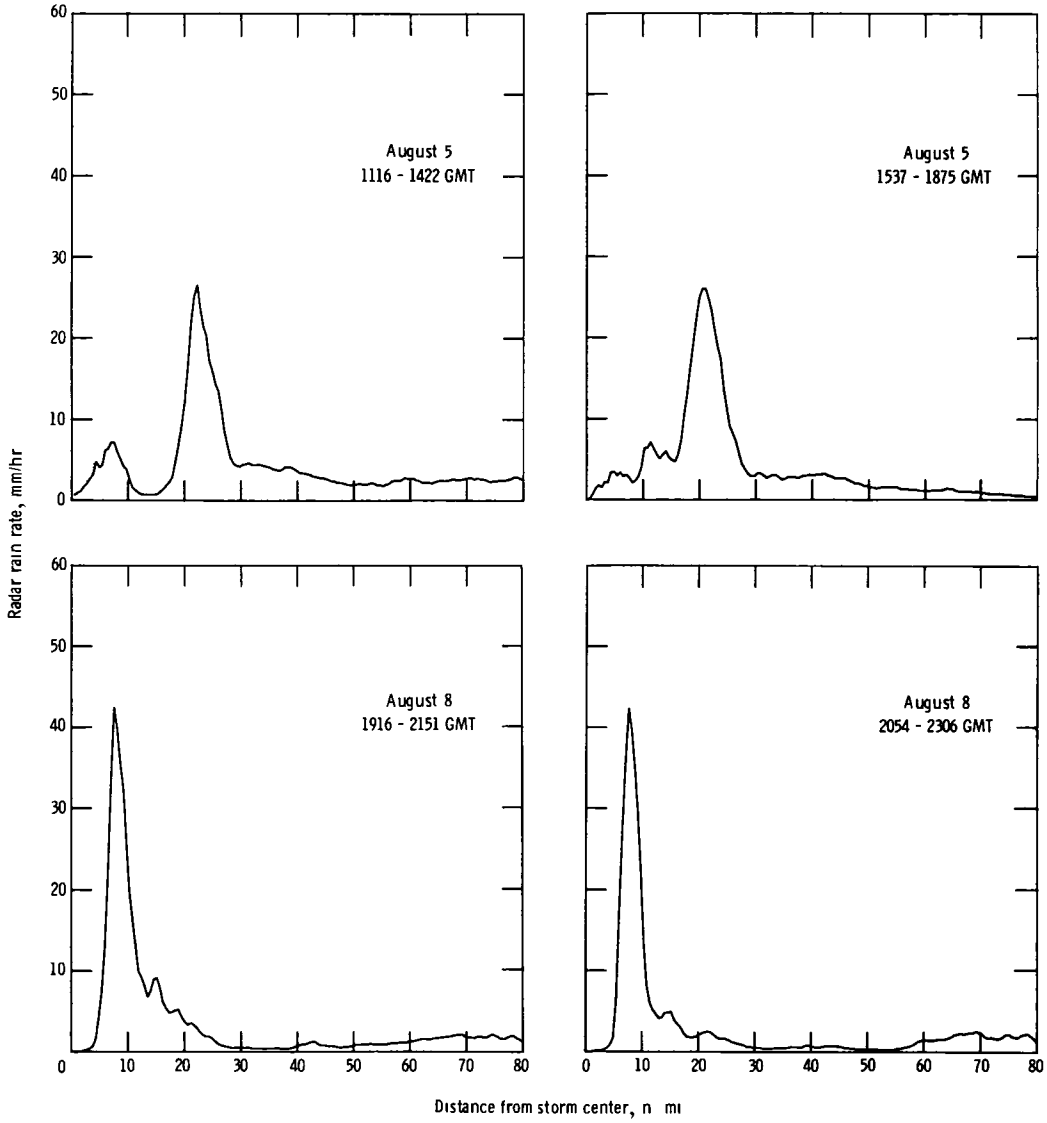

Figure 15.- Rain radar profiles accumulated over 360° azimuth.

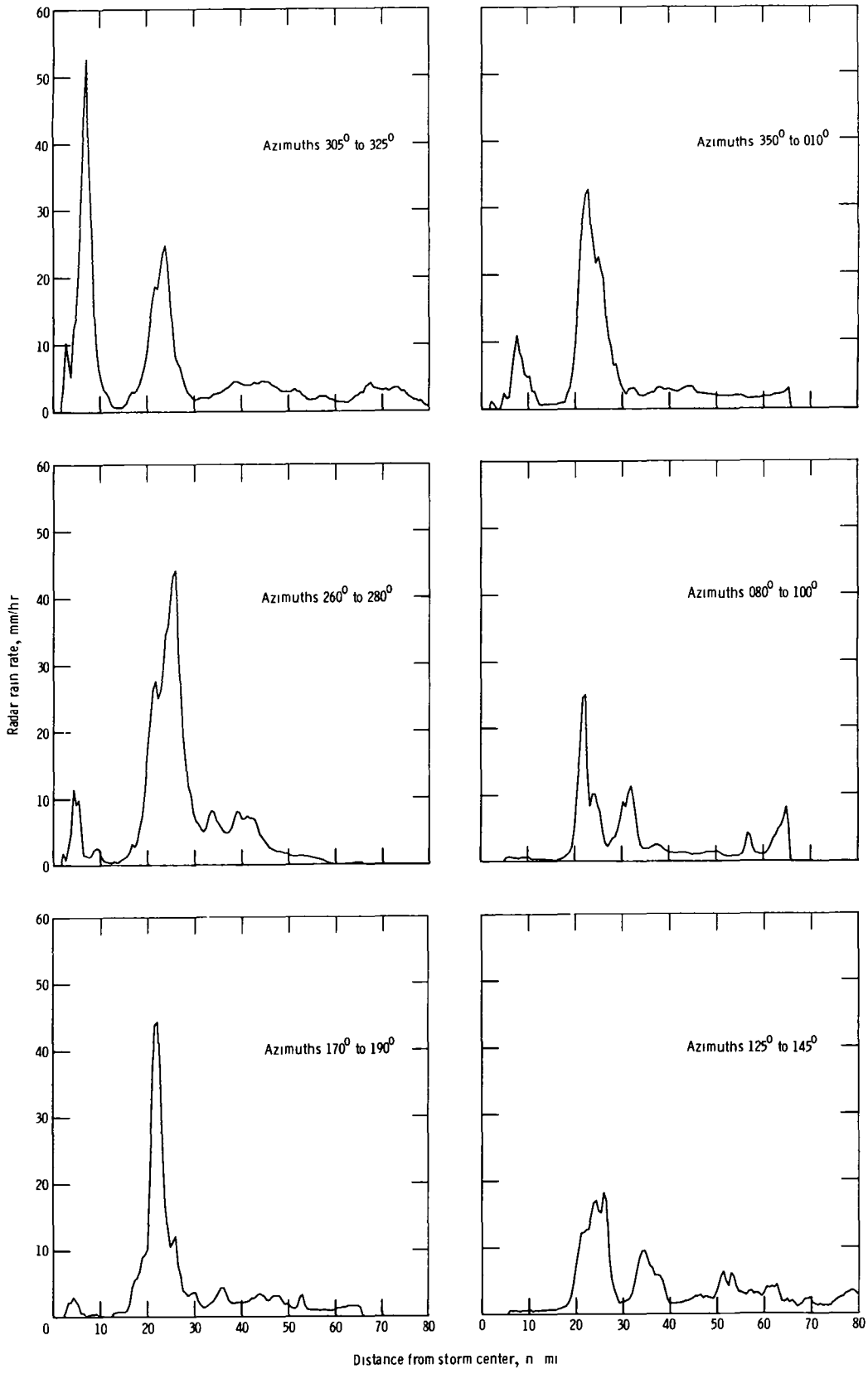

Figure 16.- Rain radar profiles for August 5, accumulated over azimuth sectors indicated.

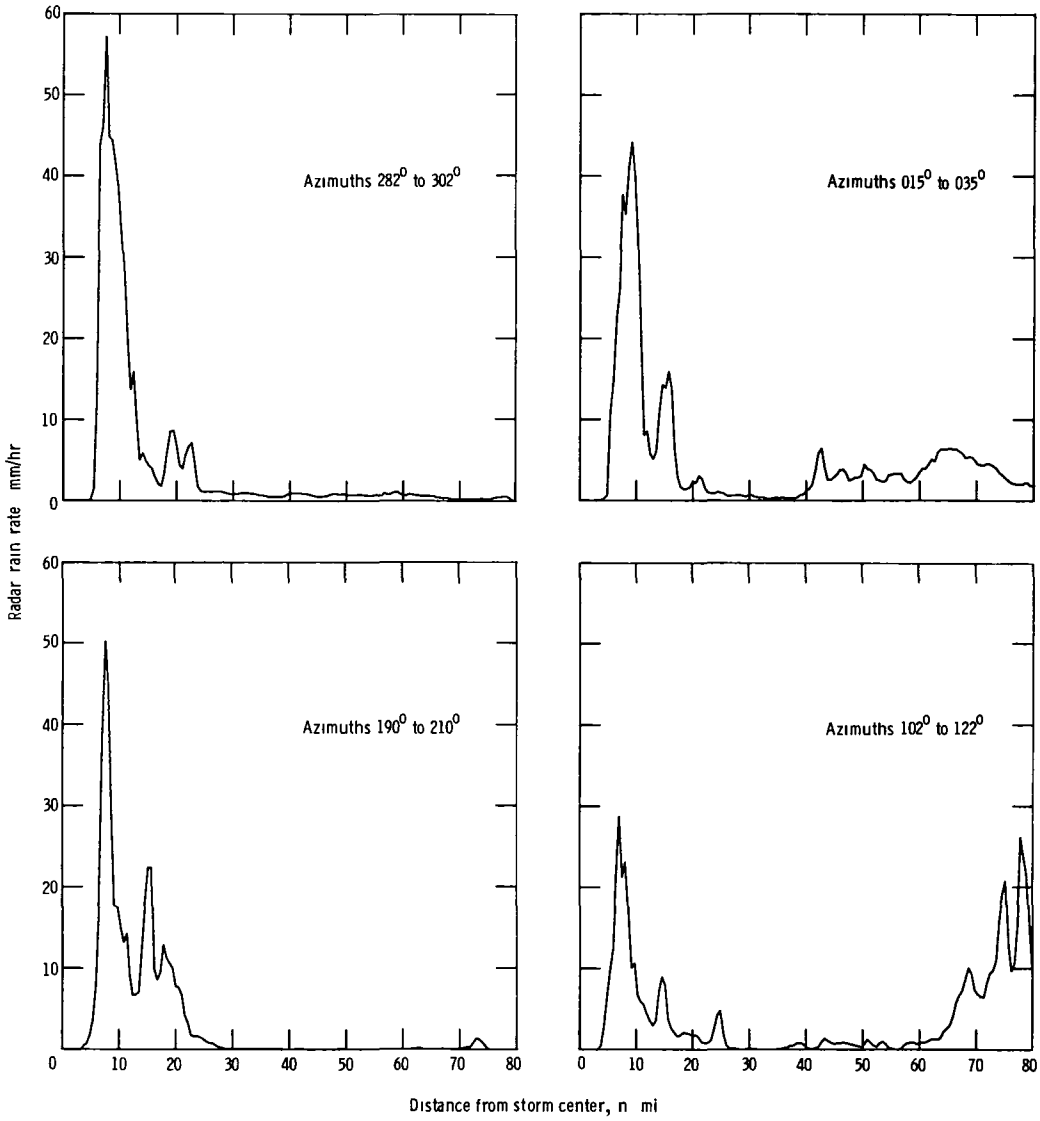

Figure 17.- Rain radar profiles for August 8, accumulated over azimuth sectors indicated.

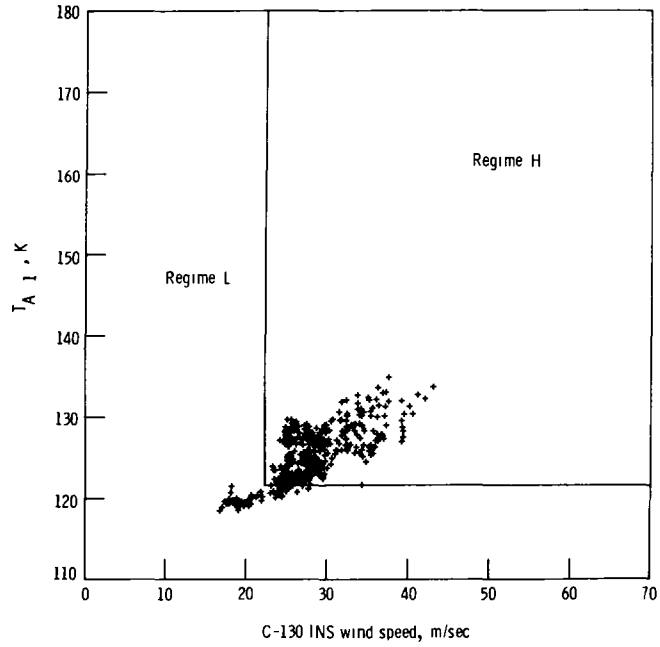

(a) C-130 INS wind speed vs. measured brightness temperature, at 10 to 50 n.mi. from the storm center.

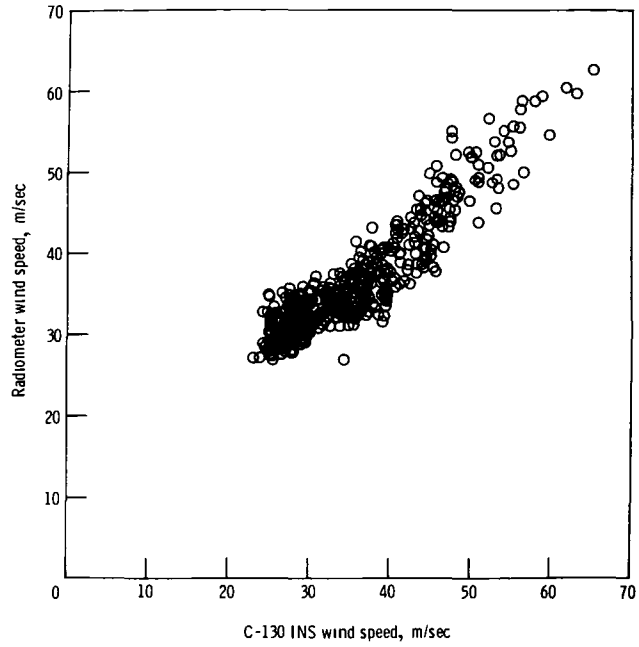

(b) C-130 INS wind speed vs. radiometer wind speed resulting from application of regression of data in (a) for regime H.

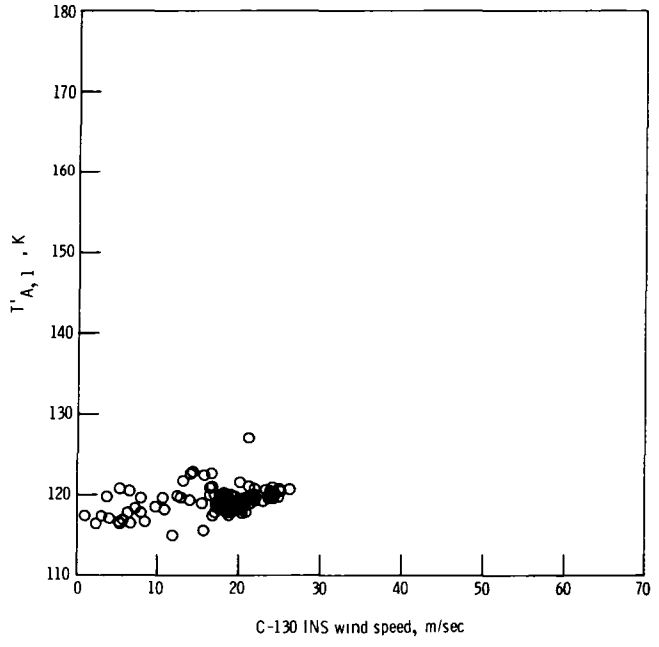

(c) C-130 INS wind speed vs. adjusted brightness temperature, regime L.

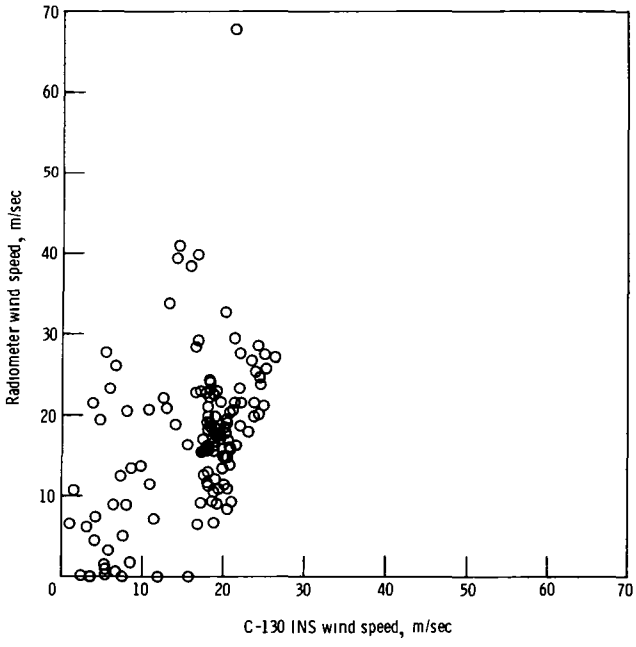

(d) C-130 INS wind speed vs. radiometer wind speed resulting from regression of data in (a) for regime L.

Figure 18.- Development of radiometer wind speed regression for data of August 8.

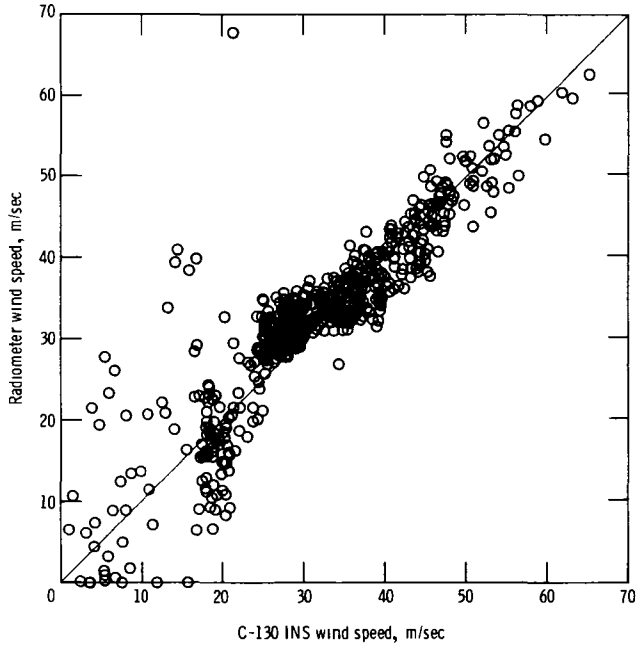

(a) C-130 INS wind speed vs. radiometer wind speed, August 8.

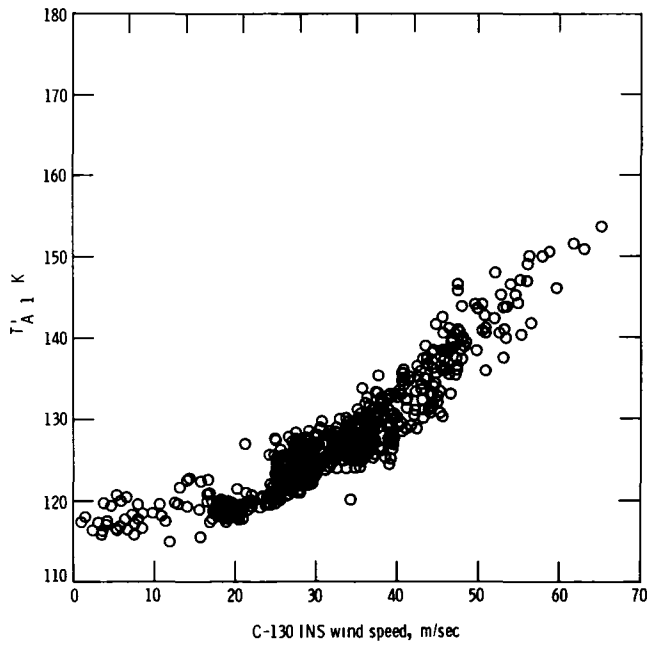

(b) C-130 INS wind speed vs. adjusted brightness temperature, August 8.

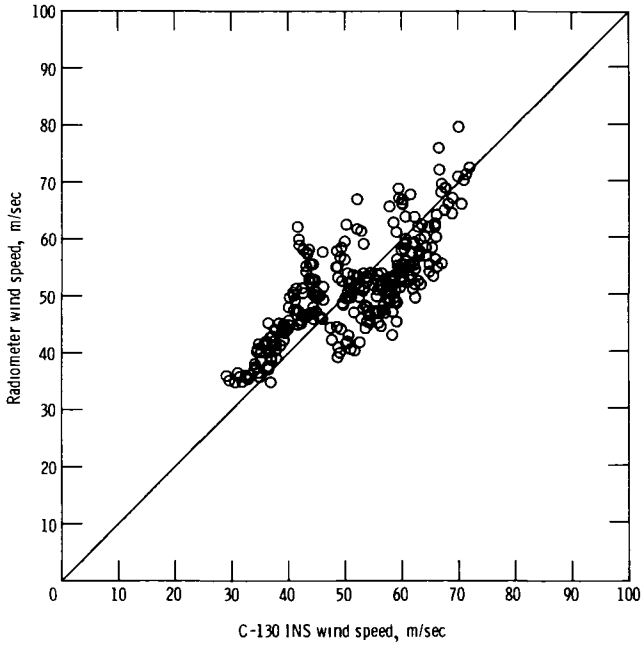

(c) C-130 INS wind speed vs. radiometer wind speed, August 5 at 20 to 40 n.mi. from storm center.

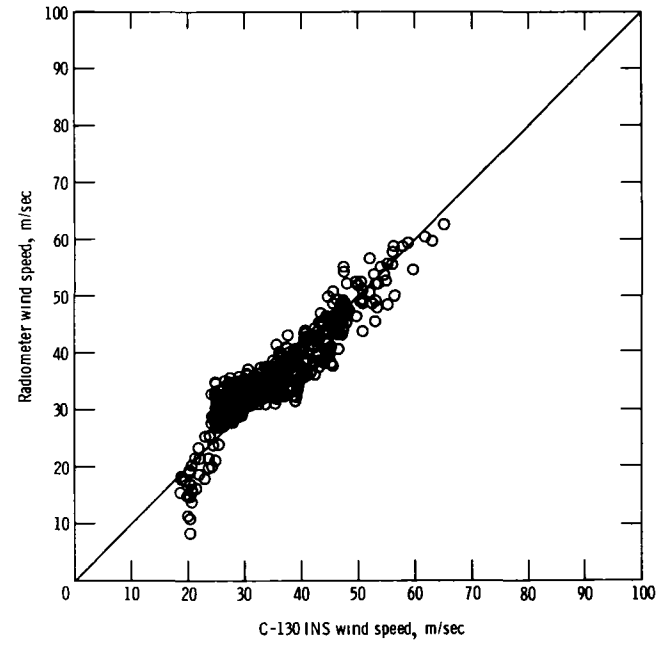

(d) C-130 INS wind speed vs. radiometer wind speed, August 8 at 10 to 40 n.mi. from storm center.

Figure 19.- Results of radiometer wind speed calculations for regimes H and L.

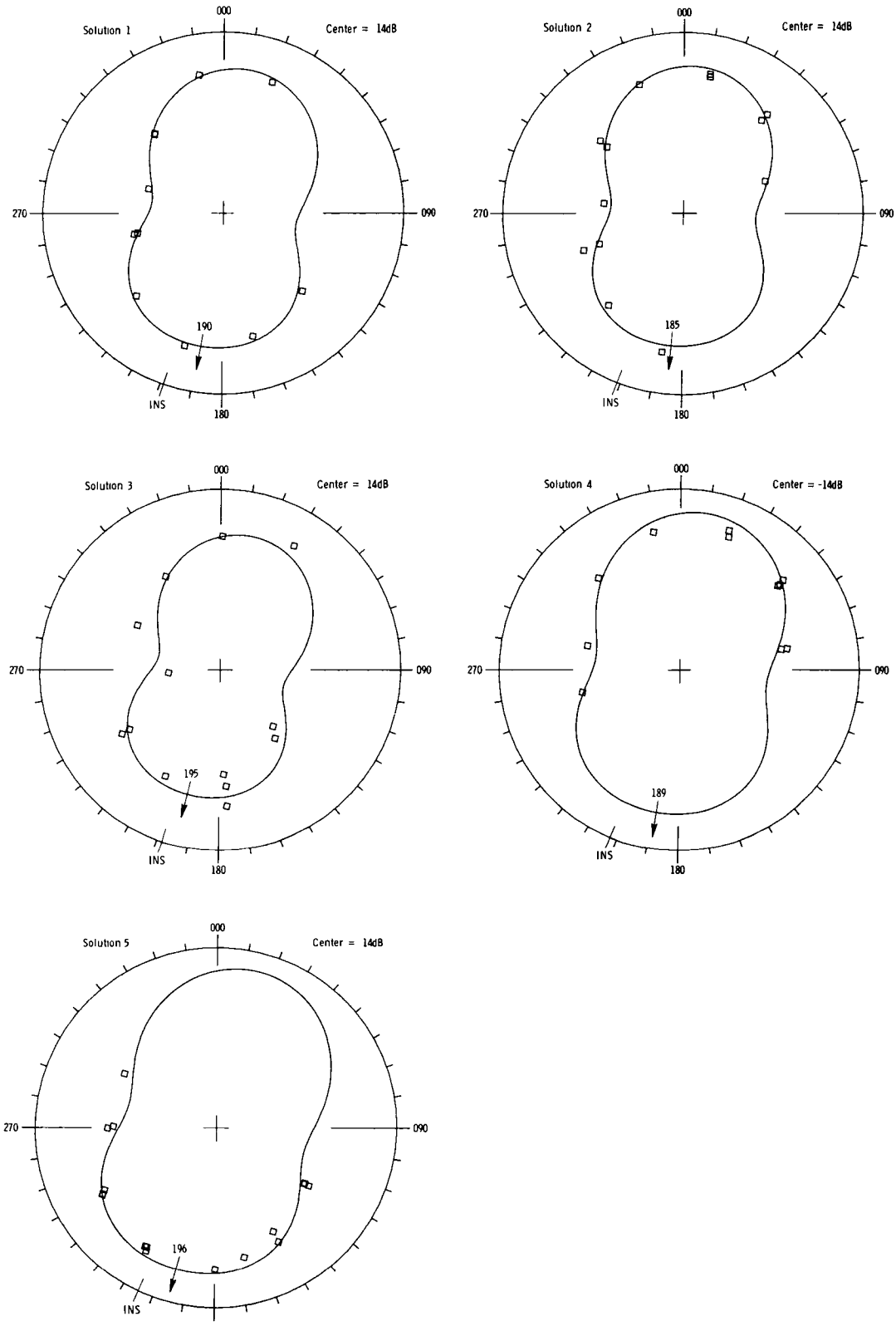

Figure 20.- Normalized radar cross section (σ^{o}) azimuth-scan data for pass 13E. See section 6.3.2 for explanation.

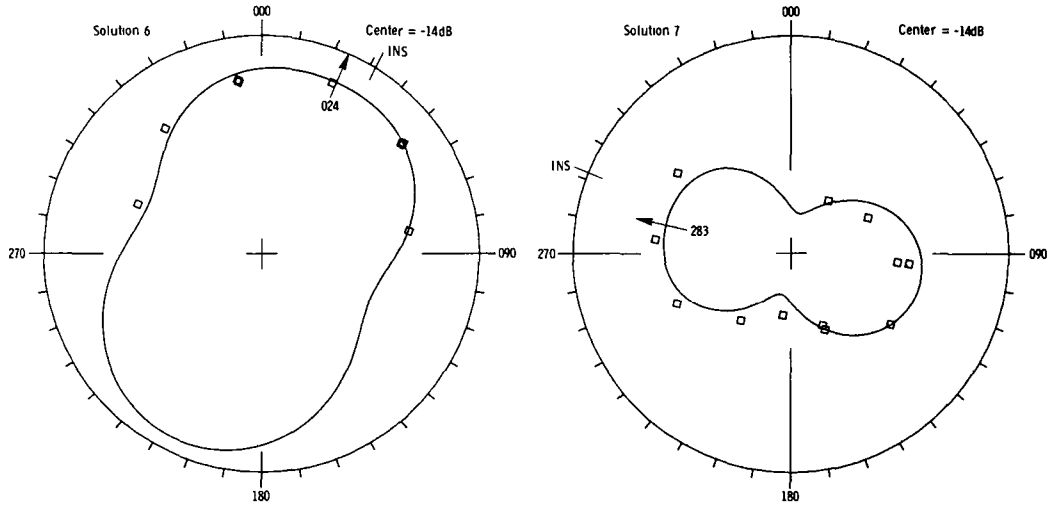

Figure 21.- Normalized radar cross section (σ^{o}) azimuth-scan data for passes 14W and 16S. See section 6.3.2 for explanation.

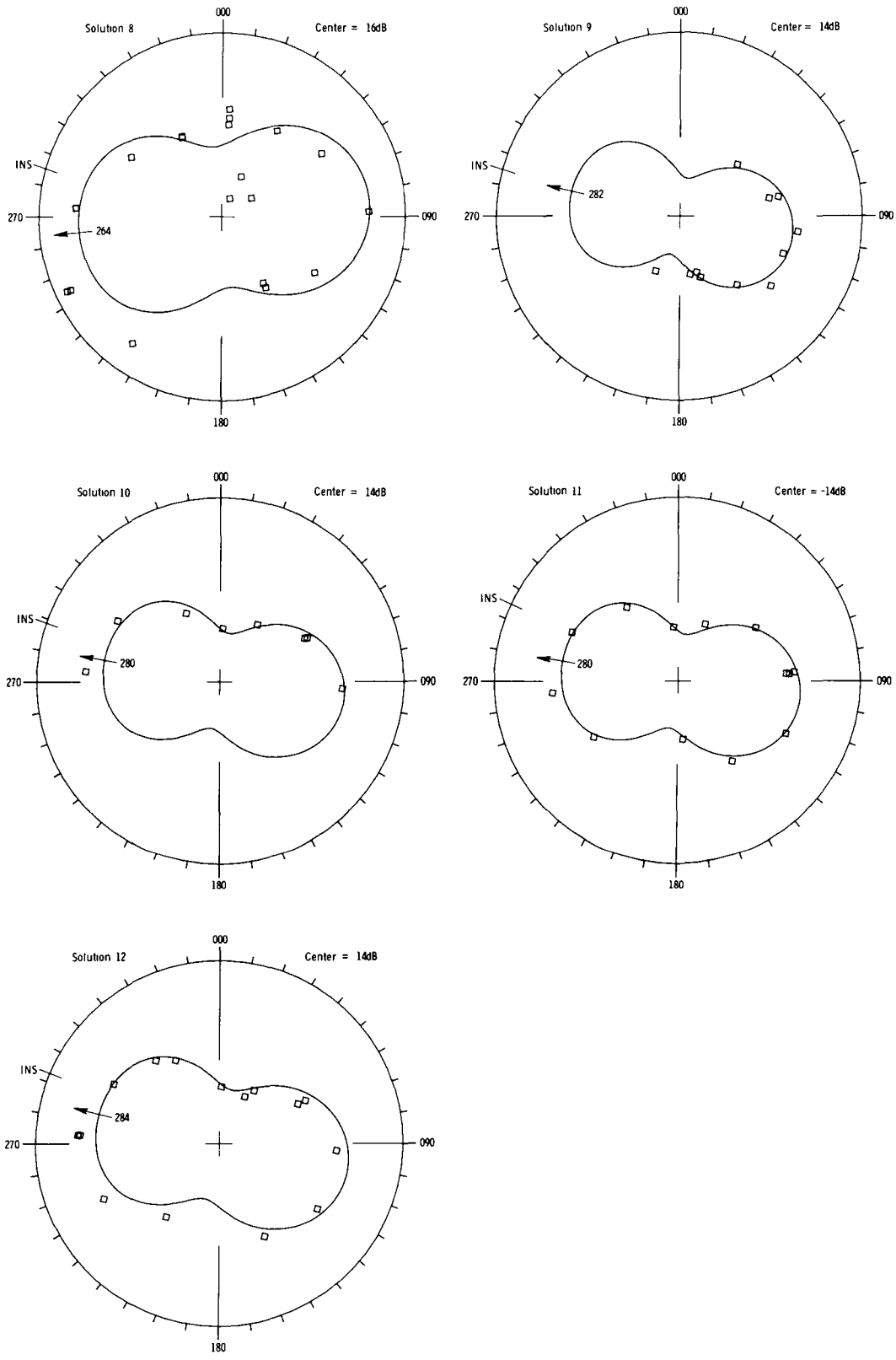

Figure 22.- Normalized radar cross section (σ^{o}) azimuth-scan data for pass 17S. See section 6.3.2 for explanation.

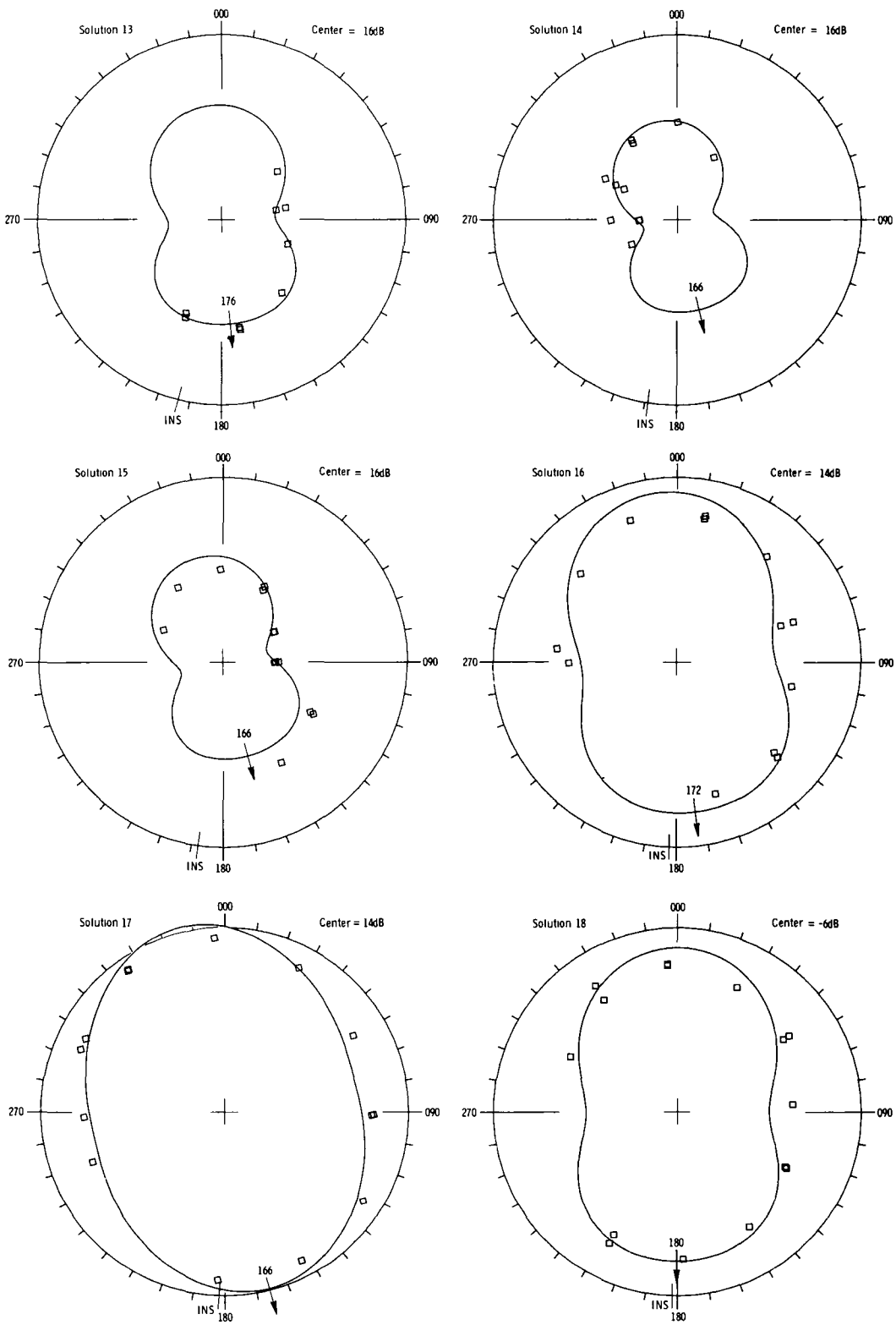

Figure 23.- Normalized radar cross section (σ^{o}) azimuth-scan data for pass 20E. See section 6.3.2 for explanation.

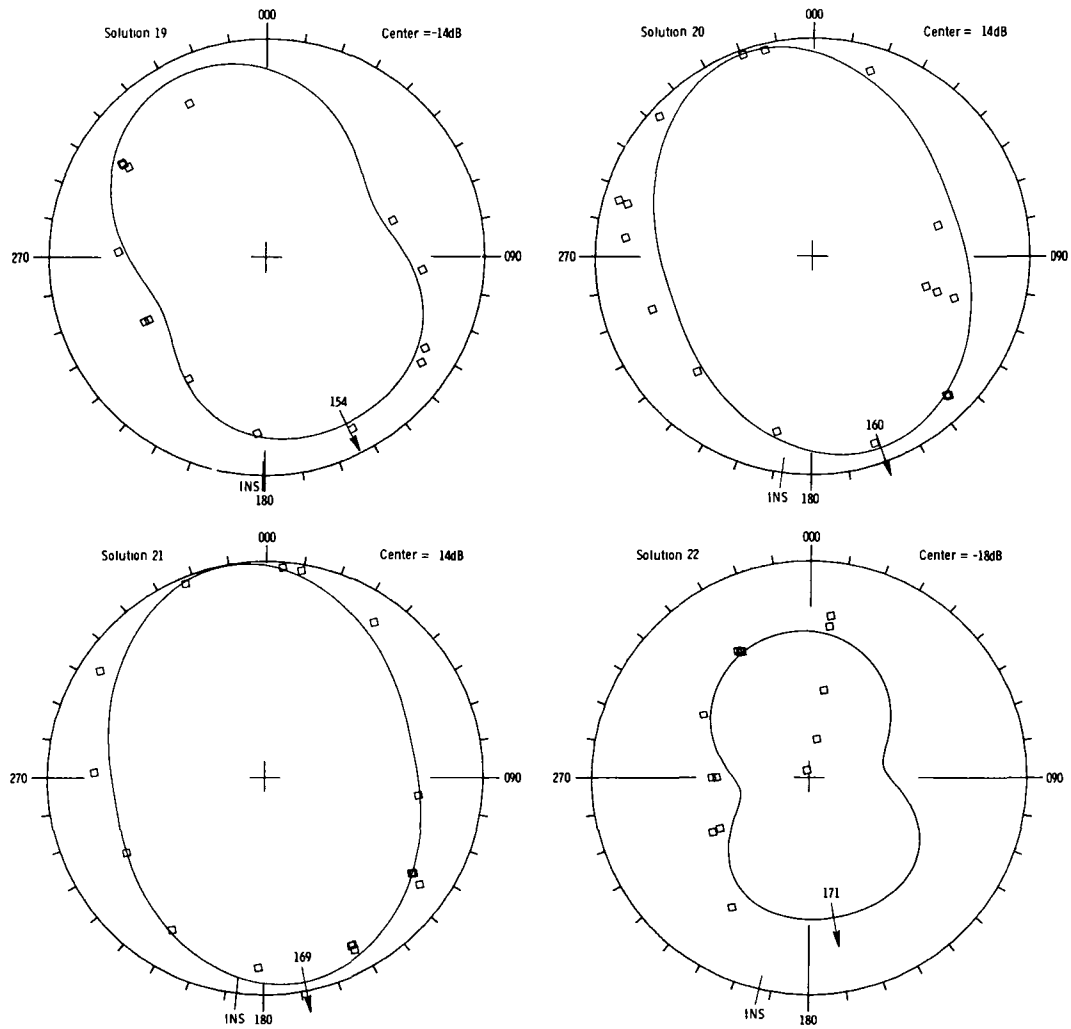

Figure 24.- Normalized radar cross section (σ^{o}) azimuth-scan data for pass 21E. See section 6.3.2 for explanation.

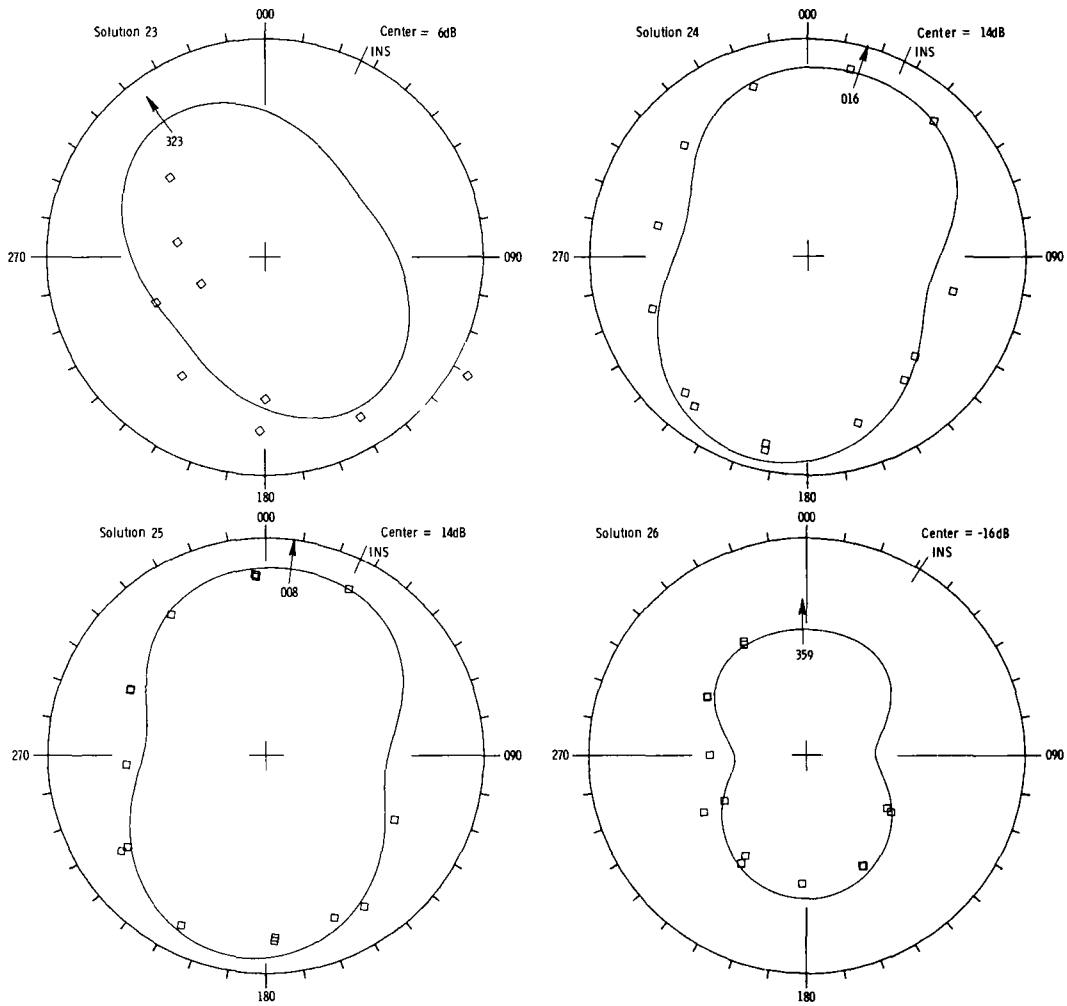

Figure 25.- Normalized radar cross section (σ^{o}) azimuth-scan data for pass 22W. See section 6.3.2 for explanation.

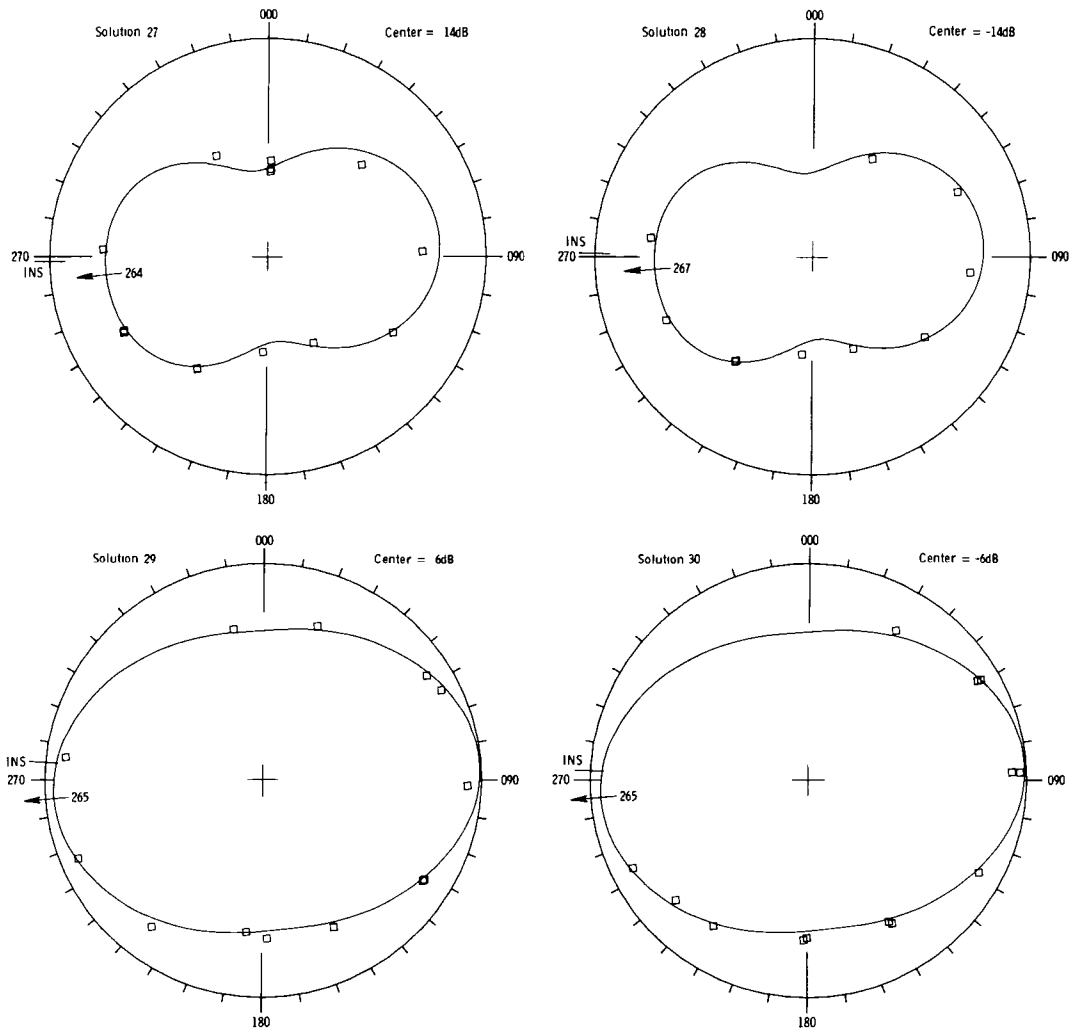

Figure 26.- Normalized radar cross section (σ^{o}) azimuth-scan data for pass 24S. See section 6.3.2 for explanation.

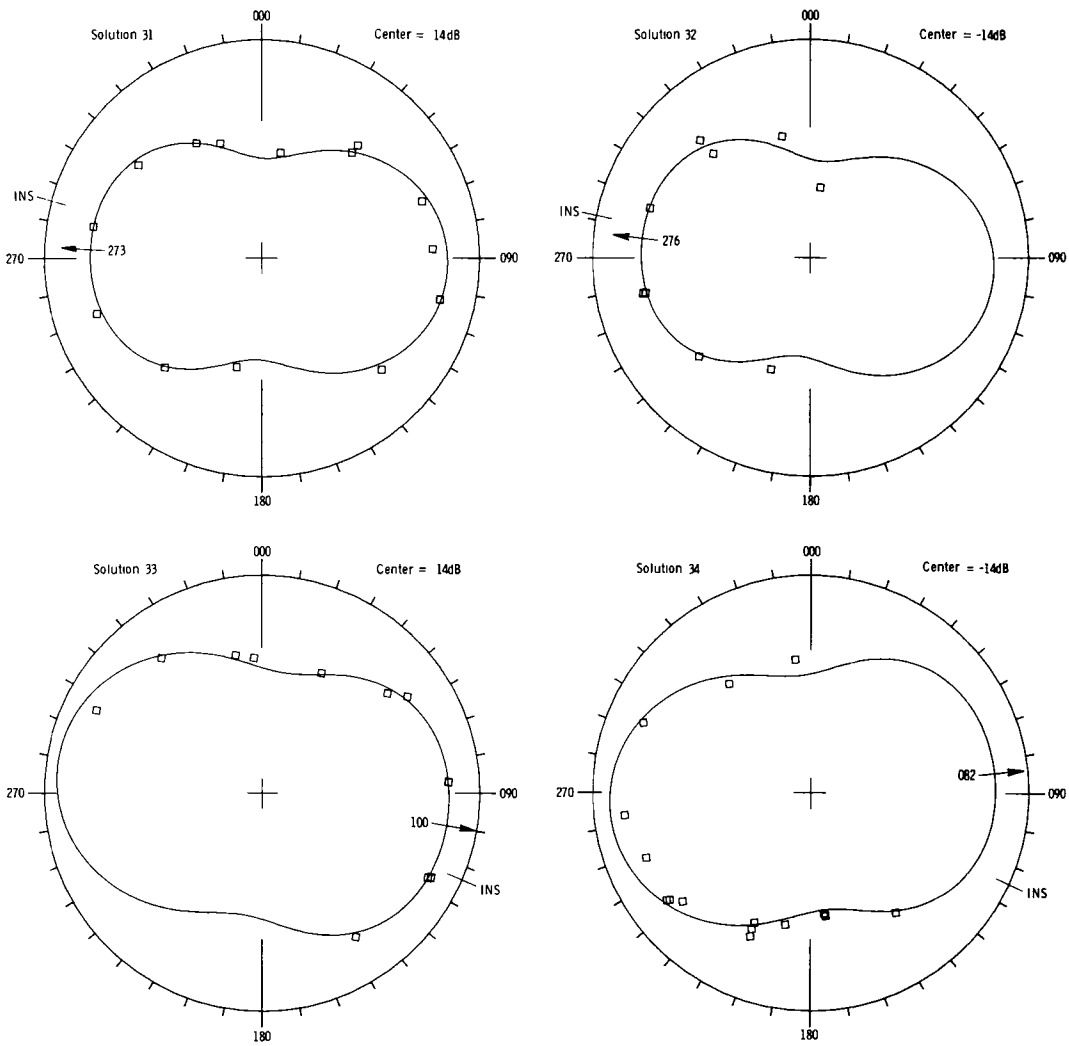

Figure 27.- Normalized radar cross section (σ^{o}) azimuth-scan data for passes 25S and 26N. See section 6.3.2 for explanation.

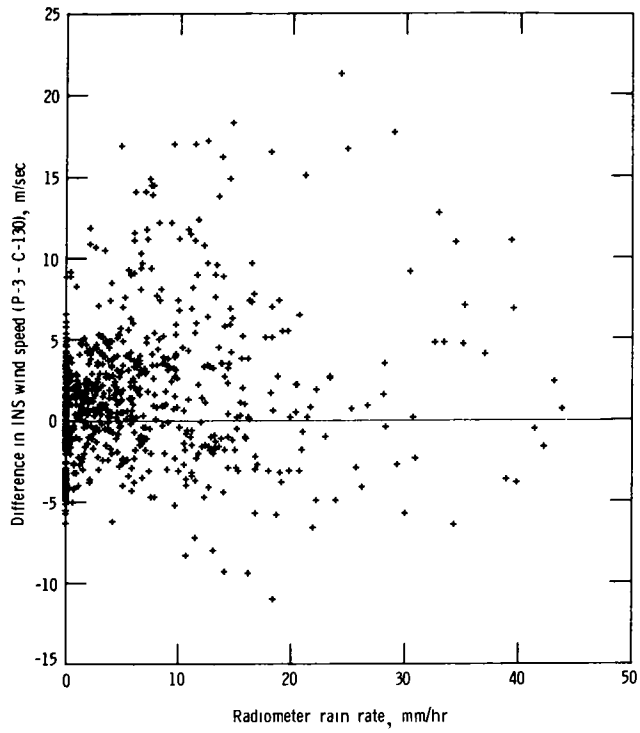

(a) Radiometer rain rate vs. difference between INS wind speeds from C-130 and P-3.

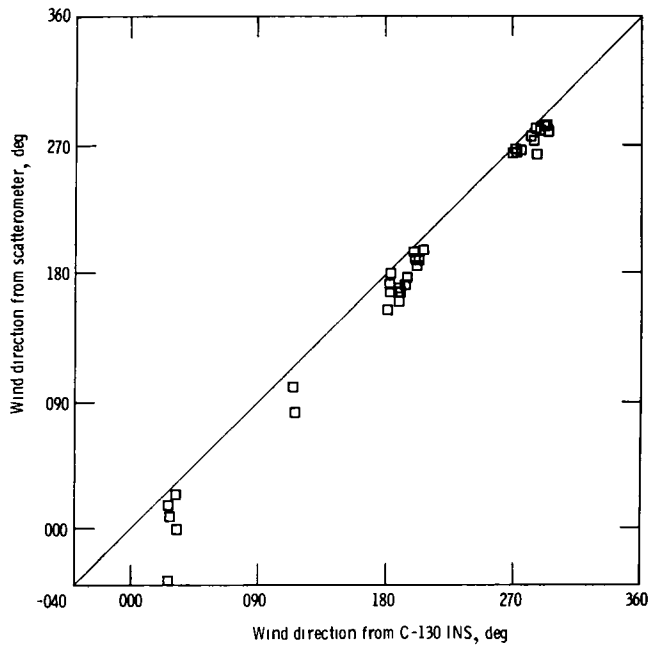

(b) Scatterometer wind direction vs. C-130 INS wind direction.

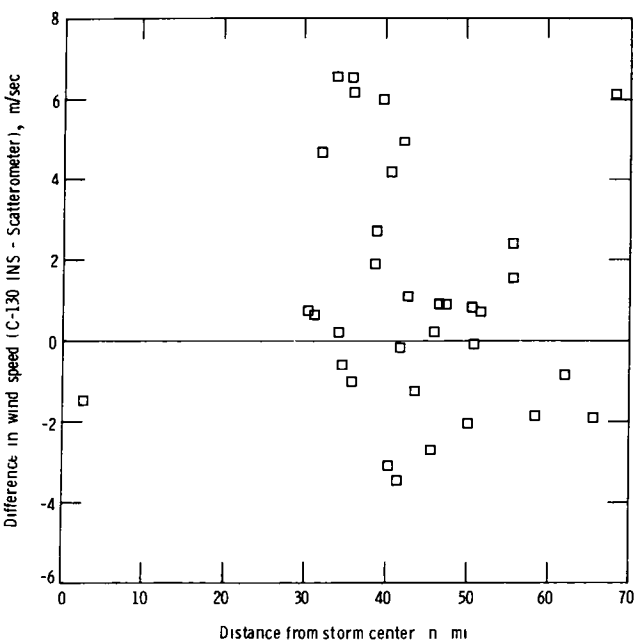

(c) Distance from storm center vs. difference between C-130 INS wind speed and scatterometer wind speed.

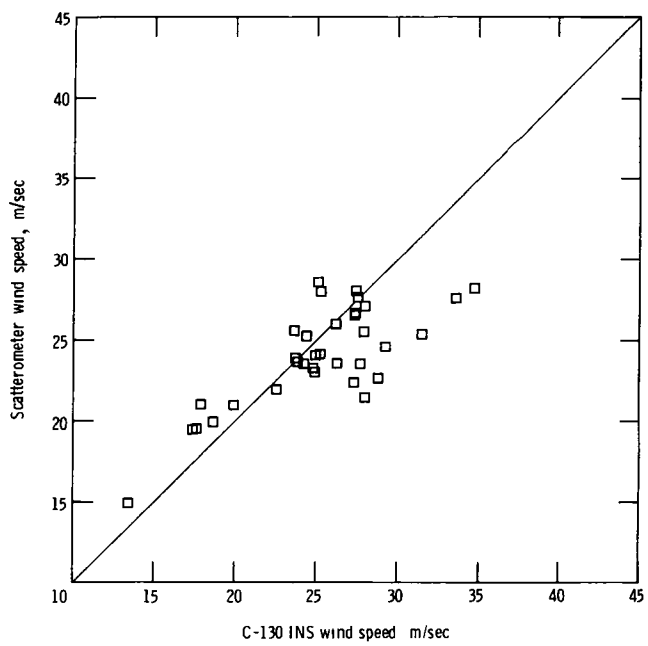

(d) Scatterometer wind speed vs. C-130 INS wind speed.

Figure 28.- Interpretation of the 34 scatterometer solutions and INS wind speed.

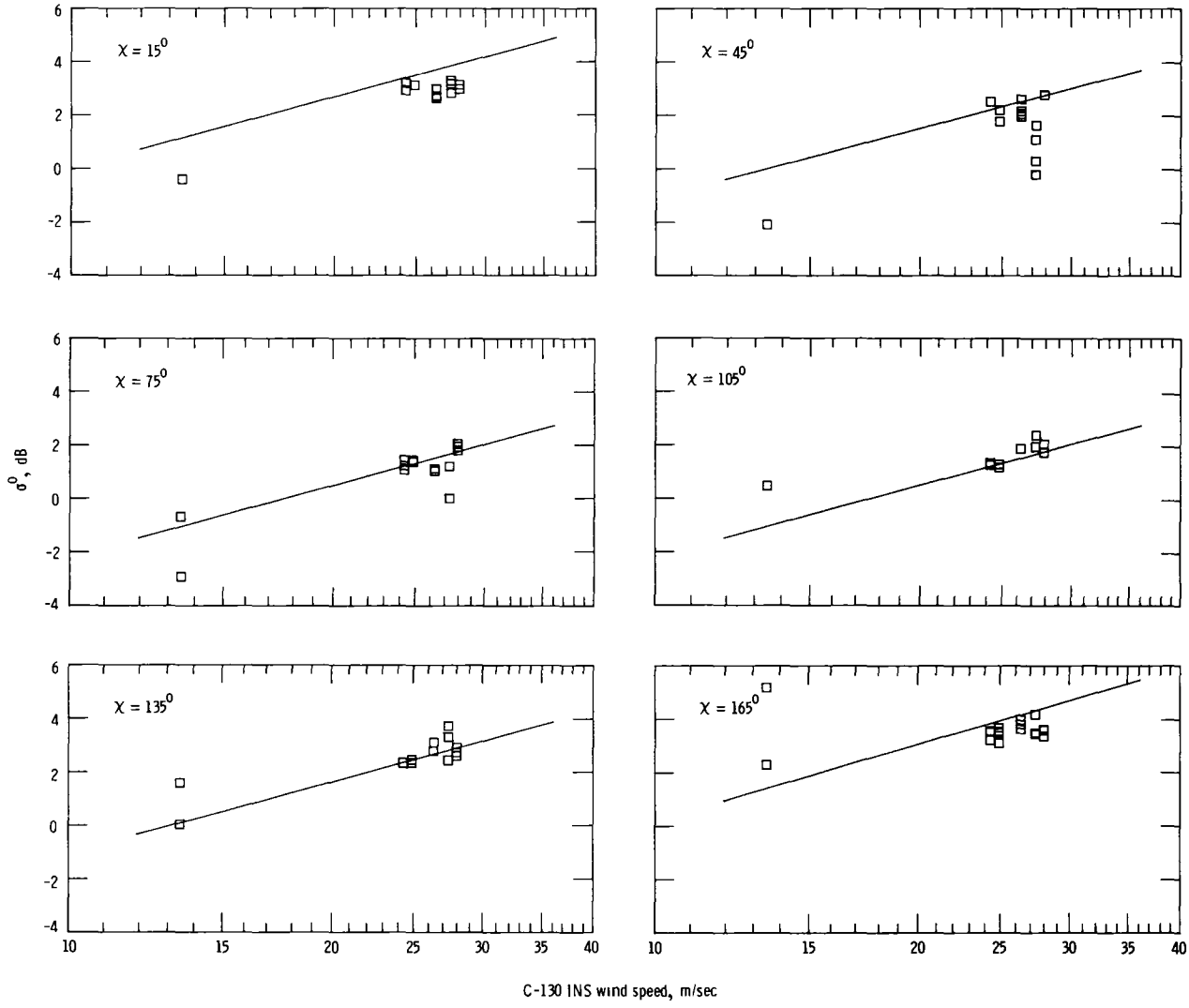

Figure 29.- Normalized radar cross section vs. C-130 INS wind speed for specified values of wind aspect angle (χ). Solid curve is σ^{o} from SASS-1 geophysical algorithm. θ = 19°.

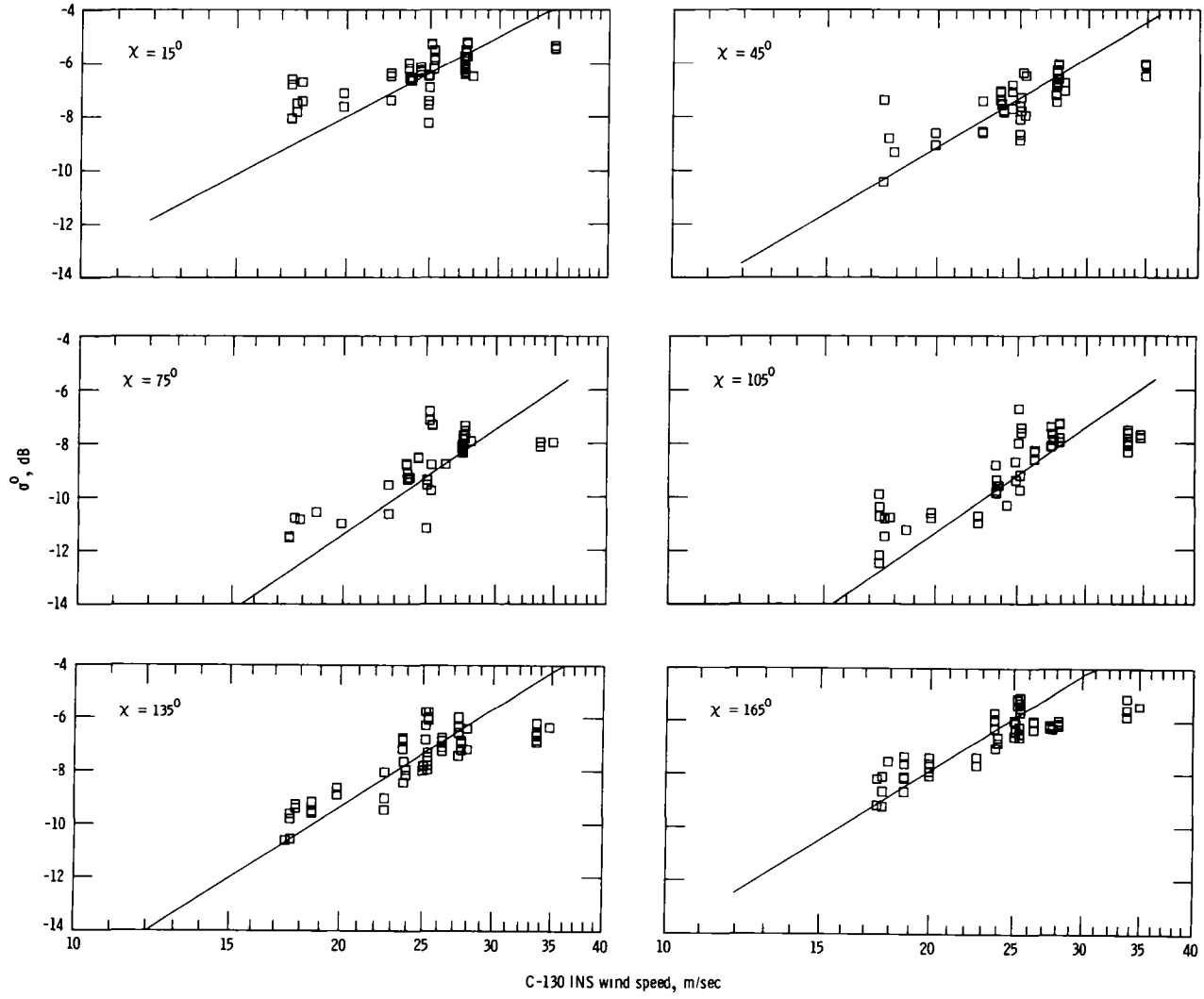

Figure 30.- Normalized radar cross section vs. C-130 INS wind speed for specified values of wind aspect angle (χ). Solid curve is σ° from SASS-1 geophysical algorithm. $\theta = 39°$.

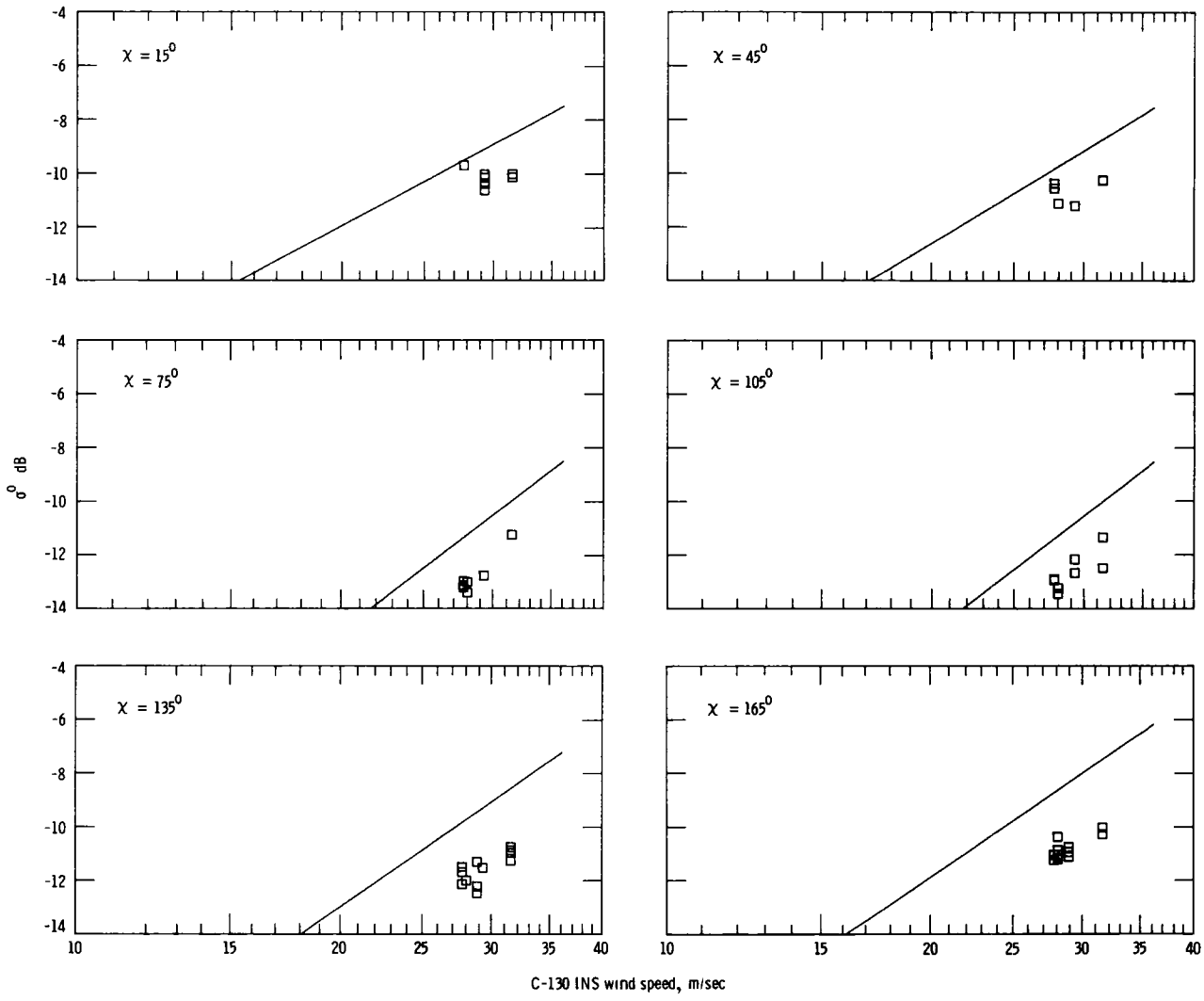

Figure 31.- Normalized radar cross section vs. C-130 INS wind speed for specified values of wind aspect angle (χ). Solid curve is σ^{o} from SASS-1 geophysical algorithm. $\theta = 52°$.

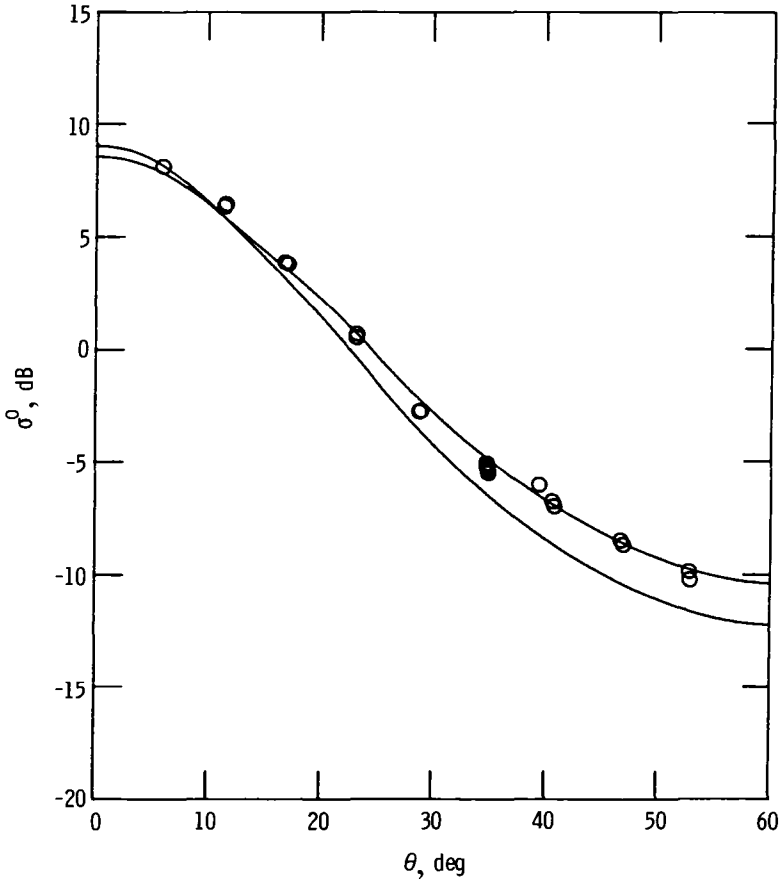

Figure 32.- Example elevation scan: σ° vs. θ. Solid lines are from SASS-1 geophysical algorithm for the appropriate wind aspect angle and INS wind speed ± 2 m/s.

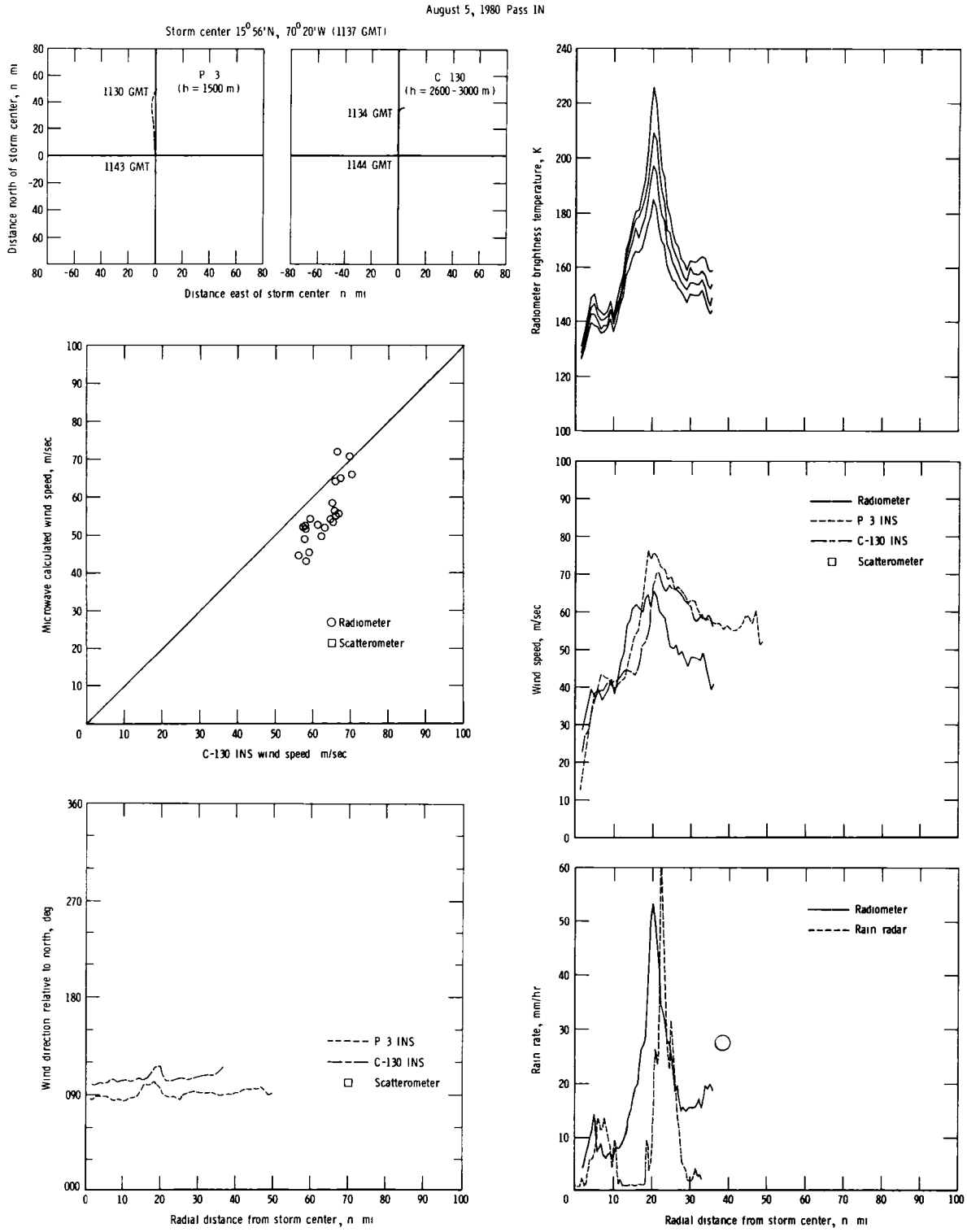

Figure 33.- Flight tracks and results of microwave and aircraft sensor measurements for pass 1N.

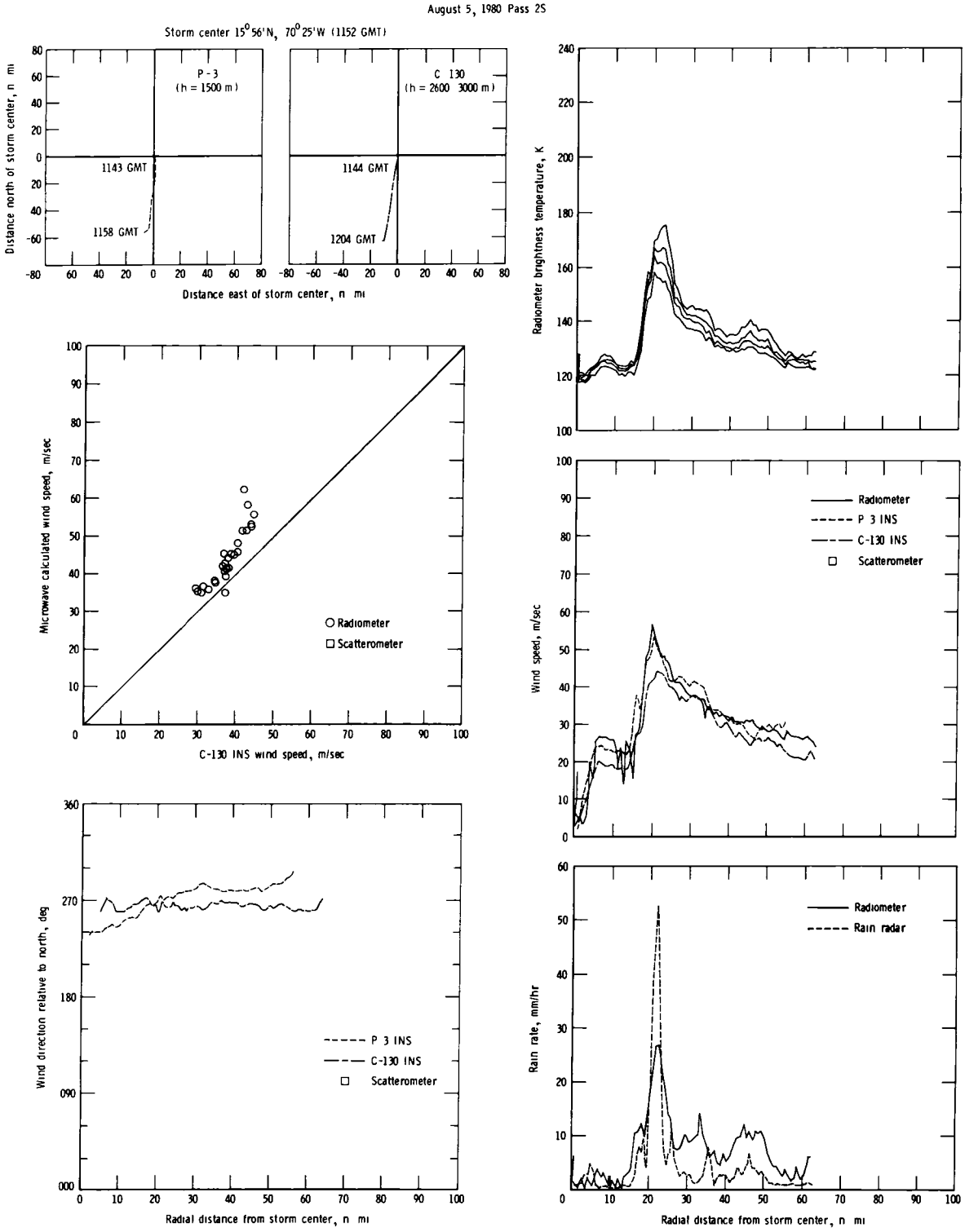

Figure 34.- Flight tracks and results of microwave and aircraft sensor measurements for pass 2S.

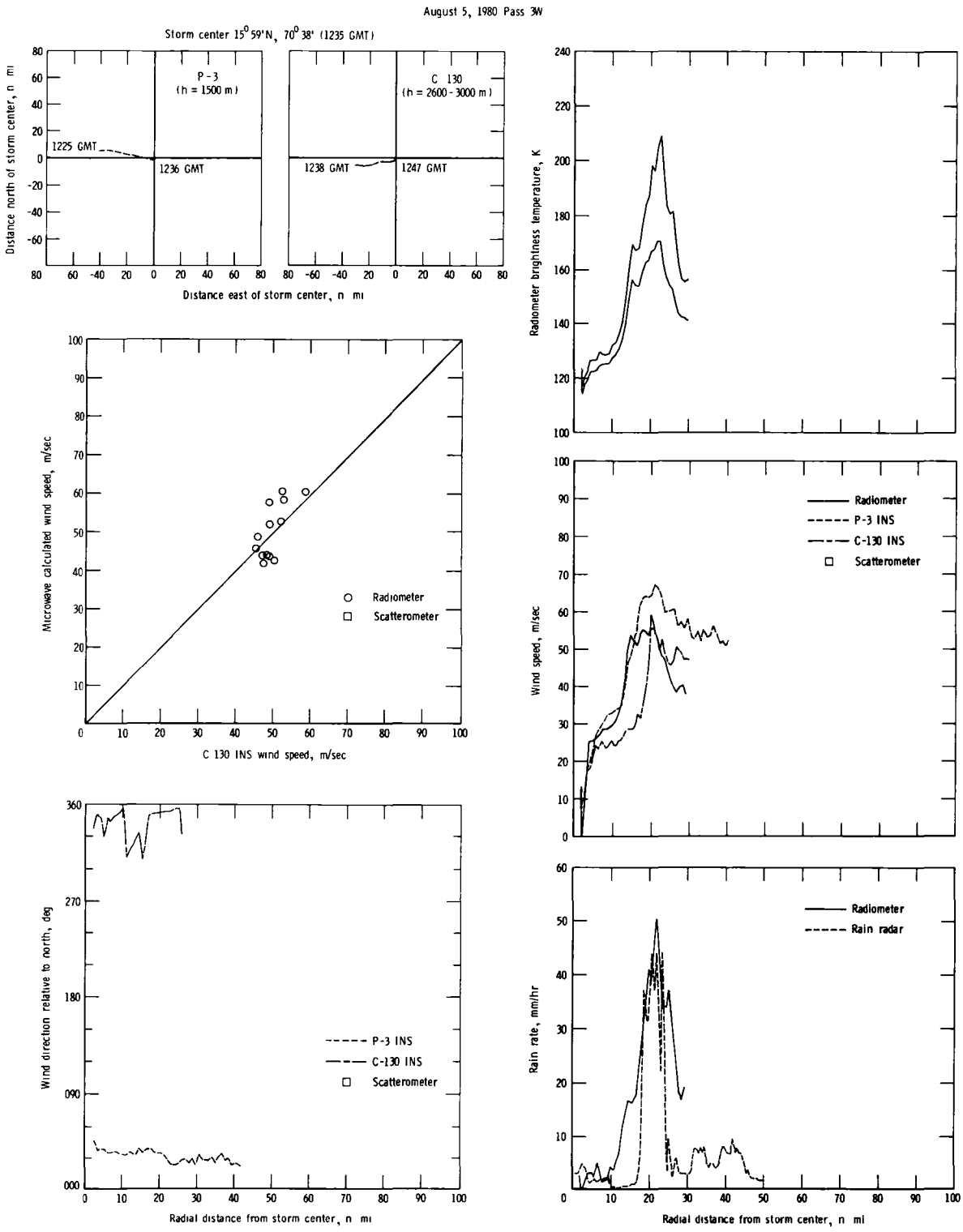

Figure 35.- Flight tracks and results of microwave and aircraft sensor measurements for pass 3W.

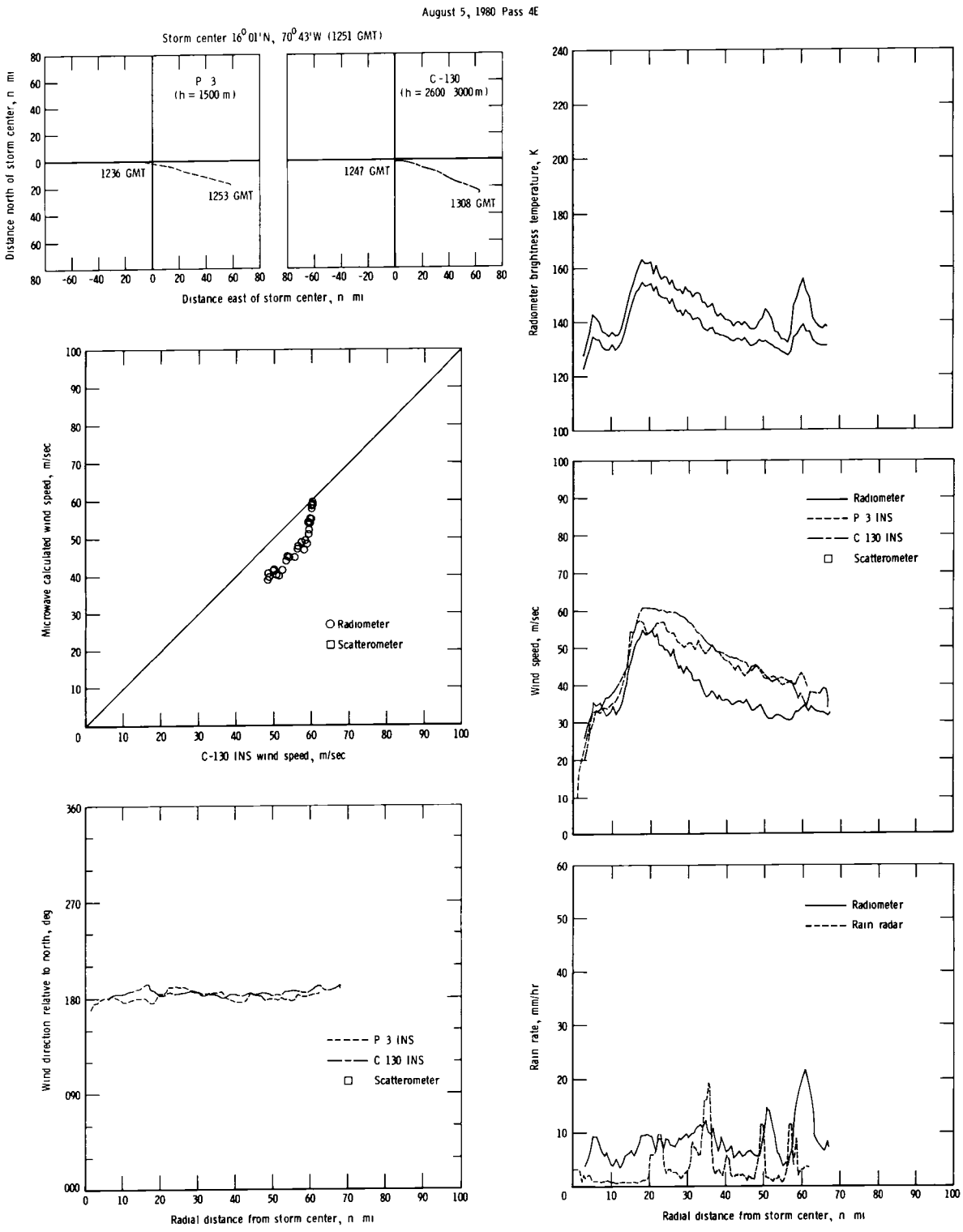

Figure 36.- Flight tracks and results of microwave and aircraft sensor measurements for pass 4E.

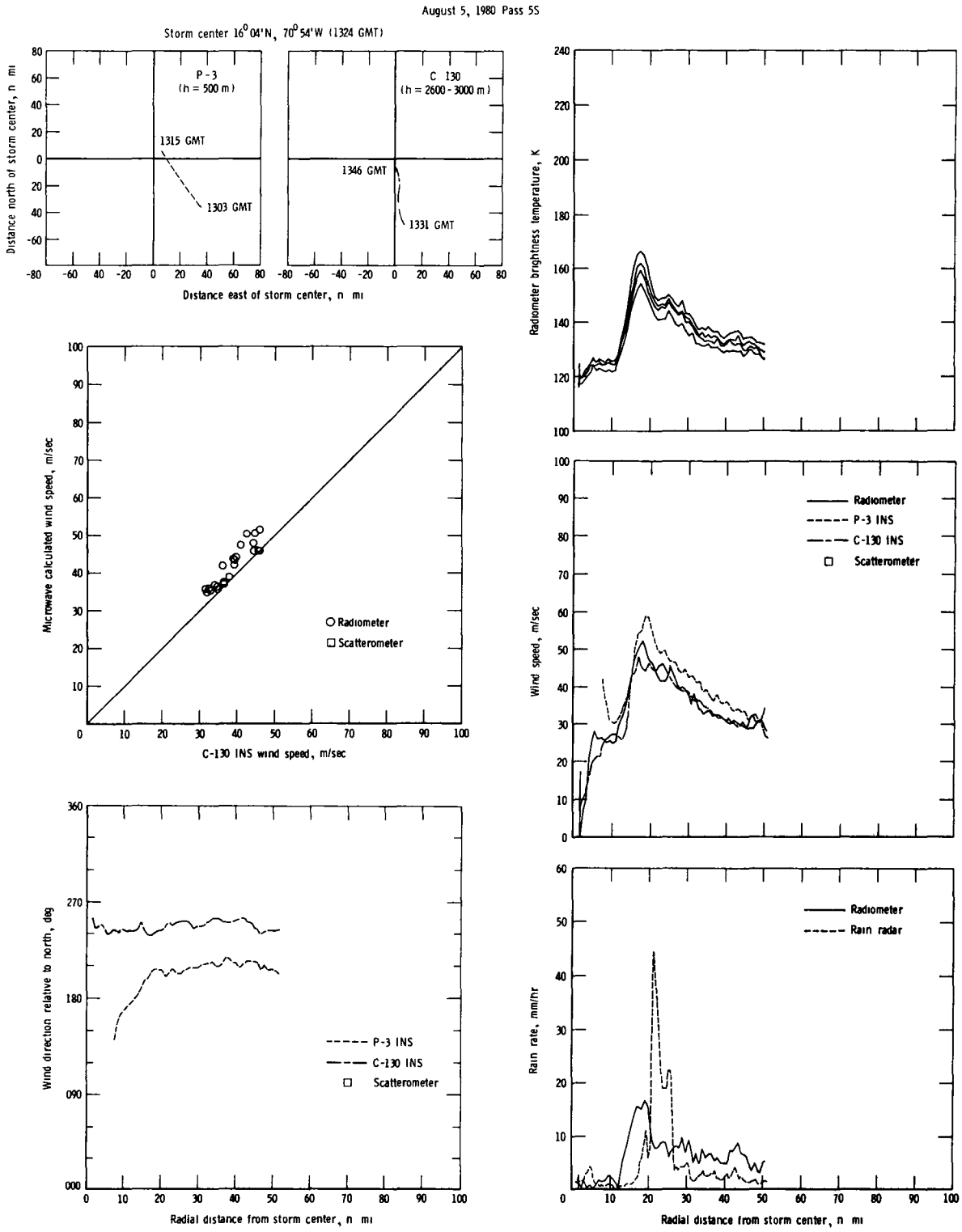

Figure 37.- Flight tracks and results of microwave and aircraft sensor measurements for pass 5S.

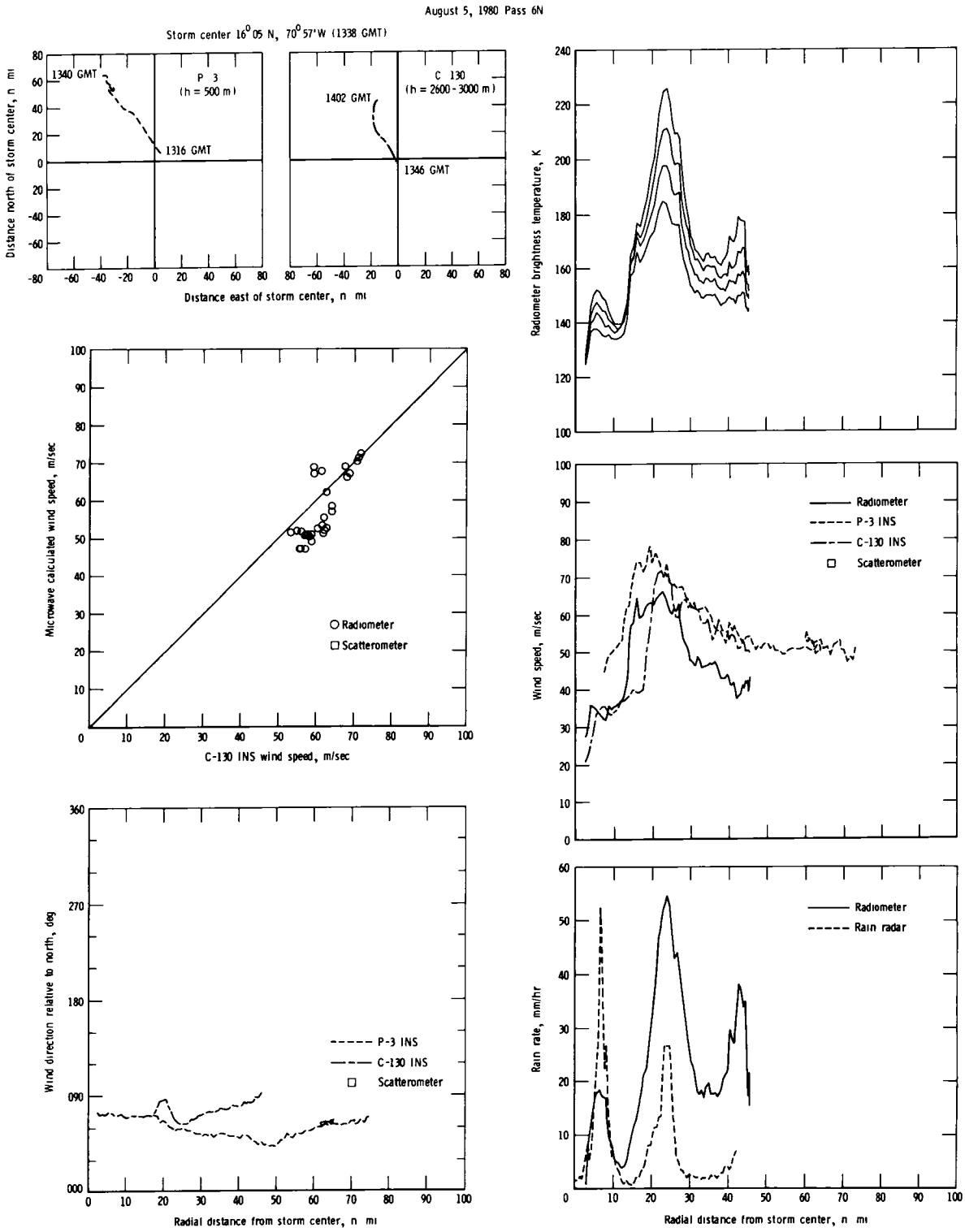

Figure 38.- Flight tracks and results of microwave and aircraft sensor measurements for pass 6N.

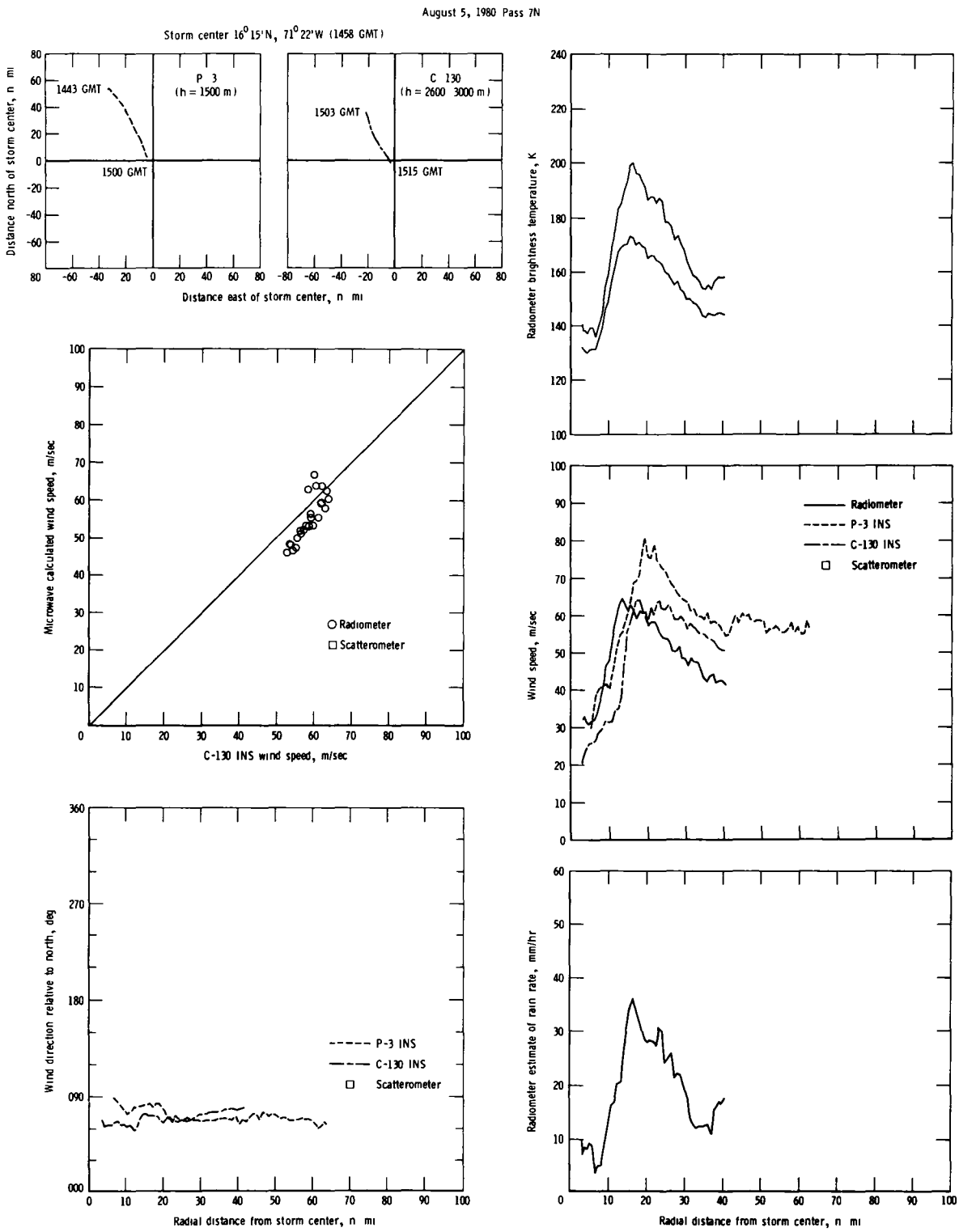

Figure 39.- Flight tracks and results of microwave and aircraft sensor measurements for pass 7N.

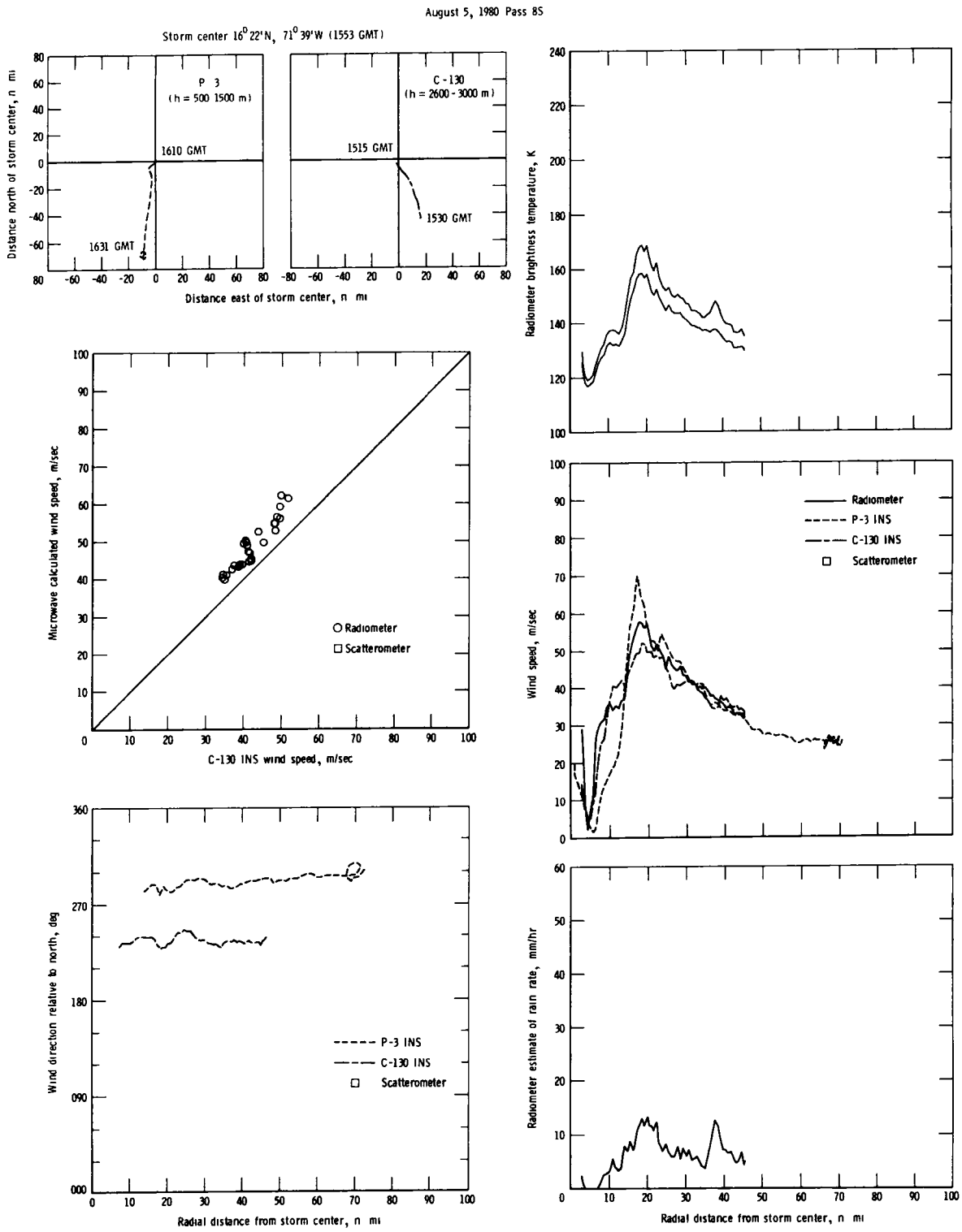

Figure 40.- Flight tracks and results of microwave and aircraft sensor measurements for pass 8S.

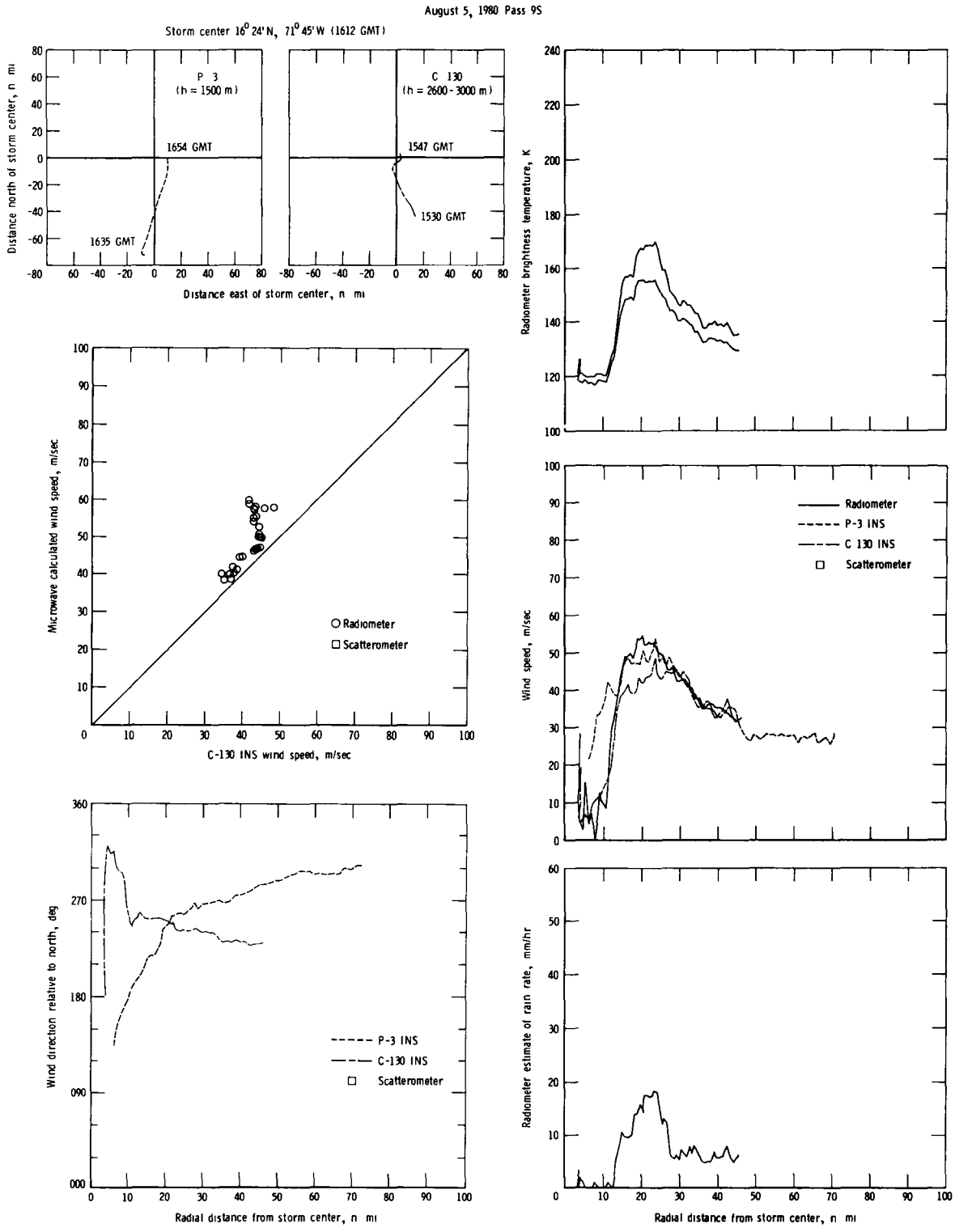

Figure 41.- Flight tracks and results of microwave and aircraft sensor measurements for pass 9S.

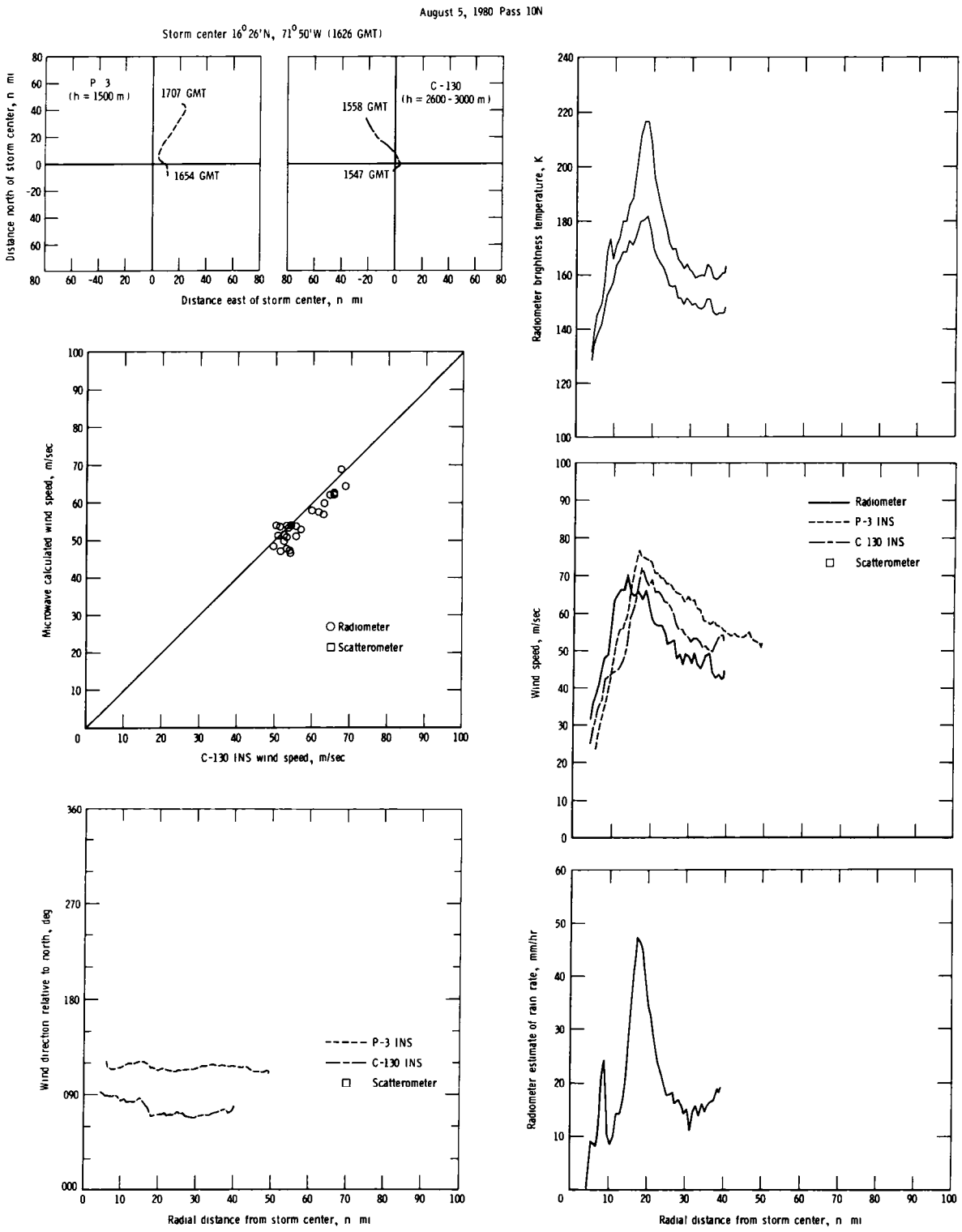

Figure 42.- Flight tracks and results of microwave and aircraft sensor measurements for pass 10N.

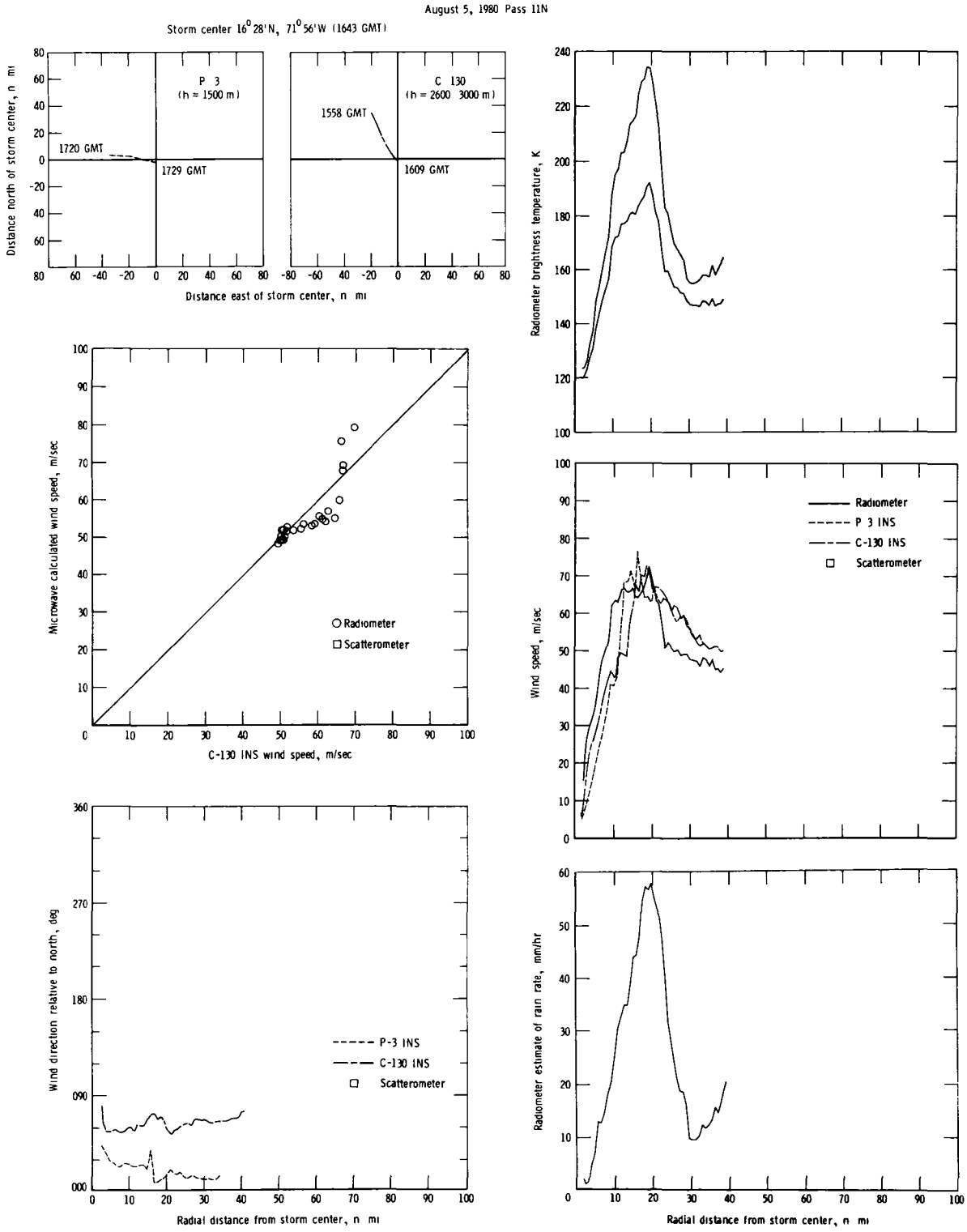

Figure 43.- Flight tracks and results of microwave and aircraft sensor measurements for pass 11N.

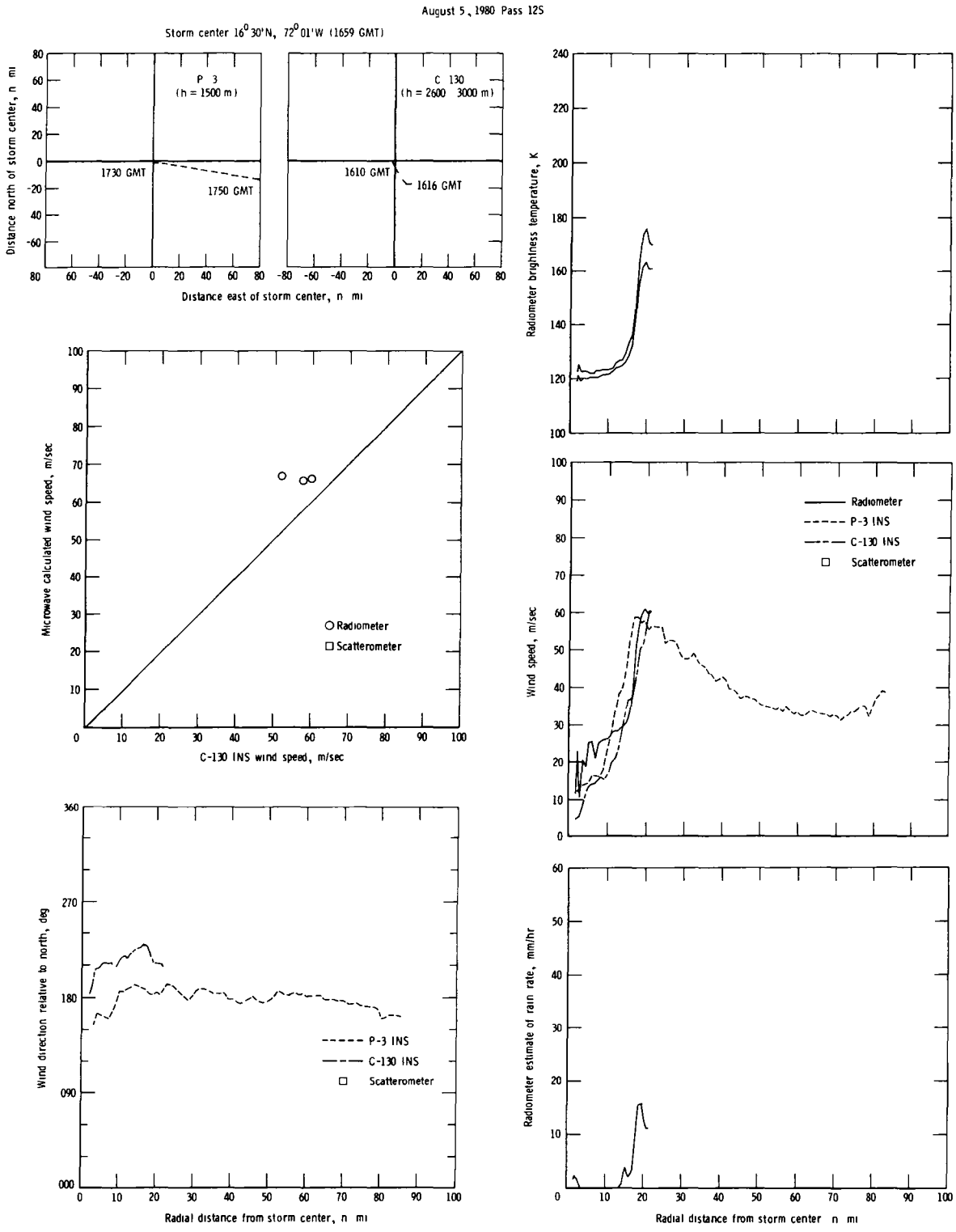

Figure 44.- Flight tracks and results of microwave and aircraft sensor measurements for pass 12S.

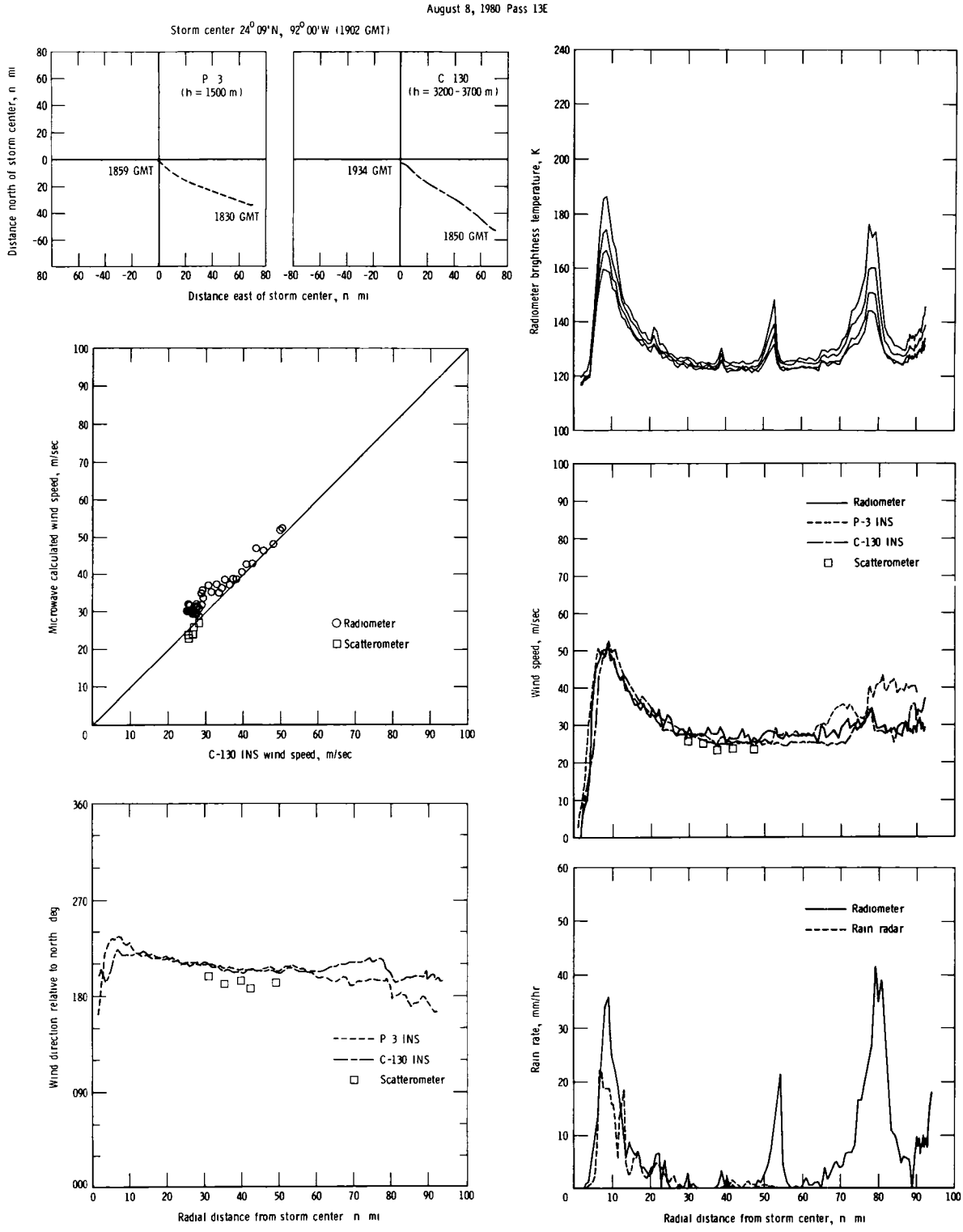

Figure 45.- Flight tracks and results of microwave and aircraft sensor measurements for pass 13E.

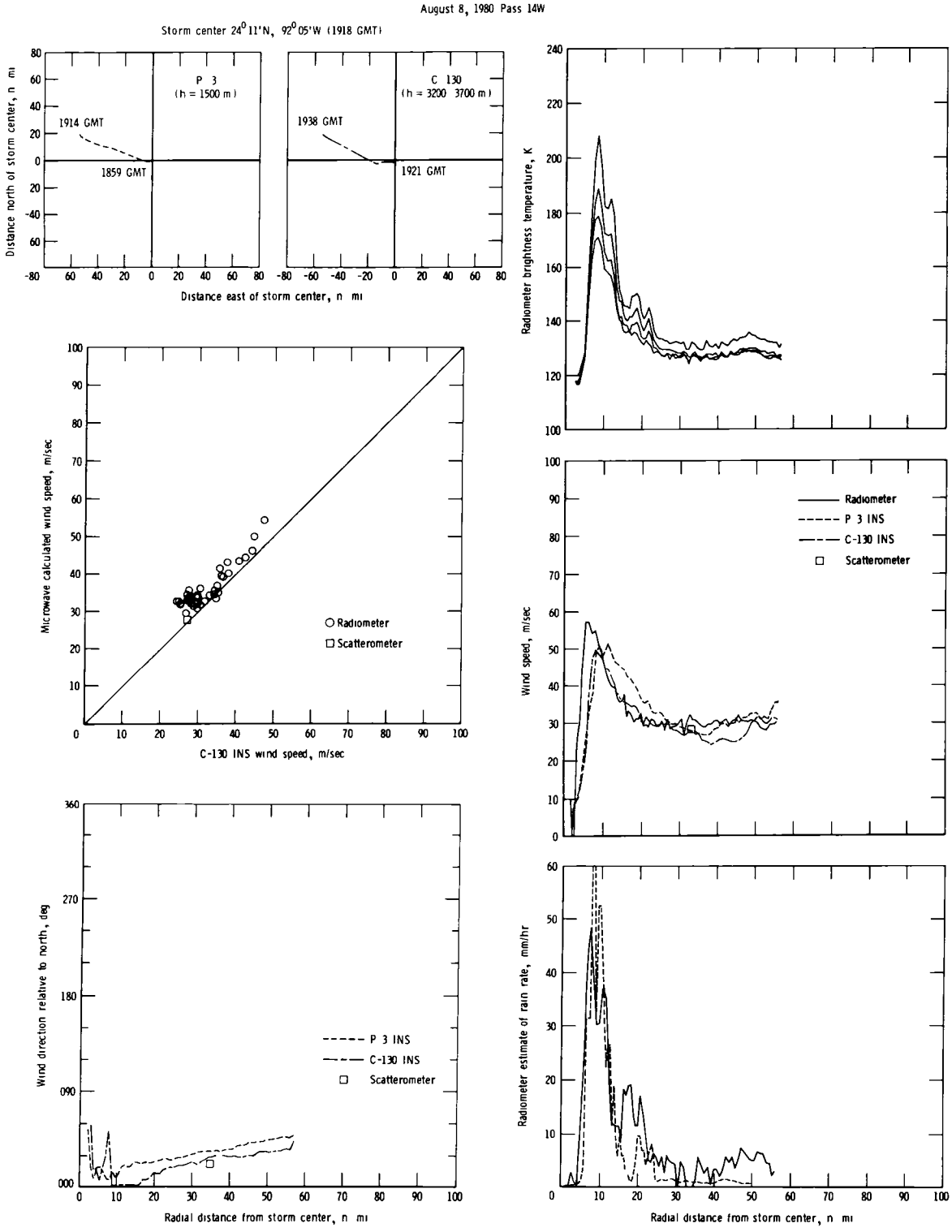

Figure 46.- Flight tracks and results of microwave and aircraft sensor measurements for pass 14W.

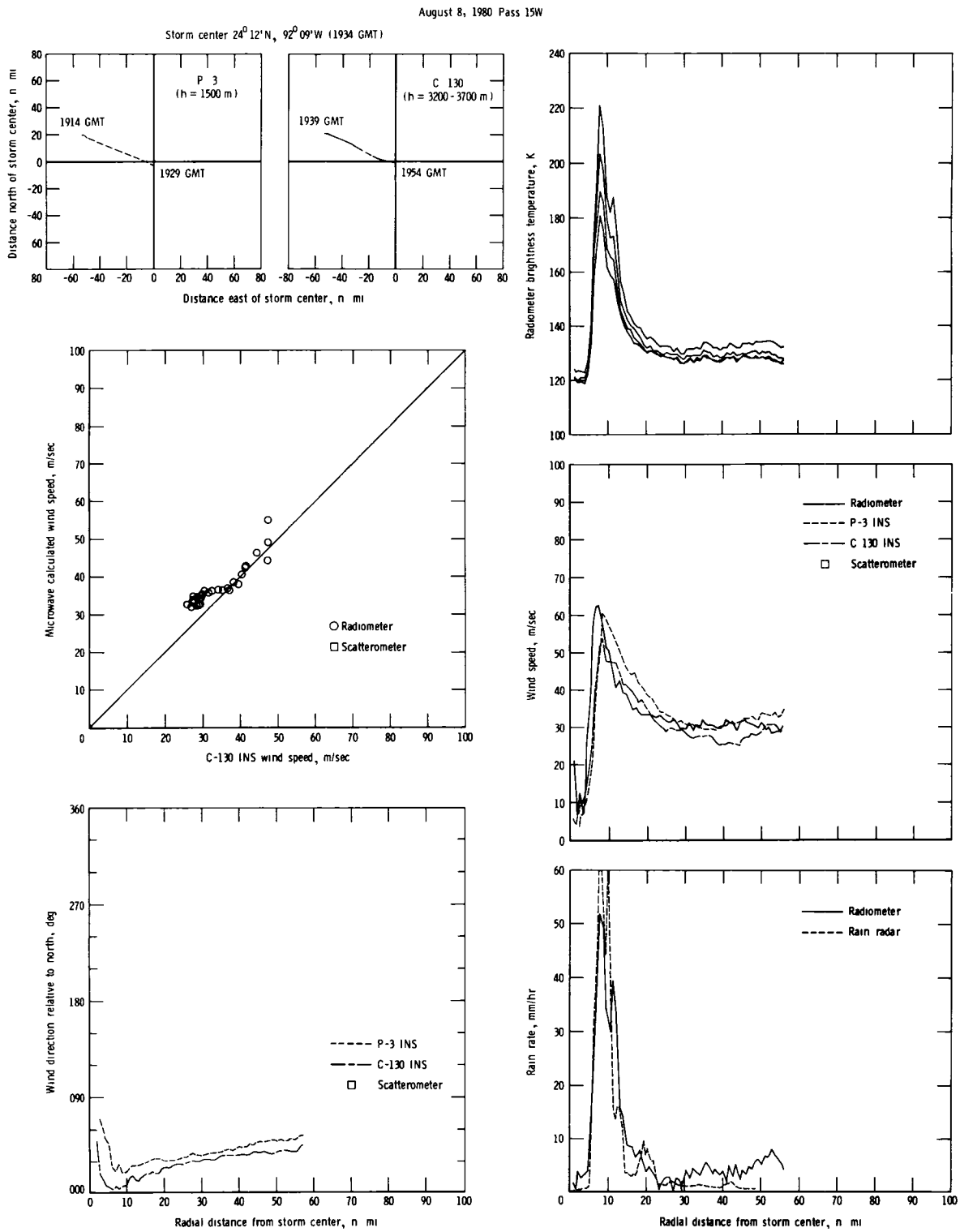

Figure 47.- Flight tracks and results of microwave and aircraft sensor measurements for pass 15W.

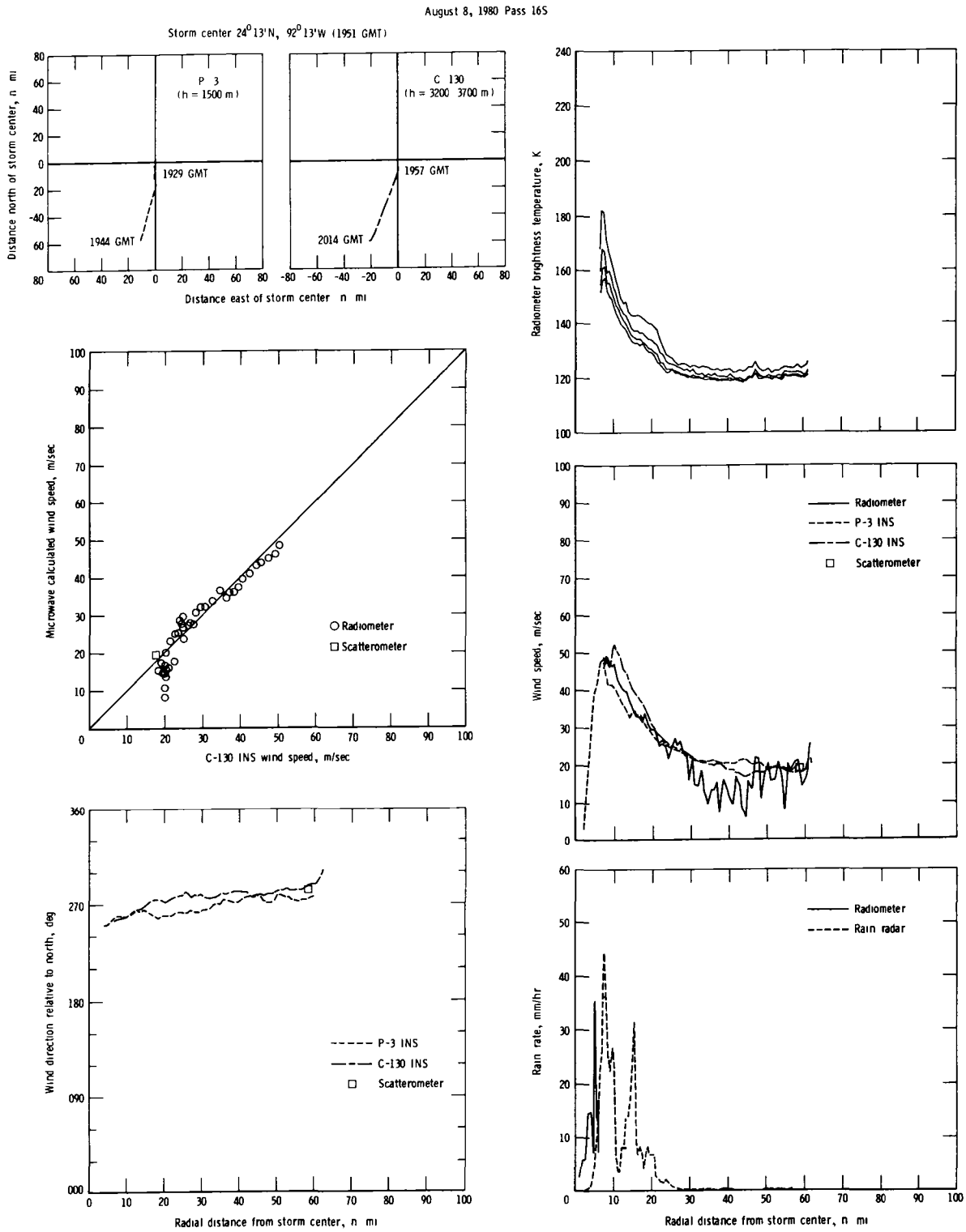

Figure 48.- Flight tracks and results of microwave and aircraft sensor measurements for pass 16S.

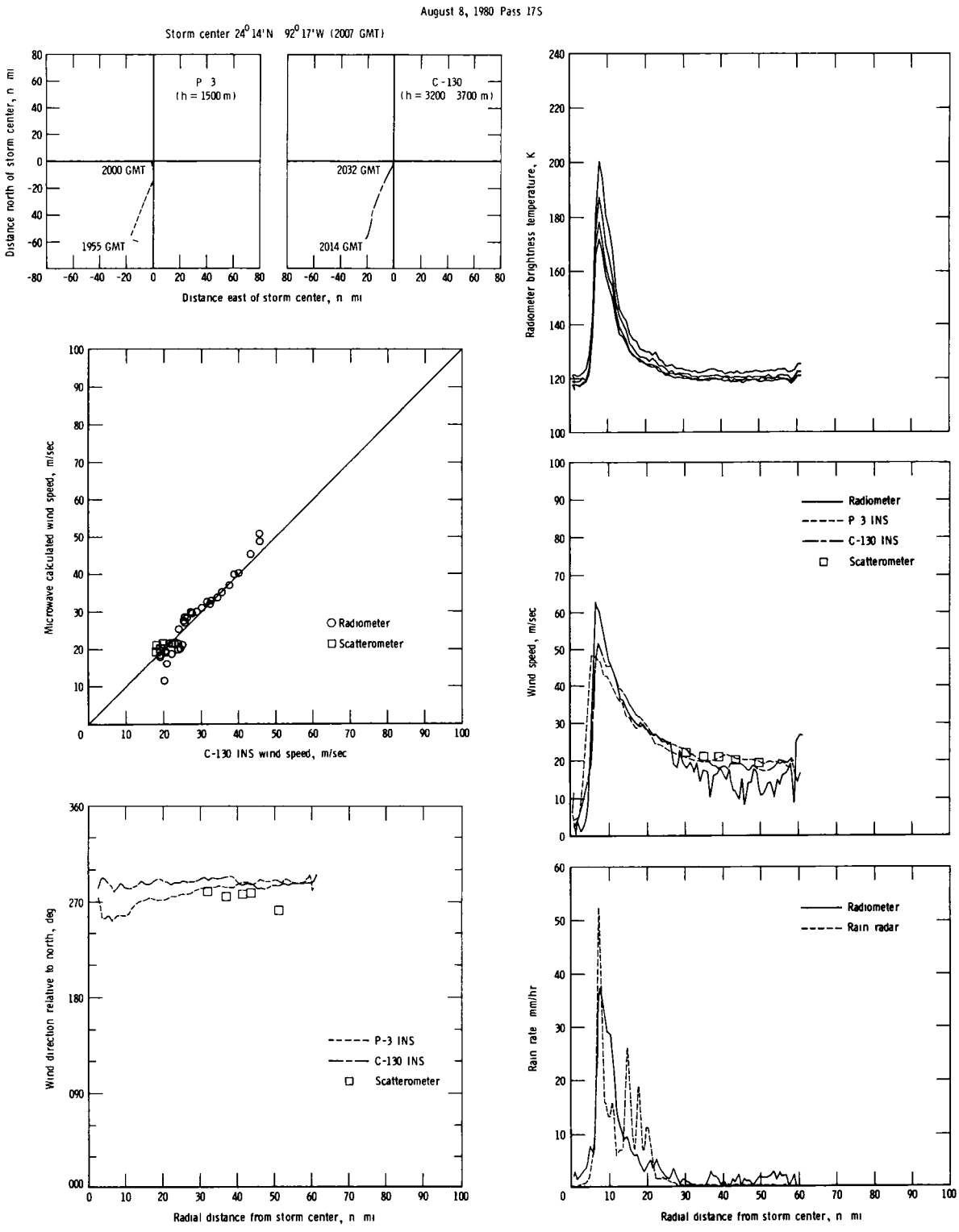

Figure 49.- Flight tracks and results of microwave and aircraft sensor measurements for pass 17S.

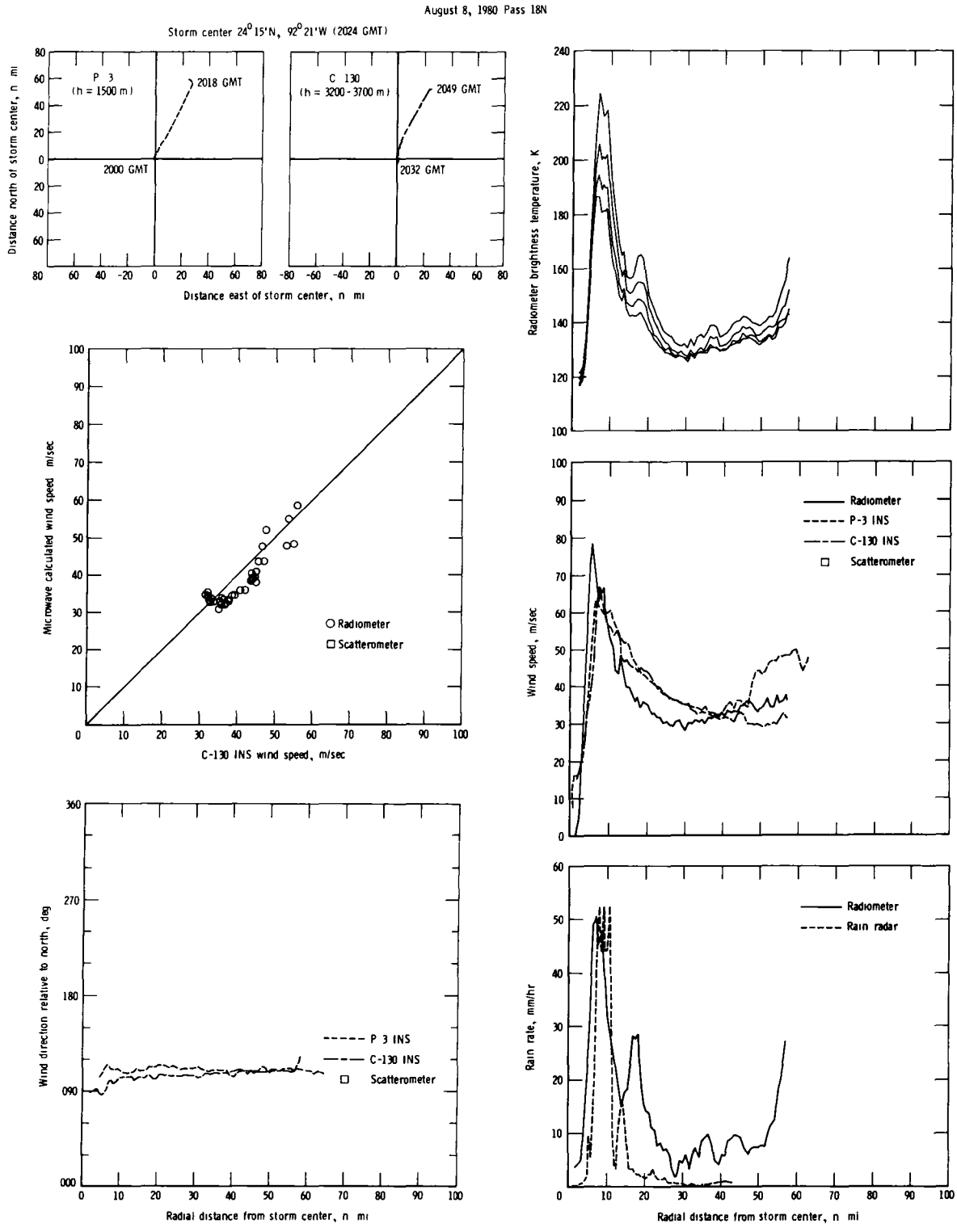

Figure 50.- Flight tracks and results of microwave and aircraft sensor measurements for pass 18N.

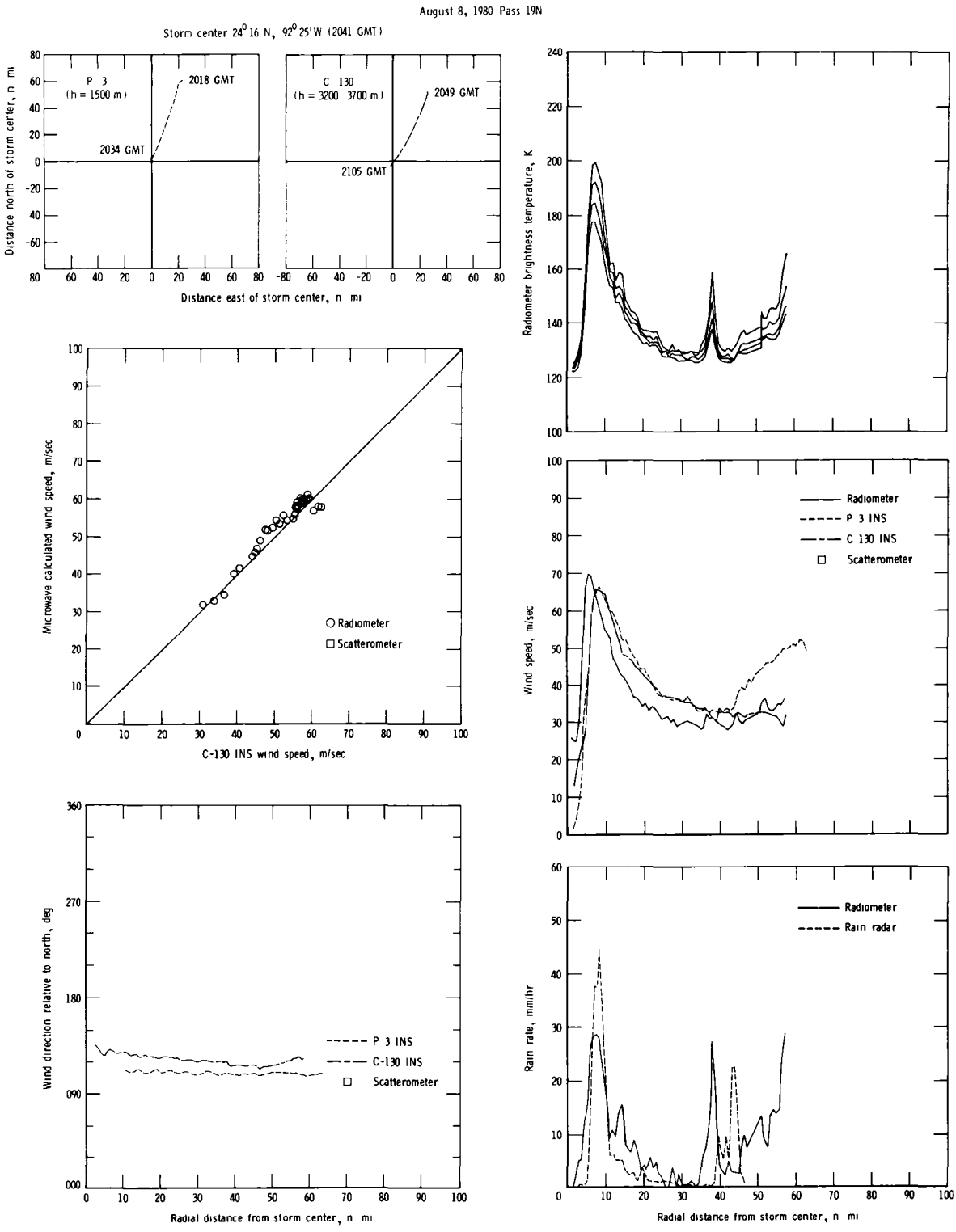

Figure 51.- Flight tracks and results of microwave and aircraft sensor measurements for pass 19N.

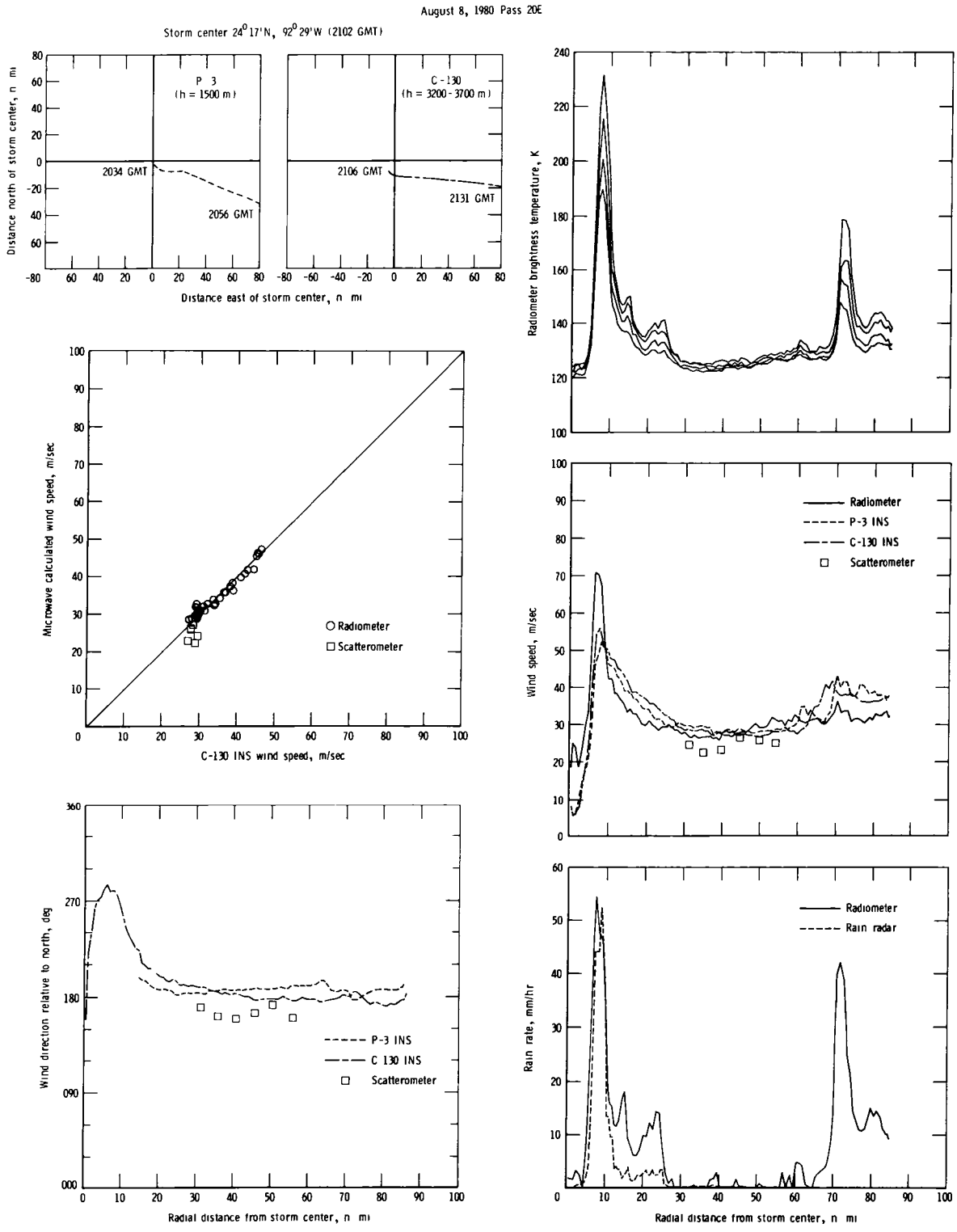

Figure 52.- Flight tracks and results of microwave and aircraft sensor measurements for pass 20E.

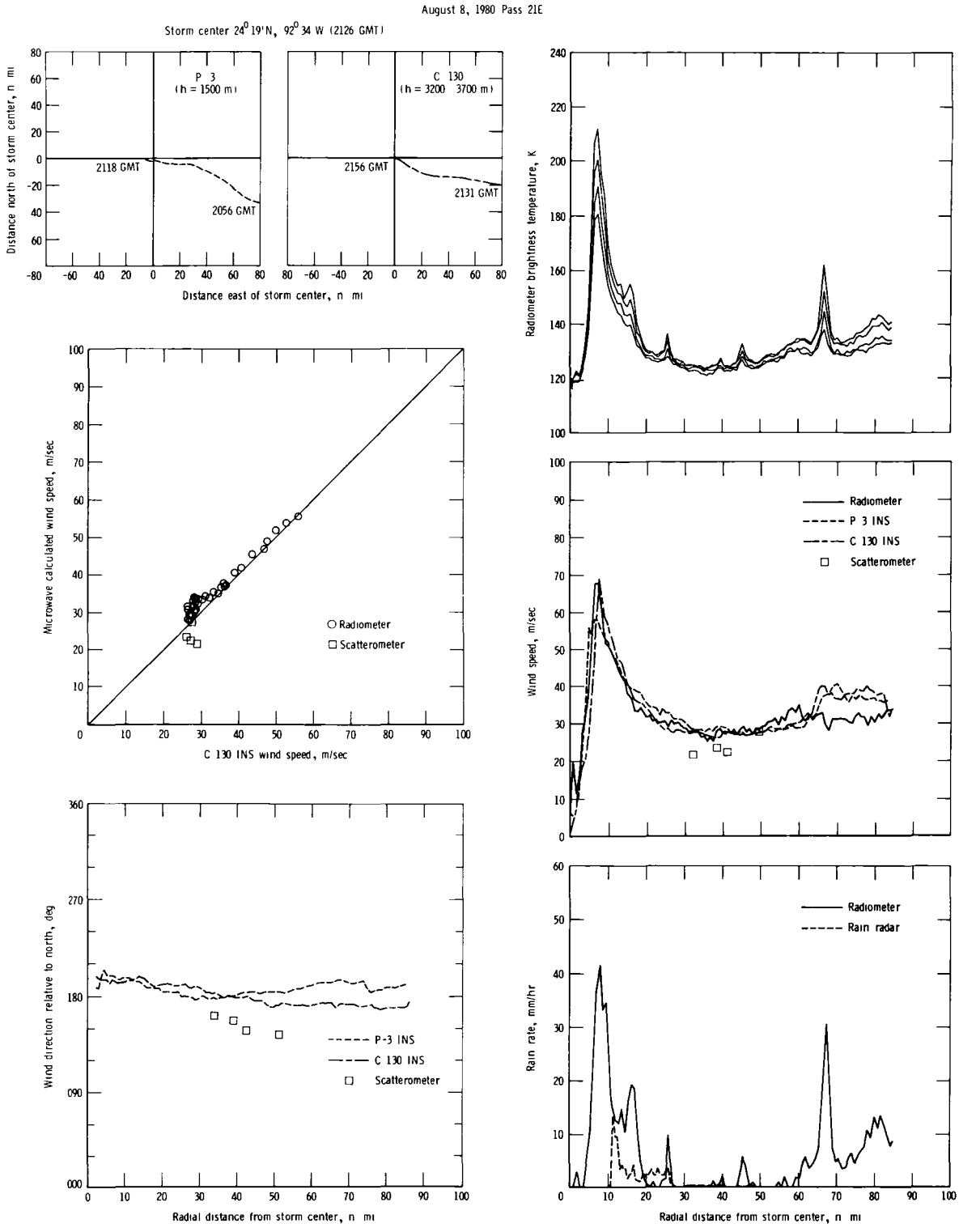

Figure 53.- Flight tracks and results of microwave and aircraft sensor measurements for pass 21E.

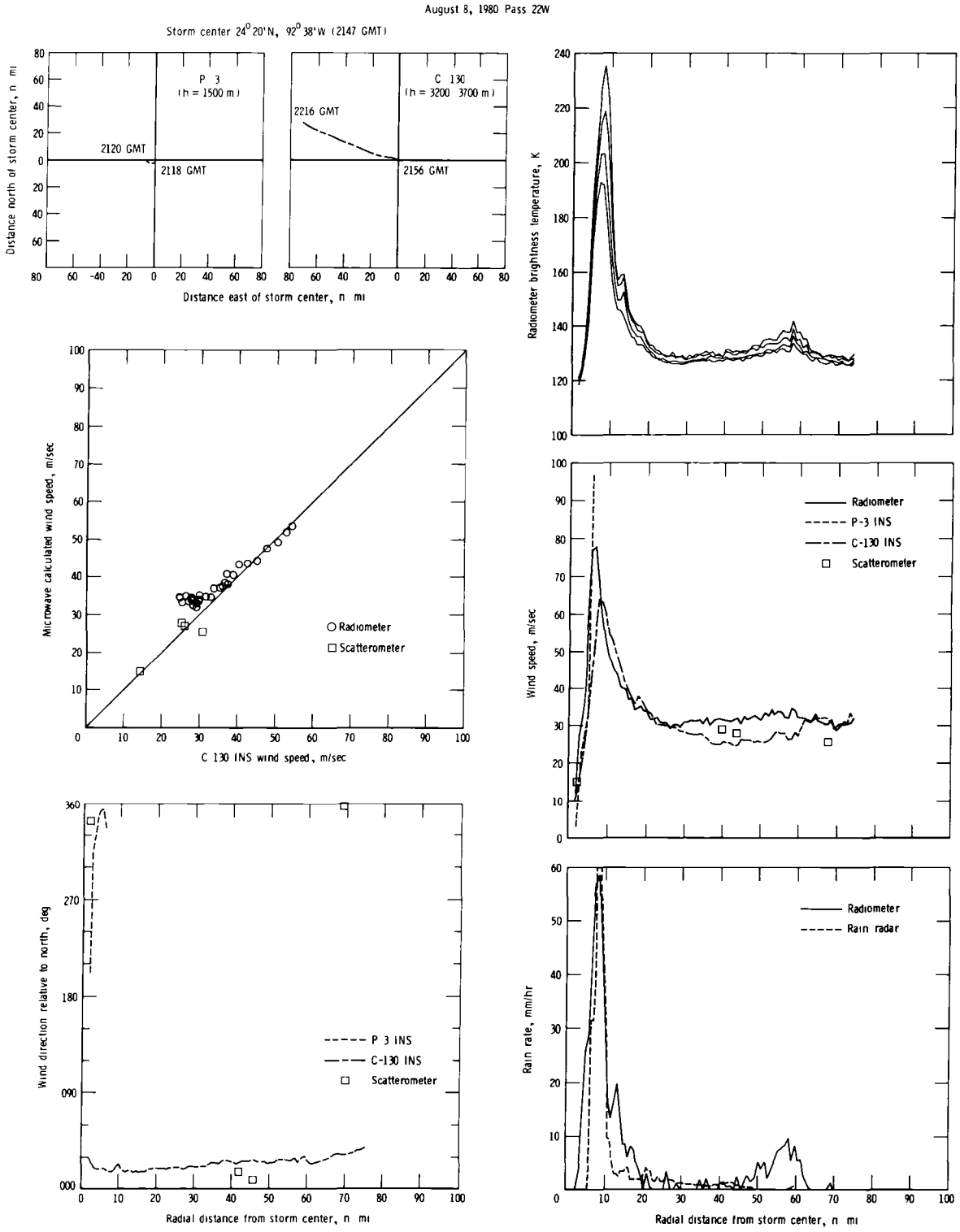

Figure 54.- Flight tracks and results of microwave and aircraft sensor measurements for pass 22W.

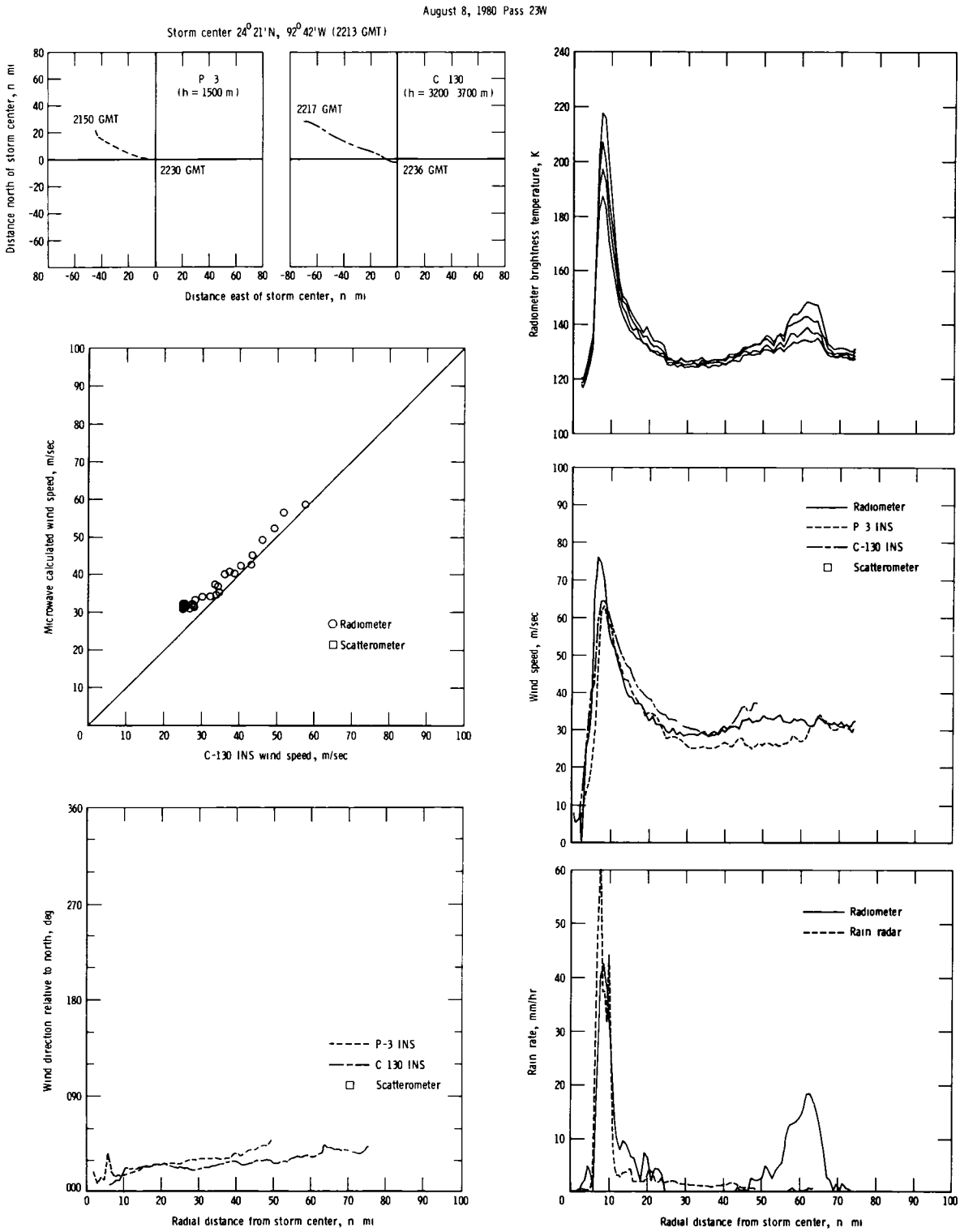

Figure 55.- Flight tracks and results of microwave and aircraft sensor measurements for pass 23W.

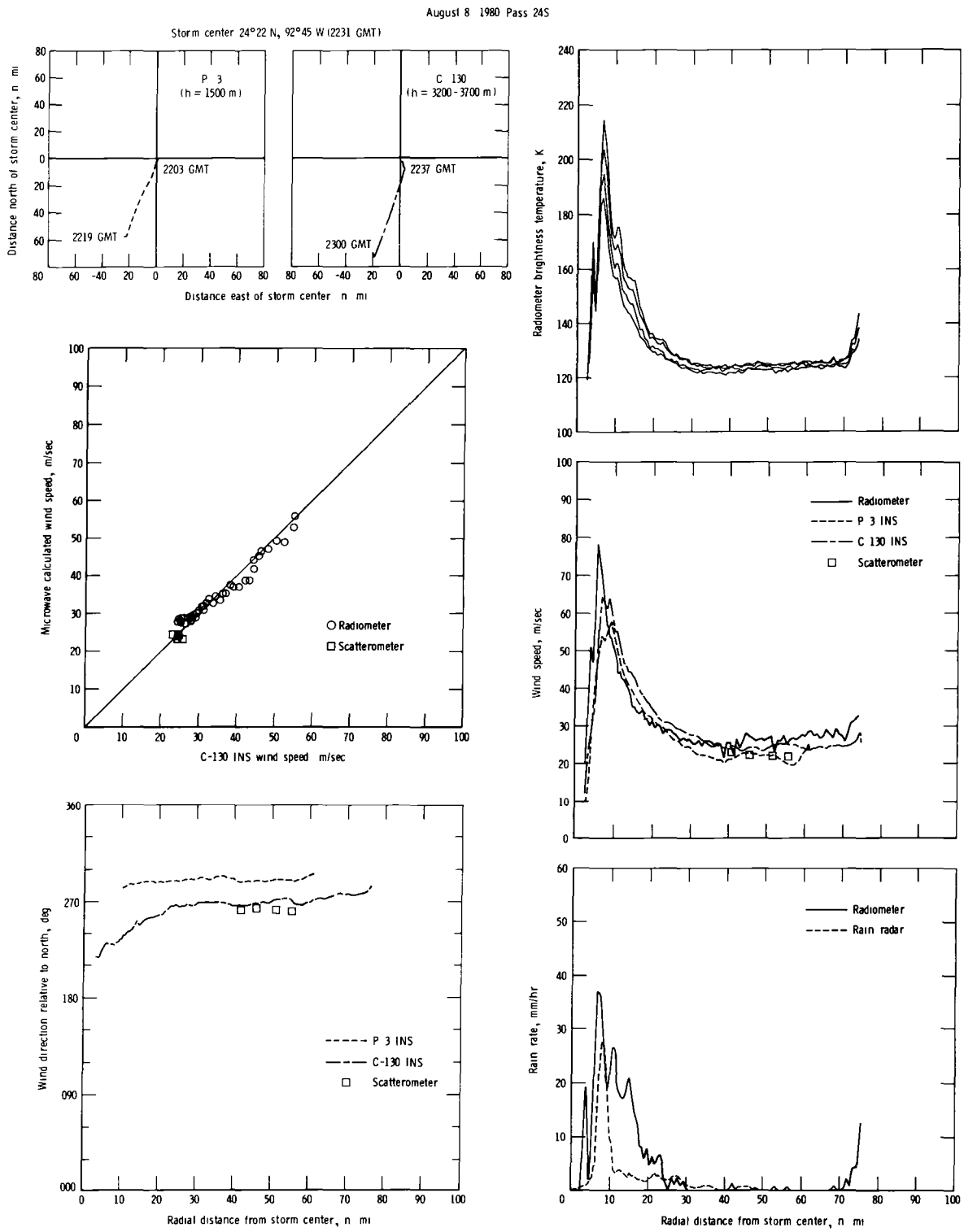

Figure 56.- Flight tracks and results of microwave and aircraft sensor measurements for pass 24S.

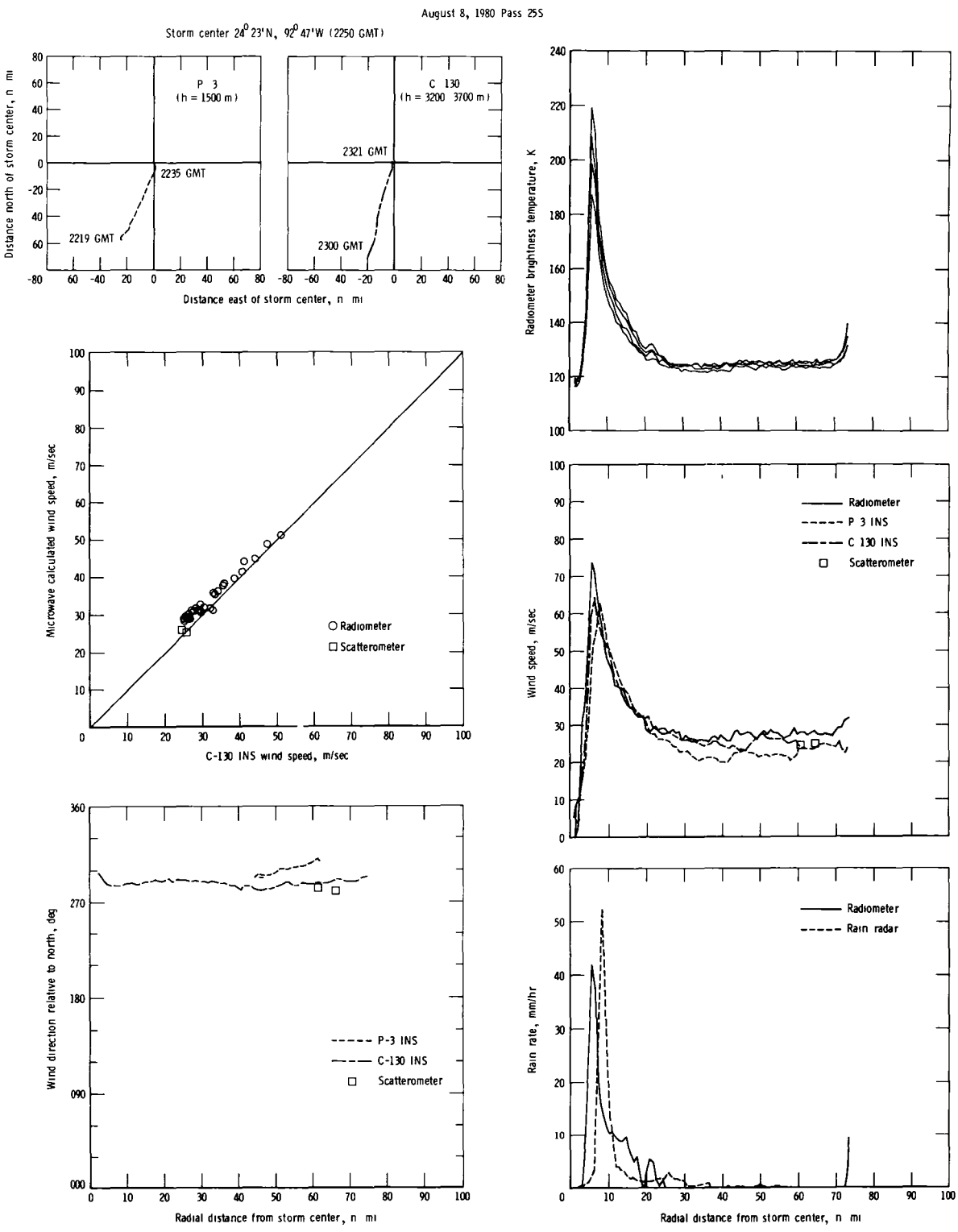

Figure 57.- Flight tracks and results of microwave and aircraft sensor measurements for pass 25S.

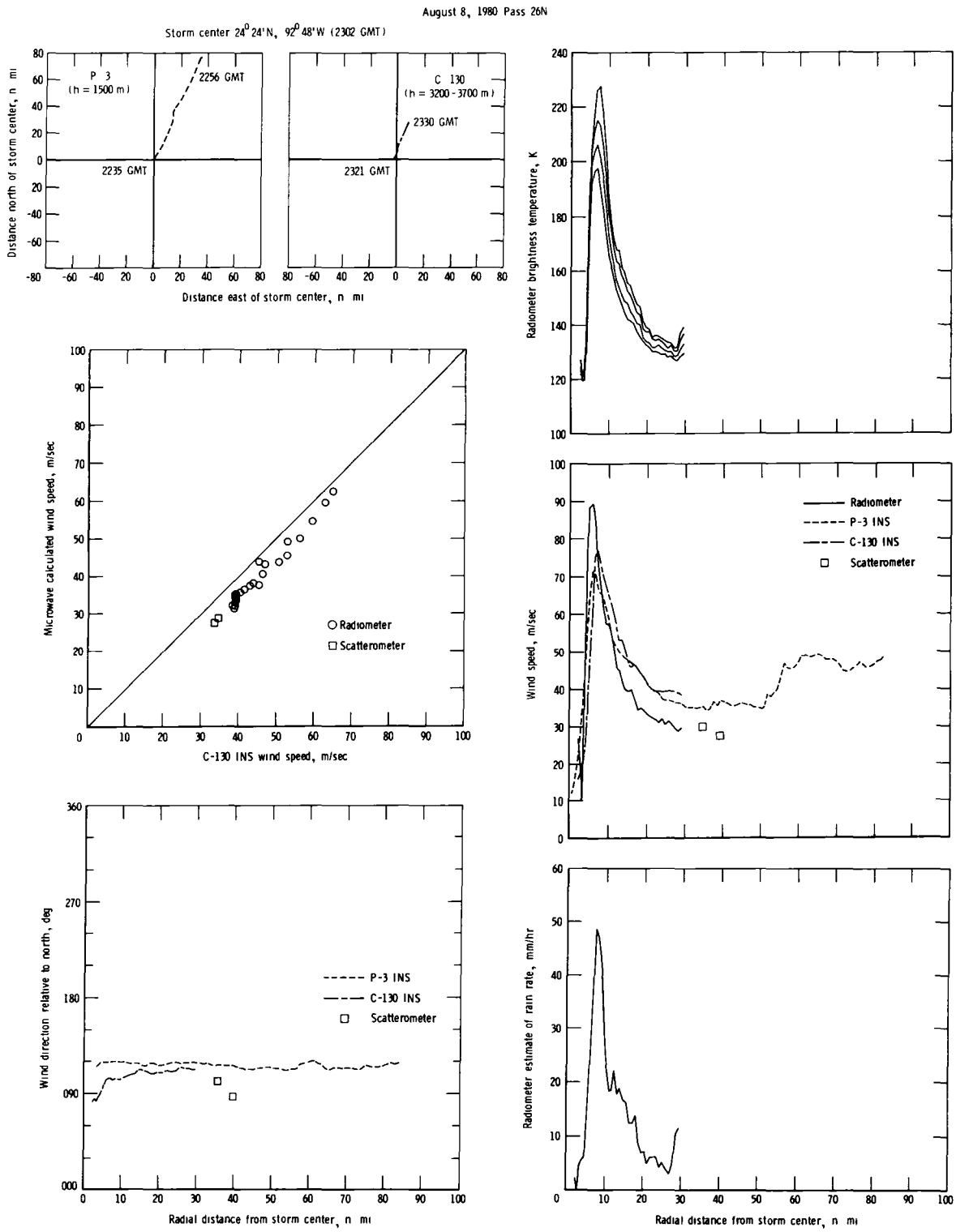

Figure 58.- Flight tracks and results of microwave and aircraft sensor measurements for pass 26N.

APPENDIX A

SENSOR DESCRIPTIONS

A.1 Sensors

A.1.1 Radiometer

The stepped frequency microwave radiometer is a precision, nadir-looking, circular polarized radiometer designed, developed, and fabricated at NASA Langley Research Center. The radiometer is believed to be the first variable-frequency microwave radiometer controlled by a digital microprocessor that provides both radiometer control functions and real-time data processing. The radiometer antenna, microwave portion, and signal processor are shown in figure A1. The front panel of the digital controller is shown in figure A2.

The radiometer is capable of operating at frequencies between 4.5 GHz and 7.2 GHz at bandwidths of 10, 50, 250, or 1000 MHz with integration times from 0.2 to 20 sec. The frequency can be varied in incremental steps from approximately 0.2 to 5 times the bandwidth per integration time. During Hurricane Allen, the radiometer was operated in one-, two-, and four-frequency modes. Analysis has shown that the radiometer exhibits an absolute precision of better than 2.0 K. Removal of absolute instrument bias was accomplished through comparison of the known local sea-surface temperature (26°C) with the physical sea-surface temperature calculated from the brightness temperature at that location. Wind speed and sea-surface salinity were taken into account in this comparison. The ideal radiometric brightness temperature sensitivity of the instrument varies between 0.012 and 1.25 K, depending on the bandwidth and integration time selected for the radiometer. The measured radiometer sensitivity at 6.6 GHz was between 0.69 and 0.88 K with 90-percent confidence, and between 0.65 and 0.94 K with 99-percent confidence. For the Hurricane Allen experiment, the ideal radiometer sensitivity was 0.25 K. The radiometer was operating with a predetection filter bandwidth of 50 MHz, and an integration time of 0.2 sec, with five samples averaged during post-flight data reduction to achieve a sample period of 1 sec.

The radiometer is a balanced Dicke-switched square-wave correlated radiometer. It utilizes a closed-loop noise feedback circuit to add noise to the received antenna noise and thereby balance to the Dicke reference noise. The microwave portion of the radiometer, including the broadband tunnel-diode low-noise amplifier, is maintained in a constant-temperature enclosure at the Dicke reference temperature within ±0.10 K. A block diagram of the radiometer is shown in figure A3.

The antenna consists of a corrugated-wall broadband horn (the 10-dB beam width for circular polarization is 20.5°). The antenna has a polarizing radome to provide for circular polarization. An 11-layer fiberglass honeycomb-sandwich radome is used over the polarizing radome in pressurized aircraft. The feed of the antenna is located within the constant-temperature enclosure. The noise injection circuit consists of a solid-state noise diode, isolator, PIN diode switch, and 20-dB directional coupler. The Dicke switch is a broadband latching circulator.

The receiver portion of the radiometer consists of a homodyne mixer, YIG-tuned local oscillator, and 1- to 1000-MHz intermediate frequency (IF) amplifier. The frequency of the radiometer is controlled by an eight-bit digital word from the digital

subsystem that is converted to 0 to 10 volts dc. This signal controls the voltage-tuned microwave oscillator. The frequency can be changed every 200 msec in steps of 16 MHz or greater over the frequency range from 4.018 to 8.098 GHz. However, the antenna limits the usable frequency range to 4.500 to 7.200 GHz. The bandwidth of the radiometer is selected by the digital subsystem using one of four paths through the filter bank.

The 1- to 1000-MHz constant-power-level noise signal is coupled by transformer into a hot-carrier diode square-law detector in the analog signal processor. The detected noise signal is amplified, synchronously detected with the Dicke switching frequency, and the resultant error signal is fed to a true integrator. The output of the integrator is filtered to remove the effect of the Dicke switching frequency and is used to control the pulse train output of a voltage-to-frequency (V/F) converter.

The V/F converter provides a variable-duty-cycle 70-μsec pulse train. The pulse repetition frequency varies linearly from 0 to 10 000 pulses per second with the dc output voltage of the integrator. This pulse train is applied to the noise-injection PIN diode switch and controls the number of injected constant-amplitude, constant-width noise pulses. The digital subsystem measures the duty cycle of the pulse train to determine the noise added to the antenna noise.

The digital subsystem provides control functions to the radiometer, data processing of the output signal from the radiometer, and physical temperature measurements of several locations in the radiometer. It also provides front panel control functions and real-time displays for the operator. The radiometer data are formatted along with time, temperatures, and other operational data and are recorded on a digital tape recorder. The integration time of the radiometer is determined by the count period of the injection time counters which compute the duty cycle of the radiometer output. The integration time of the closed-loop radiometer noise feedback is several times faster than the minimum integration time allowed by the digital subsystem.

A.1.2 Scatterometer

The airborne microwave scatterometer (referenced in earlier literature as SUS, the Seasat underflight scatterometer) is an active microwave remote sensor that was developed at the NASA Langley Research Center to measure the absolute normalized radar cross section of ocean, ice, and land targets. The scatterometer operates in a "long-pulse" mode (interrupted continuous wave), at a center frequency of 14.6 GHz. A simplified block diagram is shown in figure A4. The scatterometer is separated into three major assemblies: gimbal, transmitter-receiver assembly, and rack-mounted electronics.

The gimbal assembly comprises a dual-linear polarized parabolic antenna (3.5° beam width), a two-axis servo-controlled pedestal (to provide independent elevation and azimuth positioning), and a multilayer fiberglass honeycomb radome. For Hurricane Allen, this assembly was mounted on the underside of the fuselage beneath the vertical stabilizer (tail section) of the C-130 aircraft (fig. A5).

The transmitter-receiver assembly (fig. A6) consists of all the microwave hardware including circulator switches, 1-W and 20-W traveling wave tube (TWT) power amplifiers, low-noise tunnel-diode amplifier (TDA), and a solid-state microwave

source for generating the transmitter and receiver local oscillator signals. The system operation is digitally controlled by commands generated in the rack-mounted equipment.

The rack-mounted electronics (fig. A7) consists of power supplies, the gimbal controller, the signal processor, the digital controller and data system, and an analog strip chart recorder. The signal processor (fig. A4) has two overlapping channels that provide an instantaneous received power range of greater than 30 dB. A programmable attenuator is used as a coarse gain control to increase the total dynamic range to 60 dB. In each channel, the signals are square-law detected, integrated for 500 msec, and then converted from analog to digital (A/D) and recorded with a 7-track digital recorder. The digital controller and data system is a microprocessor that generates the precise timing and control logic needed by the scatterometer to form radio frequency (RF) pulses, operate switches and range gates, convert analog integrator voltages to digital, and format aircraft parameters and radar data needed for recording. The use of this processor enables considerable flexibility in the selection of radar operating characteristics (table A1) via an interactive programming mode.

In making scatterometer measurements, the quantity of interest is the scattering coefficient σ^o. This quantity is independent of the type of radar performing the measurement and is defined from the radar equation to be

$$\sigma^o = \frac{P_r}{P_t} \frac{(4\pi)^3 R^4}{G^2 \lambda^2 A_t L} \tag{A1}$$

where

P_r received power

P_t transmitted power

G antenna gain

R slant range

L miscellaneous losses due to couplers, waveguide, etc.

λ free-space wavelength

A_t effective area of antenna footprint on surface

For the scatterometer case of beam-limited conditions:

$$A_t = \frac{\pi}{4} \frac{(\beta_{eq} R)^2}{\cos \theta} \tag{A2}$$

where β_{eq} is the effective pencil-beam antenna width (approximately equal to the half-power antenna beam width) and θ is the incidence angle. The scattering coefficient thus becomes

$$\sigma^o = \frac{P_r}{P_t} \frac{(16\pi)^2 R^2 \cos \theta}{G^2 \lambda^2 \beta_{eq}^2 L} \tag{A3}$$

The P_r/P_t ratio was measured in two steps. First, a sample of the transmitter power, attenuated by a known value α_ℓ, was diverted into the receiver, as shown in the block diagram of figure A4. This produced a "calibration" output voltage V_c in each receiver channel, proportional to P_t. Next, the transmitter was connected to the antenna and an output voltage V_s proportional to P_r was obtained in a particular channel. Solving for the received-to-transmitted power ratio (in terms of the voltage from a particular channel) yields

$$\frac{P_r}{P_t} = \frac{V_s}{V_c} \frac{\alpha_\ell \alpha_c}{\alpha_s} \tag{A4}$$

where

V_s output voltage of integrator during surface observation

V_c output voltage of integration during calibration

α_ℓ receiver calibration loop attenuation

α_s programmable attenuation during surface observation

α_c programmable attenuation during calibration

Finally, in terms of the scatterometer transfer function, the expression for σ^o is

$$\sigma^o = (16\pi)^2 \frac{h^2 V_s \alpha_c \alpha_\ell}{\lambda^2 V_c \alpha_s G^2 \cos \theta \beta_{eq}^2 L} \tag{A5}$$

where h is the altitude of the aircraft (antenna).

The absolute σ^o value from equation (A5) is in error because of inaccuracies in the determination of the instrument transfer coefficients (G, α, L, α_ℓ, and β_{eq}) and the variables (h, θ, and V). This error can be separated into a bias and a random component. The accuracy of the bias determination is better than ±1 dB.

The major contributor to the random component of σ^o is V_s. Because of Rayleigh fading of the received power from the surface, V_s is an imperfect estimate of the mean received power used in the σ^o calculation, equation (A1). The normalized standard deviation of the cross section is approximately

$$\frac{\Delta\sigma^o}{\sigma^o} = \frac{1}{\sqrt{N}} \tag{A6}$$

where the number of independent samples, N, is

$$N = \sqrt{\beta_d \tau} \tag{A7}$$

where τ is integration time and β_d is the Doppler bandwidth of received power,

$$\beta_d = \frac{2V_g f}{c}(\sin\theta_{max} - \sin\theta_{min}) \tag{A8}$$

where

V_g ground speed

f radar frequency

c speed of light

For Hurricane Allen, $\Delta\sigma^o/\sigma^o$ was less than ±0.5 dB.

After the conclusion of the data flights, an intermittent digital command was found in the polarization switch of the scatterometer. Thus, much of the August 8 scatterometer data intended as HH polarization (see table A1) was discovered later to be actually either HV or some mixture of HH and HV. This results in an uncertainty of several dB in absolute level of the HH, HV, and VH data. Therefore, for August 8, only VV data are useful.

There are two partially overlapping channels in the signal processor, as shown in figure A4. Archived data tapes contain the calculated values of normalized radar cross section (σ^o) for both channels. The value of either was set to -99.00 or +99.00 if the integrator voltage for that channel was either too low (noise dominated) or too high (saturated), respectively. For the data flights of Hurricane Allen, only the less sensitive channel was on scale 42 percent of the time, only the more sensitive channel was on scale 47 percent of the time, and both channels were on scale simultaneously 7 percent of the time. During the remaining time, neither channel was on scale. The mean difference between the calculated values of σ^o for the two channels, near the saturation point of the more sensitive channel, was about 0.6 dB with a standard deviation of about 0.3 dB. (These statistics pertain only to VV polarization.) The total number of data points (0.5-sec integration time) was

10 075 for August 5 and 31 054 for August 8. The statistics were nearly identical for the two days. (For the computation of these statistics and totals, HH-data for August 8 were not included, for the reason discussed above.)

A.2 Sensor Footprint Geometry

In order to make full use of the data obtained during Hurricane Allen, the sensor geometry and its effect on temporal and spatial alignment of the data must be understood. Figure A8 illustrates the arrangement of sensors aboard the NOAA C-130 aircraft during the Hurricane Allen mission. The stepped frequency microwave radiometer was set to look at nadir; hence, its footprint was directly beneath the aircraft. The airborne microwave scatterometer, however, was operated at a variety of incidence angles from 0° (nadir) to 52°, and in all azimuths from the aircraft except for a 30° dead band centered on the aircraft nose.

Instantaneous footprints on both sensors at nadir would be nearly circular. However, because the sensors record data over varying integration times (usually 0.5 sec), there is a smearing of the footprint in the direction of the flight line. For example, given a beam width of 20.5° (0.37 rad), the instantaneous 10-dB footprint of the radiometer can be calculated from

$$\text{Radiometer footprint diameter} = 0.37h$$

At an aircraft altitude of 3000 m the radiometer instantaneous footprint would be a circle with a diameter of 1110 m.

The footprint is smeared, however, along the flight line by the distance the aircraft traveled during the signal integration. At an aircraft speed of 115 m/sec, the aircraft would have traveled 57 m during a 0.5-sec integration period. Therefore, the radiometer footprint would actually be an ellipse with the major axis along the flight line and the minor axis perpendicular to the flight line. For the radiometer, the time recorded was that time when the aircraft was directly over the centroid of the smeared footprint. Footprint size perpendicular to the flight line is

$$A = 0.37h$$

while footprint size along the flight line is

$$B = A + \tau V_g$$

For an altitude of 3000 m and a ground speed of 115 m/sec, footprint dimensions are as follows:

$$A = 1110 \text{ m}$$

$$B = 1167 \text{ m}$$

Calculation of footprint size for the scatterometer is slightly different because, in addition to smearing along the flight line, the instrument is not always nadir looking. The instantaneous footprint dimensions A (perpendicular to flight line) and B (along flight line) for the scatterometer are

$$A = \frac{0.0612h}{\cos \theta}$$

$$B = \frac{A}{\cos \theta}$$

where 3.5° (0.0612 rad) is the field of view of the scatterometer. Again, for an aircraft in motion, there is smearing along the flight line and B becomes

$$B = \frac{A}{\cos \theta} + \tau V_g$$

For an altitude of 3000 m, an aircraft ground speed of 115 m/sec, and an incidence angle of 45°, the scatterometer footprint size for an aft-looking antenna is approximately

$$A = 260 \text{ m}$$

$$B = 370 \text{ m}$$

For the purpose of describing the operation of the scatterometer during Hurricane Allen, the displacement of the scatterometer footprint during an azimuth scan or an elevation scan is discussed here. During an azimuth scan, the incidence angle of the antenna is held constant (with respect to the yaw axis) and the azimuth is varied in steps from 15° off one side of the aircraft nose through 330° to 15° off the other side of the nose. Meanwhile, the locus of footprint locations on the sea surface is the cycloid which results from the circular sweep of the antenna and the forward motion of the aircraft. Figure A9 illustrates the loci of footprints for incidence angles of 20°, 40°, and 54°, for an altitude of 3300 m, and a ground speed of 120 m/sec (typical for the Hurricane Allen flights).

For a straight and level flight path over spatially varying but time-stationary surface targets, the geometrical concepts discussed above are of vital importance. Although these concepts may in the future be applied to the analysis of the microwave remotely sensed data of Hurricane Allen, they were not used in the present analysis beyond a preliminary calculation of the scatterometer footprint location. Our present limited knowledge of the temporal and areal structure of the wind gusts and rain cells in the storm forced the scatterometer and radiometer data to be sorted according to time and mean radial distance only. It is with a view toward future analysis that the sensor geometry and footprint location concepts have been presented here. All parameters necessary for calculation of footprint location are available on the archived data files, discussed in appendix B.

TABLE A1.- SCATTEROMETER OPERATING CHARACTERISTICS

Selectable characteristics:	
Polarization	HH,* HV, VV, VH
Incidence angle, deg	0 to 54
Azimuth angle (relative to heading), deg	15 to 345
Nonselectable characteristics:	
Frequency, GHz	14.6
σ^{o} sampling rate, sec^{-1}	2
Absolute σ^{o} accuracy, dB	±1.0
σ^{o} precision, dB	±0.1
Antenna beam width, deg	3.5
Total σ^{o} range, dB	+20 to -40

*Transmit horizontal and receive horizontal. With transmit and receive each horizontal or vertical, there are four possible combinations. When transmit and receive are of like polarization, the system is said to be in a dominant polarization, and when opposed, in a cross-polarization.

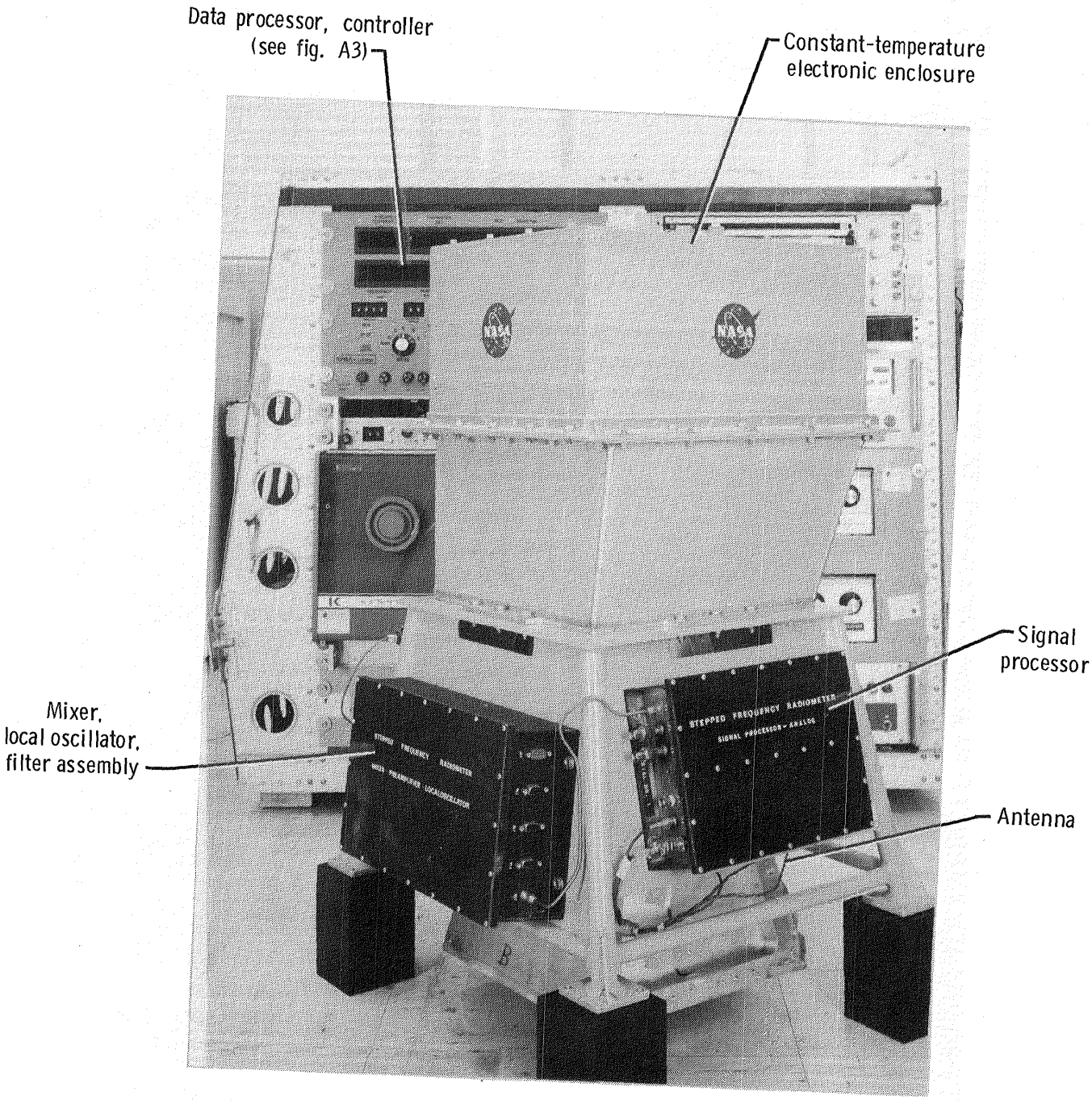

Figure A1.- Stepped frequency microwave radiometer.

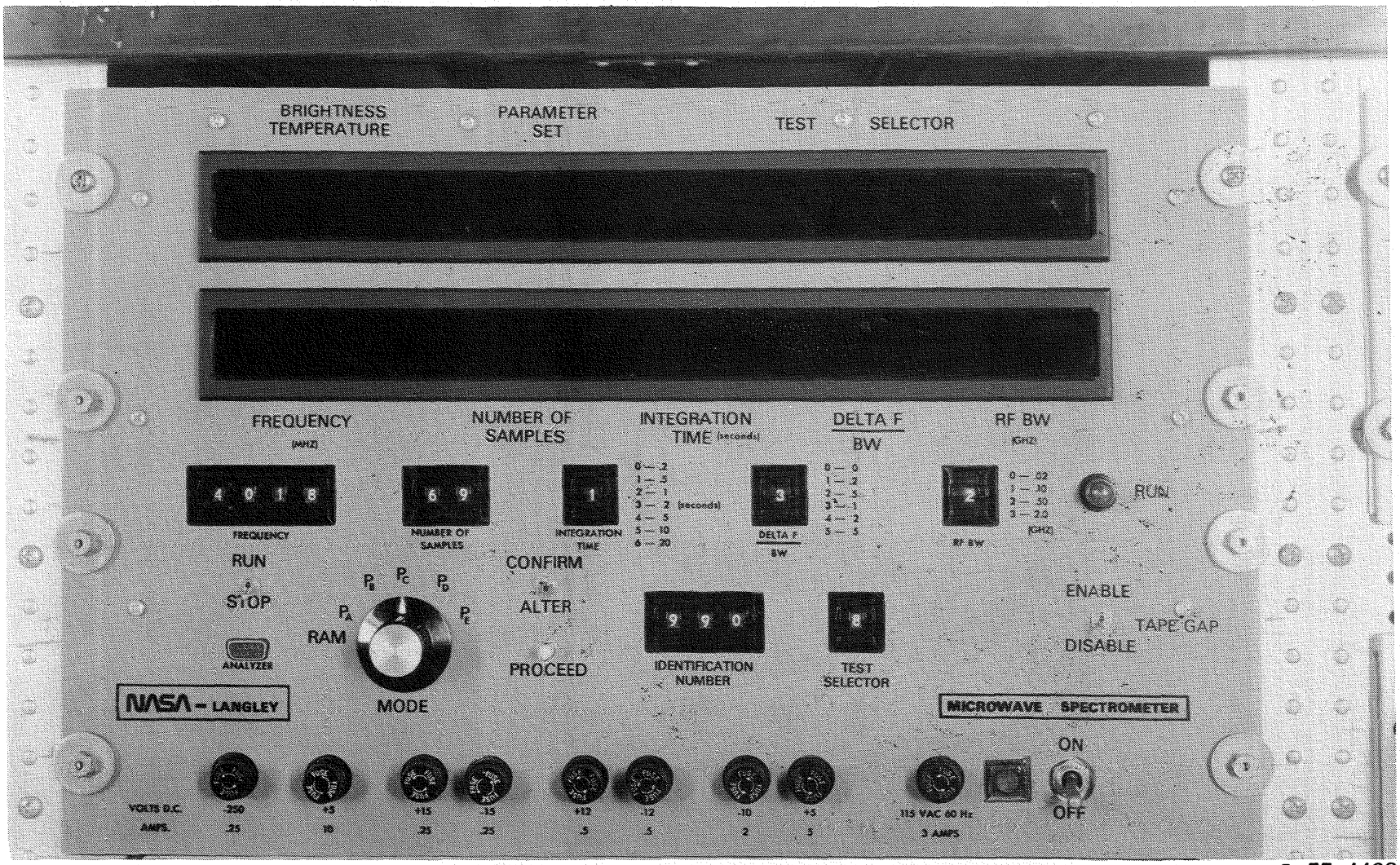

L-77-4488

Figure A2.- Front panel of digital controller for radiometer.

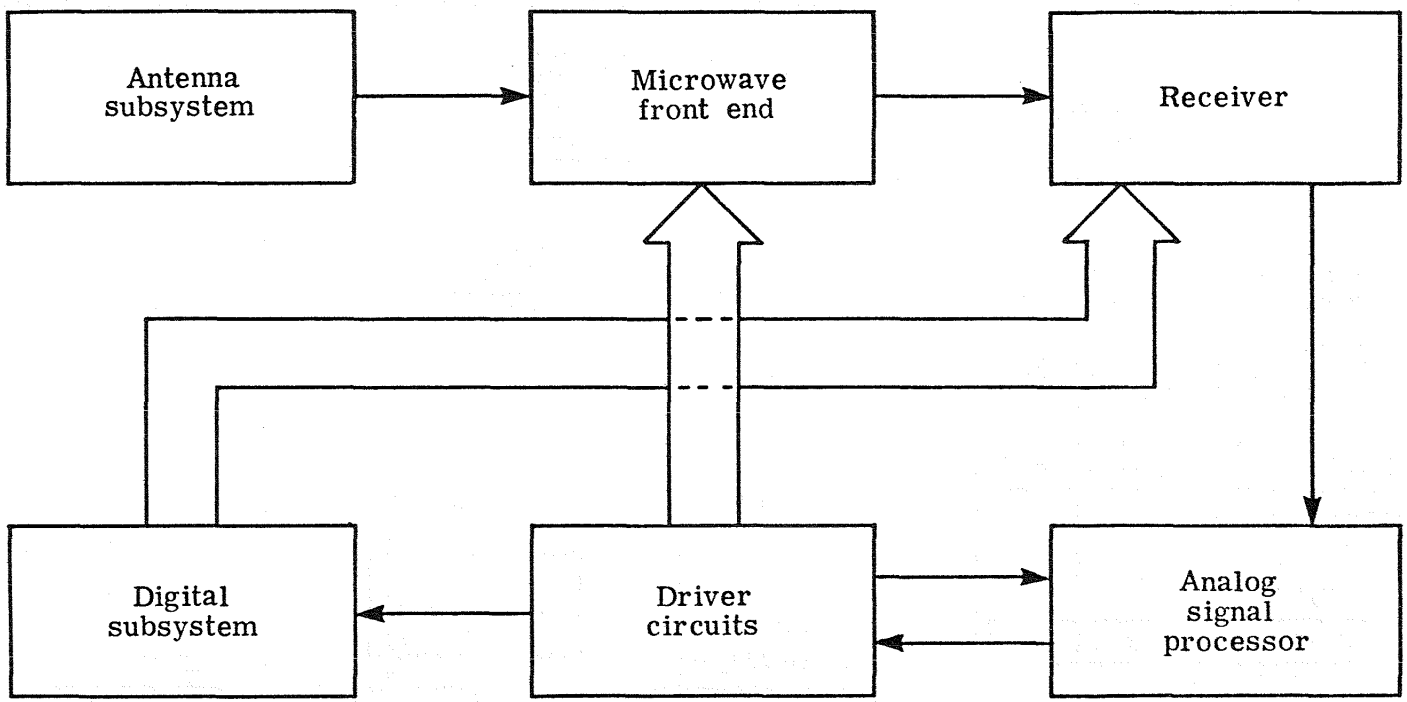

Figure A3.- Block diagram of radiometer.

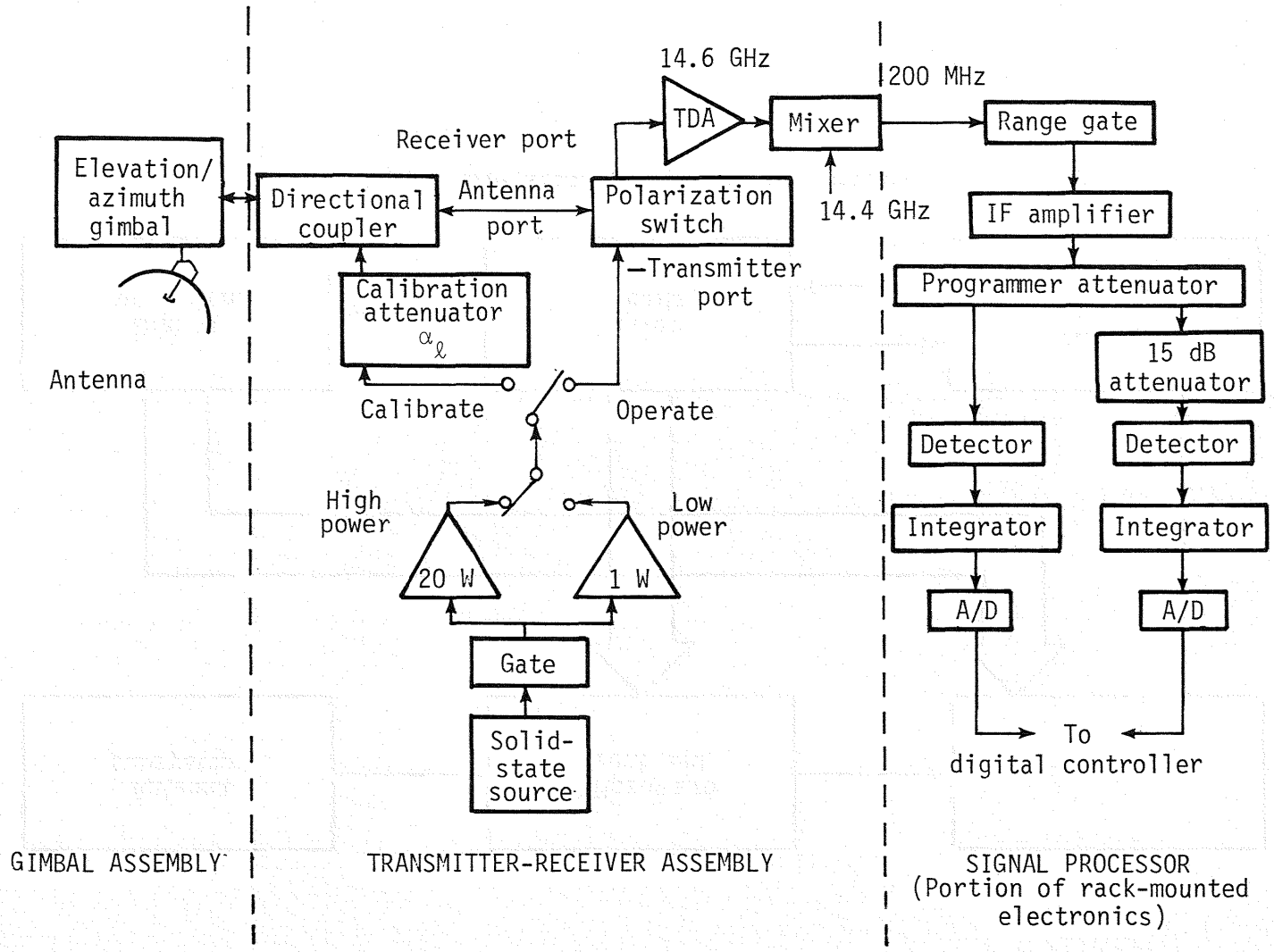

Figure A4.- Block diagram of scatterometer.

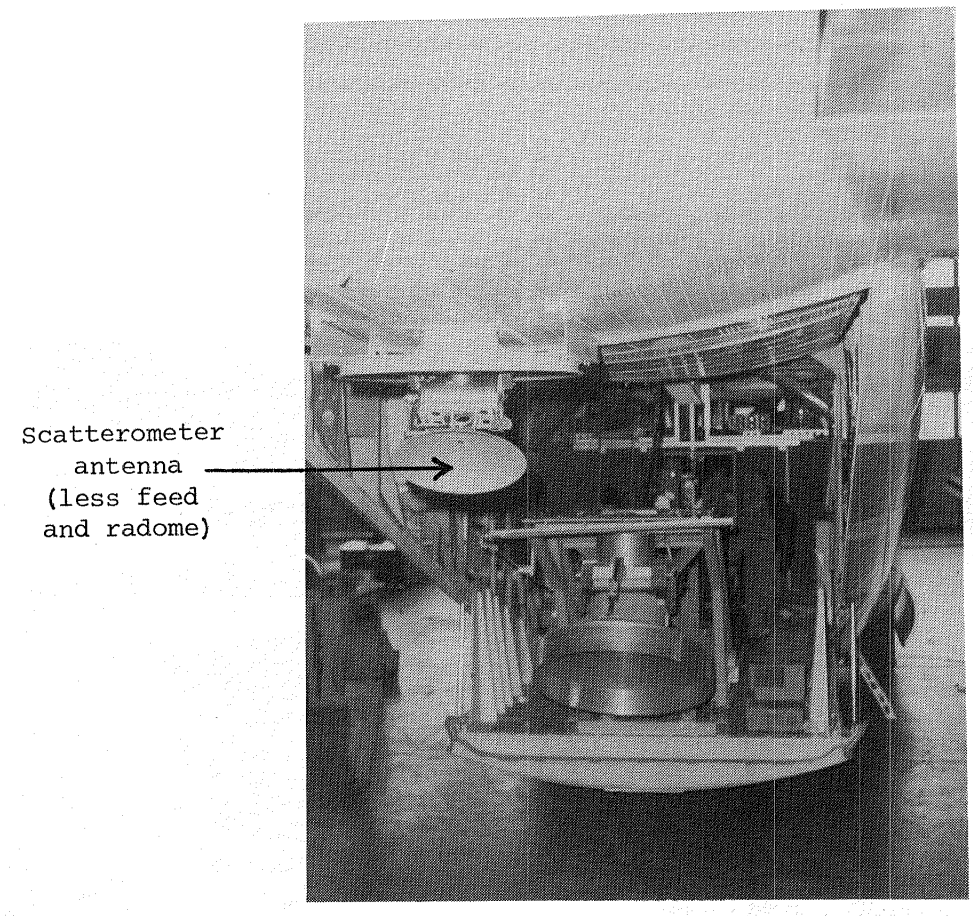

Figure A5.- Scatterometer gimbal assembly on C-130 aircraft.

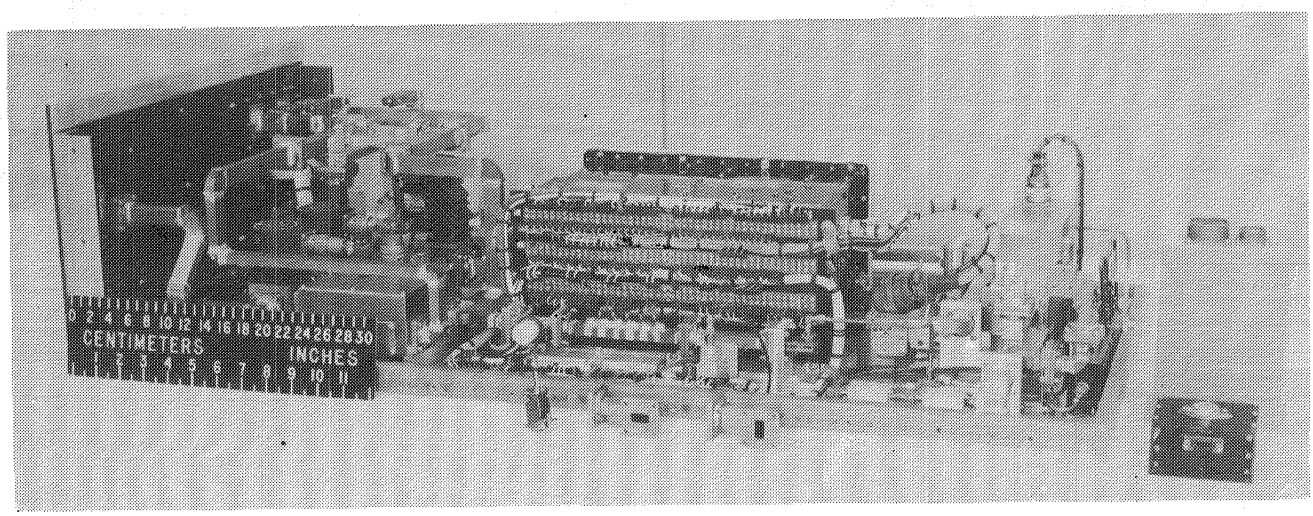

Figure A6.- Scatterometer transmitter-receiver assembly.

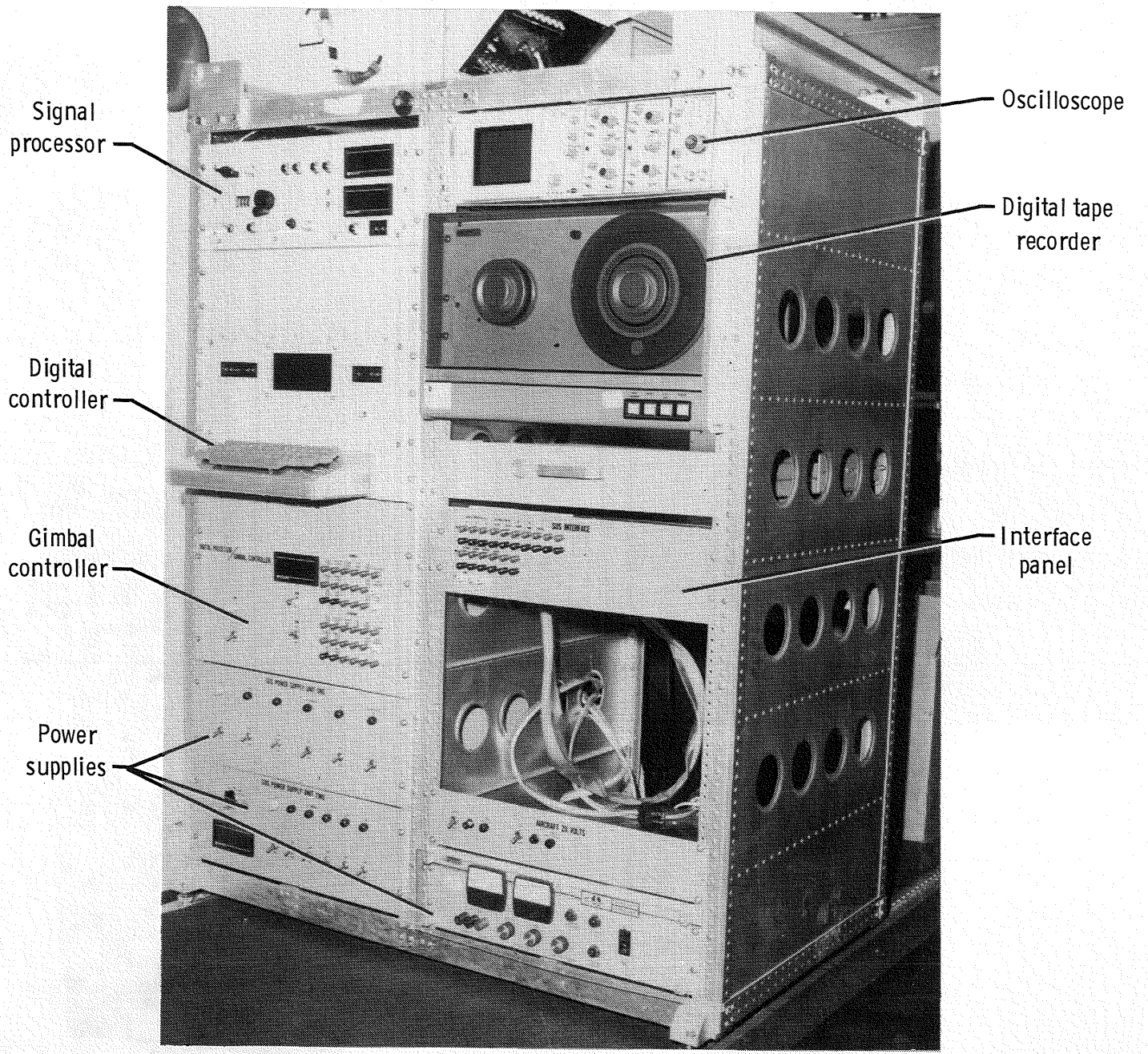

L-83-36

Figure A7.- Rack-mounted electronics for scatterometer.

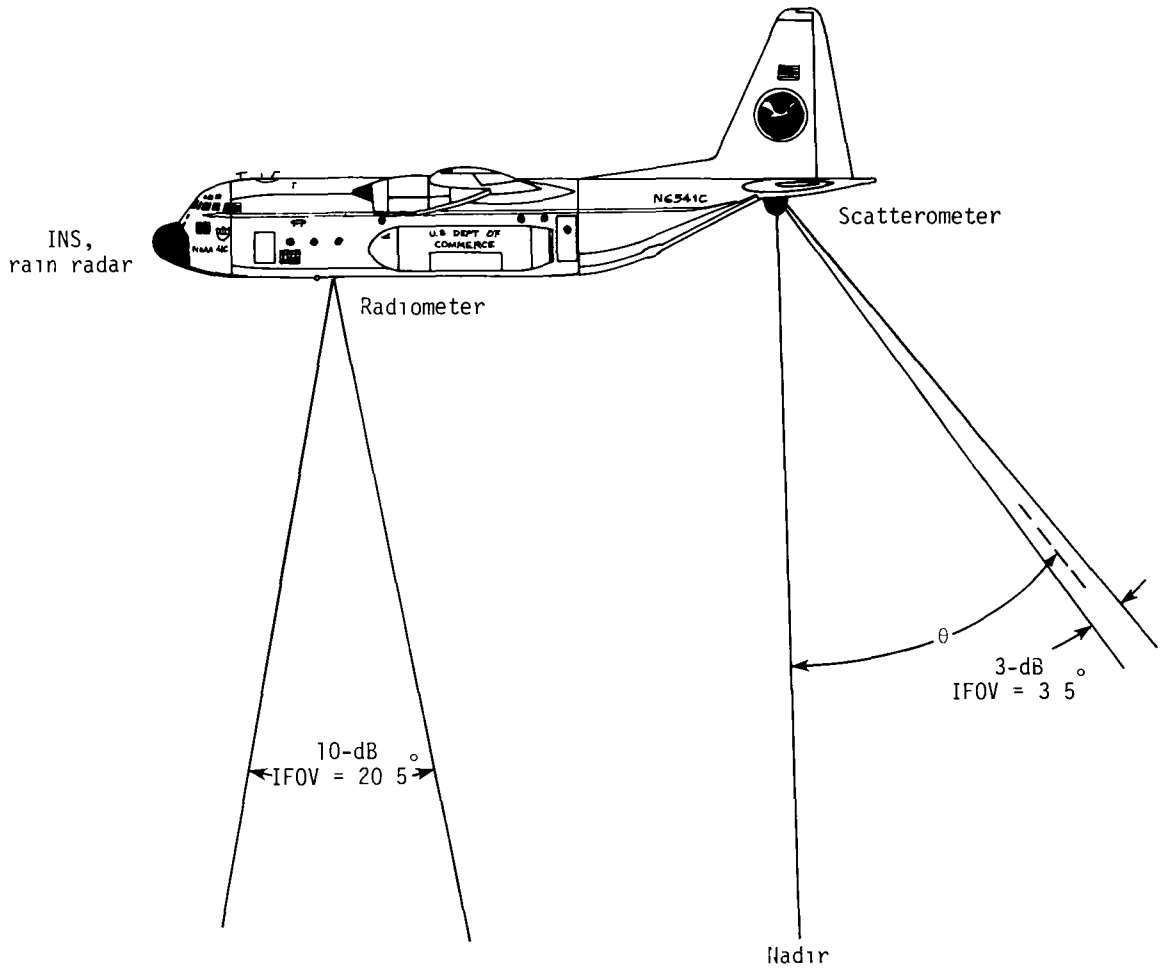

Figure A8.- Arrangement of sensors on NOAA C-130 for Hurricane Allen flights.

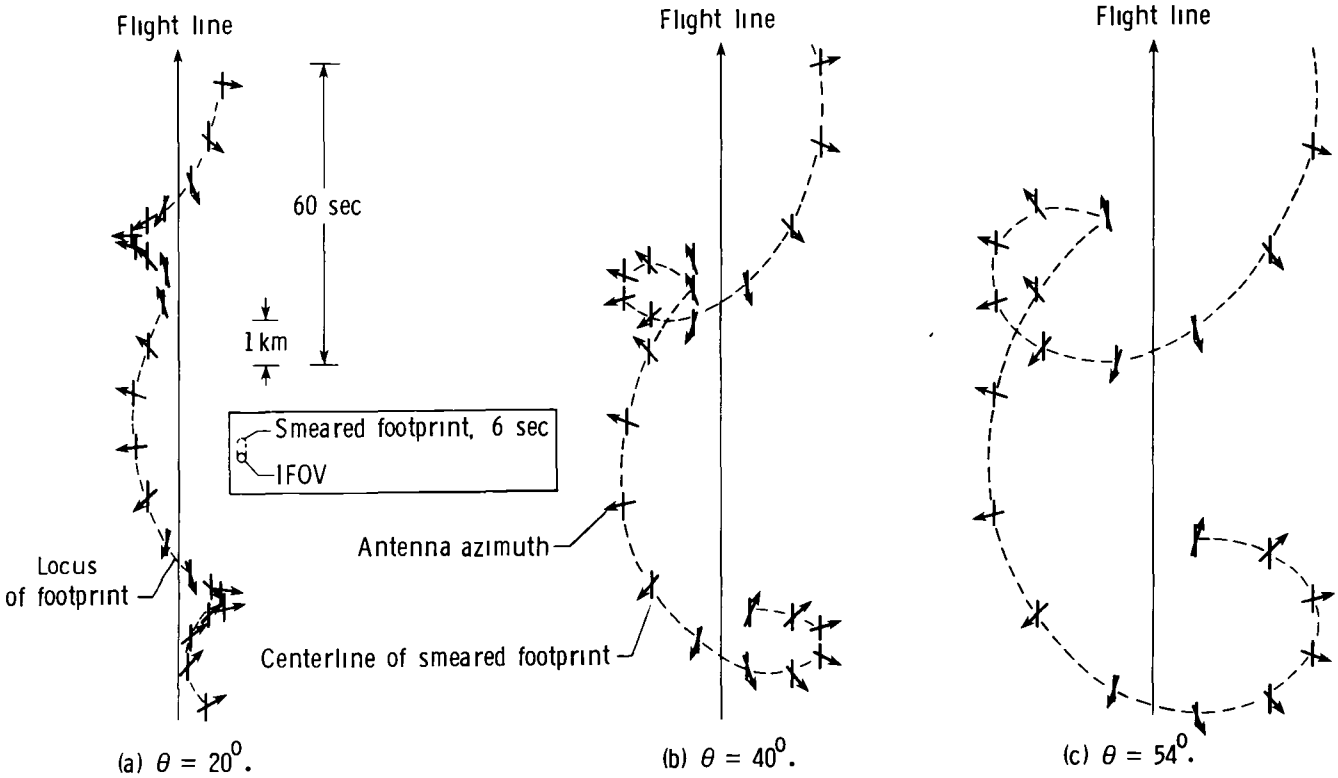

Figure A9.- Locus of scatterometer footprint for specified incidence angles.

APPENDIX B

SCOPE AND FORMAT OF ARCHIVED DATA

Hurricane Allen data are available to researchers in the form of digital tape from the National Technical Information Service, 5285 Port Royal Road, Springfield, VA 22161. The archived information is comprised of eight files in all, namely, four of INS and radiometer data, three of scatterometer data, and one of rain radar data. These files are described in sections B.1, B.2, and B.3. A supplementary section, B.4, provides some ancillary information to aid the computer programmer in the transfer of "card image" tape information into computer file space. In this appendix, time is expressed in decimal hours for convenience of the computer programmer.

B.1 INS and Radiometer Data Files

The content of the four files of compressed INS and radiometer data is given in table B1. In each file, the very first information is an identifier with day, month, year, and nominal altitude in the first four locations, followed by 32 zeros. The data have three 12-word card images per array of parameters, each with format F7.3, 3F9.4, 5F6.1, F6.0, 2F5.0. The parameters in the three card images of an array are given in tables B2, B3, and B4. The "ending time" shown in table B1 is the "bin limit time" according to table B2, that is, the first parameter of the first of three 12-word card images; these ending times are provided for convenience of a programmer in scanning the data.

Parameters 1, 2, 3, and 4 of the third card image are set to zero in the P-3 data, as are the two parameters associated with them, rain rate (parameter 9 of card image 1) and estimated surface wind speed (parameter 9 of card image 2). Otherwise, the value 999 is generally used as bulk filler in the INS and radiometer data.

For parameter 12 of card image 3:

Code = 0 is for good data

Code = 4 is exclusively for the C-130 on August 8, 1980, where a gap in INS data exists; only the bin limit time and the radiometer T_A data are meaningful; other parameters on the card image are filler.

Code = 2 is for small gaps in INS data; the previous INS data are repeated as filler, and are <u>incorrect</u> for a Code = 2 bin.

Code = 1 is for recovery from the Code = 2 condition; change in radial distance and change in INS wind speed are set to zero; all other parameters are good.

B.2 Scatterometer Data Files

The three files of scatterometer data respectively deal with vertical polarization on August 8, horizontal polarization of August 5, and vertical polarization on August 5. Each file is comprised of a single large record.

These data have two 12-word card images per array, each with format 4F9.4, 2F6.1, F7.1, F5.0, 3I4, F8.1. The parameters in these two card images are given in

tables B5 and B6. In each file, the first information is an identifier with day, month, and year in the first three locations, followed by five zeros, then an integer (1 for vertical polarization or 0 for horizontal), and fifteen trailing zeros.

The scatterometer bins are determined by time, elevation, and azimuth. Bin limit times are frequently duplicated because of intermediate change of azimuth or elevation. There is no assurance of continuity in the increment (0.004 hr) assigned for bin limit times. These files have no filler values.

B.3 Rain Radar Data Files

The rain radar file consists of 33 records of time-averaged rain rates from rain radar measurements. These were provided at increments of 1 km and have simply been stored. The format is 16F5.1, and (with fill of zeros) 160 values have been stored in ten 16-value lines, pertinent (except for zero fill) from 1 to 160 km from the storm center. Values are in mm/hr. Descriptions of the 33 records are listed in table B7.

B.4 Structure of Archived Data Tapes

Each record of information in computer file space corresponds to a file of data on the archived "card image" tapes, and each card image of data forms a separate record on tape. When the information is loaded from tape into computer file space, the programmer must assemble the records appropriately so as to reconstitute just eight separately named and independent files. The INS and radiometer data are ordered according to table B1, reading down each column and from left to right as one would expect. The scatterometer data, in the same order as cited in section B.2 (i.e., vertical polarization on August 8, horizontal on August 5, and then vertical on August 5), are followed by the rain radar data in the same order as listed in table B7.

TABLE B1.- PARTITIONED INS AND RADIOMETER DATA

C-130, Aug. 5		C-130, Aug. 8		P-3, Aug. 5		P-3, Aug. 8	
Record	Ending GMT,[a] hr	Record	Ending GMT,[a] hr	Record	Ending GMT,[a] hr	Record	Ending GMT,[a] hr
1 Approach A	11.332	1 Approach	17.636	1 Approach	11.500	1 Pass 13E	18.980
2 Approach B	11.560	2 Approach B	17.932	2 Pass 1N	11.712	2 Pass 14W	19.232
3 Pass 1N	11.740	3 Approach C	18.832	3 Pass 2S	11.960	3 Pass 15W	19.476
4 Pass 2S	12.076	4 Pass 13E	19.340	4 Transit 1	12.412	4 Pass 16S	19.732
5 Transit 1	12.632	5 Pass 14W	19.640	5 Pass 3W	12.600	5 Pass 17S	20.000
6 Pass 3W	12.780	6 Pass 15W	19.904	6 Pass 4E	12.880	6 Pass 18N	20.292
7 Pass 4E	13.132	7 Transit 1	19.948	7 Transit 2	13.052	7 Pass 19N	20.568
8 Transit 2	13.512	8 Pass 16S	20.236	8 Pass 5S	13.256	8 Pass 20E	20.935
9 Pass 5S	13.768	9 Pass 17S	20.528	9 Pass 6N	13.660	9 Pass 21E	21.296
10 Pass 6N	14.032	10 Pass 18N	20.812	10 Transit 3	14.016	10 Pass 22W	21.328
11 Transit 3	14.256	11 Pass 19N	21.088	11 Transit 4	14.400	11 Transit 1	21.832
12 Transit 4	14.568	12 Pass 20E	21.512	12 Transit 5	14.712	12 Pass 23W	22.048
13 Transit 5	14.828	13 Pass 21E	21.928	13 Pass 7N	14.992	13 Pass 24S	22.320
14 Transit 6	15.052	14 Pass 22W	22.272	14 Transit 6	15.280	14 Pass 25S	22.576
15 Pass 7N	15.248	15 Pass 23W	22.608	15 Transit 7	15.580	15 Pass 26N	22.940
16 Pass 8S	15.496	16 Pass 24S	23.004	16 Transit 8	15.856	16 Transit 2	23.312
17 Pass 9S	15.780	17 Pass 25S	23.352	17 Transit 9	16.160	17 Transit 3	23.552
18 Pass 10N	15.964	18 Pass 26N	23.500	18 Pass 8S	16.520		
19 Pass 11N	16.156	19 Departure	24.820	19 Transit 10	16.580		
20 Pass 12S	16.260			20 Pass 9S	16.900		
21 Departure A	16.500			21 Pass 10N	17.112		
22 Departure B	17.632			22 Transit 11	17.332		
				23 Pass 11W	17.488		
				24 Pass 12E	17.840		
				25 Departure	18.000		

[a]The GMT, in decimal hours, of final array (of 36 parameters) in record.

TABLE B2.- PARAMETERS IN CARD IMAGE 1 OF INS AND RADIOMETER DATA

1	Bin limit time, hr from midnight
2	Bin average time, hr from midnight
3	Latitude N, deg
4	Longitude E, deg
5	Distance north of storm center, n.mi.
6	Distance east of storm center, n.mi.
7	Radial distance from storm center, n.mi.
8	INS wind speed, m/sec
9	Wind speed at surface estimated from radiometer calculation, m/sec
10	Altitude, m
11	INS wind direction, deg
12	Bearing from storm center, deg

TABLE B3.- PARAMETERS IN CARD IMAGE 2 OF INS AND RADIOMETER DATA

1	Liquid water in air, g/m^3
2	Humidity, percent
3	Mixing ratio, g/kg
4	Dew point, °C
5	Air temperature, °C
6	Temperature measured with precision radiation thermometer (PRT-5), °C
7	Change in radial distance from previous bin value, n.mi.
8	Change in INS wind speed from previous bin value, m/sec
9	Rain rate from radiometer calculation, mm/hr
10	Atmospheric pressure, mbar
11	Horizontal angle between aircraft track and true north, deg
12	Horizontal angle between aircraft heading and true north, deg

TABLE B4.- PARAMETERS IN CARD IMAGE 3 OF INS AND RADIOMETER DATA

1	Radiometer $T_{A,1}$, K
2	Radiometer $T_{A,2}$, K
3	Radiometer $T_{A,3}$, K
4	Radiometer $T_{A,4}$, K
5	Air speed, m/sec
6	Ground speed, m/sec
7	Pitch, deg
8	Roll, deg
9	Vertical wind speed, m/sec
10	Surface pressure, mbar
11	Drift (angle between aircraft track and aircraft heading), deg
12	Code

TABLE B5.- PARAMETERS IN CARD IMAGE 1 OF SCATTEROMETER DATA

1	Bin limit time, hr from midnight
2	Bin average time, hr from midnight
3	Latitude N, deg
4	Longitude W, deg (note: without minus sign, as recorded)
5	Radial distance from storm center, n.mi.
6	Bearing from storm center, deg
7	C-130 INS wind speed, m/sec
8	C-130 INS wind direction, deg
9	Arbitrary azimuth bin index, based on aircraft heading
10	Arbitrary azimuth bin index, based on INS wind direction
11	Arbitrary elevation bin index
12	Minimum wind speed at surface estimated from radiometer calculation, m/sec

TABLE B6.- PARAMETERS IN CARD IMAGE 2 OF SCATTEROMETER DATA

1	Incidence angle, deg
2	Standard deviation of incidence angle, deg
3	Normalized radar cross section, dB
4	Standard deviation of normalized radar cross section, dB
5	Azimuth angle, deg
6	Standard deviation of azimuth angle, deg
7	Altitude, m
8	Aircraft heading, deg
9	Number of scatterometer readings averaged in bin, negative if radiometer solutions for rain rate were not available
10	Scatterometer mode (see table 2)
11	Scatterometer polarization (0 = HH, 1 = VV)
12	Rain rate from radiometer calculation, mm/hr

TABLE B7.- RAIN RADAR DATA

Record	Date	GMT[a] and bearing, or pass name
1	Aug. 5, 1980	11.27 - 14.38 hr, all compass bearings
2	Aug. 5, 1980	15.62 - 18.25 hr, all compass bearings
3	Aug. 5, 1980	11.27 - 14.38 hr, 350° to 10°
4	Aug. 5, 1980	11.27 - 14.38 hr, 80° to 100°
5	Aug. 5, 1980	11.27 - 14.38 hr, 125° to 145°
6	Aug. 5, 1980	11.27 - 14.38 hr, 170° to 190°
7	Aug. 5, 1980	11.27 - 14.38 hr, 260° to 280°
8	Aug. 5, 1980	11.27 - 14.38 hr, 305° to 325°
9	Aug. 8, 1980	19.27 - 21.85 hr, all compass bearings
10	Aug. 8, 1980	20.90 - 23.10 hr, all compass bearings
11	Aug. 8, 1980	19.27 - 21.85 hr, 15° to 35°
12	Aug. 8, 1980	19.27 - 21.85 hr, 102° to 122°
13	Aug. 8, 1980	19.27 - 21.85 hr, 190° to 210°
14	Aug. 8, 1980	19.27 - 21.85 hr, 282° to 302°
15	Aug. 5, 1980	C-130 Pass 1N
16	Aug. 5, 1980	C-130 Pass 2S
17	Aug. 5, 1980	C-130 Pass 3W
18	Aug. 5, 1980	C-130 Pass 4E
19	Aug. 5, 1980	C-130 Pass 5S
20	Aug. 5, 1980	C-130 Pass 6N
21	Aug. 8, 1980	C-130 Pass 13E
22	Aug. 8, 1980	C-130 Pass 14W
23	Aug. 8, 1980	C-130 Pass 15W
24	Aug. 8, 1980	C-130 Pass 16S
25	Aug. 8, 1980	C-130 Pass 17S
26	Aug. 8, 1980	C-130 Pass 18N
27	Aug. 8, 1980	C-130 Pass 19N
28	Aug. 8, 1980	C-130 Pass 20E
29	Aug. 8, 1980	C-130 Pass 21E
30	Aug. 8, 1980	C-130 Pass 22E
31	Aug. 8, 1980	C-130 Pass 23W
32	Aug. 8, 1980	C-130 Pass 24S
33	Aug. 8, 1980	C-130 Pass 25S

[a]GMT is in decimal hours.

APPENDIX C

RECORD OF ADDITIONAL INS AND RADIOMETER DATA

This appendix serves as a visual catalog of the INS and radiometer data not encompassed within the 26 defined pass pairs. These data pertain to approaches to the storm, so-called "transits," and departures from the storm. Some of the transits are actually radial profiles that could not be usefully matched into pass pairs, while others are transits in the customary sense. Where the same radial distance is duplicated on a particular figure, necessarily within a reasonably short time interval, conditions can be isolated for study of the extent to which the storm structure was relatively constant or subject to relatively random deviation. It is not intended that such figures, or other figures, be read for numerical values; these should be taken from the archived data files.

Of the INS data available, only wind speed and direction are of interest here. Consequently, for the P-3 aircraft, the figures display data for two flight segments, side by side. From the C-130 aircraft, radiometer data are also available (except at extremes of approach and departure). Thus, the C-130 figures display the flight path and the INS data on the left, the radiometric brightness temperature at the upper right, and (if the radiometer was operating at more than one frequency) the computed wind speed and rain rate. The flight segments of these figures are identified in table C1.

Changes in altitude shown on some figures should be noted carefully, to preclude erroneous interpretations. It is emphasized that these figures are intended to serve as a key to available information, and not as working tools themselves.

TABLE C1.- AIRCRAFT APPROACHES, TRANSITS, AND DEPARTURES

Aircraft and date	Flight segment	Altitude, m	GMT range	Position of storm center	Radiometer freq.[a]	Scatterometer mode[b]	Fig.
P-3, Aug. 5	Approach A	400	1052-1115	15°55'N, 70°09'W			C1
	Approach B	400	1115-1130	15°55'N, 70°15'W			C1
	Transit 1	1500	1158-1225	15°58'N, 70°31'W			C2
	Transit 2	1600-500	1253-1303	16°02'N, 70°46'W			C2
	Transit 3	1500	1340-1401	16°07'N, 71°02'W			C3
	Transit 4	1500	1401-1424	16°10'N, 71°08'W			C3
	Transit 5	1500	1425-1443	16°12'N, 71°15'W			C4
	Transit 6	1500	1500-1517	16°17'N, 71°26'W			C4
	Transit 7	1500	1517-1535	16°19'N, 71°31'W			C5
	Transit 8	1500	1535-1551	16°21'N, 71°36'W			C5
	Transit 9	1500-300	1551-1609	16°23'N, 71°42'W			C6
	Transit 10	1500	1631-1635	16°27'N, 71°53'W			C6
	Transit 11	1500	1707-1720	16°32'N, 72°06'W			C7
	Departure	1600-4700	1751-1800	16°36'N, 72°21'W			C7
C-130, Aug. 5	Approach A	1700-4500	1026-1041	15°55'N, 69°59'W		3	C8
	Approach B	4500-3100	1041-1113	15°55'N, 70°07'W	2	2,3	C9
	Approach C	3000	1113-1120	15°55'N, 70°13'W	2	2,3	C10
	Approach D	3000	1120-1133	15°56'N, 70°17'W	2,4	2,3	C11
	Transit 1	3000	1205-1238	15°59'N, 70°34'W	4,1	2,3	C12
	Transit 2	3000	1319-1331	16°04'N, 70°54'W	4	8	C13
	Transit 3	2900	1402-1415	16°09'N, 71°07'W	4,1	8	C14
	Transit 4	2900	1415-1434	16°11'N, 71°12'W	1	8	C15
	Transit 5	2900	1434-1450	16°13'N, 71°17'W	1	8	C16
	Transit 6	2900	1450-1503	16°15'N, 71°22'W	1	2,8	C17
	Departure A	3000-4300	1616-1630	16°26'N, 71°49'W	2	2	C18
	Departure B	4300-6100	1630-1637	16°27'N, 71°53'W	2	2,3	C19
	Departure C	6100	1637-1659	16°29'N, 71°58'W	2	2,3	C20
	Departure D	6100-1800	1659-1724	16°32'N, 72°06'W	2	2,3	C21
	Departure E	1800-500	1724-1738	16°34'N, 72°13'W		2	C22
P-3, Aug. 8	Transit 1	1500	2143-2150	24°20'N, 92°38'W			C23
	Transit 2	1500	2257-2319	24°24'N, 92°38'W			C23
	Transit 3	1500	2319-2339	24°25'N, 92°51'W			C24
C-130, Aug. 8	Approach A	4600-5900	1640-1703	23°55'N, 91°27'W		2	C25
	Approach B	5900	1703-1729	23°58'N, 91°33'W		2,3	C25
	Approach C	5900	1729-1751	24°01'N, 91°39'W	4	2	C26
	Approach D	5800	1751-1817	24°04'N, 91°46'W	4	2,3	C27
	Approach E	5800	1817-1845	24°07'N, 91°53'W	4	2,3	C28
	Approach F	5700-3700	1845-1850	24°09'N, 91°57'W	4	2	C29
	Transit 1	3300	1954-1957	24°14'N, 92°14'W	4	2	C30
	Departure A	3600-5600	2330-2350	24°26'N, 92°52'W	4	2,3	C31
	Departure B	5600-6800	2350-2414	24°27'N, 92°53'W	4	2,3	C32
	Departure C	6800-6200	2414-2439	24°29'N, 92°53'W	4	2	C33
	Departure D	6200-1900	2439-2449	24°31'N, 92°53'W		2,8	C34

[a]See text for description of frequency numbers.
[b]See table 2 for description of modes.

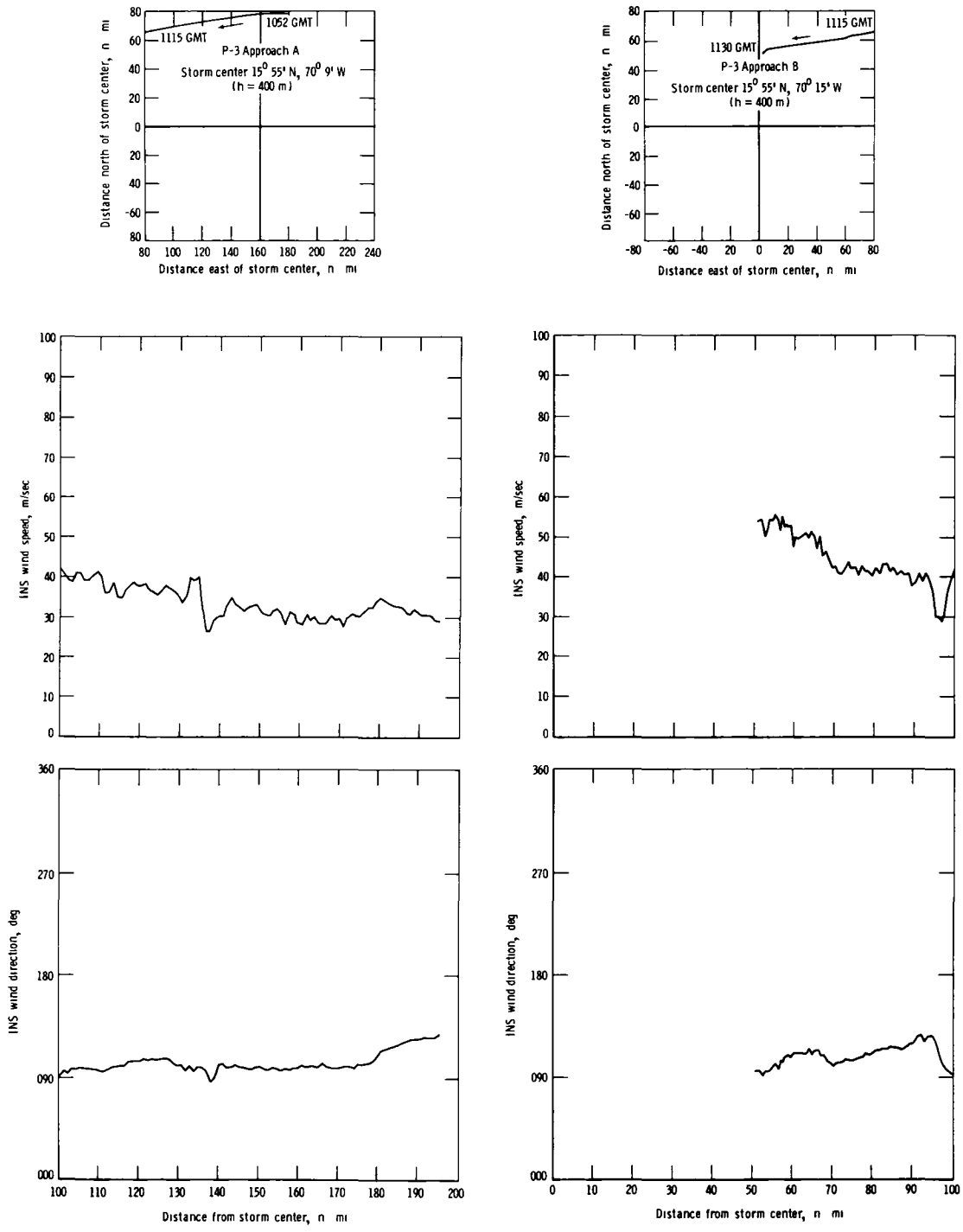

Figure C1.- Flight track, INS wind speed, and INS wind direction for P-3 approaches A and B, August 5, 1980.

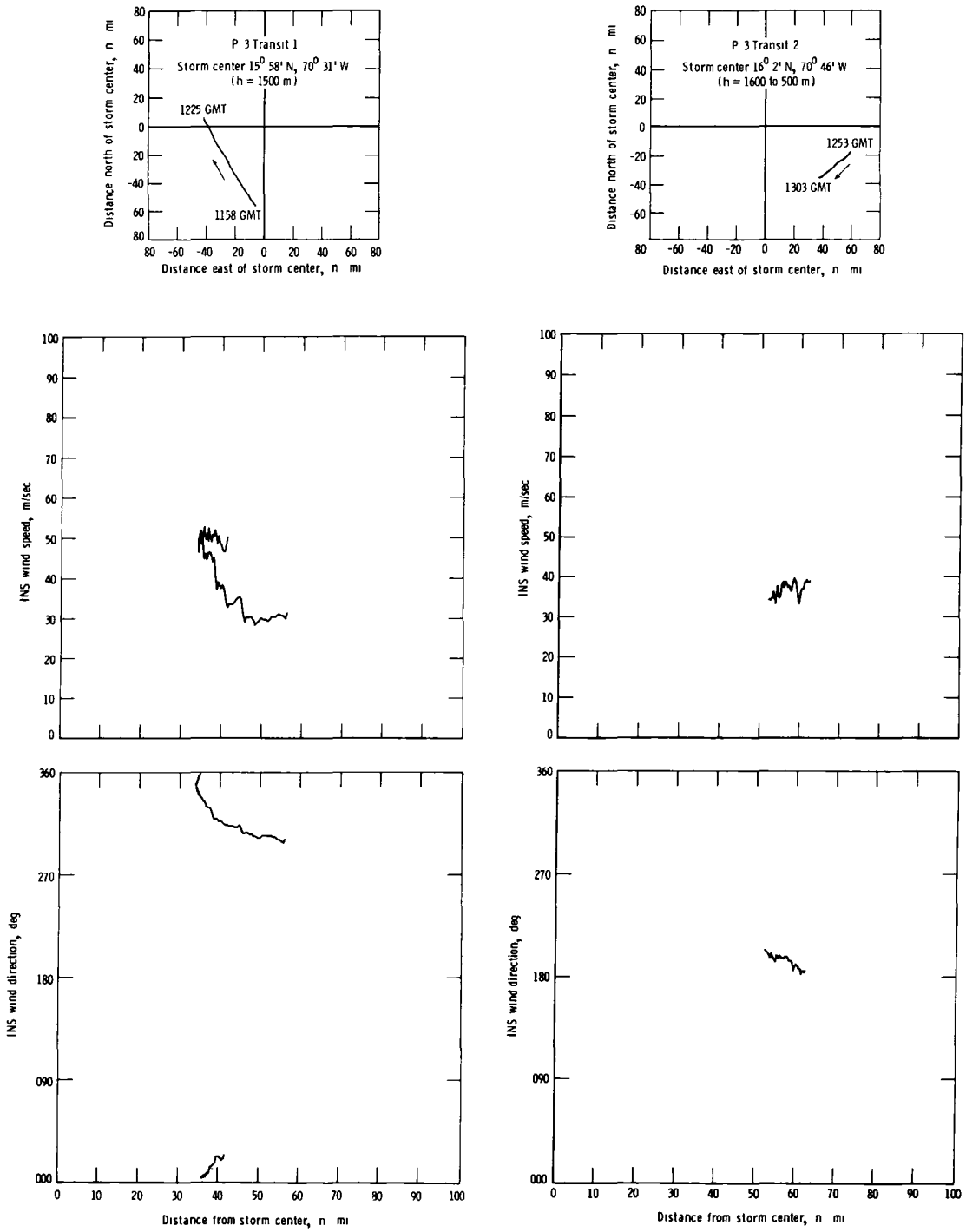

Figure C2.- Flight track, INS wind speed, and INS wind direction for P-3 transits I and II, August 5, 1980.

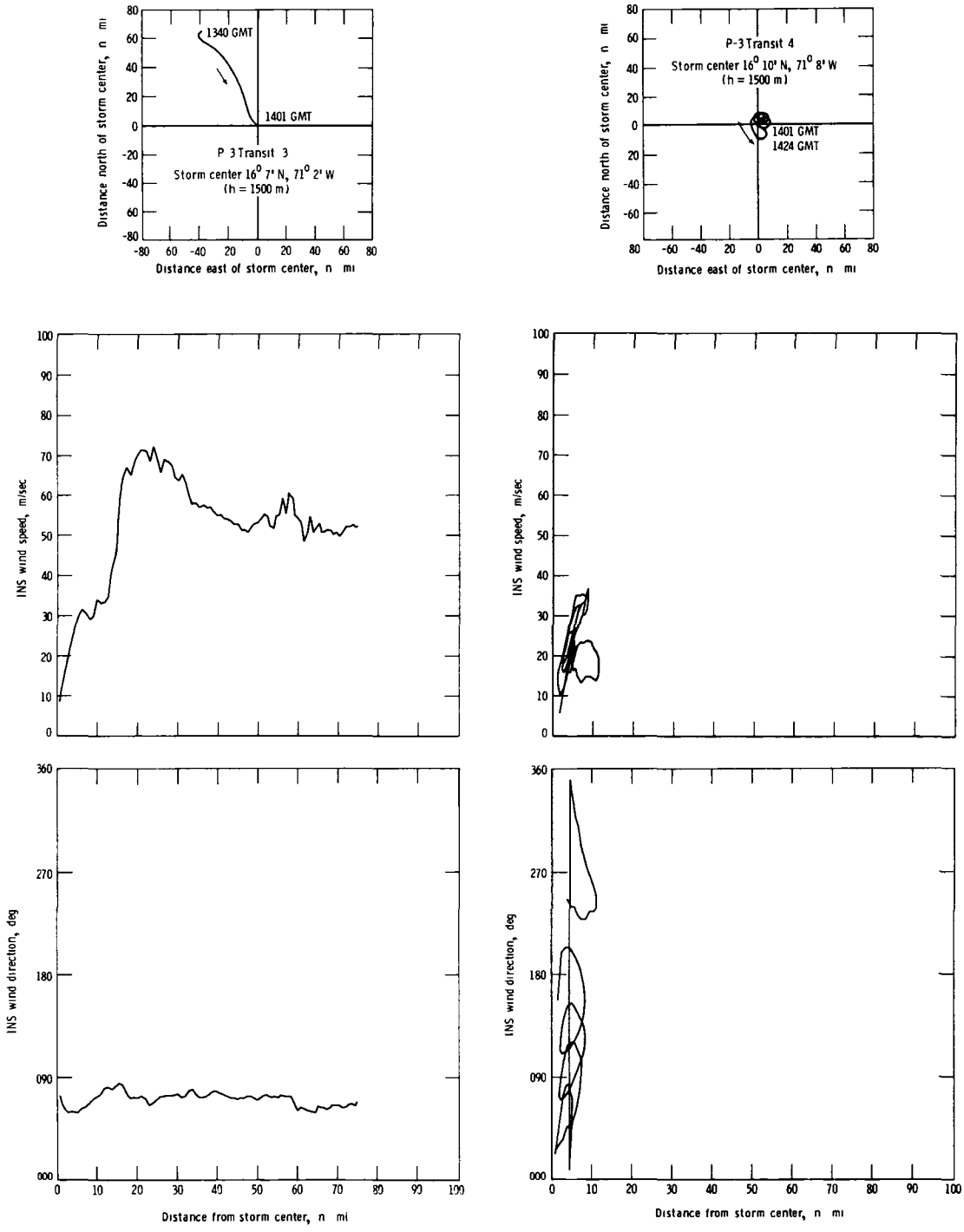

Figure C3.- Flight track, INS wind speed, and INS wind direction for P-3 transits III and IV, August 5, 1980.

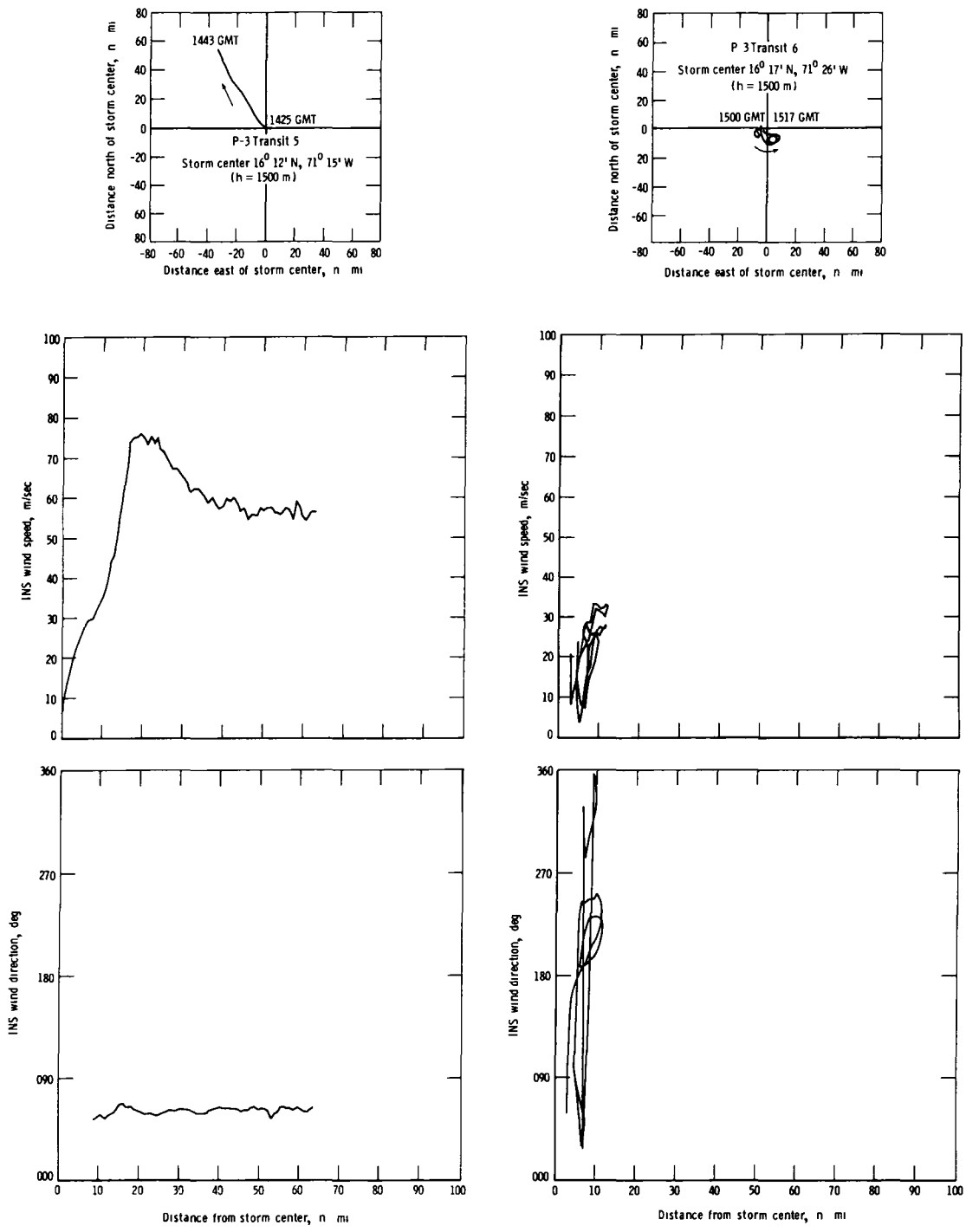

Figure C4.- Flight track, INS wind speed, and INS wind direction for P-3 transits V and VI, August 5, 1980.

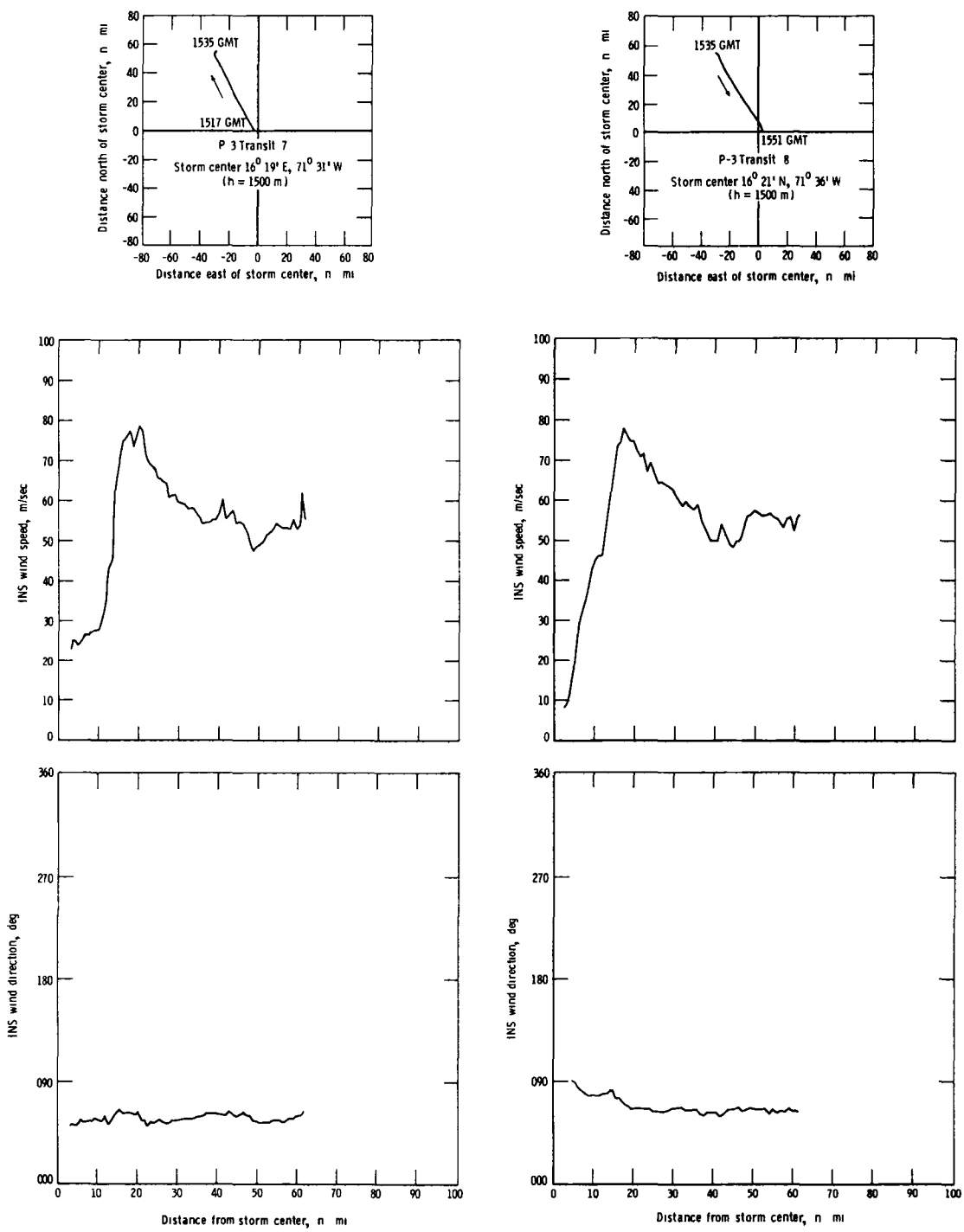

Figure C5.- Flight track, INS wind speed, and INS wind direction for P-3 transits VII and VIII, August 5, 1980.

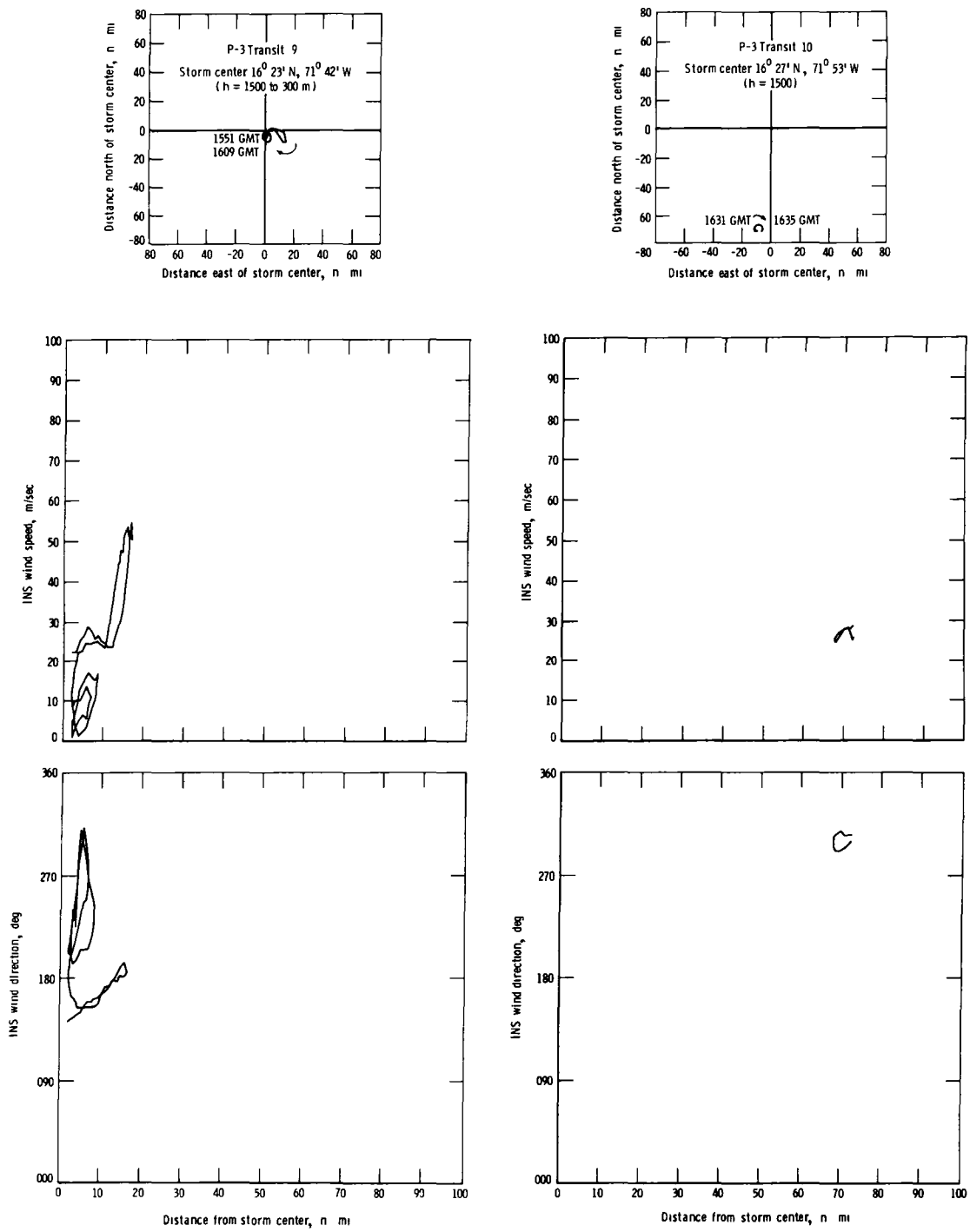

Figure C6.- Flight track, INS wind speed, and INS wind direction for P-3 transits IX and X, August 5, 1980.

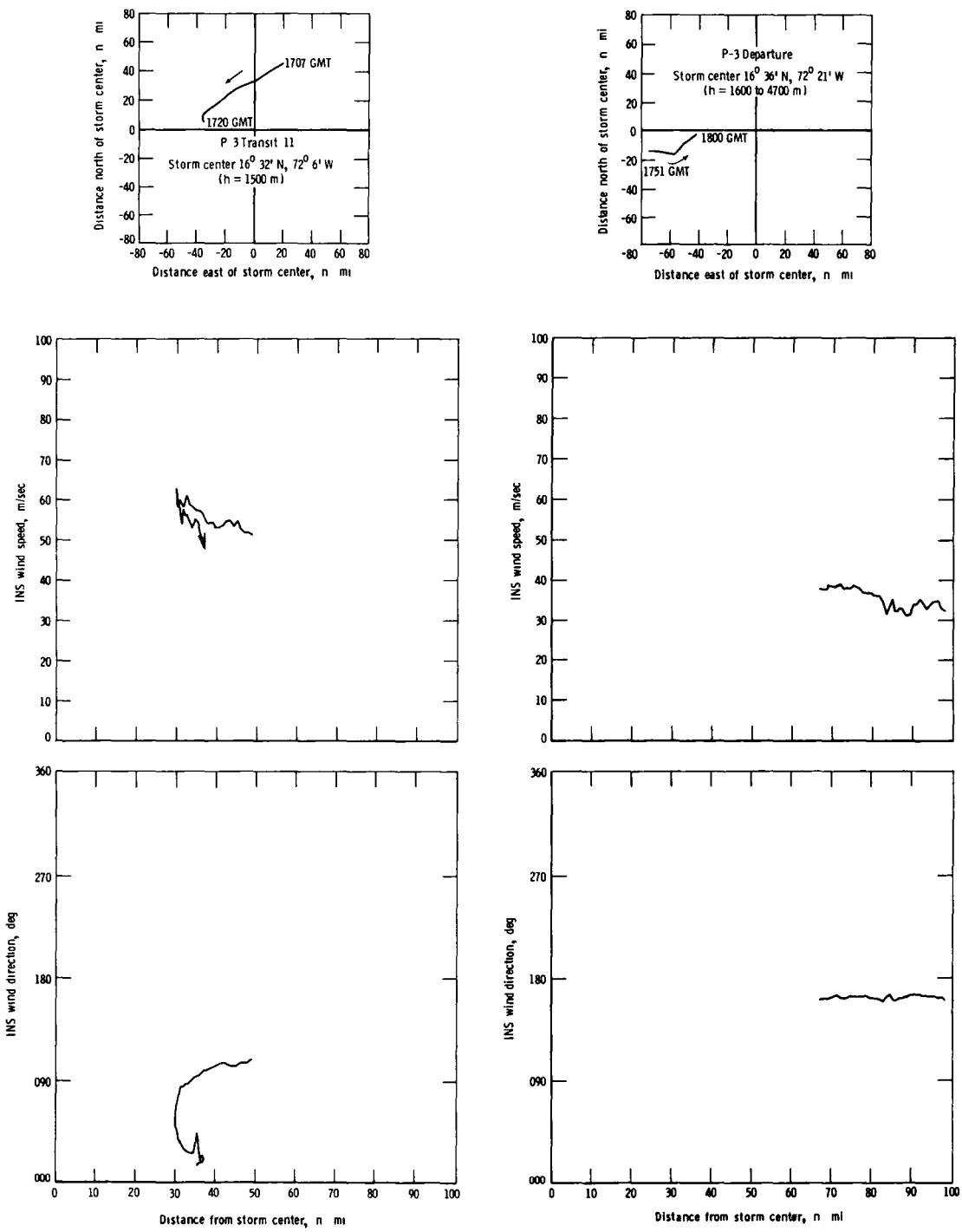

Figure C7.- Flight track, INS wind speed, and INS wind direction for P-3 transits XI and departure, August 5, 1980.

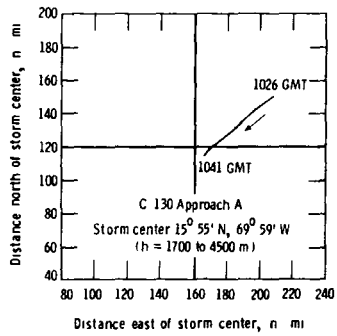

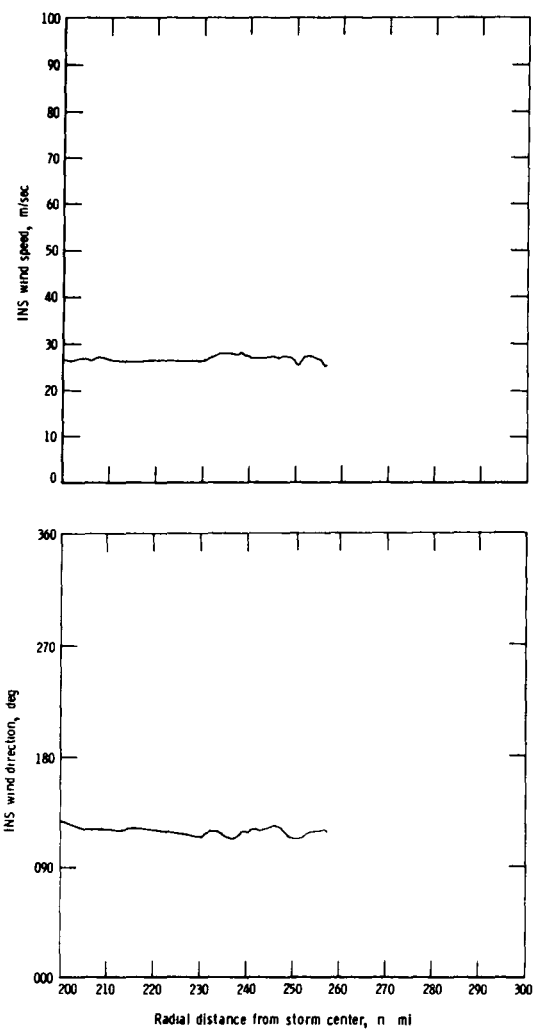

Figure C8.- Flight track, INS wind speed, and INS wind direction for C-130 approach A, August 5, 1980.

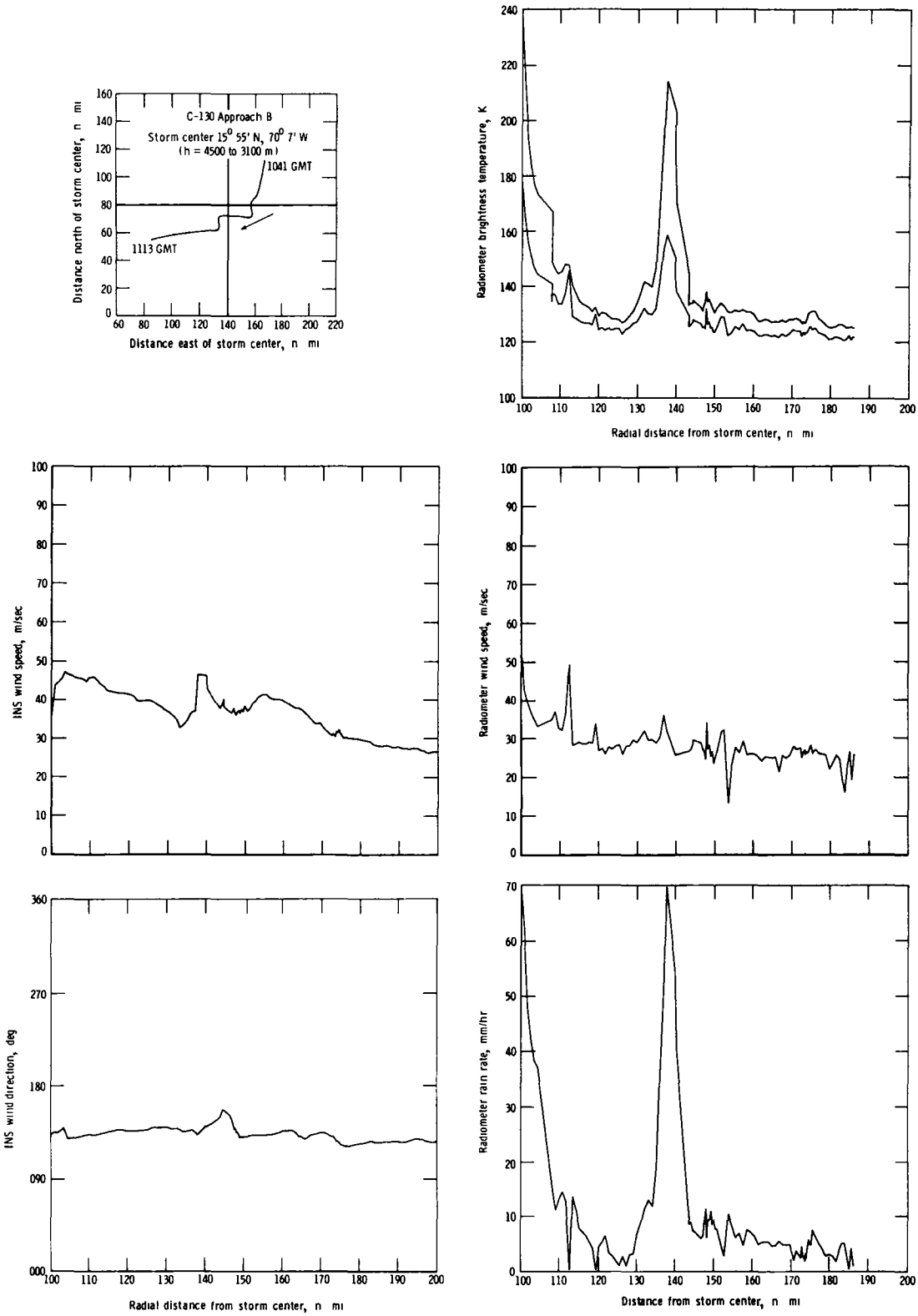

Figure C9.- Flight track, INS wind speed, INS wind direction, radiometric brightness temperatures, radiometer wind speed, and radiometer rain rate for C-130 approach B, August 5, 1980.

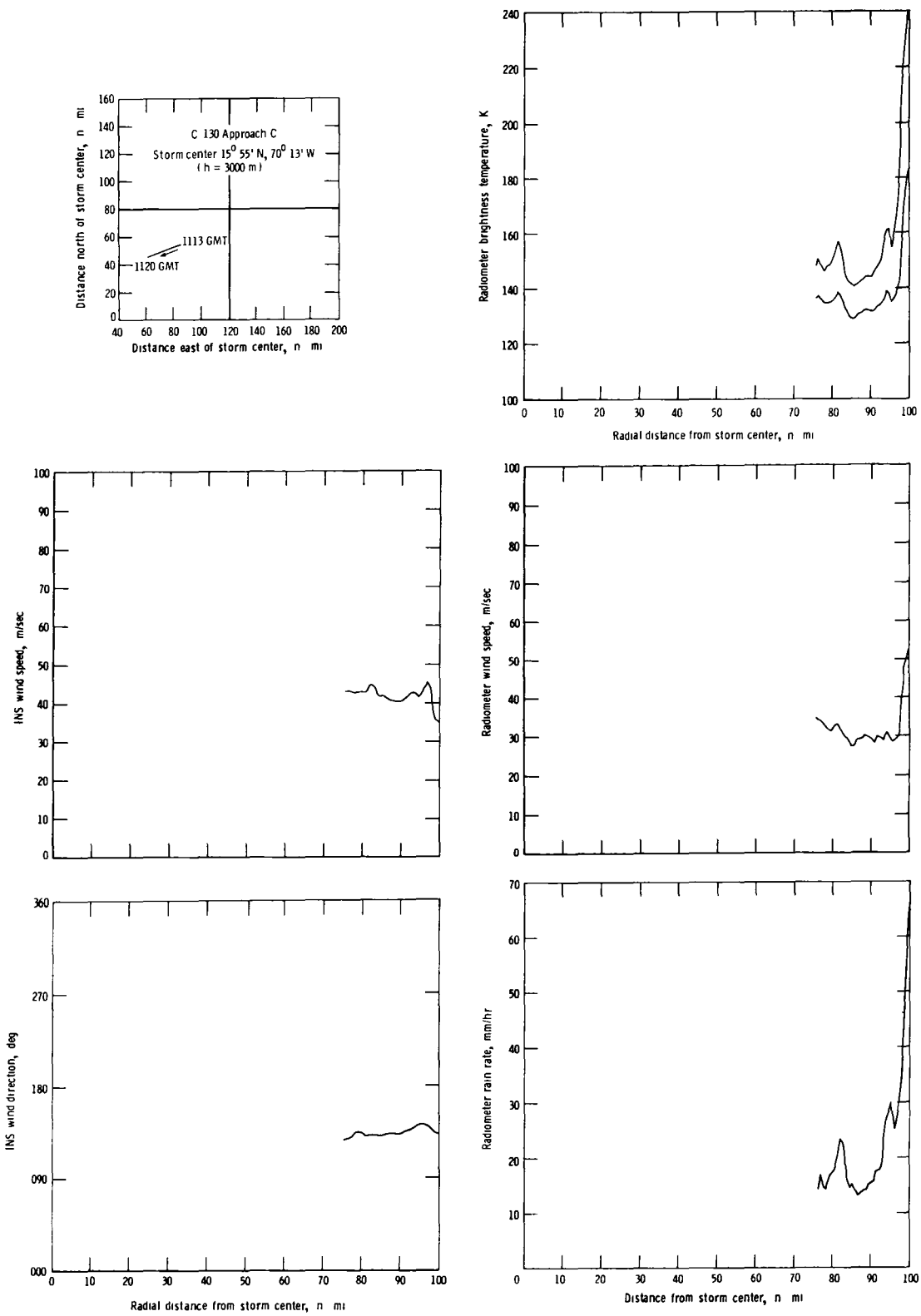

Figure C10.- Flight track, INS wind speed, INS wind direction, radiometric brightness temperatures, radiometer wind speed, and radiometer rain rate for C-130 approach C, August 5, 1980.

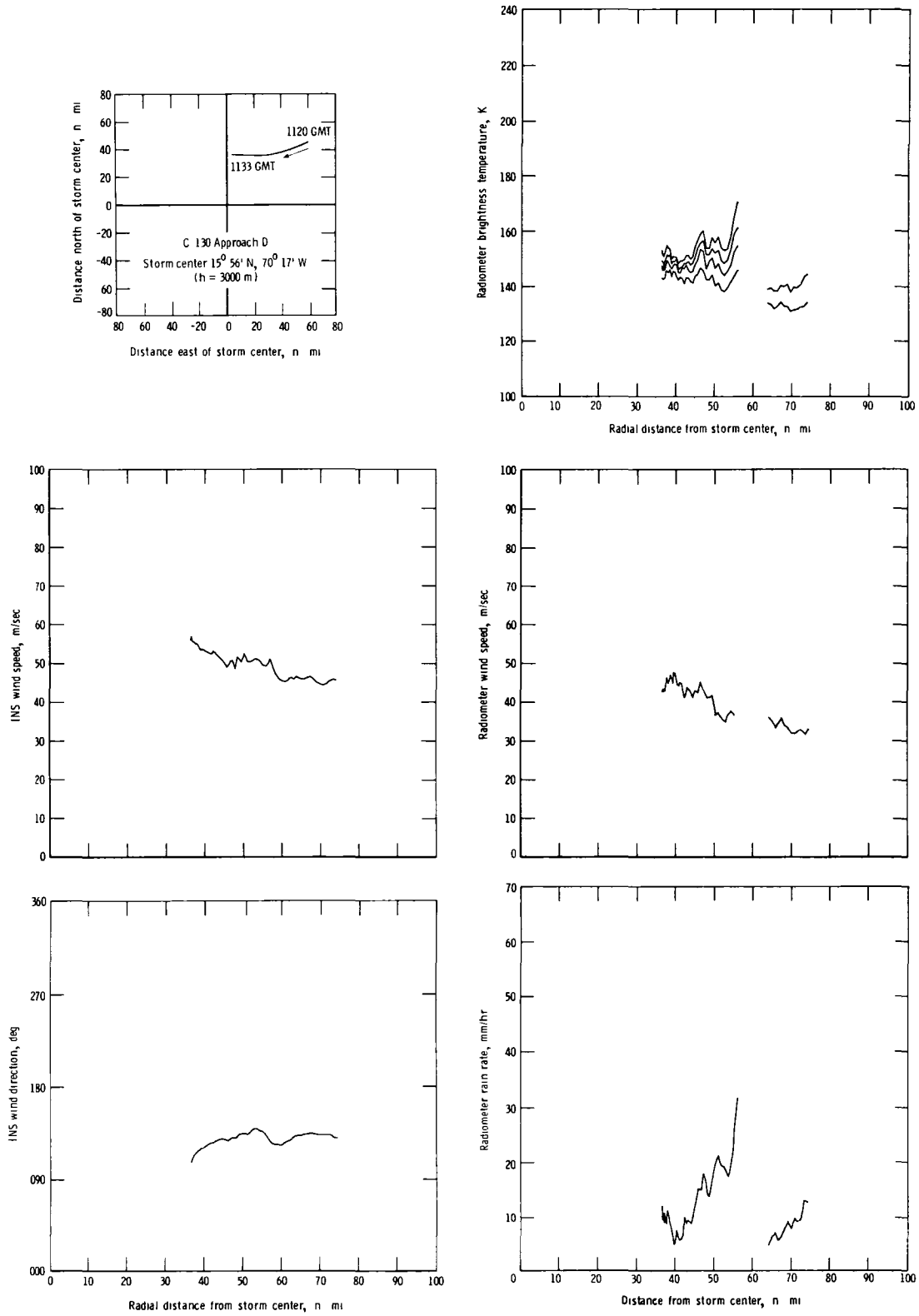

Figure C11.- Flight track, INS wind speed, INS wind direction, radiometric brightness temperatures, radiometer wind speed, and radiometer rain rate for C-130 approach D, August 5, 1980.

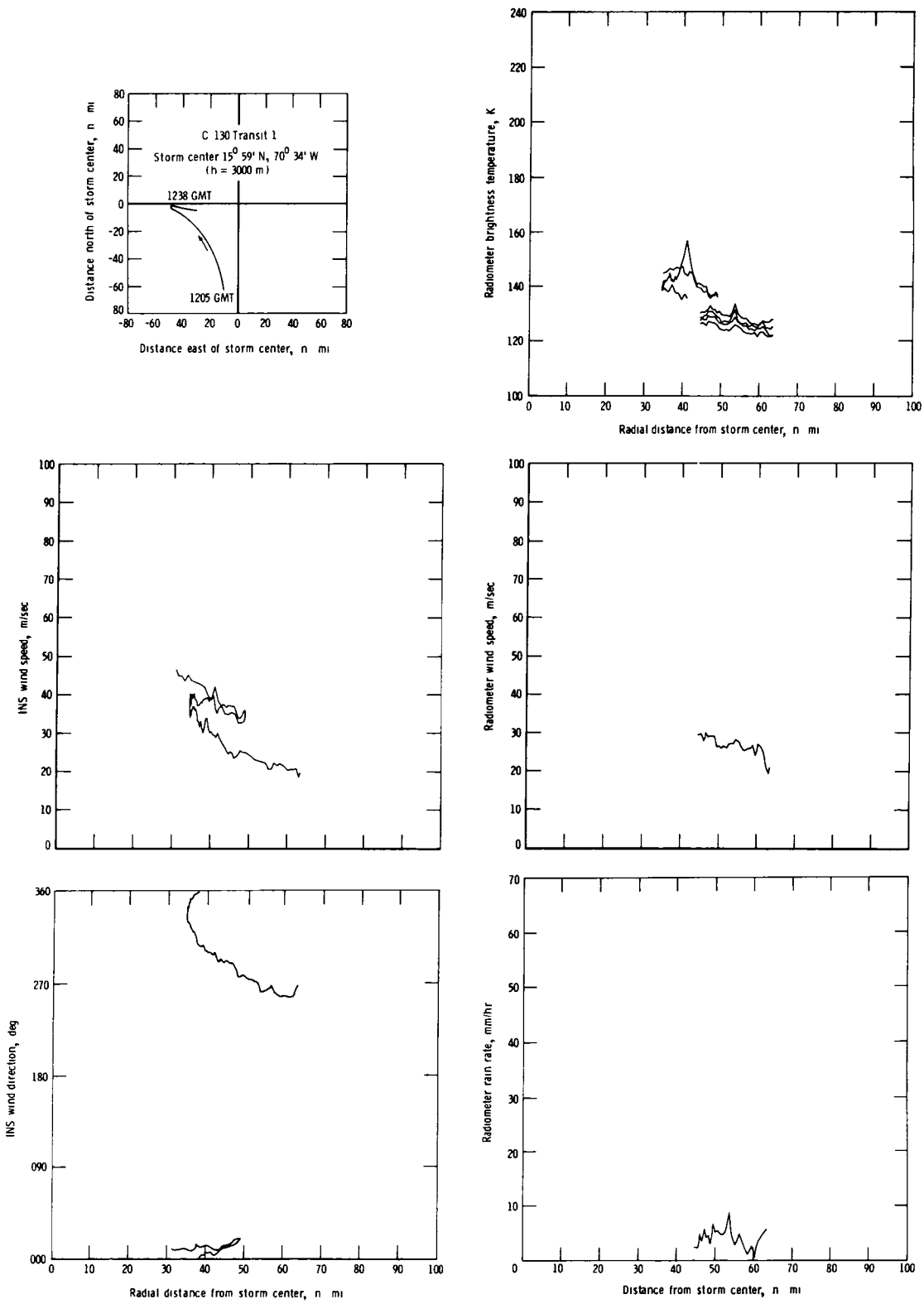

Figure C12.- Flight track, INS wind speed, INS wind direction, radiometric brightness temperatures, radiometer wind speed, and radiometer rain rate for C-130 transit I, August 5, 1980.

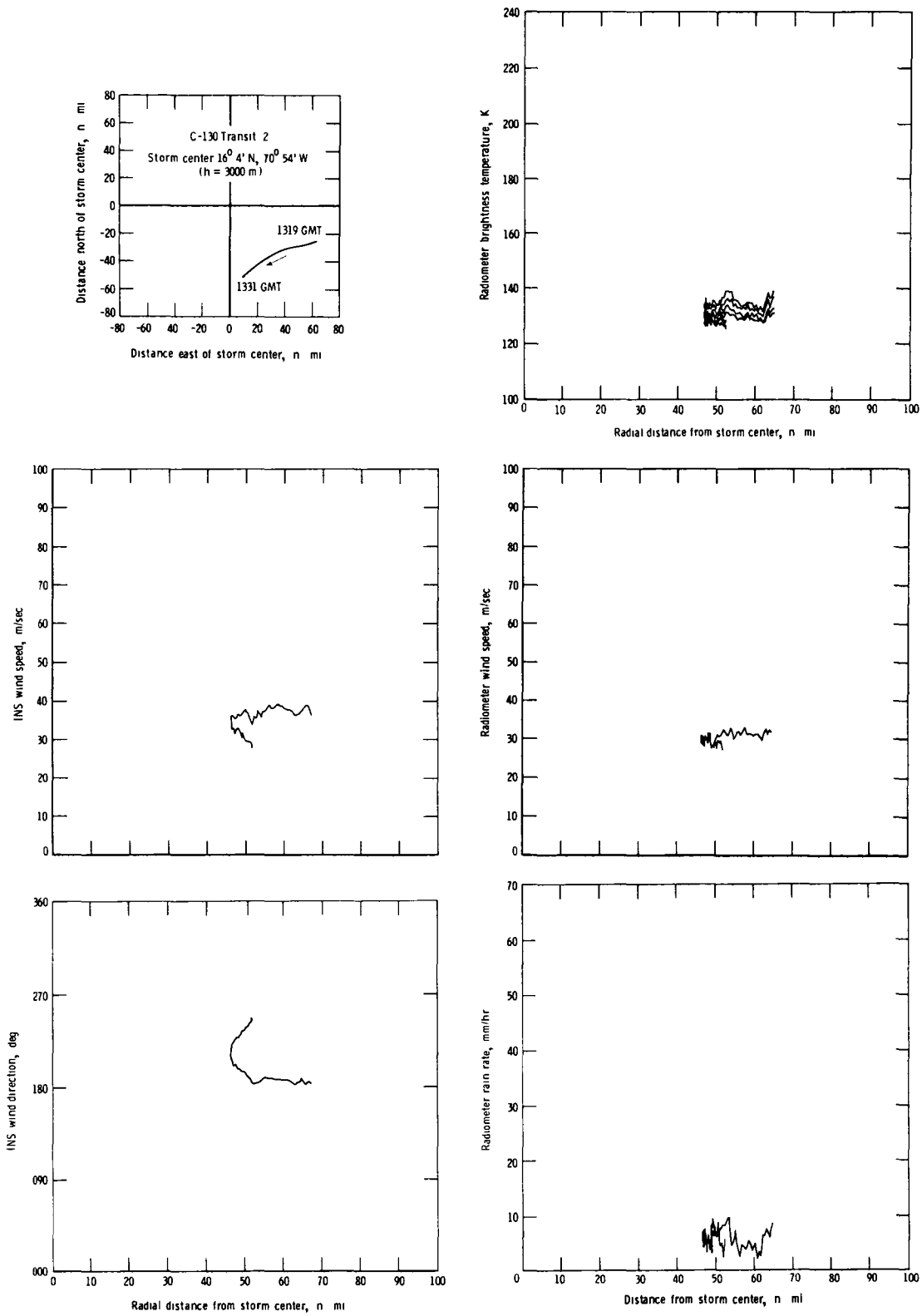

Figure C13.- Flight track, INS wind speed, INS wind direction, radiometric brightness temperatures, radiometer wind speed, and radiometer rain rate for C-130 transit II, August 5, 1980.

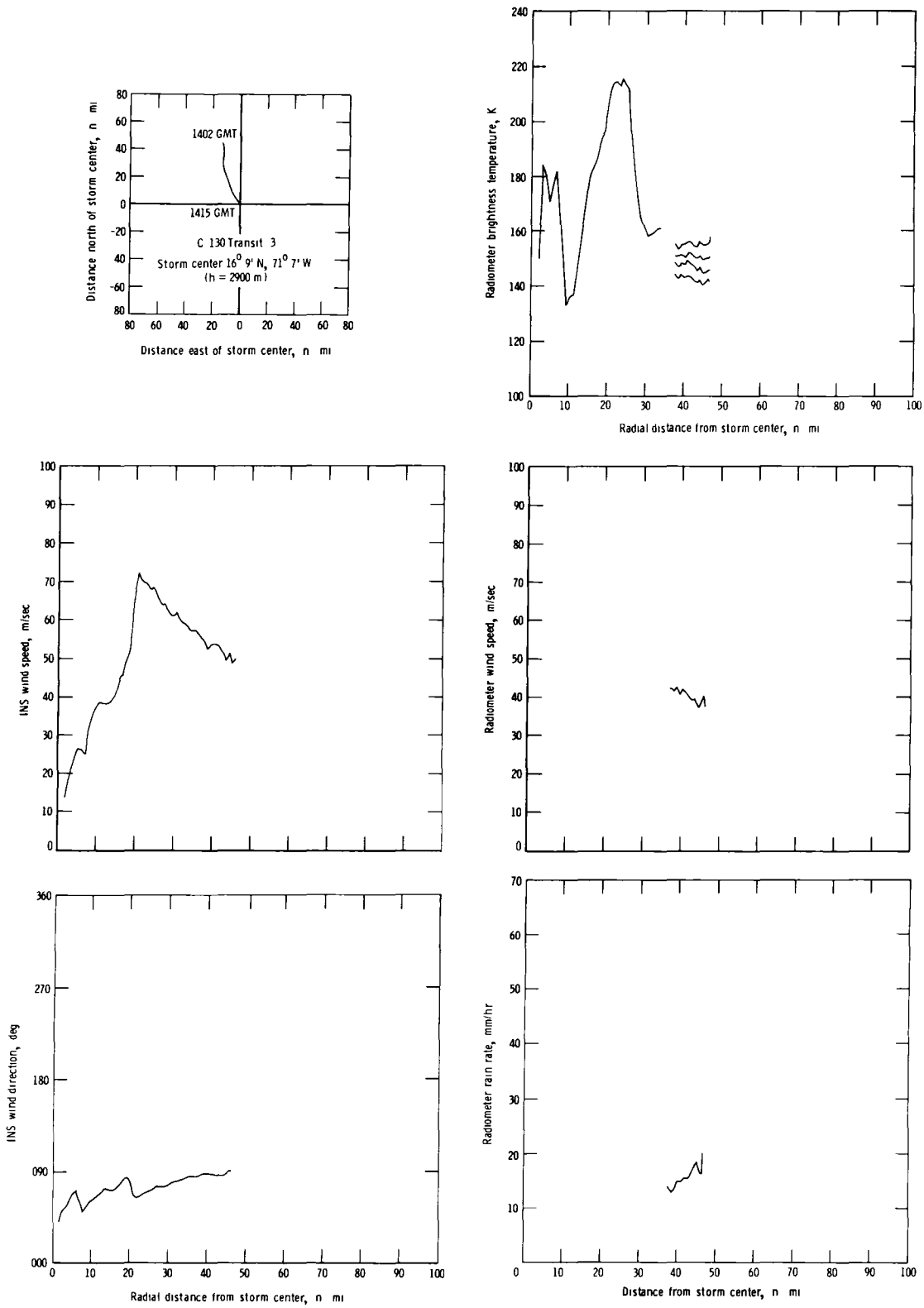

Figure C14.- Flight track, INS wind speed, INS wind direction, radiometric brightness temperatures, radiometer wind speed, and radiometer rain rate for C-130 transit III, August 5, 1980.

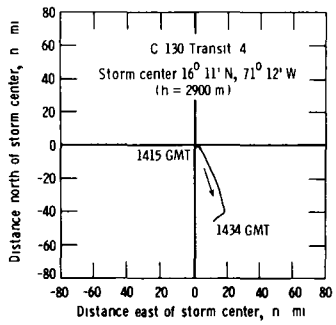

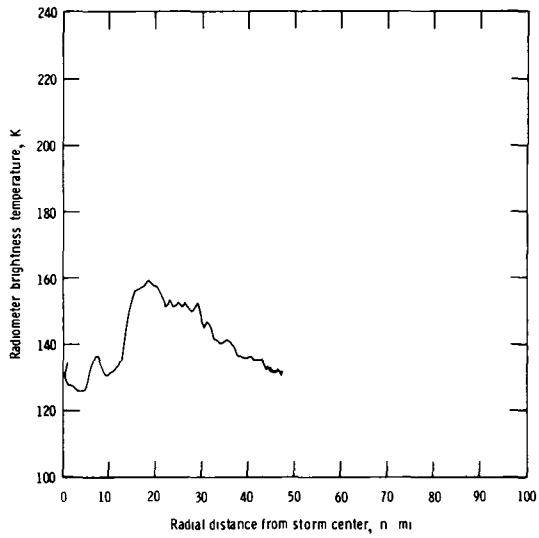

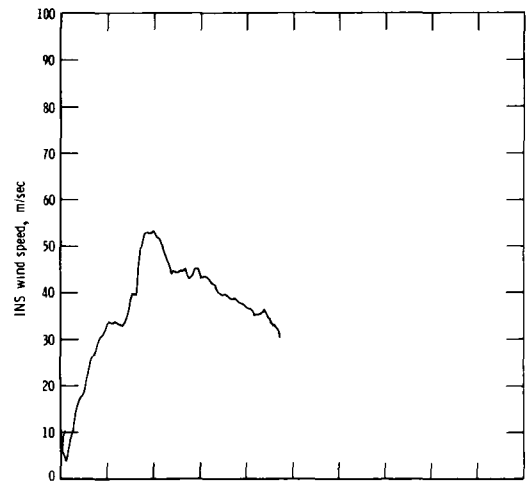

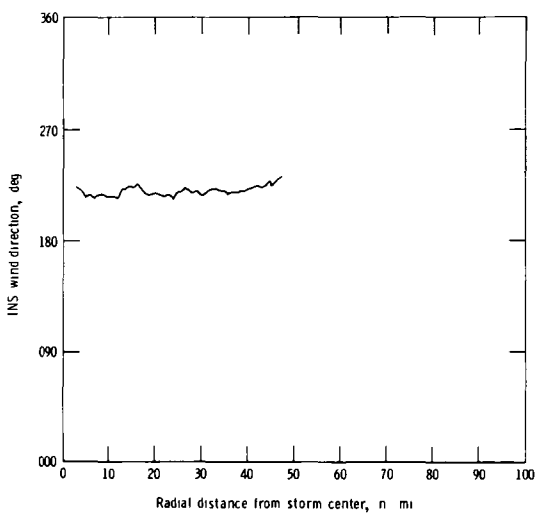

Figure C15.- Flight track, INS wind speed, INS wind direction, and radiometric brightness temperature, for C-130 transit IV, August 5, 1980.

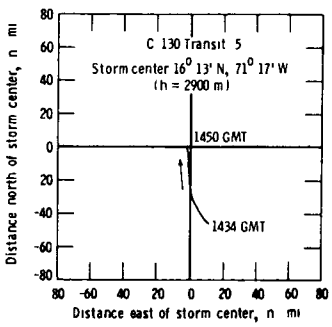

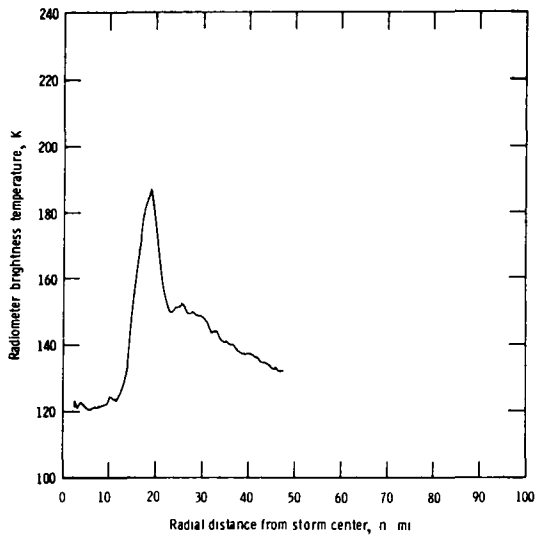

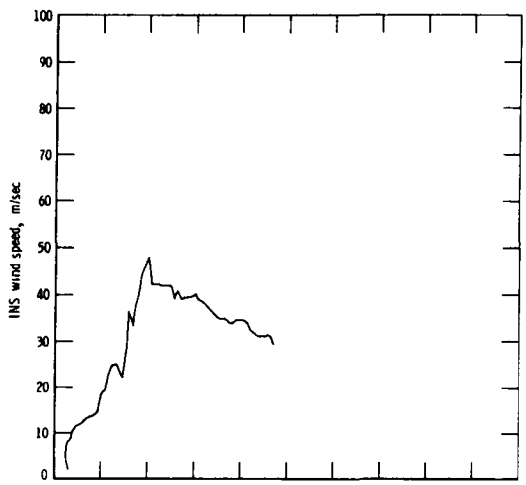

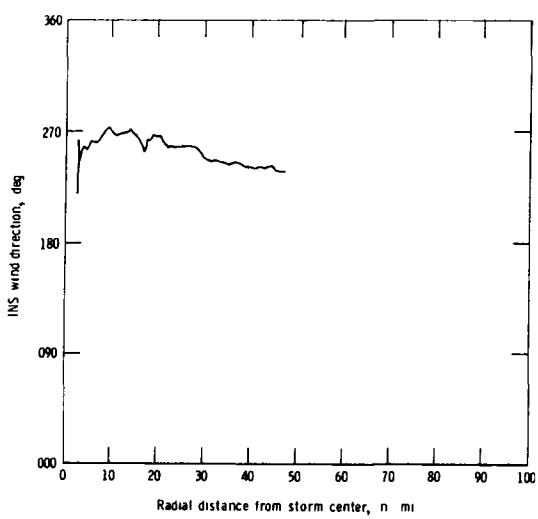

Figure C16.- Flight track, INS wind speed, INS wind direction, and radiometric brightness temperature for C-130 transit V, August 5, 1980.

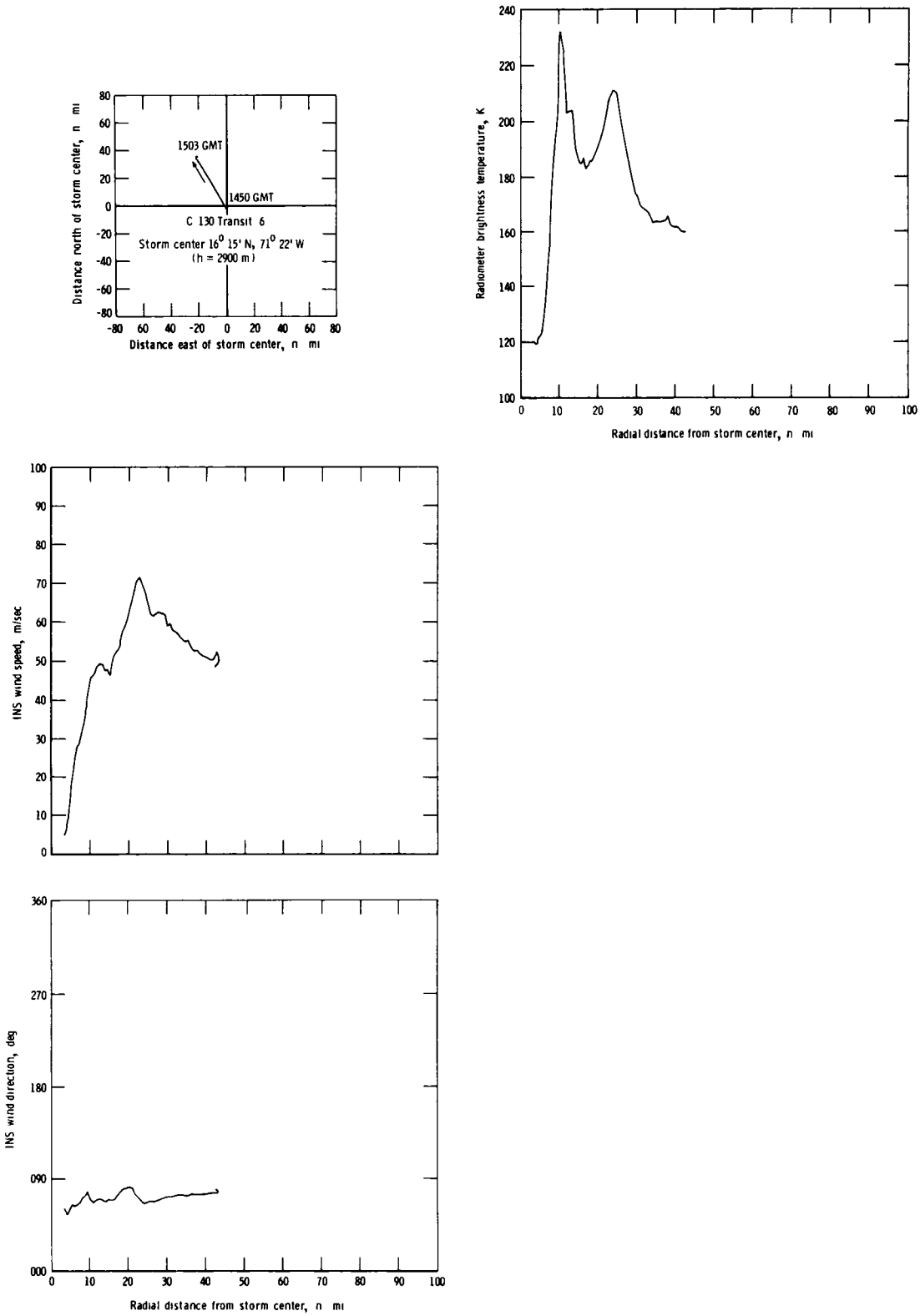

Figure C17.- Flight track, INS wind speed, INS wind direction, and radiometric brightness temperature for C-130 transit VI, August 5, 1980.

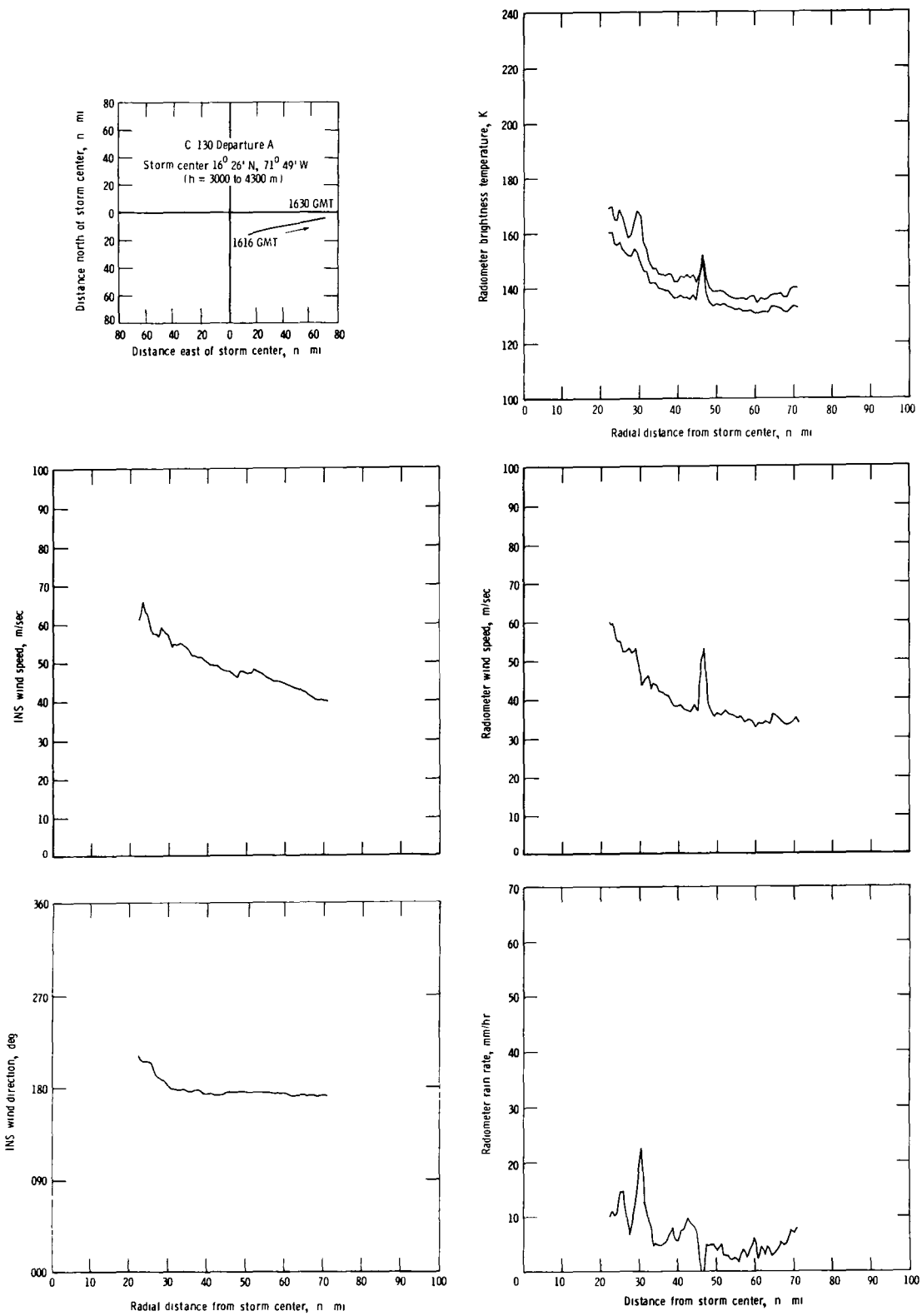

Figure C18.- Flight track, INS wind speed, INS wind direction, radiometric brightness temperatures, radiometer wind speed, and radiometer rain rate for C-130 departure A, August 5, 1980.

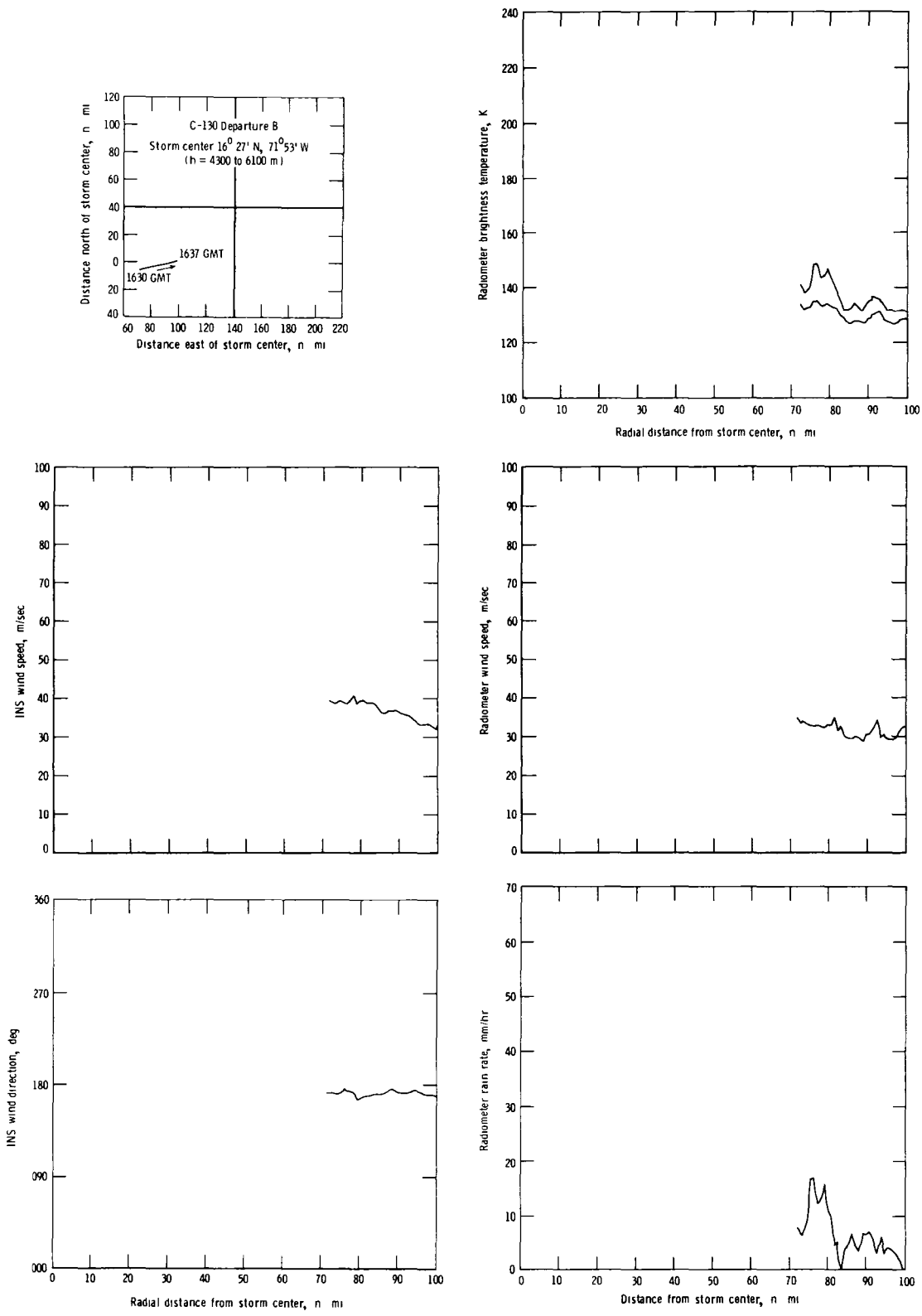

Figure C19.- Flight track, INS wind speed, INS wind direction, radiometric brightness temperatures, radiometer wind speed, and radiometer rain rate for C-130 departure B, August 5, 1980.

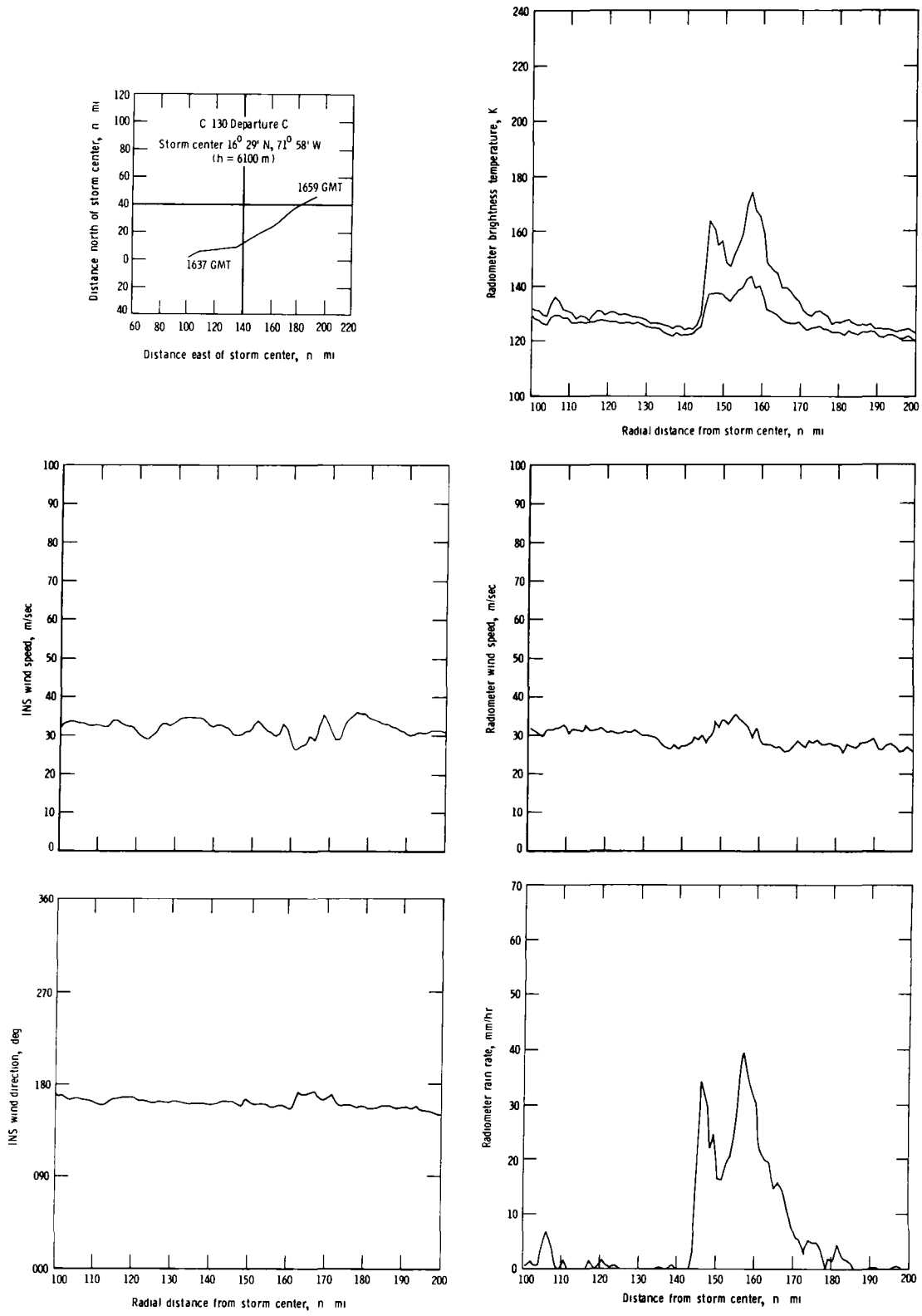

Figure C20.- Flight track, INS wind speed, INS wind direction, radiometric brightness temperatures, radiometer wind speed, and radiometer rain rate for C-130 departure C, August 5, 1980.

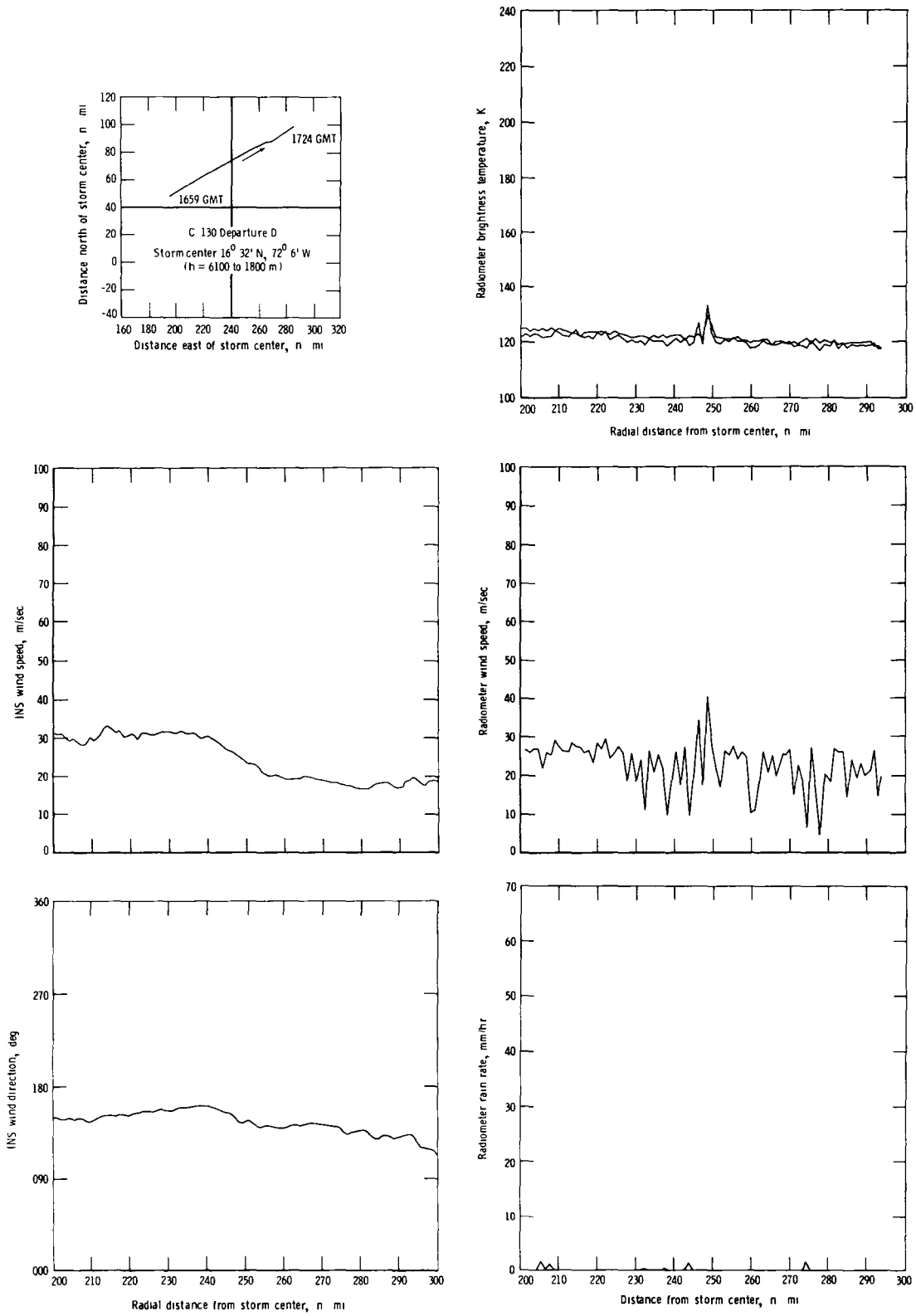

Figure C21.- Flight track, INS wind speed, INS wind direction, radiometric brightness temperatures, radiometer wind speed, and radiometer rain rate for C-130 departure D, August 5, 1980.

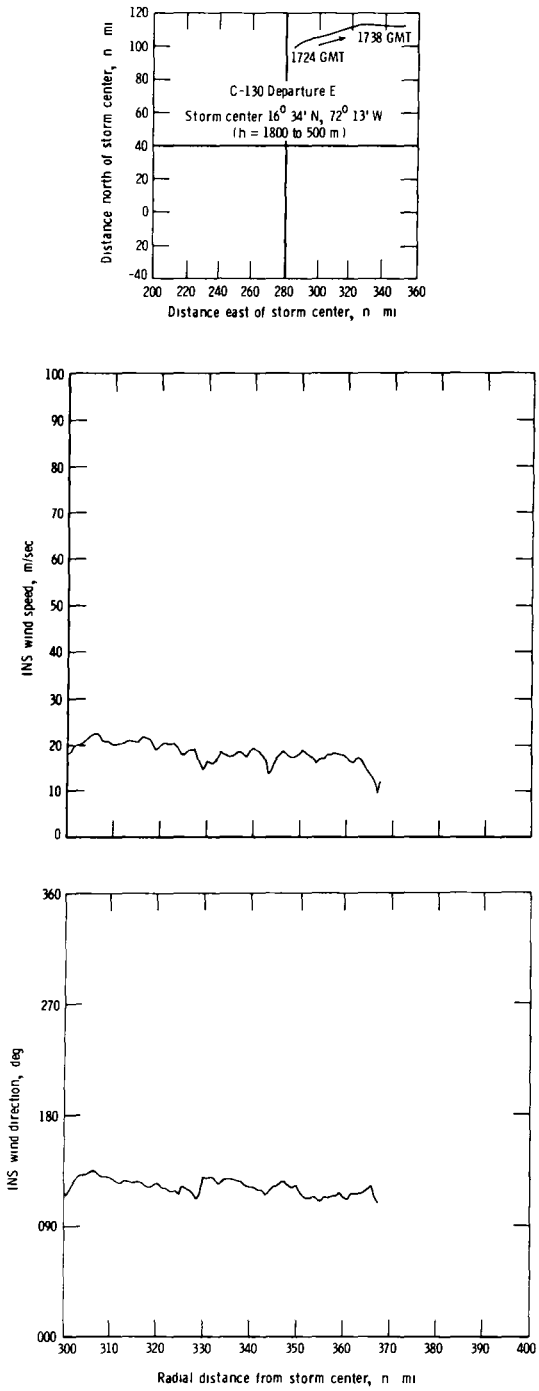

Figure C22.- Flight track, INS wind speed, and INS wind direction for C-130 departure E, August 5, 1980.

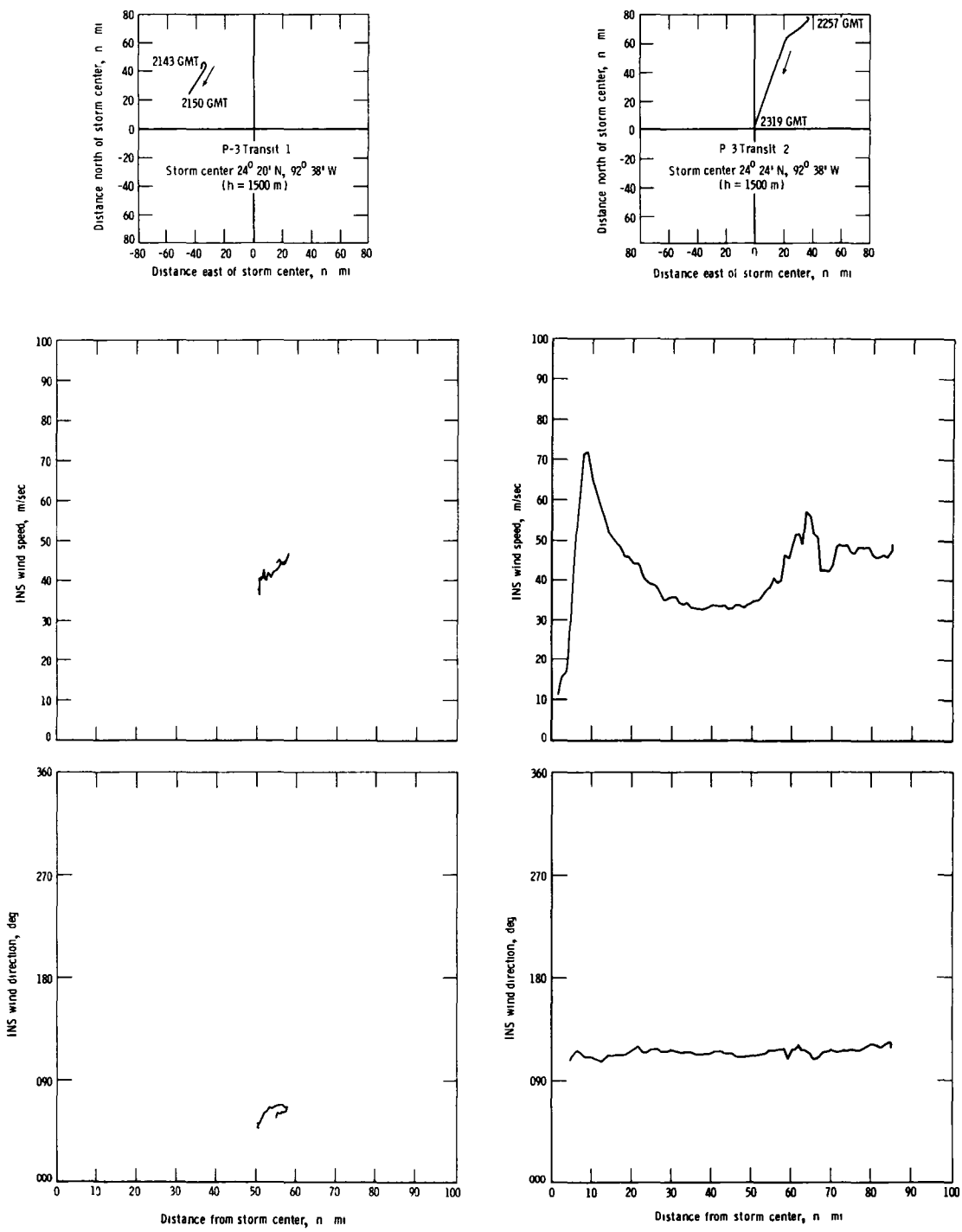

Figure C23.- Flight track, INS wind speed, and INS wind direction for P-3 transits I and II, August 8, 1980.

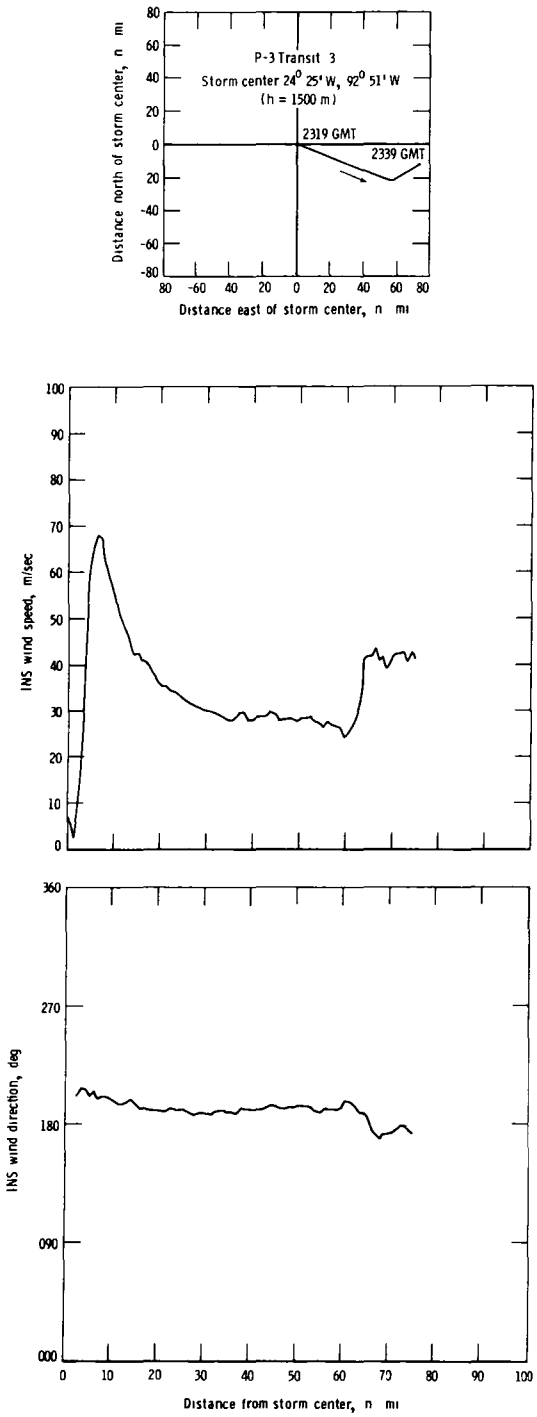

Figure C24.- Flight track, INS wind speed, and INS wind direction for P-3 transit III, August 8, 1980.

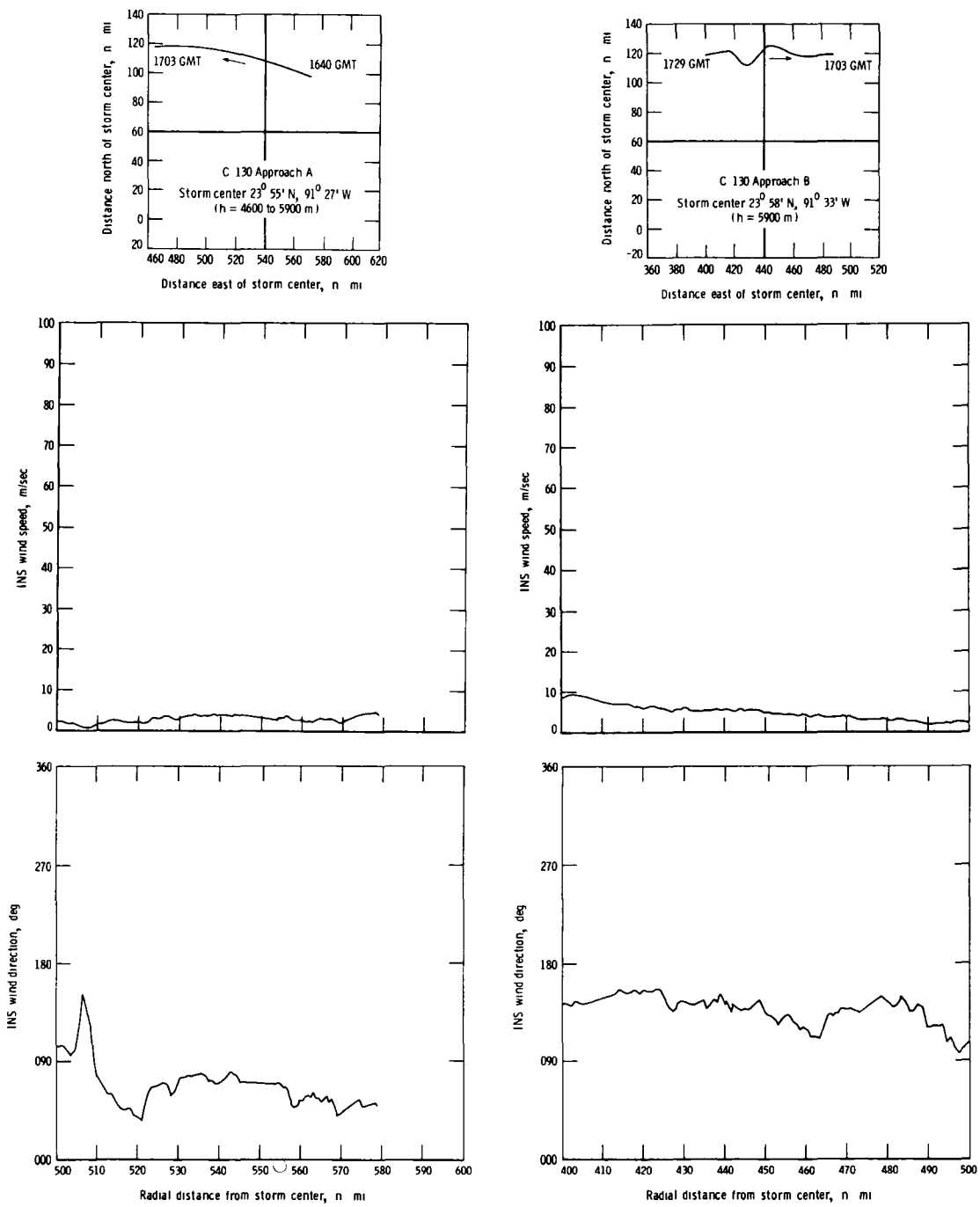

Figure C25.- Flight track, INS wind speed, and INS wind direction for C-130 approaches A and B, August 8, 1980.

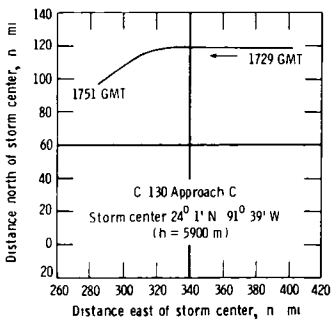

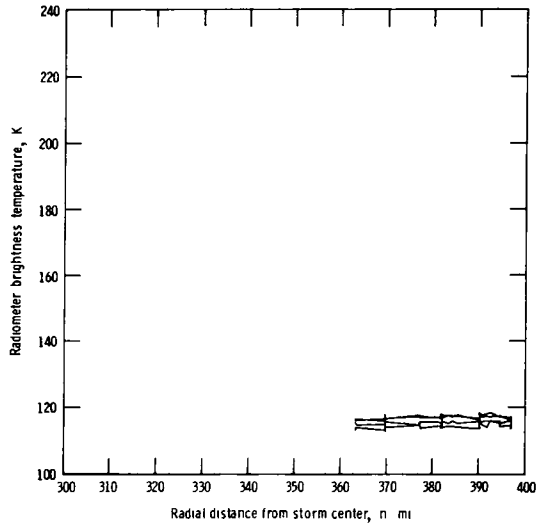

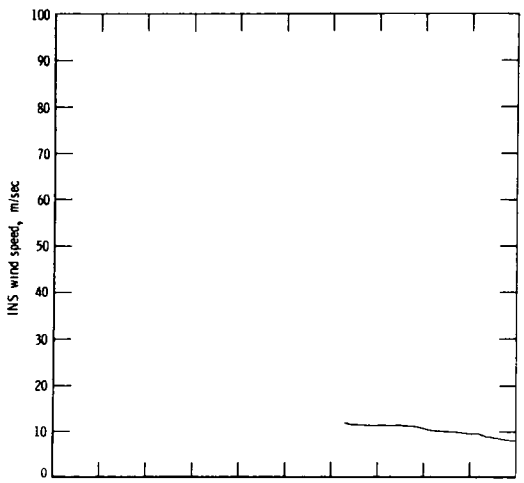

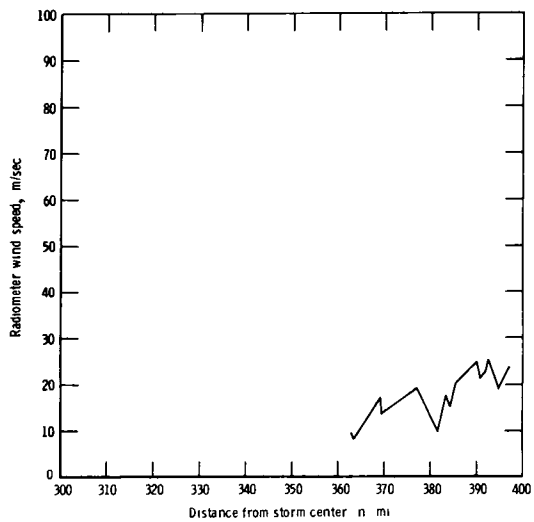

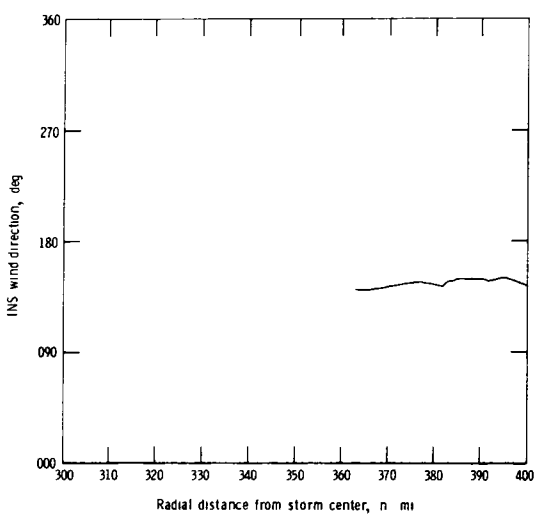

Computed rain rate of zero between 363 and 397 n mi

Figure C26.- Flight track, INS wind speed, INS wind direction, radiometric brightness temperatures, radiometer wind speed, and radiometer rain rate for C-130 approach C, August 8, 1980.

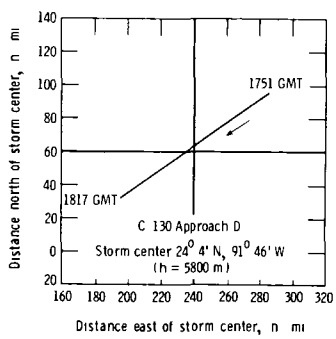

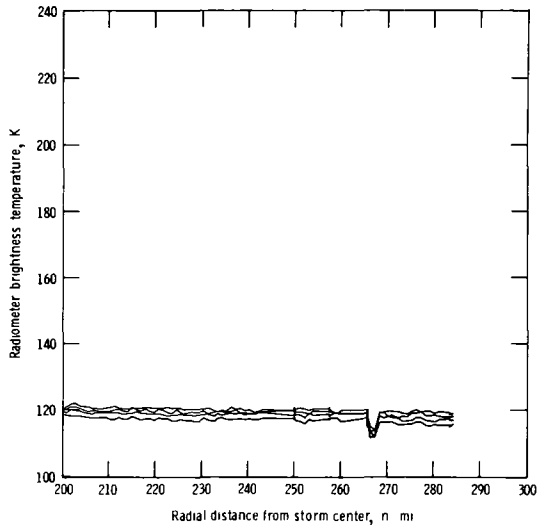

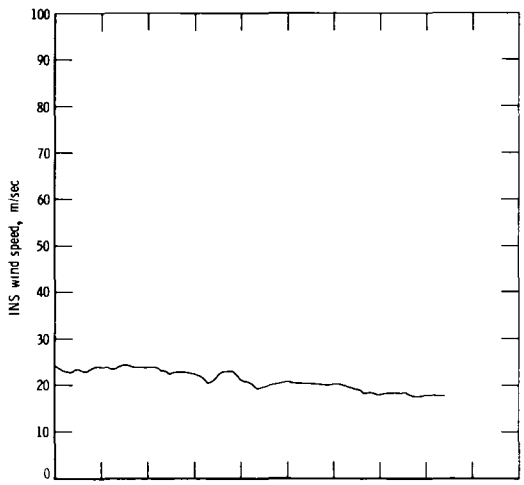

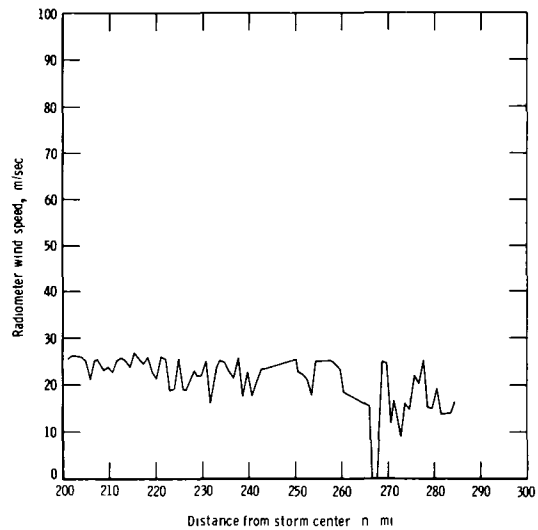

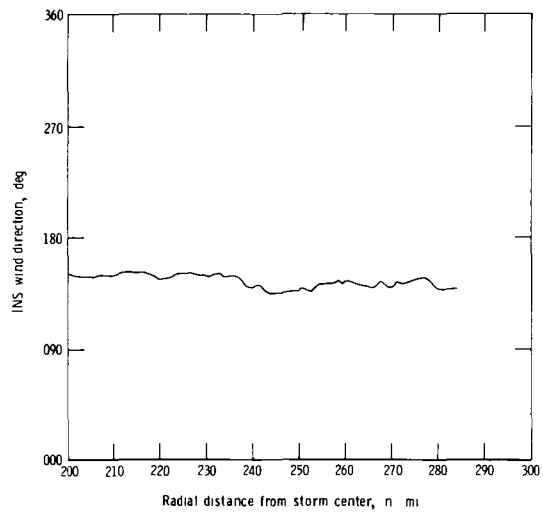

Computed rain rate of zero between 200 and 285 n mi

Figure C27.- Flight track, INS wind speed, INS wind direction, radiometric brightness temperatures, radiometer wind speed, and radiometer rain rate for C-130 approach D, August 8, 1980.

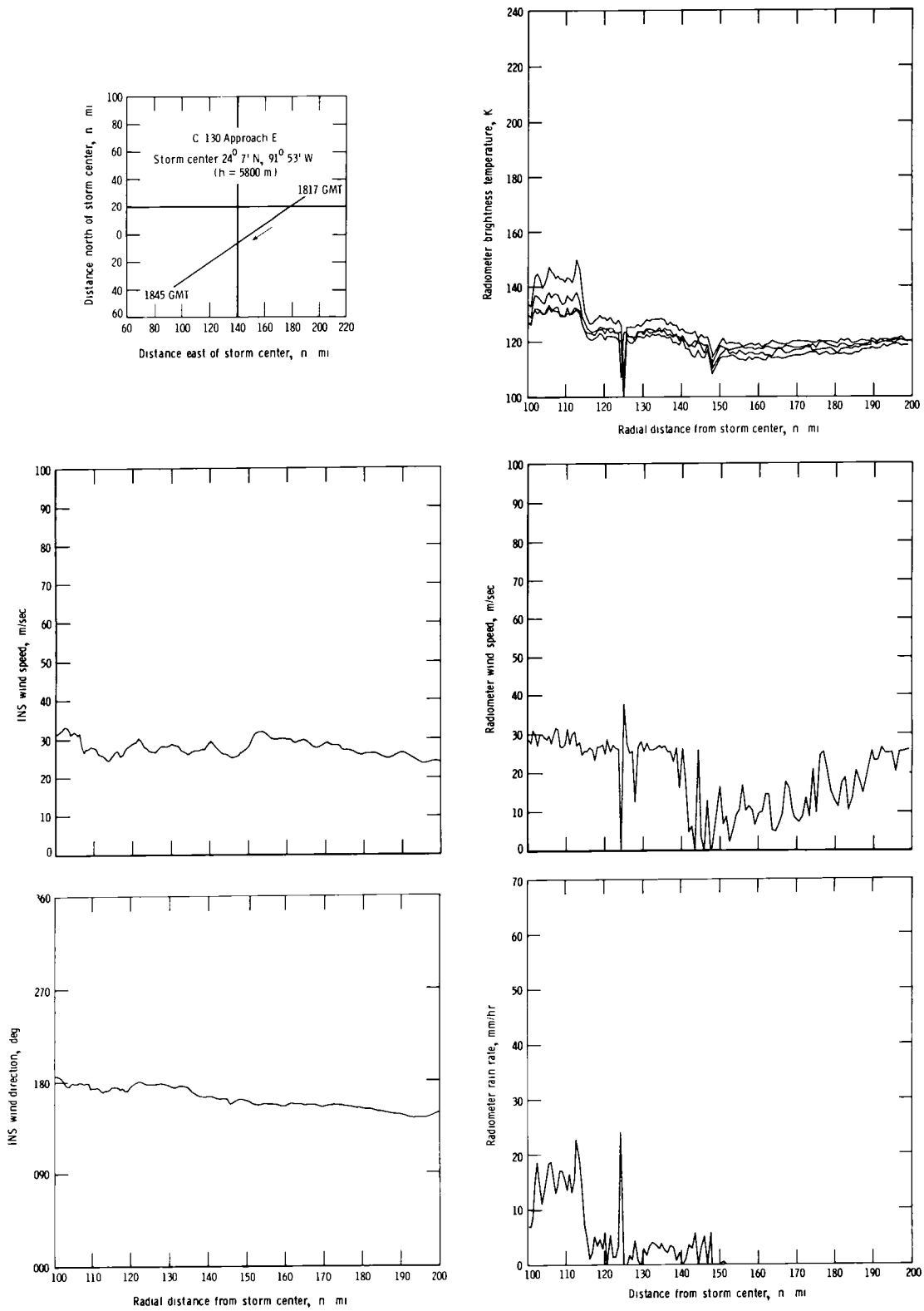

Figure C28.- Flight track, INS wind speed, INS wind direction, radiometric brightness temperatures, radiometer wind speed, and radiometer rain rate for C-130 approach E, August 8, 1980.

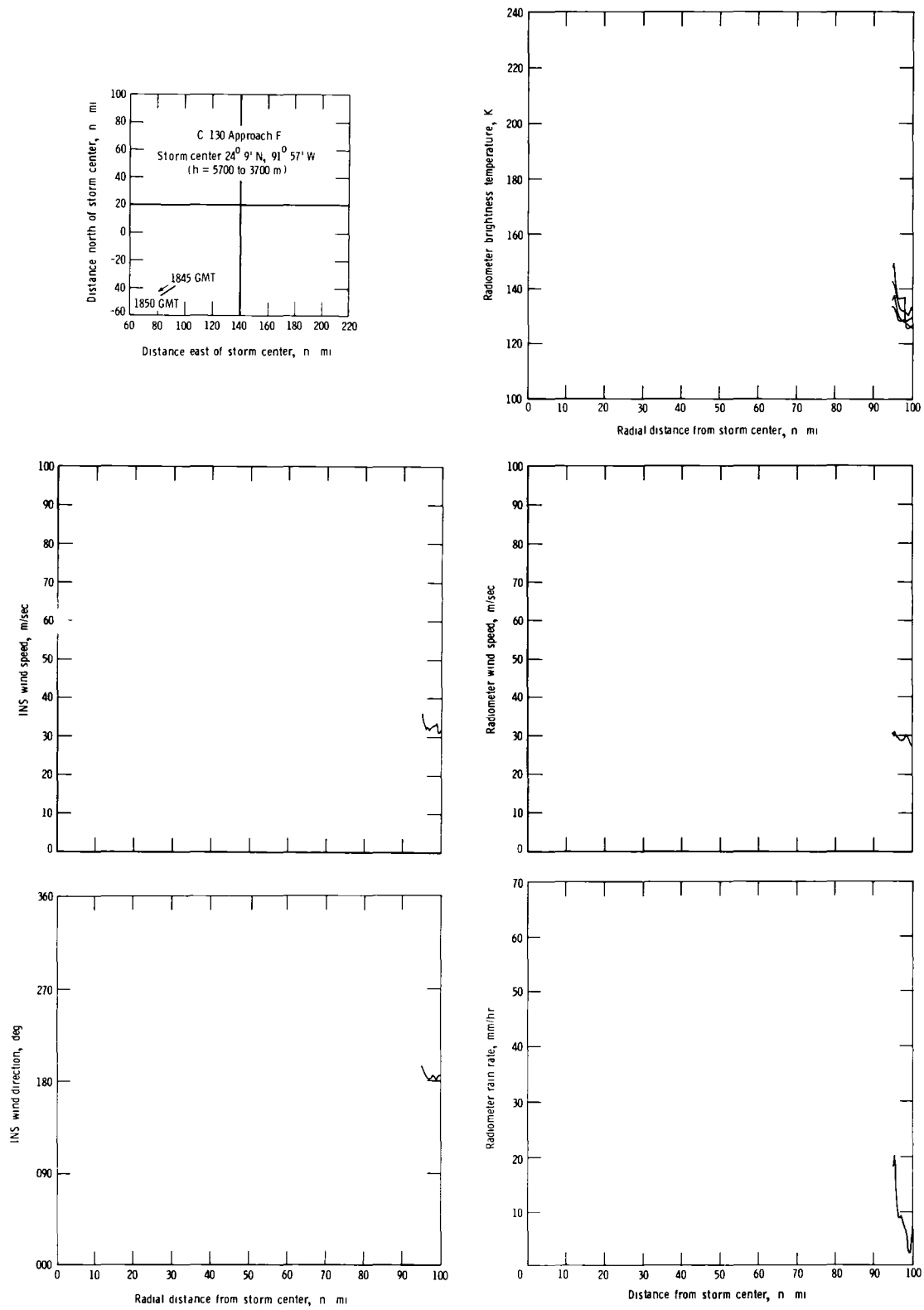

Figure C29.- Flight track, INS wind speed, INS wind direction, radiometric brightness temperatures, radiometer wind speed, and radiometer rain rate for C-130 approach F, August 8, 1980.

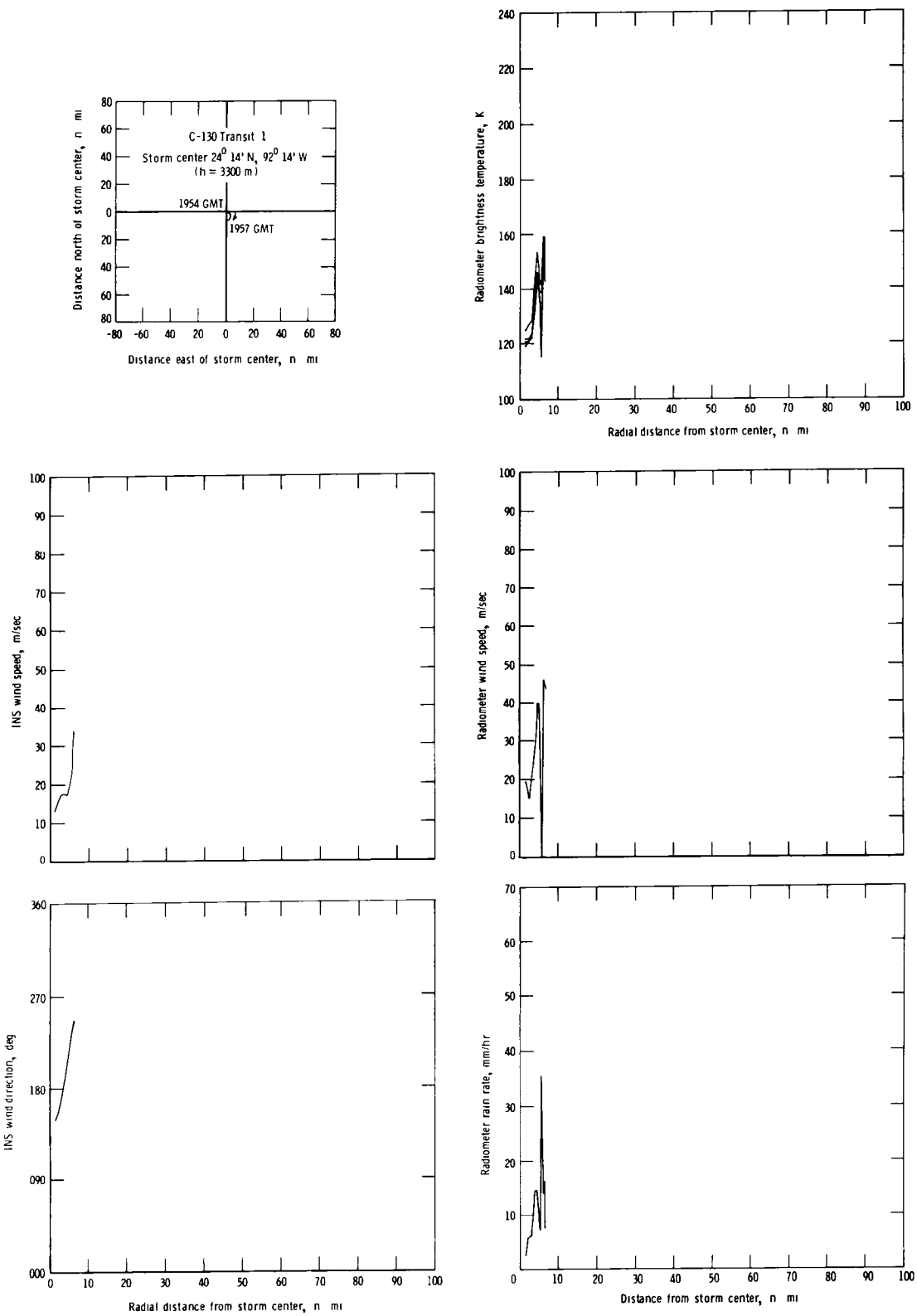

Figure C30.- Flight track, INS wind speed, INS wind direction, radiometric brightness temperatures, radiometer wind speed, and radiometer rain rate for C-130 transit I, August 8, 1980.

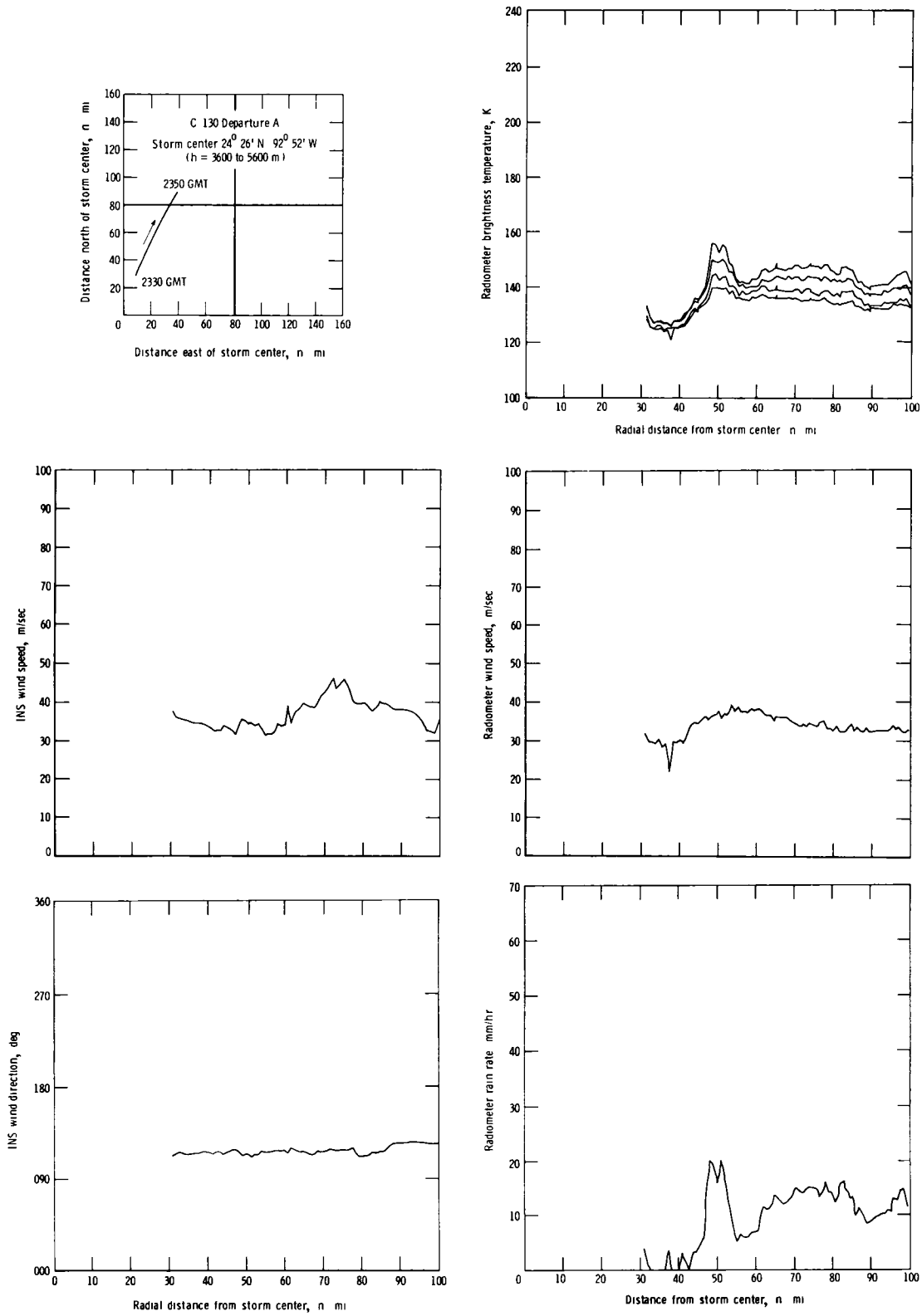

Figure C31.- Flight track, INS wind speed, INS wind direction, radiometric brightness temperatures, radiometer wind speed, and radiometer rain rate for C-130 departure A, August 8, 1980.

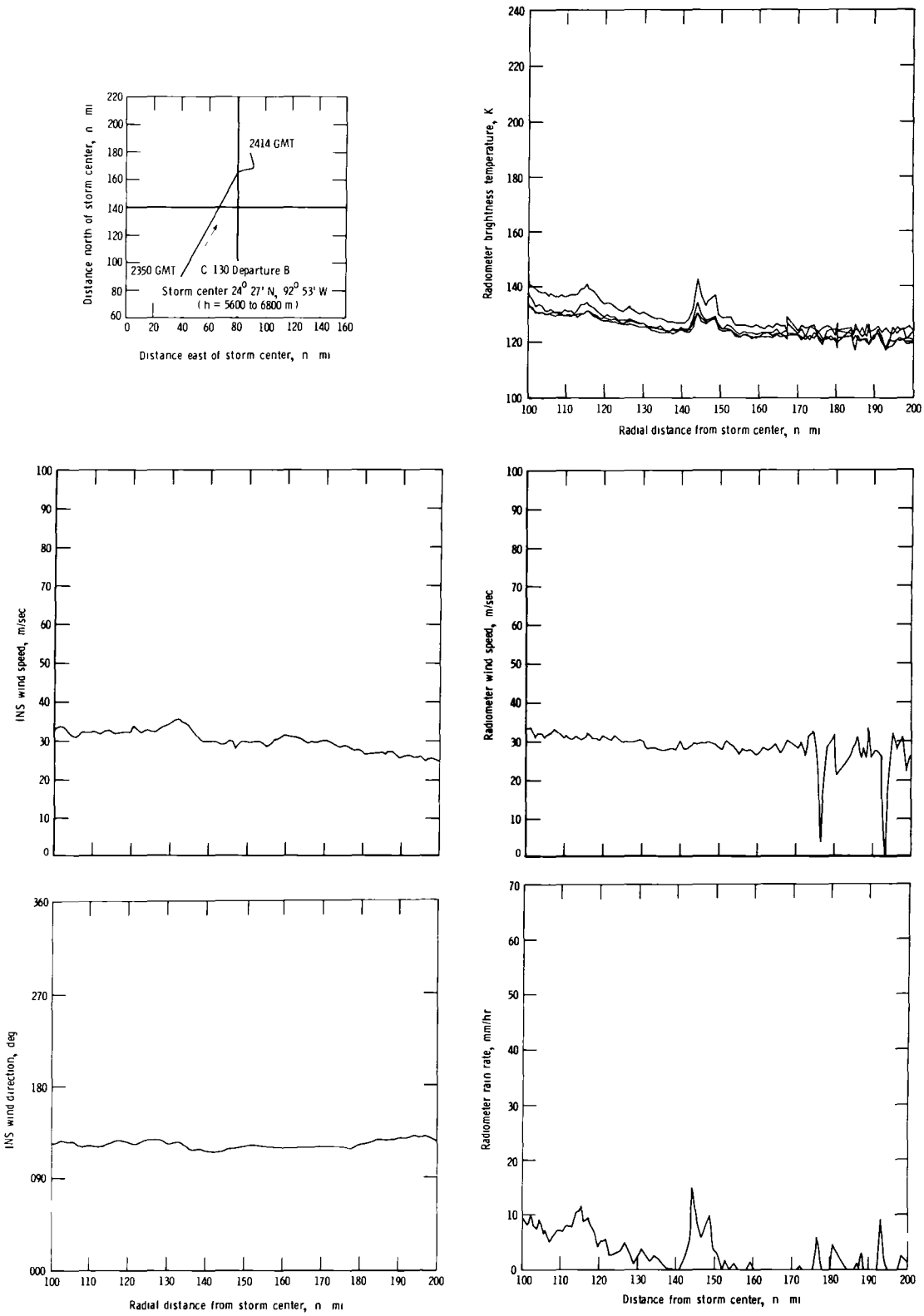

Figure C32.- Flight track, INS wind speed, INS wind direction, radiometric brightness temperatures, radiometer wind speed, and radiometer rain rate for C-130 departure B, August 8, 1980.

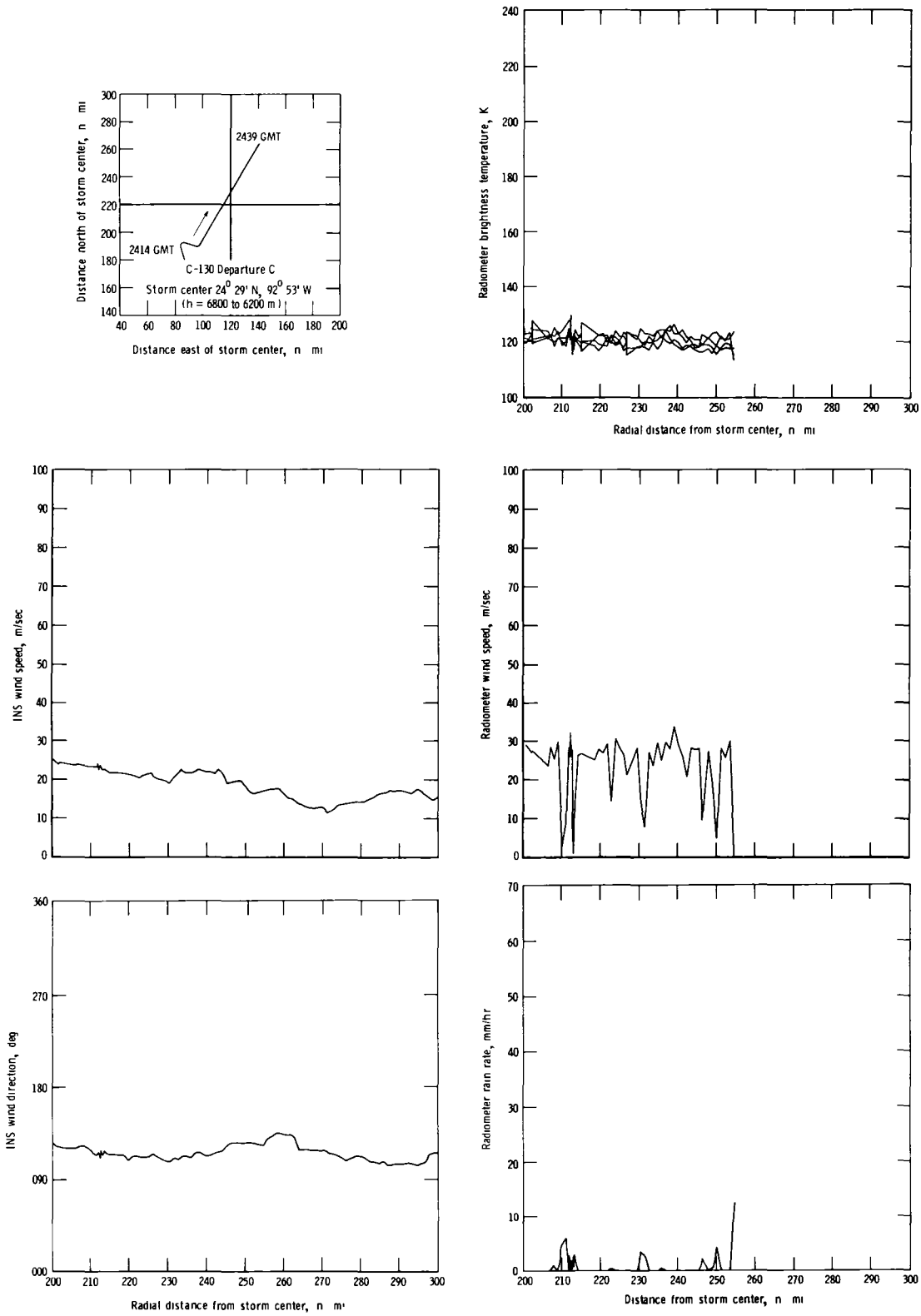

Figure C33.- Flight track, INS wind speed, INS wind direction, radiometric brightness temperatures, radiometer wind speed, and radiometer rain rate for C-130 departure C, August 8, 1980.

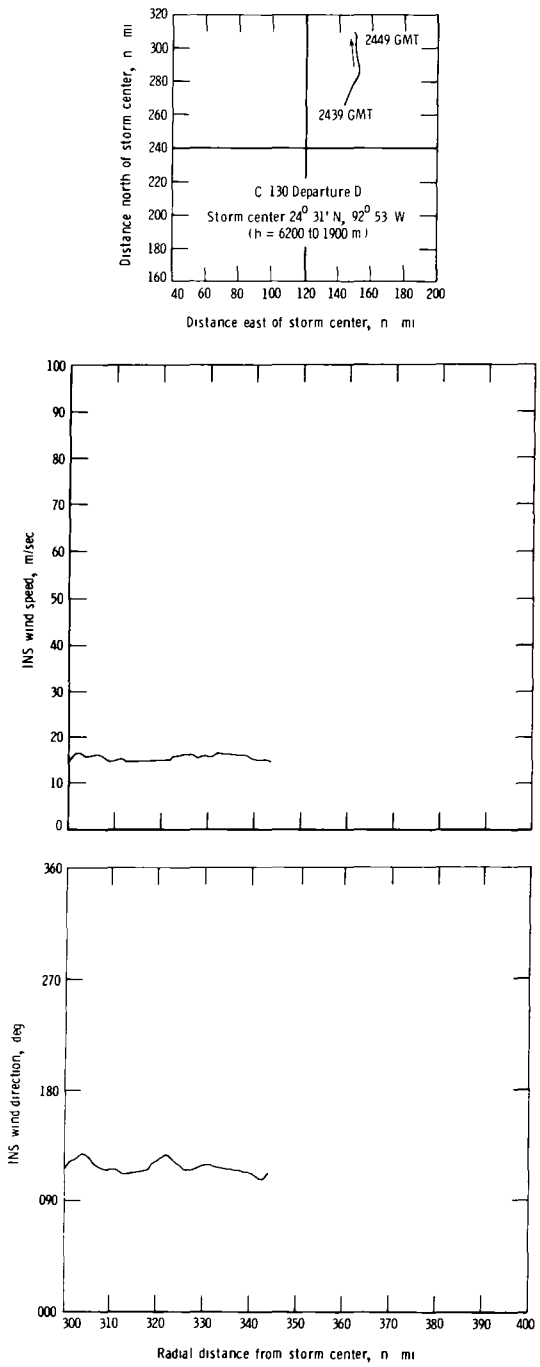

Figure C34.- Flight track, INS wind speed, and INS wind direction for C-130 departure D, August 8, 1980.

1 Report No	2 Government Accession No	3 Recipient's Catalog No
NASA TM-86390		

4 Title and Subtitle	5 Report Date
Active and Passive Microwave Measurements in Hurricane Allen	November 1985
	6 Performing Organization Code 506-58-23-01

7 Author(s)	8 Performing Organization Report No
Victor E. Delnore, Gilbert S. Bahn, William L. Grantham, Richard F. Harrington, and W. Linwood Jones	L-15775
	10 Work Unit No

9 Performing Organization Name and Address	11 Contract or Grant No
NASA Langley Research Center Hampton, VA 23665-5225	
	13 Type of Report and Period Covered Technical Memorandum

12 Sponsoring Agency Name and Address	14 Sponsoring Agency Code
National Aeronautics and Space Administration Washington, DC 20546-0001	

15 Supplementary Notes

The Hurricane Allen data are available on magnetic tape as a supplement to this report.

Victor E. Delnore and Gilbert S. Bahn: PRC Kentron, Inc., Hampton, Virginia.
William L. Grantham and Richard F. Harrington: Langley Research Center, Hampton, Virginia.
W. Linwood Jones: Harris Corp., Melbourne, Florida.

16 Abstract

This report summarizes the NASA Langley Research Center analysis of the airborne microwave remote sensing measurements of Hurricane Allen obtained on August 5 and 8, 1980. The instruments were the C-band stepped frequency microwave radiometer and the Ku-band airborne microwave scatterometer. They were carried aboard a NOAA aircraft making storm penetrations at an altitude of 3000 m and are sensitive to rain rate, surface wind speed, and surface wind vector. The wind speed is calculated from the increase in antenna brightness temperature above the estimated calm-sea value. The rain rate is obtained from the difference between antenna temperature increases measured at two frequencies, and wind vector is determined from the sea-surface normalized radar cross section measured at several azimuths.

Comparison wind data were provided from the inertial navigation systems aboard both the C-130 aircraft at 3000 m and a second NOAA aircraft (a P-3) operating between 500 and 1500 m. Comparison rain rate data were obtained with a rain radar aboard the P-3. Evaluation of the surface winds obtained with the two microwave instruments was limited to comparisons with each other and with the flight-level winds.

Two important conclusions are drawn from these comparisons: (1) the radiometer is accurate when predicting flight-level wind speeds and rain rate and (2) the scatterometer produces well-behaved and consistent wind vectors for the rain-free periods.

17 Key Words (Suggested by Author(s))	18 Distribution Statement
Remote sensing Microwave technology Hurricane reconnaissance Radiometer Scatterometer	Unclassified - Unlimited Subject Category 43

19 Security Classif (of this report)	20 Security Classif (of this page)	21 No of Pages	22 Price
Unclassified	Unclassified	145	A07

For sale by the National Technical Information Service, Springfield, Virginia 22161

End of Document